Physical and Chemical Approaches to Improving the Stability of Perovskite Solar Cells

A Thesis Submitted to the College of Graduate and Postdoctoral Studies and

Research

In Partial Fulfillment of the Requirements for the Degree of

Doctor of Philosophy

In the Department of Chemistry

University of Saskatchewan

Saskatoon

By

Soumya Kundu

Permission to Use

In presenting this thesis/dissertation in partial fulfillment of the requirements for a Postgraduate degree from the University of Saskatchewan, I agree that the Libraries of this University may make it freely available for inspection. I further agree that permission for copying of this thesis/dissertation in any manner, in whole or in part, for scholarly purposes may be granted by the professor or professors who supervised my thesis/dissertation work or, in their absence, by the Head of the Department or the Dean of the College in which my thesis work was done. It is understood that any copying or publication or use of this thesis/dissertation or parts thereof for financial gain shall not be allowed without my written permission. It is also understood that due recognition shall be given to me and to the University of Saskatchewan in any scholarly use which may be made of any material in my thesis.

Requests for permission to copy or to make other uses of materials in this thesis/dissertation in whole or part should be addressed to:

Dean
College of Graduate and Postdoctoral Studies
116 Thorvaldson Building, 110 Science Place
University of Saskatchewan
Saskatoon, Saskatchewan S7N 5C9
Canada

Department Head
Department of Chemistry
University of Saskatchewan
110 Science Place
Saskatoon, Saskatchewan S7N 5C9
Canada

Abstract

In recent years, perovskite solar cells (PSCs) have emerged as one of the most promising photovoltaic technologies. Their compatibility with low cost, simple fabrication techniques, high performance, and industrial scalability make them attractive for commercialization. However, moisture can cause serious damage to PSCs, resulting in complete device failure in a period of hours to days. Improved lifetimes are necessary for their future success. This thesis focuses on my efforts to improve the moisture stability of PSCs using two different approaches. The first approach focuses on applying hydrophobic barrier layers as hole-transport layers (HTLs) to improve the lifetime of PSCs, whereas the second approach is to find a stable perovskite composition.

The first section of this thesis focuses on polythiophene-based HTLs. According to previous studies, hydrophobic HTLs like poly(3-hexylthiophene) improve the stability of the underlying perovskite layer by blocking moisture ingress. This section discusses the synthesis of four poly(3-alkoxythiophenes) with different side chains having different degrees of hydrophobicity. The effect of the side chain is discussed in terms of its ability to protect thin films of $MAPbI_3$.

The second section builds on this work. Here, the problems with the poor device performance of the polythiophene HTLs are addressed. A new device architecture is introduced which uses a poly(3-hexylthiophene) nanowire network in a poly(methyl methacrylate) matrix as the HTL. Due to the incorporation of the poly(methyl methacrylate) matrix, there was a large increase in the stability of the device towards both liquid and vapor-phase water.

The third portion of this thesis investigates the decomposition processes of different well-known perovskite compositions. It focuses on the perovskites themselves and screens different perovskites for their moisture stability using in situ absorption spectroscopy and in situ grazing

incidence wide angle x-ray scattering. It provides a better understanding of perovskite degradation processes and takes us one step closer to PSCs with longer lifetimes.

This thesis discusses two approaches to improve the lifetime of PSCs. As moisture instability is an intrinsic problem of the PSCs, a stable perovskite composition is necessary for longer-lived devices. Similarly, it is also essential to develop better barrier layers to prevent moisture ingress.

Acknowledgements

First and foremost, I would like to express my gratitude to my supervisor Dr. Timothy L. Kelly for his continuous support and guidance in every step of my Ph.D. career. His continuous supervision and patience helped me to achieve better writing and presentation skills. I heartily thank you for being such an amusing influencer in my professional career.

I would also like to thank my advisory committee members; Dr. Ian Burgess, Dr. Stephen Urquhart, and Dr. Yansun Yao for discussion and positive feedback. I am grateful to all the faculty members; particularly, to Dr. Matthew Paige for providing me access to his laboratory facilities. I would like to thank the stuff at HXMA beamline in the Canadian Light Source. I would like to also thank all of the staffs of Department of Chemistry and Saskatchewan Structural Sciences Centre for their help.

I would like to thank all of my friends and colleagues, especially the past and present Kelly group members for their continuous support. I want to thank my friends outside lab.

I have been teaching several labs with different lab-managers over the past years. I would like to thank Dr. Pearson W. K. Ahiahonu, Dr. Adrian Clark, and Dr. Alexandra Bartole-Scott for their suggestions to improve my personal and presentation skills.

Finally, I would like to thank my parents, uncle and my little sister for their love, care and endless support. Without their support it would have been impossible to come so far.

Dedications

I would like to dedicate this thesis to my parents and my supervisor Dr.

Timothy L. Kelly

Table of Contents

Permission to Use ..... **i**

Abstract ..... **ii**

Acknowledgements ..... **iv**

Dedications ..... **v**

Table of Contents ..... **vi**

List of Figures ..... **xiii**

List of Equations ..... **xxiii**

List of Schemes ..... **xxiv**

List of Tables ..... **xxv**

List of Abbreviations ..... **xxvi**

1. Introduction **1**

1.1. Solar Cells *1*

1.1.1. Solar Energy 1

1.1.2. Different Types of Solar Cells 1

1.2. Perovskite Solar Cells *3*

1.2.1. Lead Halide Perovskites 3

1.2.1.1. Optical Properties 4

1.2.1.2. Crystal Structure 6

$MAPbI_3$ 7

$MAPbBr_3$ 8

$FAPbI_3$ 8

$CsPbI_3$ 9
$CsPbBr_3$ 11
1.2.2. Working Principles 11
1.2.2.1. Basic Principles 11
Short-Circuit Current Density (J_{SC}) 14
Open-Circuit Voltage (V_{OC}) 15
Fill Factor (FF) 15
Power Conversion Efficiency (PCE) 16
1.2.3. PSCs Device Physics 18
1.2.3.1. Working Principle 18
Mechanisms: 18
1.2.3.2. Principles of the Heterojunction Interface 23
1.2.3.3. Solar Cell Architectures 25
1.2.3.4. Evolution of Device Structures 26
1.2.3.5. Hysteresis 27
1.3. Stability of PSCs 28
1.3.1. Humidity 29
1.3.2. Heat 30
1.3.3. Light 31
1.3.4. Light and Air (Oxygen, Humidity) 32
1.3.5. Other Factors 33
1.4. Strategies to Improve Moisture Stability 35
1.4.1. Perovskite Materials 35
1.4.2. Hole-transport Materials (HTMs) 39
1.4.3. Electron-transport Materials (ETMs) 42

1.4.4. Electrodes 43
1.4.5. Additional Interfacial Layers 45
1.5. Experimental Techniques 48
1.5.1. GIWAXS 48
1.5.1.1. Theory 48
X-ray Diffraction 48
1.5.1.2. GIWAXS 52
1.5.1.3. GIWAXS as a Tool to Study Lead Halide Perovskites 59
1.6. Thesis Objectives 61
2. Hydrophobic Polythiophene Hole-transport Layers to Address the Moisture-induced Decomposition Problem of Perovskite Solar Cells 63
2.1. Introduction 63
2.2. Experimental Section 66
2.2.1. Materials 66
2.2.2. Synthesis 67
2.2.2.1. Synthesis of 3-((3,3,4,4,5,5,6,6,6-Nonafluorohexyl)oxy)thiophene (**1**) 67
2.2.2.2. Representative Synthesis of 3-(Alkoxy)thiophenes (**2**-**4**) 68
2.2.2.3. Representative Synthesis of 2,5-Dibromo-3-alkoxythiophene (**5**-**8**) 70
2.2.2.4. Representative Synthesis of Poly(3-alkoxythiophenes) (**9**-**12**) by Grignard Metathesis (GRIM) 71
2.2.2.5. Synthesis of ZnO Nanoparticles 72
2.2.2.6. Synthesis of Methylammonium Iodide 72
2.2.3. Solar Cell Fabrication 73

2.2.4. Characterization: 74
2.2.4.1. ^{1}H NMR and ^{13}C NMR 74
2.2.4.2. UV-visible Spectroscopy 74
2.2.4.3. Powder X-ray Diffraction 74
2.2.4.4. Scanning Electron Microscopy 75
2.2.4.5. Gel Permeation Chromatography (GPC) 75
2.2.4.6. Solar Cell Characterization 75
2.2.4.7. Water Vapor Stability Tests 76
2.3. Results and Discussion 76
2.3.1. Synthesis and Properties of the Polymers 76
2.3.2. Device Performance 87
2.3.3. Effect of Different Side Chains on Film Stability 92
2.4. Conclusions 97
3. Improving the Moisture Stability of Perovskite Solar Cells by Using PMMA/P3HT Based Hole-transport Layers 98
3.1. Introduction 98
3.2. Experimental Section 101
3.2.1. Materials 101
3.2.2. Characterization 102
3.2.2.1. UV-visible Spectroscopy 102
3.2.2.2. Powder X-ray Diffraction 102
3.2.2.3. Scanning Electron Microscopy 102
3.2.2.4. Atomic Force Microscopy 102

3.2.3. P3HT Nanowire Synthesis 102
3.2.4. Solar Cell Fabrication 103
3.2.5. Solar Cell Characterization 104
3.2.6. Liquid Water Stability Tests 104
3.2.7. Water Vapor Stability Tests 104
3.3. Results and Discussion 106
3.3.1. Device Design 106
3.3.2. PMMA/P3HT Film Morphology 106
3.3.3. Device Performance 109
3.3.4. Effect of Liquid Water on Device Performance 112
3.3.5. Effect of Water Vapor on Device Performance 116
3.3.6. In Situ UV/vis Spectroscopy 126
3.4. Conclusions 128
4. Moisture-induced Decomposition Mechanisms of Lead Halide Perovskites: an in Situ Absorption Spectroscopy and X-ray Scattering Study 129
4.1. Introduction 129
4.2. Experimental Section 131
4.2.1. Materials 131
4.2.2. Film Formation 131
4.2.3. Characterization 133
4.2.3.1. UV/vis Spectroscopy 133

4.2.3.2. GIWAXS 133
4.2.3.3. Data Processing 134
4.2.3.4. Powder X-ray Diffraction 135
4.3. Results and Discussion 135
4.3.1. Decomposition Rates of Different Perovskite Compositions 136
4.3.2. Degradation Mechanisms of Different Perovskite Compositions 140
4.3.2.1. $MAPbI_3$ 141
4.3.2.2. $FAPbI_3$ 144
4.3.2.3. $CsPbI_3$ 147
4.3.2.4. $Cs_{0.1}FA_{0.9}PbI_3$ 151
4.3.2.5. $Cs_{0.1}MA_{0.15}FA_{0.75}Pb(Br_{0.15}I_{0.85})_3$ 157
4.3.2.6. Comparison of the Degradation Process in $FAPbI_3$, $Cs_{0.1}FA_{0.9}PbI_3$, and $Cs_{0.1}MA_{0.15}FA_{0.75}Pb(Br_{0.15}I_{0.85})_3$ 164
4.3.2.7. $MAPbBr_3$ and $FAPbBr_3$ 165
4.3.2.8. $CsPbBr_3$ 170
4.4. Conclusion 176
5. Discussion, Conclusion and Future Work 178
5.1. Discussion and General Conclusion 178
5.2. Future Work 180
5.2.1. Proposed Project 1: Designing New Moisture-resistive Layers 180
5.2.1.1. Deposition of AgNW/PMMA or PET 181
5.2.2. Proposed Project 2: Study the Decomposition Kinetics of Ag Electrodes in Iodide and Bromide Perovskites in the Presence of Humidity 182
5.2.2.1. Experiment Design 182

5.2.3. Proposed Project 3: In situ Investigation of Decomposition of Layered Perovskites by UV-vis Spectroscopy and GIWAXS 183

6. References 184

List of Figures

Figure 1.1 The highest performance of solar cells in 2019 for various solar technologies.[7, 8] 3
Figure 1.2 Perovskite crystal structure. This illustration represents a unit cell (shown by a yellow dotted line) of perovskite ABX_3. 4
Figure 1.3 (**a**) UV–visible absorption spectra of $MAPb(Br_xI_{1-x})_3$ thin films for x values between 0 and 1. (**b**) Photograph of $MAPb(Br_xI_{1-x})_3$ thin films where x is between 0 and 1. 5
Figure 1.4 UV–visible absorption spectra of different perovskite absorbers: $MAPbI_3$ (black), $FAPbI_3$ (red), $CsPbI_3$ (blue), and $Cs_{0.1}MA_{0.15}FA_{0.75}Pb(Br_{0.85}I_{0.15})_3$ (olive). 6
Figure 1.5 Different phases of $MAPbI_3$: orthorhombic, tetragonal, and cubic. 8
Figure 1.6 Different phases of $FAPbI_3$: hexagonal and cubic. 9
Figure 1.7 Different phases of $CsPbI_3$: cubic (α), tetragonal (β), and two orthorhombic phases (a black γ- and a non-perovskite yellow δ-phase). 10
Figure 1.8 A solar cell is equivalent to a battery in a simple circuit. 12
Figure 1.9 The effect of light on the current-voltage characteristics of a p-junction. (**a**) In the dark, a solar cell has the same characteristics as diode with a small amount of dark current; (**b**) represents the equivalent circuit model in the dark; (**c**) upon illumination, the cell generates photocurrent, (**d**) represents the equivalent circuit model upon illumination; (**e**) and (**f**) represent a increase in light intensity increases the generation of photocurrent; (**g**) As the cell produces power the sign of the generated photocurrent is positive, represented by inverting the Y-axis. 13
Figure 1.10 Current voltage (*J-V*) cure of a solar cell in light and dark with all the *J-V* parameters: open-circuit voltage (V_{OC}), short-circuit current density (J_{SC}), maximum power density (P_{max}), fill factor (FF), and PCE. 14
Figure 1.11 Equivalent circuit models for (**a**) ideal and (**b**) non-ideal solar cells. 17
Figure 1.12 Effect of (**a**) increasing series resistance and (**b**) reducing shunt resistance. 18
Figure 1.13 Absorption through the band-to-band transition when an incident photon has higher energy than the bandgap. 19
Figure 1.14 Absorption assisted by defect states when an incident photon has lower energy than the bandgap. 20

Figure 1.15 Schematic illustration of all three-recombination process in PSC (**a**) band-to-band recombination involving a direct recombination between electron and hole from band-to-band, (**b**) trap-assisted recombination involving capture of either electron or hole in the trap state and (**c**) Auger recombination involving transfer of energy of an electron (or hole) to other charge carrier to allow non-radiative recombination either with electron (or hole). 23
Figure 1.16 Illustration of the operation of a p-i-n diode, showing a cross-section, the energy band diagram under forward bias, and the carrier generation characteristics. V is the applied bias, I is the current, R_L is the load resistance, and V_{bi} is the built-in potential, E_F is the quasi-Fermi level of the respective semiconductors. 24
Figure 1.17 Illustration of the operation of a p-i-n diode under open (**a**) and short-circuit (**b**) conditions. V is the applied bias, I is the current, R_L is the load resistance, and V_{bi} is the built-in potential..... 25
Figure 1.18 PSCs architectures: illustration of different types of PSCs; left based on presence of mesoscopic layer mesoscopic and planar structures; and right based on arrangement of charge transport layers regular (n-i-p) and inverted (p-i-n) structures. 26
Figure 1.19 Hysteresis in current-voltage measurement of a PSC measured under AM 1.5 G illumination. 28
Figure 1.20 Decomposition of $MAPbI_3$ perovskite proceeds via hydration to $MAPbI_3 \cdot H_2O$, followed by the formation of PbI_2 in presence of humidity..... 30
Figure 1.21 Strategies to produce perovskites with reduced dimensionality (2D/3D perovskites): (**a**) Variation of perovskite dimensionality from 3D to 2D with improved device stability. Reproduced from ref ([149]). Copyright 2016 American Chemical Society. (**b**) Device architecture used by Grancini et al. to achieve employing a 2D/3D perovskite with 1 year stability under 1 sun illumination in an ambient atmosphere. Reprinted with permission from ref ([150]). Copyright 2017 Springer Nature, under a Creative Commons 4.0 License. (**c**) Schematic showing 2D perovskite that resides at the grain boundaries of the bulk 3D perovskite. Reprinted with permission from ref ([151]). Copyright 2017 Springer Nature..... 38
Figure 1.22 Bragg's law: A two-dimensional crystal lattice and a set of imaginary planes is represented by the grid. The diffracted x-rays exhibit constructive interference when the distance

between paths of the incident x-rays and scattered x-rays differs by an integer number of wavelength ($n\lambda$)..... 50
Figure 1.23 Scattering vector $\boldsymbol{q}$ and its relation with wave vectors..... 51
Figure 1.24 An illustration of the diffractometer used in the GIWAXS experiment at the beamline of CLS..... 55
Figure 1.25 Data processing: (**a**) raw diffraction pattern as collected by a 2D detector, (**b**) the same diffraction pattern after reshaping with respect to q_z and q_r, (**c**) the same diffraction pattern after reshaping and accounted for the missing wedge along the q_z..... 57
Figure 1.26 Schematic diagram of grazing-incidence scattering geometry in the sample reference frame. Reproduced with permission of the International Union of Crystallography from reference [214]..... 58
Figure 1.27 Illustration of film crystallinity and the corresponding GIWAXS patterns of: (**a**) crystallites with isotropic distribution, (**b**) crystallites with out-of-plane preferential orientation, (**c**) crystallites with highly oriented out-of-plane preferential orientation..... 59
Figure 2.1 (**a**) Normalized absorbance at 410 nm as a function of time for $MAPbI_3$ (open circles), $MAPbI_3$/spiro-OMeTAD (open squares), $MAPbI_3$/PTAA (open diamonds), and $MAPbI_3$/P3HT (open triangles) films exposed to a 98 ± 2% RH environment at 22.8 ± 0.5 °C. Reproduced with permission of the American Chemical Society from reference ([68]). (**b**) Schematic diagram of dense, crystalline regioregular P3HT. The lamellae of polymer chains in the ac plane are stacking to the b axis, which corresponds to the longitudinal axis of nanofibers, by π - π interaction. Reproduced with permission of the American Physical Society from reference ([233])..... 64
Figure 2.2 Structures of the poly(3-alkoxythiophene) HTLs, arranged in order from hydrophobic to hydrophilic (left to right, respectively)..... 66
Figure 2.3 Schematic of fabrication of solar cells..... 74
Figure 2.4 Schematic illustration of the RH control setup for in situ UV/vis spectroscopy..... 76
Figure 2.5 ^{1}H NMR of P3HT in $CDCl_3$..... 80
Figure 2.6 ^{1}H NMR of α-methylene protons in the 3-position of the P3HT in $CDCl_3$..... 81
Figure 2.7 ^{1}H NMR of P3OFHT in $CDCl_3$..... 81
Figure 2.8 ^{1}HNMR of α-methylene protons in the 3-position of the P3OFHT in $CDCl_3$..... 82
Figure 2.9 ^{1}H NMR of P3ODDT in $CDCl_3$..... 82

Figure 2.10 ^{1}H NMR of α-methylene protons in the 3-position of the P3ODDT in $CDCl_3$. 83
Figure 2.11 ^{1}H NMR of P3OHT in $CDCl_3$. 83
Figure 2.12 ^{1}H NMR of α-methylene protons in the 3-position of the P3OHT in $CDCl_3$. 84
Figure 2.13 ^{1}H NMR of P3OEGT in $CDCl_3$. 84
Figure 2.14 ^{1}H NMR of α-methylene protons in the 3-position of the P3OEGT in $CDCl_3$. 85
Figure 2.15 Normalized absorbance of different polymers in $CHCl_3$ solutions. 87
Figure 2.16 (**a**) Schematic of the PSC architecture used in this work; (**b**) *J-V* curves of the highest performing devices with different polymer HTLs. 88
Figure 2.17 Box and whisker plots of device parameters for PSCs with different polymer HTLs: (**a**) short-circuit current density, (**b**) open-circuit voltage, (**c**) fill factor, and (**d**) power conversion efficiency. The solid square denotes the mean, the horizontal line denotes the median, the box boundaries mark the 25th and 75th percentiles, the whiskers mark 1.5 × the interquartile range, and the crosses denote maximum and minimum values. 89
Figure 2.18 *J-V* curves in both scan directions for devices with various HTLs: (**a**) P3OFHT, (**b**) P3ODDT, (**c**) P3OHT, (**d**) P3HT. *J-V* curves were measured at a scan rate of 0.83 $V \cdot s^{-1}$. 92
Figure 2.19 Water contact angle for different polymers. 93
Figure 2.20 (**a**) Absorption spectra of a $MAPbI_3$ film in a high RH (98% ± 2%) environment; spectra were acquired at 15 min intervals and the inset shows the absorbance at 410 nm as a function of time; (**b**) normalized absorbance at 410 nm as a function of time for $MAPbI_3$ films with different polymer coatings. 95
Figure 2.21 UV/vis absorption spectra of glass/$MAPbI_3$/HTL films in a RH = 98 ± 2% environment, acquired at 15 min intervals: (**a**) P3OFHT, (**b**) P3ODDT, (**c**) P3OHT, (**d**) P3HT, and (**e**) P3OEGT. 96
Figure 3.1 (**a**) Schematic architecture of the investigated device consisting of sequential layers of FTO as transparent electrode, a TiO_2 compact layer, a mesostructured layer of Al_2O_3 coated with $MAPbI_{3-x}Cl_x$ and the hole-transporting structure composed of a P3HT/SWNT layer in-filled with a PMMA matrix. (**b**) A photograph of a complete perovskite solar cell employing a SWNT hole-extraction layer placed under a flowing tap with the active layer on the top side of the glass directly under the water flow (left-hand side). Current density–voltage plots measured under AM1.5 simulated sunlight of 100 $mW \cdot cm^{-2}$ irradiance of the same perovskite solar cell before and after

being placed under the running water for 1 minute. Reproduced with permission of the American Chemical Society from reference ([118]). 99
Figure 3.2 Schematic of the device architecture used in this study. The HTL consists of a thin, compact layer of P3HT, followed by a thicker layer of P3HT nanowires suspended in a PMMA matrix. 101
Figure 3.3 Schematic illustration of the RH control setup for in situ UV/vis spectroscopy..... 105
Figure 3.4 Schematic illustration of the RH control setup for measuring device lifetime. 105
Figure 3.5 AFM images (height image) of PMMA/P3HT thin films on glass substrates, with varying PMMA/P3HT ratios: (**a**) 95 : 5; (**b**) 90 : 10; (**c**) 85 : 15; (**d**) 80 : 20. (**e**) AFM image (phase image) and (**f**) SEM image of 85 : 15 PMMA/P3HT films deposited on SiO_2/ZnO/$MAPbI_3$/P3HT substrates. 107
Figure 3.6 AFM images of PMMA/P3HT thin films on SiO_2/ZnO/$MAPbI_3$/P3HT substrates with different PMMA/P3HT ratios: (**a**) 95:5, height image; (**b**) 95:5, phase image; (**c**) 90:10, height image; (**d**) 90:10, phase image; (**e**) 85:15, height image; (**f**) 85:15, phase image; (**g**) 80:20, height image; (**h**) 80:20, phase image. 108
Figure 3.7 Cell performance parameters for devices made with varying HTLs: (**a**) J_{SC}; (**b**) V_{OC}; (**c**) FF; (**d**) PCE. The crosses denote the 1st and 99th percentiles; the bars denote the maximum and minimum values; the box boundaries mark the 25th and 75th percentiles; the horizontal line denotes the median; the solid square denotes the mean. (**e**) *J–V* curve of the champion devices with the various HTLs, measured at a scan rate of 0.1 $V \cdot s^{-1}$. (**f**) *J–V* curves for devices made with 90 : 10 PMMA/P3HT HTLs, deposited at different spin speeds. 111
Figure 3.8 *J-V* curves in both scan directions for devices with various HTLs: (**a**) P3HT; (**b**) 95:5 (**c**) 90:10, (**d**) 85:15, (**e**) 80:20 PMMA/P3HT. *J-V* curves were measured at a scan rate of 0.1 $V \cdot s^{-1}$. 112
Figure 3.9 Photographs of polymer-coated perovskite films exposed to liquid water for 1 minute: (**a**) 90:10 PMMA/P3HT-coated, before; (**b**) 90:10 PMMA/P3HT-coated, after; (**c**) P3HT-coated, before; (**d**) P3HT-coated, after. 113
Figure 3.10 Absorption spectra of polymer-coated perovskite films, before and after exposure to liquid water for 1 minute: (**a**) P3HT; (**b**) 95:5, (**c**) 90:10, (**d**) 85:15, and (**e**) 80:20 PMMA/P3HT. 114

Figure 3.11 pXRD patterns of polymer-coated perovskite films, before and after exposure to liquid water for 1 minute: (**a**) P3HT; (**b**) 95:5, (**c**) 90:10, (**d**) 85:15, and (**e**) 80:20 PMMA/P3HT..... 115
Figure 3.12 *J-V* curves for devices with various HTLs, measured before and after exposure to liquid water for 1 minute: (**a**) P3HT-only; (**b**) 95:5, (**c**) 90:10, (**d**) 85:15, (**e**) 80:20 PMMA/P3HT. Scans were performed at a scan rate of 0.83 $V \cdot s^{-1}$ from forward bias to short-circuit..... 116
Figure 3.13 Normalized power conversion efficiency as a function of time for perovskite solar cells with silver electrodes, stored in a 35-45% RH environment. Error bars denote plus-or-minus one standard deviation from the mean. 118
Figure 3.14 Absorption spectra of perovskite solar cells with various HTLs before and after aging in air (RH = 35 – 45%): (**a**) P3HT; (**b**) 95:5, (**c**) 90:10, (**d**) 85:15, and (**e**) 80:20 PMMA/P3HT. 120
Figure 3.15 Photographs of the ITO/ZnO/$MAPbI_3$/HTLs/Ag devices after aging in air; the corrosion of the silver electrode in the P3HT control samples is easily apparent. 121
Figure 3.16 SEM images of the silver electrode of a P3HT control device: (**a**) as prepared, and (**b-d**) after 6 days of aging in air; (**c**) and (**d**) are higher magnification images of the electrode edge. 122
Figure 3.17 SEM images of the silver electrode of a 95:5 PMMA/P3HT device: (**a**) as prepared, (**b-d**) after 6 days of aging in air; (**c**) and (**d**) are higher magnification images of the electrode edge. 123
Figure 3.18 Normalized power conversion efficiency as a function of time for perovskite solar cells with (**a**) silver electrodes and (**b**) gold electrodes, stored in a 99 ± 1% RH environment. Error bars denote plus-or-minus one standard deviation from the mean. 125
Figure 3.19 Normalized absorbance at 410 nm as a function of time for polymer-coated perovskite films exposed to a 99 ± 1% RH environment. 127
Figure 4.1 Schematic illustration of the RH control setup to control the chamber humidity. ... 134
Figure 4.2 Representation of a cubic lead perovskite ($APbX_3$) unit cell and a list of the perovskite compositions studied..... 136
Figure 4.3 (**a**) Schematic representation of experimental setup; (**b**) a schematic representation of the films used for this experiment; (**c**) UV–vis spectra of a $MAPbI_3$ film exposed to flowing N_2 gas

with RH = 95 ± 5%, data acquired at 15 min intervals; (**d**) Normalized absorbance at 500 nm as a function of time for perovskite films with different compositions. 137
Figure 4.4 UV-vis spectra, acquired at 15 min intervals, of a perovskite thin films exposed to high humidity RH = 95 ± 5%; (**a**) $MAPbI_3$, (**b**) $FAPbI_3$, (**c**) $CsPbI_3$, (**d**) $Cs_{0.1}FA_{0.9}PbI_3$, (**e**) $Cs_{0.1}MA_{0.15}FA_{0.75}Pb(Br_{0.15}I_{0.85})_3$, (**f**) $MAPbBr_3$, (**g**) $FAPbBr_3$, (**h**) $CsPbBr_3$. 138
Figure 4.5 (**a**) Absorption spectra of a $FAPbBr_3$ thin film on glass: as-prepared (black line), after exposure to high relative humidity (RH = 95 ± 5%) for 16.75 hours (blue line) and after 71 hours (red line); (**b**) absorption spectra of a $MAPbBr_3$ thin film on glass: as-prepared (black line), after exposure to high relative humidity (RH = 95% ± 5%) for 0.75 hours (blue line) and 114.75 hours (red line). 140
Figure 4.6 2D GIWAXS patterns of $MAPbI_3$ films on glass when exposed to a 90 ± 5% RH environment. 142
Figure 4.7 Degradation of $MAPbI_3$ film when exposed to 90 ± 5% RH; (**a**) 2D contour plot showing the azimuthally integrated diffraction intensity as a function of both scattering vector (q) and time, (**b**) azimuthally-integrated GIWAXS pattern for $MAPbI_3$ exposed to high humidity (RH 90 ± 5%) at different time compared with predicted pXRD pattern of $MAPbI_3$, $MAPbI_3{\cdot}H_2O$, and PbI_2, and (**c**) absorption spectra of a $MAPbI_3$ thin film on glass: as-prepared (black line), after exposed to high relative humidity (RH = 95%) for 2 hours (red line) or after 4.25 hours (blue line). 143
Figure 4.8 2D GIWAXS patterns of $FAPbI_3$ films on glass when exposed to a 90 ± 5% RH environment. 145
Figure 4.9 Degradation of $FAPbI_3$ film when exposed to 90 ± 5% RH; (**a**) 2D contour plot showing the azimuthally integrated diffraction intensity as a function of both scattering vector (q) and time, (**b**) azimuthally-integrated GIWAXS pattern for $FAPbI_3$ exposed to high humidity (RH = 90 ± 5%) at different time compared with predicted pXRD pattern of α and δ-$FAPbI_3$, and PbI_2, (**c**) absorption spectra of a $FAPbI_3$ thin film on glass: as-prepared (black line), after exposed to high relative humidity (RH ≈ 95%) for 1.75 hours (red line) or after 3 hours (blue line). 146
Figure 4.10 2D GIWAXS patterns of $CsPbI_3$ films on glass, after 0 h, 0.02 h, and 0.24 h exposure to a 90 ± 5% RH environment. 148

Figure 4.11 Degradation of $CsPbI_3$ film when exposed to 90 ± 5% RH; (**a**) 2D contour plot showing the azimuthally integrated diffraction intensity as a function of both scattering vector (q) and time, (**b**) azimuthally-integrated GIWAXS pattern for $CsPbI_3$ exposed to high humidity (RH 90 ± 5%) at different time compared with predicted pXRD pattern of α and δ-$CsPbI_3$, (**c**) UV-vis spectra, acquired at 15 min intervals, of a $CsPbI_3$ film exposed to high humidity RH = 95 ± 5%; red line as prepared and blue line after 15 minutes. 149
Figure 4.12 2D contour plot showing the azimuthally integrated diffraction intensity as a function of both scattering vector (q) and time of $CsPbI_3$..... 151
Figure 4.13 2D GIWAXS patterns of $Cs_{0.1}FA_{0.9}PbI_3$ films on glass, after 0 h, 0.037 h, 0.56 h, 1.49 h, 2.23 h, 2.98, 3.72 h, 5.58 h, 7.07 h, and 7.56 h exposure to a 90 ± 5% RH environment. 153
Figure 4.14 Degradation of $Cs_{0.1}FA_{0.9}PbI_3$ film when exposed to 90 ± 5% RH; (**a**) 2D contour plot showing the azimuthally integrated diffraction intensity as a function of both scattering vector (q) and time, (**b**) azimuthally-integrated GIWAXS pattern for $Cs_{0.1}FA_{0.9}PbI_3$ exposed to high humidity (RH 90 ± 5%) at different time compared with predicted pXRD pattern of α and δ-$FAPbI_3$ and α and δ-$CsPbI_3$, and PbI_2, (**c**) absorption spectra of a $Cs_{0.1}FA_{0.9}PbI_3$ thin film on glass: as-prepared (black line), after exposed to high relative humidity (RH ≈ 95%) for 4 hours (red line), after 8 hours (blue line), after 16 hours, (green line) after 24 hours (purple line) and after 43.5 hours (orange line), (**d**) absorption spectra of a $Cs_{0.1}FA_{0.9}PbI_3$ thin film on glass fitted to $FAPbI_3$ (after 1.75 h, blue dotted line) and δ-$FAPbI_3$ (after 3 h, olive dotted line); $Cs_{0.1}FA_{0.9}PbI_3$ thin film after exposed to high relative humidity (RH ≈ 95%) for 8 hours (red solid line), 16 h or 24 h (magenta solid line). 154
Figure 4.15 Azimuthally-integrated GIWAXS pattern for $Cs_{0.1}FA_{0.9}PbI_3$ at t = 7.07 h and 7.56 h compared with predicted pXRD patterns of α-$FAPbI_3$, δ-$FAPbI_3$, and PbI_2. 156
Figure 4.16 2D GIWAXS patterns of $Cs_{0.1}MA_{0.15}FA_{0.75}Pb(Br_{0.15}I_{0.85})_3$ films on glass, at different time when exposed to a 90 ± 5% RH environment. 158
Figure 4.17 Degradation of $Cs_{0.1}MA_{0.15}FA_{0.75}Pb(Br_{0.15}I_{0.85})_3$ film when exposed to 90 ± 5% RH; (**a**) 2D contour plot showing the azimuthally integrated diffraction intensity as a function of both scattering vector (q) and time, (**b**) azimuthally-integrated GIWAXS pattern for $Cs_{0.1}MA_{0.15}FA_{0.75}Pb(Br_{0.15}I_{0.85})_3$ exposed to high humidity (RH 90 ± 5%) at different time compared with predicted pXRD pattern of α and δ-$FAPbI_3$, δ-$CsPbI_3$, and PbI_2, (**c**) UV-vis spectra,

acquired at 15 min intervals, at high humidity RH (95 ± 5%); black line as prepared and red line at t = 7 h , and blue line at t = 67 h. 159
Figure 4.18 Azimuthally-integrated GIWAXS pattern for $Cs_{0.1}MA_{0.15}FA_{0.75}Pb(Br_{0.15}I_{0.85})_3$ at t = 3.25 h and 3.55 h (after drying) compared with predicted pXRD patterns of α-$FAPbI_3$, δ-$FAPbI_3$, PbI_2, and δ-$CsPbI_3$..... 160
Figure 4.19 (**a**) 2D contour plot showing the azimuthally integrated diffraction intensity as a function of both scattering vector (q) and time $Cs_{0.1}MA_{0.15}FA_{0.75}Pb(Br_{0.15}I_{0.85})_3$ when exposed to 90 ± 5% RH, (**b**) azimuthally-integrated GIWAXS pattern for $FAPbI_3$ exposed to high humidity (RH 90 ± 5%) at different time compared with predicted pXRD pattern of α-$FAPbI_3$, δ-$FAPbI_3$, PbI_2, and δ-$CsPbI_3$..... 162
Figure 4.20 Azimuthally-integrated GIWAXS pattern for $Cs_{0.1}MA_{0.15}FA_{0.75}Pb(Br_{0.15}I_{0.85})_3$ at t = 1.02 h and t = 1.05 h compared with predicted pXRD patterns of α-$FAPbI_3$, δ-$FAPbI_3$, PbI_2, and δ-$CsPbI_3$. 163
Figure 4.21 Decomposition of $FAPbI_3$, $Cs_{0.1}FA_{0.90}PbI_3$, and $Cs_{0.1}MA_{0.15}FA_{0.75}Pb(Br_{0.15}I_{0.85})_3$; (**a**) Normalized absorbance at 500 nm as a function of time, azimuthally-integrated GIWAXS pattern at 90 ± 5% RH for (**b**) $FAPbI_3$, (**c**) $Cs_{0.1}FA_{0.90}PbI_3$, and (**d**) $Cs_{0.1}MA_{0.15}FA_{0.75}Pb(Br_{0.15}I_{0.85})_3$ respectively. 165
Figure 4.22 2D GIWAXS patterns of $MAPbBr_3$ films on glass, at different time when exposed to a 90 ± 5% RH environment. 166
Figure 4.23 (**a**) 2D contour plot showing the azimuthally integrated diffraction intensity as a function of both scattering vector (q) and time for $MAPbBr_3$, (**b**) azimuthally-integrated GIWAXS pattern for $MAPbBr_3$ at t = 0 h, and t = 8 h compared with predicted pXRD pattern. 166
Figure 4.24 2D GIWAXS patterns of $FAPbBr_3$ films on glass, at different time when exposed to a 90 ± 5% RH environment. 167
Figure 4.25 (**a**) 2D contour plot showing the azimuthally integrated diffraction intensity as a function of both scattering vector (q) and time for $FAPbBr_3$, (**b**) azimuthally-integrated GIWAXS pattern for $FAPbBr_3$ at t = 0 h, and t = 7.5 h compared with predicted pXRD pattern. 168
Figure 4.26 pXRD of $MAPbBr_3$ subjected to high humidity (RH 90 ± 5%). 169
Figure 4.27 pXRD of $FAPbBr_3$ subjected to high humidity (RH 90 ± 5%). 170

Figure 4.28 2D GIWAXS patterns of $CsPbBr_3$ films on glass, at different time when exposed to 90 ± 5% RH. 172
Figure 4.29 2D contour plot showing the azimuthally integrated diffraction intensity as a function of both scattering vector (q) and time of $CsPbBr_3$. 173
Figure 4.30 Azimuthally-integrated GIWAXS pattern for $CsPbBr_3$ exposed to high humidity (RH 90 ± 5%) at different time. 174
Figure 4.31 Effect of drying for $CsPbBr_3$, azimuthally-integrated GIWAXS pattern for $CsPbBr_3$ at t = 6.74 h, and t = 7.23 h. 175
Figure 4.32 Summary of the moisture-induced decomposition mechanism observed in different perovskite compositions..... 176
Figure 5.1 Schematic representation of the proposed architecture: FTO/TiO_2/ $Cs_{0.1}FA_{0.75}MA_{0.15}Pb(Br_{0.15}I_{0.85})_3$/spiro-OMeTAD/Au/(AgNW/PMMA or PET layer)/Au 181

List of Equations

Equation 1.1 6
Equation 1.2 7
Equation 1.3 12
Equation 1.4 13
Equation 1.5 14
Equation 1.6 15
Equation 1.7 15
Equation 1.8 15
Equation 1.9 16
Equation 1.10 17
Equation 1.11 20
Equation 1.12 21
Equation 1.13 21
Equation 1.14 49
Equation 1.15 50
Equation 1.16 50
Equation 1.17 50
Equation 1.18 50
Equation 1.19 52
Equation 1.20 57
Equation 1.21 58
Equation 1.22 58

List of Schemes

Scheme 1.1 29
Scheme 1.2 29
Scheme 1.3 30
Scheme 1.4 30
Scheme 1.5 31
Scheme 1.6 31
Scheme 1.7 32
Scheme 1.8 32
Scheme 1.9 32
Scheme 1.10 33
Scheme 1.11 33
Scheme 1.12 33
Scheme 2.1. 69

List of Tables

Table 1.1: A survey of HTMs used in PSCs to improve the long-term stability of PSCs with relevant parameters such as relative humidity, atmosphere, illumination, and UV irradiation. The figures of merit are the initial power-conversion efficiency, the rate of decreasing efficiency (in %/100 h), the total decrease in efficiency, as well as the decline in efficiency of the respective control system. 42

Table 1.2: Different top contact layer of PSCs and their corresponding stability in humid environments. 45

Table 1.3: Different passivation layers reported to improve moisture resistance of PSCs. 47

Table 2.1: Tabulated data for of different polymers with different parameters like contact angle, molecular weight and absorbance. 79

Table 2.2: Average device performance parameters for ITO/ZnO/$MAPbI_3$/HTLs/Ag devices with different HTMs. The associated uncertainties represent plus-or-minus one standard deviation from the mean. 90

Table 3.1: Average device performance parameters for ITO/ZnO/$MAPbI_3$/HTLs/Ag devices. The associated uncertainties represent plus-or-minus one standard deviation from the mean. 110

List of Abbreviations

1D	1 Dimensional
2D	2 Dimensional
3D	3 Dimensional
AFM	Atomic force microscopy
AVAI	Aminovaleric acid iodide
BA	*n*-butylammonium
CB	Conduction band
CBM	Conduction band minimum
CIGS	Copper indium gallium selenide
CLS	Canadian Light Source
$Đ$	Dispersity
E_g	Bandgap energy
ETL	Electron-transport layer
FA	Formamidinium
FB	Forward bias
FF	Fill factor
FTO	Fluorine doped tin oxide
GIWAXS	Grazing incidence wide angle x-ray scattering
GPC	Gel permeation chromatography
HTL	Hole-transport layer
HXMA	Hard X-ray MicroAnalysis

I_0	Reverse saturation current
I_{SC}	Short-circuit current
ITO	Indium tin oxide
J	Current density
J_0	Reverse saturation current density
J_{max}	Current density at maximum power point
J_{ph}	Photocurrent density
J_{SC}	Short-circuit current density
J-V	Current density-voltage
k_b	Boltzmann's constant
LED	Light emitting diode
Li-TFSI	Lithium-bis(trifluoromethanesulfonyl)imide
MA	Methylammonium
MFC	Mass flow controller
M_n	Number average molecular weight of polymer
M_w	Weight average molecular weight of polymer
n	Empirical ideality factor
NMR	Nuclear magnetic resonance
P3HT	Poly(3-hexylthiophene)
PCE	Power conversion efficiency
P_{max}	Maximum power density
PMMA	Poly(methyl methacrylate)

PV	Photovoltaics
pXRD	Powder x-ray diffraction
RH	Relative humidity
R_S	Series resistance
R_{Sh}	Shunt resistance
SC	Short-circuit
SEM	Scanning electron microscopy
Spiro-OMeTAD	2,2',7,7'-Tetrakis[*N*,*N*-di(4-methoxyphenyl)amino]-9,9'-spirobifluorene
T	Temperature
$\boldsymbol{t}$	Goldschmidt's tolerance factor
TBP	4-tert-butylpyridine
TCO	Transparent conductive oxide
THF	Tetrahydrofuran
UV-vis	Ultra violet and visible light
V	Applied voltage
VB	Valence band
VBM	Valence band maximum
V_{max}	Voltage at maximum power point
V_{OC}	Open-circuit voltage
X_n	Degree of polymerization
μ	Charge carrier mobility

μ	Octahedral factor

1. Introduction

1.1. Solar Cells

1.1.1. Solar Energy

In order to meet the rising energy demand of the twenty first century and to mitigate the damage caused by global warming, the demand for renewable energy is increasing. Wind, hydroelectric, geothermal and solar energy are the major sources of renewable energy. As of 2017, renewable energy accounted for an estimated 18.1% of total energy consumption.[1] Among them, solar energy is one of the most abundant, clean and desirable alternative energy sources. According to a study in 2001, the amount of solar energy received by the earth in 1.5 hours could supply the overall global energy consumed in one year.[2] Photovoltaic technologies can convert solar energy into electricity.

1.1.2. Different Types of Solar Cells

In 1839 French physicist Antoine-César Becquerel discovered the photovoltaic effect, a phenomenon of converting light into electricity.[3, 4] About 50 years later, solar cells based on selenium were constructed with a power conversion efficiency (PCE) of ca. 1% by Charles Fritts.[5] In the mid-twentieth century, silicon solar cells were introduced and later in the twentieth century there was a boost in solar cell research.[6] Since then, solar cells with more than 20% PCE have been reported based on different technologies.[7, 8] Among different solar technologies, the current commercial market is dominated by multi-crystalline silicon solar cells.[9] Silicon has a bandgap of 1.1 eV with a maximum calculated PCE of 32% based on the Shockley–Queisser limit. Even though multi-crystalline silicon solar cells are cheaper and more popular, they have lower

performance than single crystalline silicon solar cells. This is due to the presence of grain boundaries and dislocations resulting in lower *V*oc. Although silicon solar cells have PCEs of up to 26.6% this technology has some drawbacks.[7] Silicon has an indirect bandgap resulting in weak absorption which demands a very thick (200−400 μm) Si active layer.[10] High purity Si is also essential. As silicon solar cells are rigid, this technology is not suitable for high throughput roll-to-roll manufacturing.

Another commercial photovoltaic technology is GaAs based solar cells. They have the highest PCEs (28.8%) among all single-junction solar devices due to having a favorable bandgap of 1.4 eV and lower *V*oc losses.[7] However, due to the epitaxial growth of the GaAs layers, this technology is very expensive. Therefore, this technology is usually used for space applications such as satellites and spacecraft.[11]

CdTe and CIGS based solar cells are cheap thin film-based technologies. However, they have the lowest PCEs (record of 22.1%) among all commercially available technologies.[7] The toxicity of cadmium is also a major concern, though it can be minimized by recycling the cells and taking safety precautions. CdTe has a bandgap of 1.5 eV with a calculated Shockley–Queisser limit of 31.6%.

Besides these established commercial solar technologies, there are emerging photovoltaic technologies such as organic photovoltaics, quantum dots, and perovskites. These solar cells address some of the major issues faced by their predecessors such as cost-effectiveness, solution-based fabrication techniques, and scalability (**Figure 1.1**). In addition, they are flexible which allows them to make use of higher throughput methods like roll-to-roll manufacturing and inkjet printing.

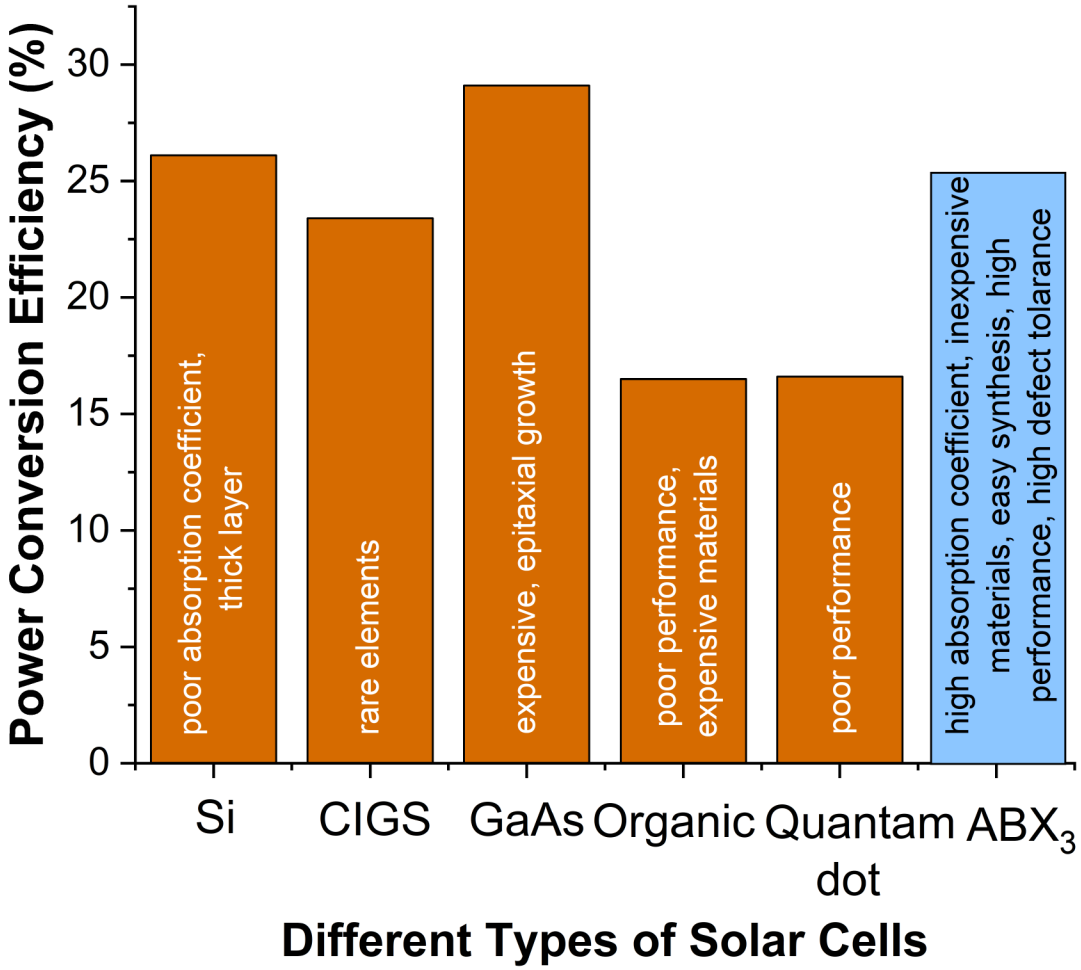

Figure 1.1 The highest performance of solar cells in 2019 for various solar technologies.[7, 8]

1.2. Perovskite Solar Cells

1.2.1. Lead Halide Perovskites

Lead halide perovskites are a family of hybrid organic-inorganic light-absorbing materials that have a perovskite crystal structure. They have a general formula of ABX_3, where A is either an organic cation like methylammonium, (MA, $CH_3NH_3^+$), formamidinium (FA, $NH_2CH{=}NH_2^+$) or an inorganic cation like Cs^+; B is Pb^{2+}; and X is a halogen anion (i.e., Cl^-, Br^-, I^-) (**Figure 1.2**). Based on the cation and anion choice, different types of simple perovskite compositions can be

formulated, such as $MAPbI_3$, $FAPbI_3$, and $CsPbI_3$, or $MAPbI_3$, $MAPbBr_3$, and $MAPbCl_3$. Mixed perovskites can also be formulated by replacing the A site by two or more cations and/or when the X site has multiple halides. For example, a complicated mixed perovskite like $Cs_{0.1}MA_{0.15}FA_{0.75}Pb(Br_{0.15}I_{0.85})_3$ can be made by having 10% Cs, 15% MA and 75% FA in the A site and 15% Br and 85% I in the X site.

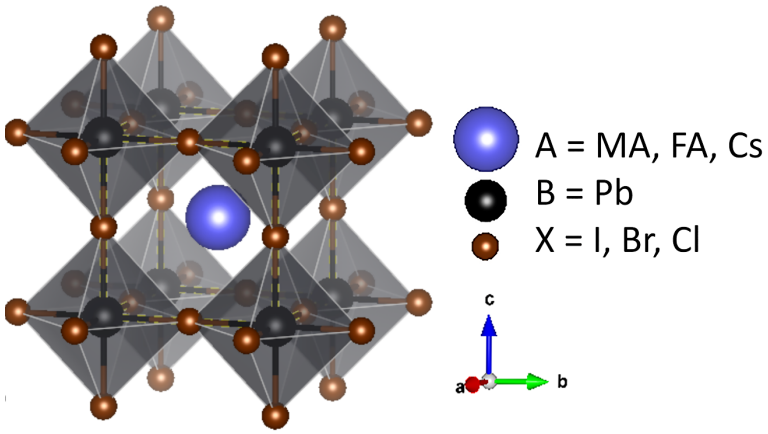

Figure 1.2 Perovskite crystal structure. This illustration represents a unit cell (shown by a yellow dotted line) of perovskite ABX_3.

1.2.1.1. Optical Properties

The optical properties of the perovskites are mainly dependent on the identity of A, B, and X. The valence band of these semiconductors is derived from the orbitals of the more electronegative halides, whereas the divalent metal B contributes to the conduction band.[12] The monovalent cation A helps to stabilize the perovskite crystal structure. Usually, the perovskites have a bandgap of 1.4 to 2.3 eV, depending upon the nature of the halides. For example, $MAPbI_3$, $MAPbBr_3$, and $MAPbCl_3$ have bandgaps of 1.55 eV, 2.24 eV, and 2.90 eV, respectively.[13] The bandgap can be tuned between 1.5 – 2.2 eV by varying the ratios of I^-/Br^- in $MAPbI_{3-x}Br_x$ (**Figure 1.3**).[14] Even though the monovalent cation "A" does not have any direct contribution to the valence or conduction

band, changing it can lead to a change in crystal structure which eventually causes a change in the bandgap.[14, 15] For example, replacing MA (ionic radius = 2.17 Å)[16] with FA cations (ionic radius = 2.53 Å)[16] can lead to alteration of the Pb-I bond angles, which causes the bandgap to change from 1.55 eV to 1.48 eV (**Figure 1.4**).[14, 17, 18] On the other hand, replacement of the MA cation by Cs (ionic radius = 1.67 Å)[16] leads to a blue-shifted absorption onset (1.73 eV) in $CsPbI_3$.[17, 18]

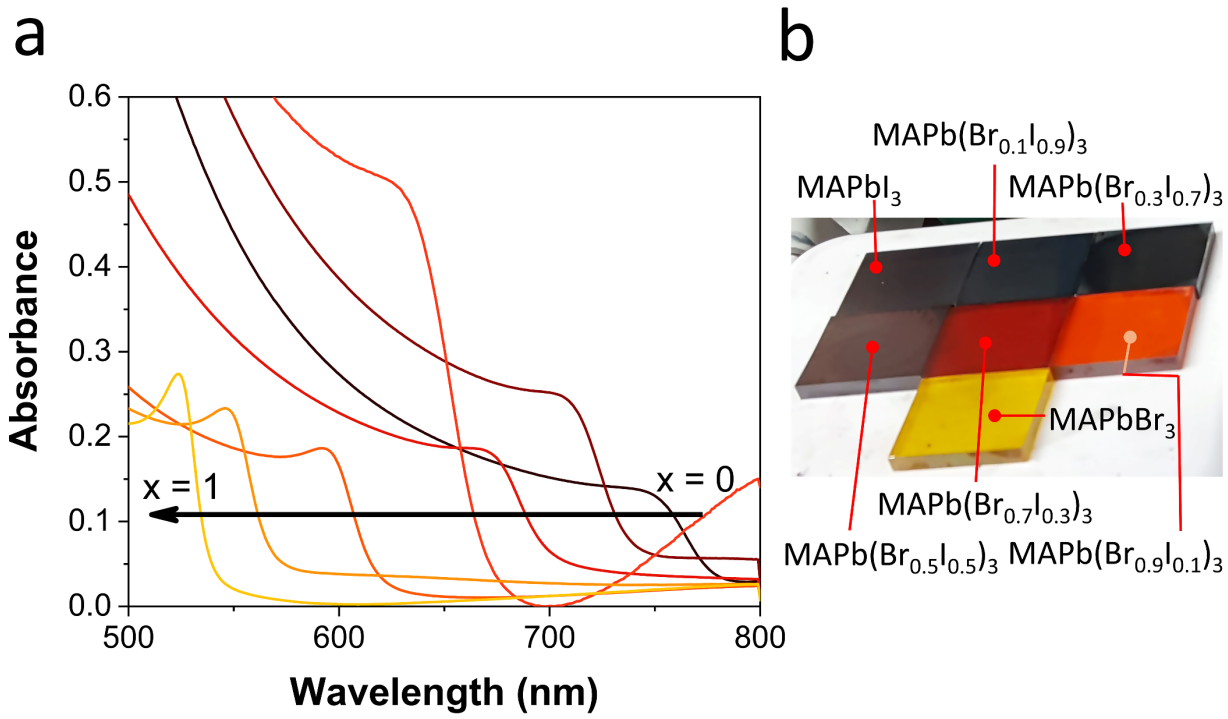

Figure 1.3 (**a**) UV–visible absorption spectra of $MAPb(Br_xI_{1-x})_3$ thin films for x values between 0 and 1. (**b**) Photograph of $MAPb(Br_xI_{1-x})_3$ thin films where x is between 0 and 1.

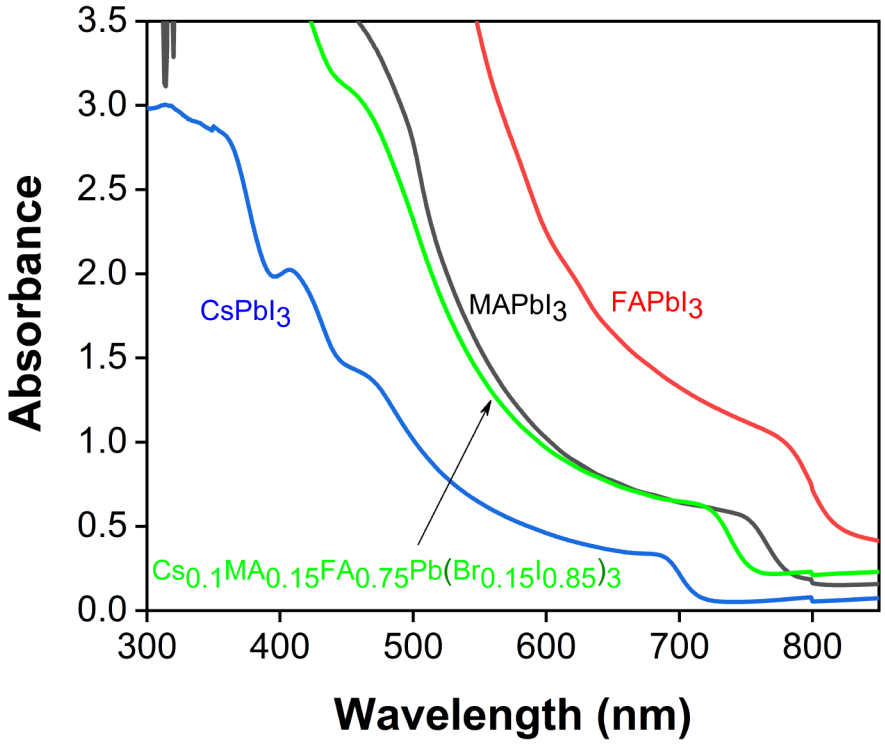

Figure 1.4 UV–visible absorption spectra of different perovskite absorbers: $MAPbI_3$ (black), $FAPbI_3$ (red), $CsPbI_3$ (blue), and $Cs_{0.1}MA_{0.15}FA_{0.75}Pb(Br_{0.85}I_{0.15})_3$ (olive).

1.2.1.2. Crystal Structure

A representative perovskite crystal structure is shown in **Figure 1.2**. A three dimensional framework of corner-sharing $[BX_6]$ octahedra can be seen, where the A site cations occupy the body-centered sites. In the framework, the B site cations are sixfold coordinated by X anions, and the A site cations are coordinated 12-fold by the halides. Two parameters can be used to predict the stability of the perovskite crystal structure: Goldschmidt's tolerance factor and the octahedral factor. Goldschmidt's tolerance factor (***t***) is used to calculate the distortion in the perovskite crystal structure and described by:

$$t = \frac{(r_A + r_X)}{\sqrt{2}(r_B + r_X)} \qquad \textbf{Equation 1.1}$$

Where, r_A, r_B, and r_X are the ionic radii of the A, B, and X-site ions, respectively. The octahedral factor ($\boldsymbol{\mu}$) can predict the structural stability of the perovskite and is described as:

$$\boldsymbol{\mu} = \frac{r_B}{r_X} \qquad \textbf{Equation 1.2}$$

For the stabilization of perovskite structure the two parameters should be $0.81 < \boldsymbol{t} < 1.11$ and $0.44 < \boldsymbol{\mu} < 0.90$. Under ideal conditions, $\boldsymbol{t}$ is close to 1, and there is no distortion in the unit cell implying that the unit cell has cubic symmetry. At high temperatures, the cubic structure (usually the α-phase) may still exist even though $\boldsymbol{t}$ is between 0.9 and 1. In the cubic structure, the A and B site cations have an ideal size. A slight deviation from that can cause lattice distortion, resulting in a reduction of the symmetry of the unit cell. Usually, when the A-site cation is smaller than the B-site cation, $\boldsymbol{t}$ lies between 0.71 and 0.89, which leads to lower symmetry phases, such as tetragonal (β-phase) or orthorhombic (γ-phase). When the A-site cation is too small, $\boldsymbol{t} < 0.71$, the perovskite structure does not form. On the other hand, if $\boldsymbol{t} > 1$, it implies that A is much bigger than B, and a distorted structure with hexagonal or tetragonal unit cells are formed. The 3D perovskite framework is reduced to a 2D layered structure or 1D chain structure (e.g., Aurivillius, Ruddlesden-Popper, and Dion-Jacobson phases) when $\boldsymbol{t}$ becomes significantly > 1.[19, 20]

Three-dimensional (3D) Lead Halide Perovskites

$MAPbI_3$

$MAPbI_3$ has $\boldsymbol{t} = 0.91$, owing to the ionic radii of MA, Pb, and I (2.17 Å, 1.19 Å and 2.20 Å).[16] It has three structural phases; a cubic *Pm-3m* phase, a tetragonal *I4/mcm* phase, and an orthorhombic *Pnma* phase depending upon temperature. At room temperature, it adopts a tetragonal structure. A phase transition from tetragonal to cubic occurs at 327 K due to weakening

of the N-H---I bonding and an increase in the orientational motion of the MA (**Figure 1.5**).[21] At lower temperature, below 162 K, $MAPbI_3$ exists in an orthorhombic phase (**Figure 1.5**).[21]

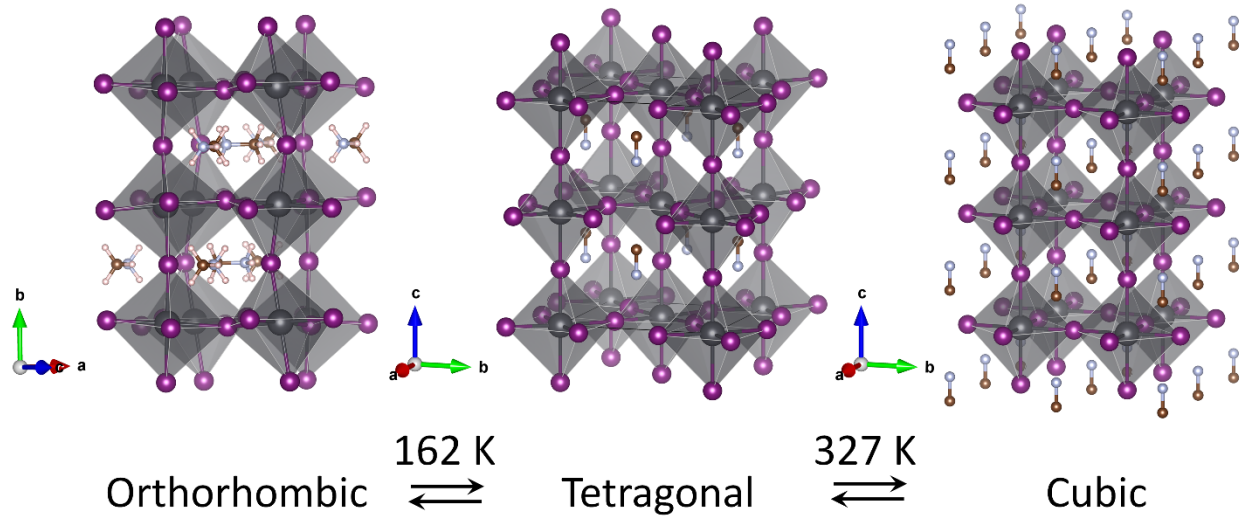

Figure 1.5 Different phases of $MAPbI_3$: orthorhombic, tetragonal, and cubic.

$MAPbBr_3$

$MAPbBr_3$ also exists in three different phases, depending upon the temperature. However, due to the smaller size of the bromide ion (1.96 Å), at room temperature, $MAPbBr_3$ has a cubic phase. $MAPbBr_3$ usually exists in an orthorhombic phase below 144.5 K, in a tetragonal phase with the *P4/mmm* space group at 149.5 K–155.1 K, and a tetragonal phase with the *I4/mcm* space group at 155.1 K–236.9 K.[22] It has a cubic phase above 236.9 K.[23]

$FAPbI_3$

Due to the larger size of the FA (2.53 Å)[16] cation, the tolerance factor increases and is ~1 (0.99) at room temperature.[24] At room temperature, $FAPbI_3$ crystallizes as a yellow hexagonal 2H-nonperovskite (δ) phase ($P6_3mc$). At 390 K, δ-$FAPbI_3$ undergoes a phase transformation to a pseudo-cubic or cubic perovskite ($Pm\bar{3}m$) which corresponds to the black α-phase (**Figure 1.6**).[25]

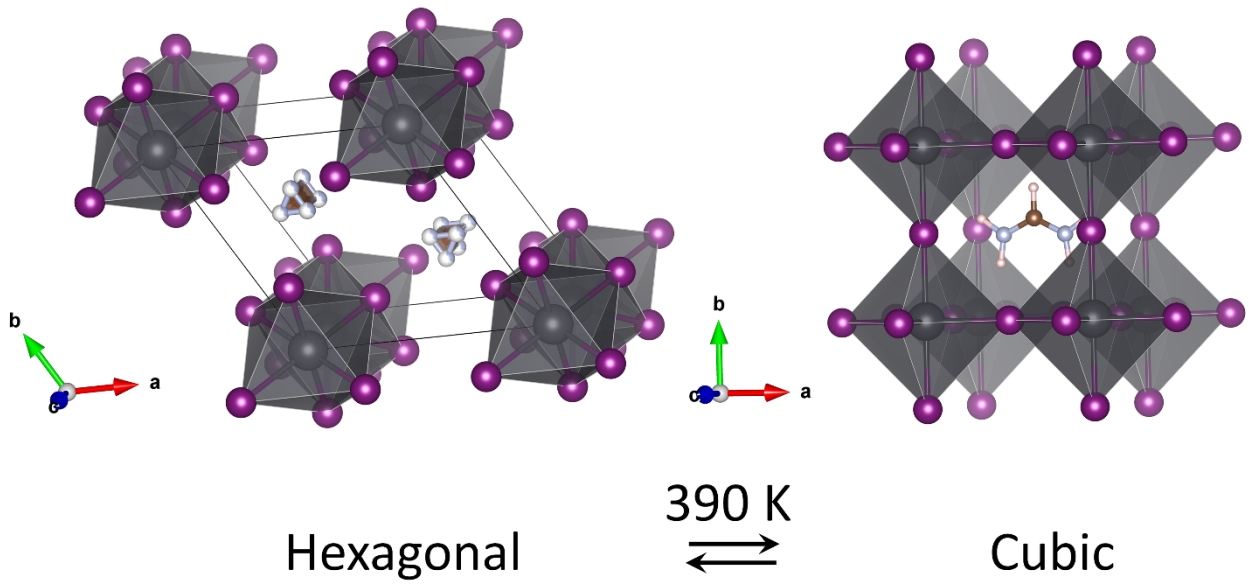

Figure 1.6 Different phases of $FAPbI_3$: hexagonal and cubic.

$CsPbI_3$

Due to the small size of Cs^+ (r = 1.67 Å)[16], $CsPbI_3$ unavoidably has a small Goldschmidt tolerance factor (t = 0.81).[16, 26] Therefore, at room temperature, it has a non-perovskite yellow δ-phase (orthorhombic, *Pnma*). $CsPbI_3$ has four different phases: a cubic (α), a tetragonal (β), and two orthorhombic phases (a black γ- and a non-perovskite yellow δ-phase) (**Figure 1.7**). At room temperature, $CsPbI_3$ usually crystallizes in the orthorhombic δ-phase (**Figure 1.7**). Upon heating above 600 K, δ-$CsPbI_3$ (*Pnma*) expands linearly and a phase transition occurs from δ- to α-$CsPbI_3$ (*Pm3m*).[27] Upon cooling, the high-symmetry cubic phase (α-phase, *Pm3m*) distorts initially to a tetragonal phase (β-phase, *P4/mbm*) followed by a further change to the orthorhombic (γ-phase, *Pbnm*) (**Figure 1.7**).[27] If the cubic α-$CsPbI_3$ is slowly cooled to room temperature from 650 K, yellow δ-$CsPbI_3$ forms; however, if it is cooled rapidly, γ-$CsPbI_3$ forms (**Figure 1.7**). This implies that δ-$CsPbI_3$ is the thermodynamic product and γ-$CsPbI_3$ is the kinetic product.[28] Both the black γ-$CsPbI_3$ and the yellow δ-$CsPbI_3$ are orthorhombic with the *Pnma* space

group. However, γ-$CsPbI_3$ has the $GdFeO_3$ structure whereas the δ-$CsPbI_3$ is a non-perovskite NH_4CdCl_3 structure type.[28, 29]

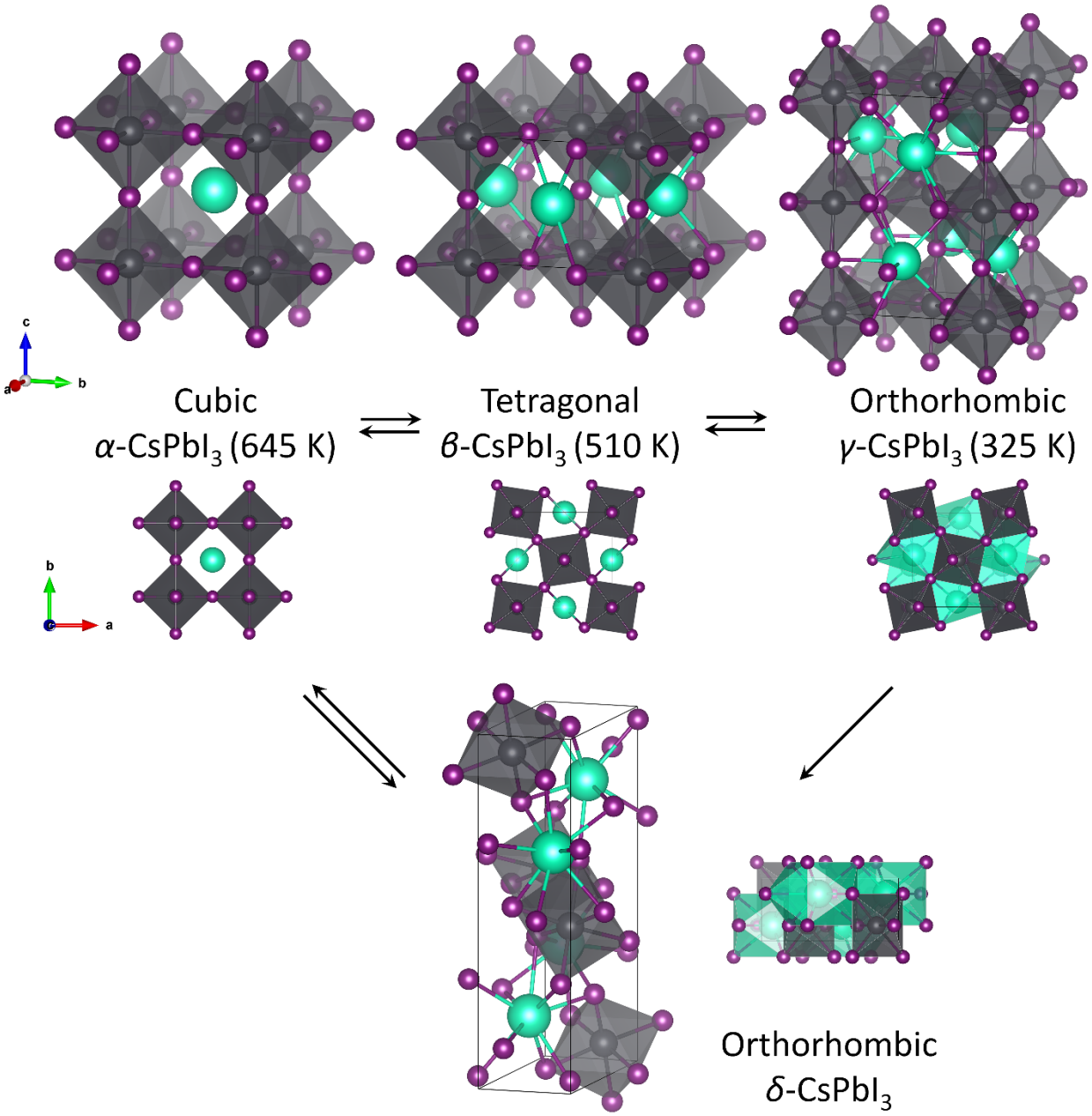

Figure 1.7 Different phases of $CsPbI_3$: cubic (α), tetragonal (β), and two orthorhombic phases (a black γ- and a non-perovskite yellow δ-phase).

$CsPbBr_3$

Due to the larger size of the I anion and the smaller size of the Cs cation, the tolerance factor of $CsPbI_3$ is only 0.807, and therefore, it undergoes more octahedral rotation distortion. When iodide is replaced by bromide, the tolerance factor increases to 0.824 for $CsPbBr_3$.[30, 31] Therefore, $CsPbBr_3$ becomes more stable at room temperature, although similar to $CsPbI_3$, three phases exist for $CsPbBr_3$. The orthorhombic (*Pnma*) to cubic ($Pm\bar{3}m$) perovskite phase transition occurs at a much lower temperature (~ 403 K)[31, 32] and there is a monoclinic (*P21/n*) to orthorhombic (*Pnma*) transition at 361 K[32].

1.2.2.Working Principles

1.2.2.1. Basic Principles

In order to understand the working principles of a perovskite solar cell (PSC), it is very important to comprehend the basic principles of a solar device. A solar device can be compared to a battery and can be represented by a simple electrical circuit as shown in **Figure 1.8**. In a battery, chemical energy is converted into electrical energy which develops a voltage between the two terminals of the battery. Similarly, in a solar cell, solar energy is used to develop a voltage between two terminals. When a solar cell is illuminated, it produces positive and negative charge carriers. With continuous illumination, an electrical potential is generated between the two terminals of the cell, which when connected by an external circuit, produce electricity.

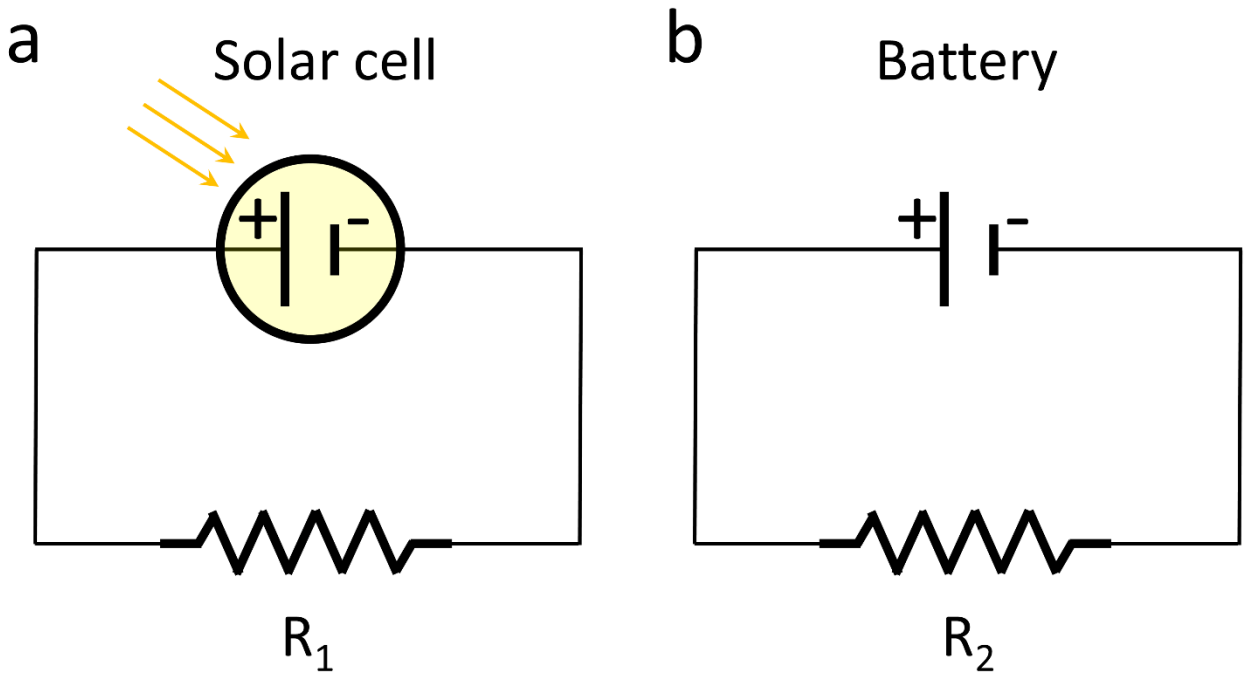

Figure 1.8 A solar cell is equivalent to a battery in a simple circuit.

In the absence of light (dark), a solar cell behaves like a diode. A diode is an electronic device which conducts current in one direction. An ideal diode has zero resistance in one direction, and infinite resistance in the other. In the dark, when an external bias (V) is applied, a current flows which can be expressed by the Shockley diode equation (**Equation 1.3**). As this current is generated in the dark, it is called the dark current ($I_{\text{dark}}(V)$).

$$I_{dark}(V) = I_0\,(e^{\frac{qV}{k_B T}} - 1) \qquad \textbf{Equation 1.3}$$

Where I_0 is a constant, k_B is Boltzmann's constant and T is the temperature in Kelvin. The dark current is a function of the applied bias (V) (**Figure 1.19a-b**). I_0 is the reverse saturation current density which is a measure of the leakage current through the diode. It is usually very small. It depends on temperature but is independent of the applied bias. Under illumination, the solar cell generates a current which is called the photocurrent (I_{light}) (**Figure 1.9c-d**). The photocurrent acts

in the opposite direction to the dark current. Therefore, the Shockley diode equation can be written as shown in **Equation 1.4**

$$I\,(V) = I_{light} - I_0\left(e^{\frac{qV}{k_B T}} - 1\right) \qquad \textbf{Equation 1.4}$$

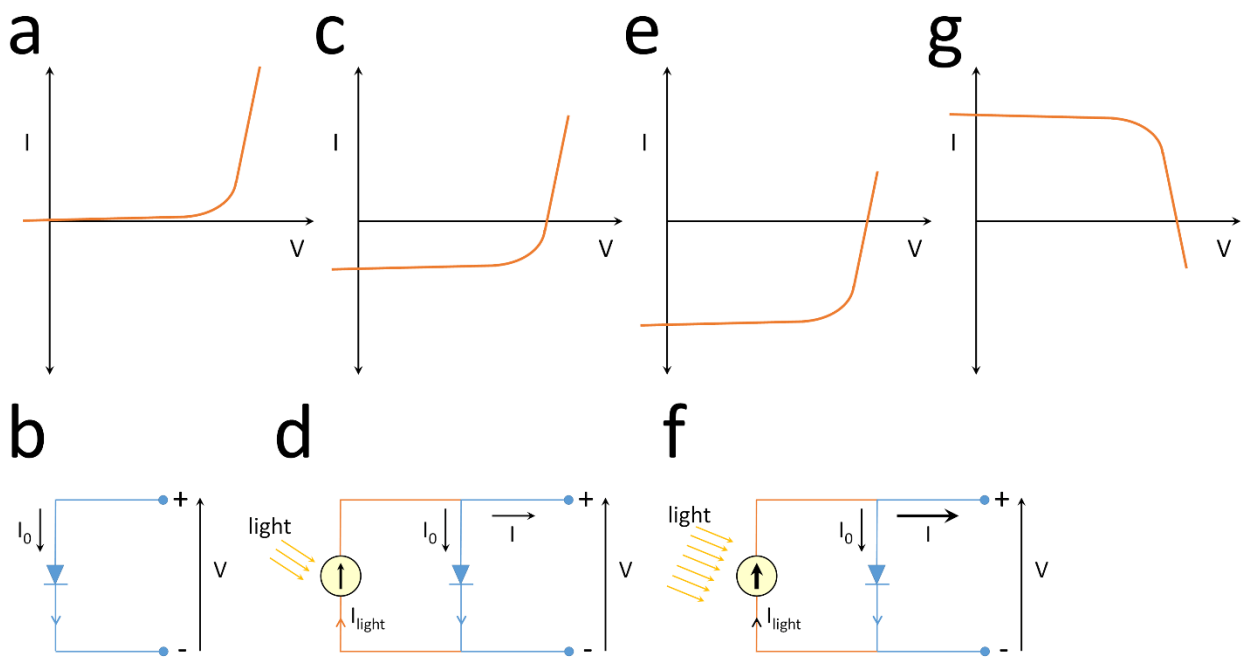

Figure 1.9 The effect of light on the current-voltage characteristics of a p-junction. (**a**) In the dark, a solar cell has the same characteristics as diode with a small amount of dark current; (**b**) represents the equivalent circuit model in the dark; (**c**) upon illumination, the cell generates photocurrent, (**d**) represents the equivalent circuit model upon illumination; (**e**) and (**f**) represent a increase in light intensity increases the generation of photocurrent; (**g**) As the cell produces power the sign of the generated photocurrent is positive, represented by inverting the Y-axis.

The photocurrent depends upon the light intensity (**Figure 1.9e-f**). The higher the intensity of the illuminated light, the greater the photocurrent. As current is generated by the solar cell, the direction of the photocurrent is considered positive. Since the current is proportional to the

illuminated area of a cell, current density (current over the illuminated area) is more reverent (**Figure 1.9g**). Therefore, rewriting **Equation 1.4** we get:

$$J\,(V) = J_{light} - J_0\,(e^{\frac{qV}{k_B T}} - 1) \qquad \textbf{Equation 1.5}$$

Plotting the above equation we get the current-voltage characteristic or *J-V* curve of a solar cell. **Figure 1.10** shows a representative *J-V* curve of a solar cell which provides all the parameters needed to compare the performance of one solar cell to another.

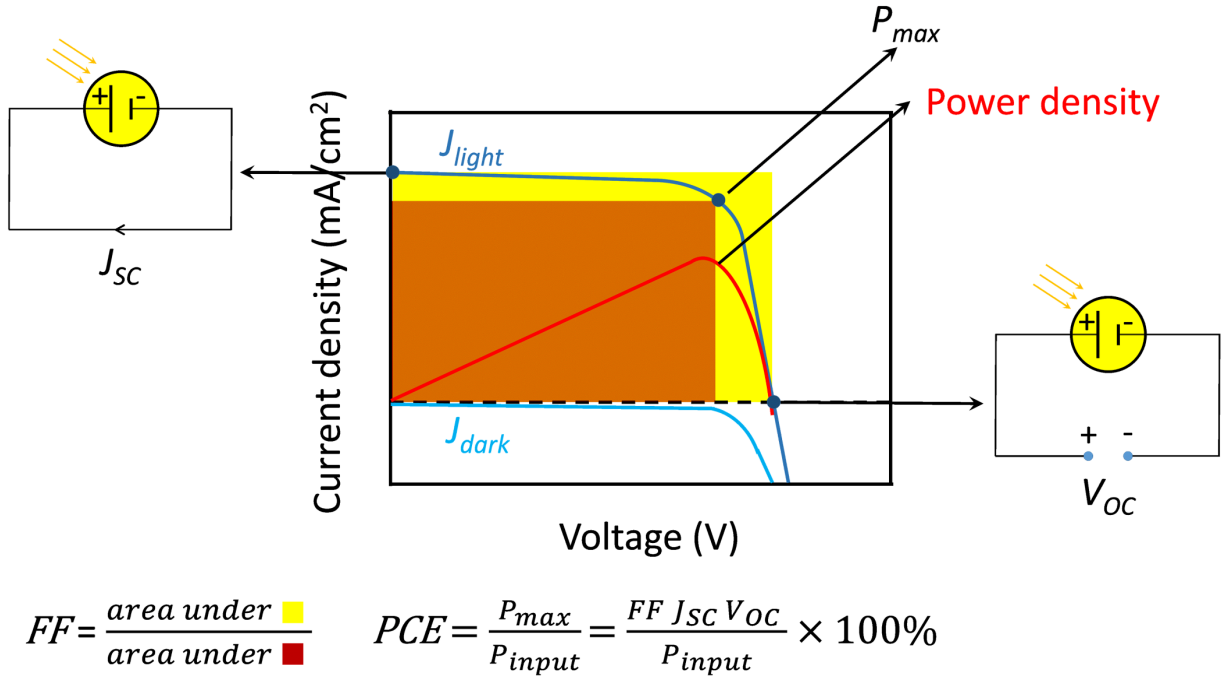

$$FF = \frac{area\ under\ \blacksquare}{area\ under\ \blacksquare} \qquad PCE = \frac{P_{max}}{P_{input}} = \frac{FF\ J_{SC}\ V_{OC}}{P_{input}} \times 100\%$$

Figure 1.10 Current voltage (*J-V*) cure of a solar cell in light and dark with all the *J-V* parameters: open-circuit voltage (V_{OC}), short-circuit current density (J_{SC}), maximum power density (P_{max}), fill factor (FF), and PCE.

Short-Circuit Current Density (J_{SC})

The short-circuit current density is the current density through the device when the voltage across the solar cell is zero. That means when the positive and negative terminals of the cell are

shorted together. It is the resulting current density due to charge generation and collection. In ideal conditions, the short-circuit current density and the photo-generated current density are identical. At $V = 0$, $J_{dark} = 0$. So, from **Equation 1.5** we get:

$$J\,(V) = \ 0 = J_{light} = J_{\mathrm{SC}} \qquad \textbf{Equation 1.6}$$

Several factors can influence J_{SC}, such as carrier generation and carrier mobility in the absorber, film morphology, and the composition of different layers (such as selective layers and electrodes) in a solar cell.

Open-Circuit Voltage (V_{OC})

The open-circuit voltage is the voltage at which no current is flowing. It occurs when the terminals are isolated (i.e. infinite resistance). It is the maximum voltage available from a solar cell. This occurs when the dark current and photocurrent are equal. Under ideal diode conditions, from **Equation 1.5**, we get:

$$V_{OC} = \frac{kT}{q}\ln\left(\frac{J_{SC}}{J_0} + 1\right) \qquad \textbf{Equation 1.7}$$

The V_{OC} depends on the bandgap of the absorber and the solar cell architecture.

The maximum power density (P_{max}) of the cell is the point on the *J-V* curve where the cell has maximum power output. J_{max} and V_{max} are the current density and voltage at this point.

Fill Factor (FF)

The fill factor of a solar cell is defined as the ratio of the maximum power density (P_{max}) to the product of V_{OC} and I_{SC}. It can be expressed as follows:

$$FF = \frac{P_{max}}{JscVoc} = \frac{J_{max}V_{max}}{JscVoc} \qquad \textbf{Equation 1.8}$$

Graphically, FF is measured by the ratio of the area of the red rectangle to the area of the yellow one in **Figure 1.10** Therefore, it is a measure of the 'squareness' of the *J-V* curve. FF in solar cells is always lower than 1 due to the presence of parasitic resistive losses.

Power Conversion Efficiency (PCE)

The power conversion efficiency is the most commonly used parameter to represent the performance of a solar cell. It is the ratio of the maximum output power (P_{output}) to the input power (P_{input}) from the illumination source. It is calculated using **Equation 1.9:**

$$PCE = \frac{P_{output}}{P_{input}} \times 100\% = \frac{J_{max}V_{max}}{P_{input}} \times 100\% = \frac{J_{SC}V_{OC}FF}{P_{input}} \times 100\% \qquad \textbf{Equation 1.9}$$

So far, for simplicity the behavior of an ideal solar cell has been depicted by **Figure 1.11a** and **Equation 1.5**. However, in reality, solar cells do not behave ideally. Parasitic resistances reduce the performance of the solar cell by dissipating power. Commonly, there are two major parasitic resistances; one is called the series resistance (R_S) and the other is called shunt resistance (R_{Sh}). Series resistance is the resistance in series which impedes current flow in the desired direction. Therefore, for an ideal solar cell it should be zero. Series resistance arises due to a number of factors like poor surface contacts, poor charge carrier mobility, the presence of impurities, and degradation. Due to high series resistance, the *J-V* curve near the V_{OC} is strongly affected, resulting in a decrease in the fill factor (**Figure 1.12a**). The shunt resistance arises when the current flows in alternative pathways. Therefore, to minimize the effect, R_{Sh} should be infinitely large for an ideal cell. A low shunt resistance is usually caused by several factors such as defects in the active layer, pinholes, degradation which aid in providing pathways leading to the leakage of current through the cell. Due to low shunt resistance, the *J-V* curve near the J_{SC} is strongly affected, resulting in a decrease in the fill factor (**Figure 1.12b**). Assuming the cell behaves as a linear

Ohmic resistor, the series and shunt resistances can be calculated from a *J-V* curve. The series resistance is equal to the inverse of the slope of the tangent at V_{OC} whereas the shunt resistance is the inverse of the slope of the tangent at J_{SC}. **Figure 1.11b** represents a simple circuit diagram of a solar cell after including the two resistances. After incorporating the contributions from R_s and R_{sh} **Equation 1.5** can be modified as follows:

$$J\,(V) = J_{light} - J_0\left[e^{\frac{e(V+JR_S)}{nk_BT}} - 1\right] - \frac{V+JR_S}{R_{Sh}} \qquad \textbf{Equation 1.10}$$

Here, '*n*' represents the empirical ideality factor of a diode. Generally, its value lies between 1 and 2. It indicates the type of recombination mechanisms occurring in the device and also accounts for the non-ideal behavior of the device.

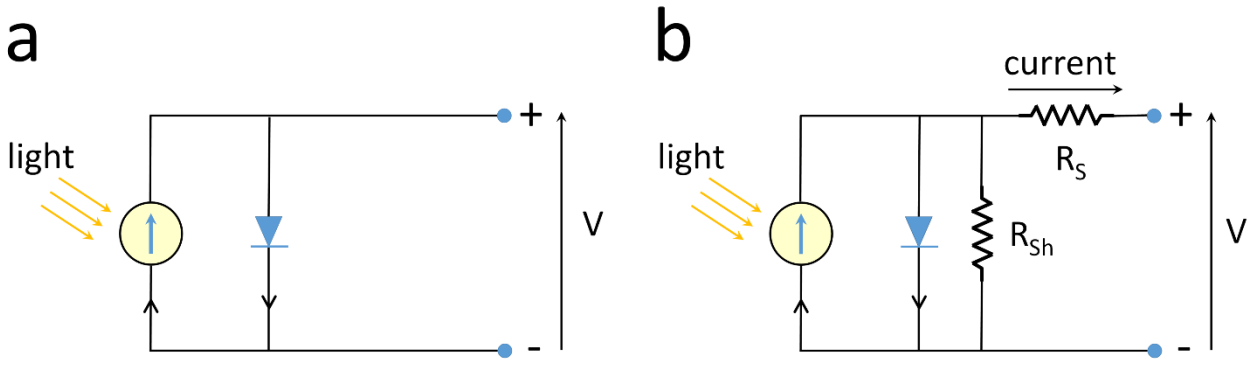

Figure 1.11 Equivalent circuit models for (**a**) ideal and (**b**) non-ideal solar cells.

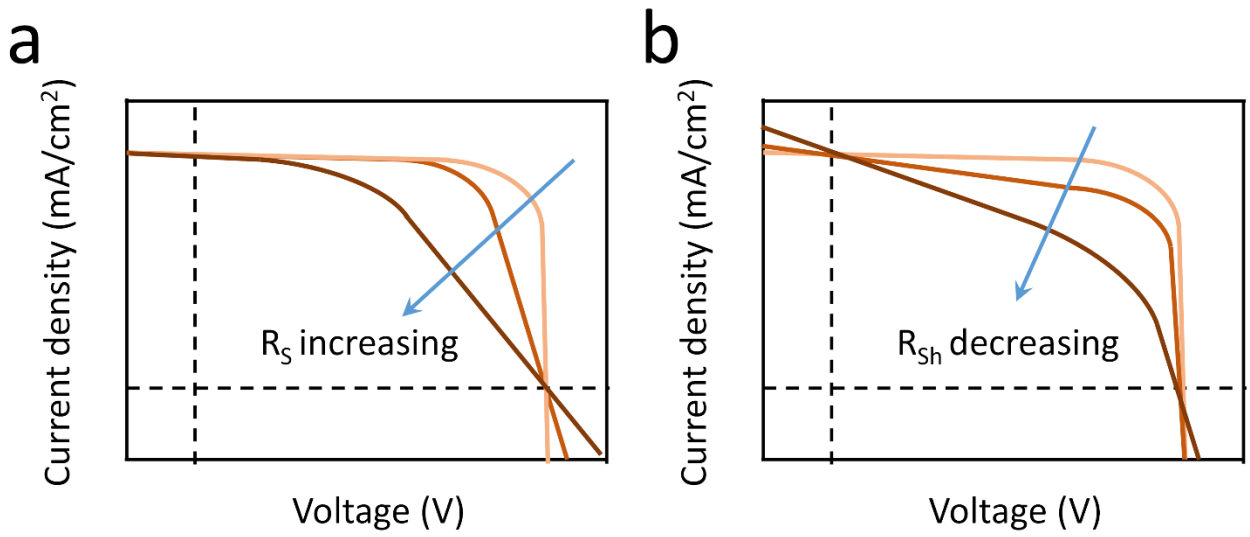

Figure 1.12 Effect of (**a**) increasing series resistance and (**b**) reducing shunt resistance.

1.2.3.PSCs Device Physics

1.2.3.1. Working Principle

Mechanisms:

The general working processes of PSCs include the following steps: (i) absorption of incident photons; (ii) generation of free electron-hole pairs; (iii) transport of photo-generated carriers; and (iv) collection of photo-generated carriers.

First, photons are absorbed by the perovskite absorption layer. This process depends on the quantum energy of each photon and the bandgap of the perovskite material (e.g. the bandgap of $MAPbI_3$ is 1.55 eV). When the photon energy is equal to or higher than the bandgap, only then are photons absorbed. Due to the absorption of a photon, an electron is excited from the valance band (VB) to the conduction band (CB). In a semiconductor material, this transition from the VB to the CB can happen in two different ways:

(i) Band-to-band transition (**Figure 1.13**), where the incident photon has a higher energy than the bandgap and the excess energy is lost through relaxation.

(ii) Transition assisted by defect states (**Figure 1.14**), where the transition occurs through the defect states within the bandgap. This can happen if the incident photon has energy lower than the bandgap.

If these two transitions cannot happen due to the energy mismatch of the incident photon, then it is transmitted through the material and contributes to the loss mechanism of a solar cell.

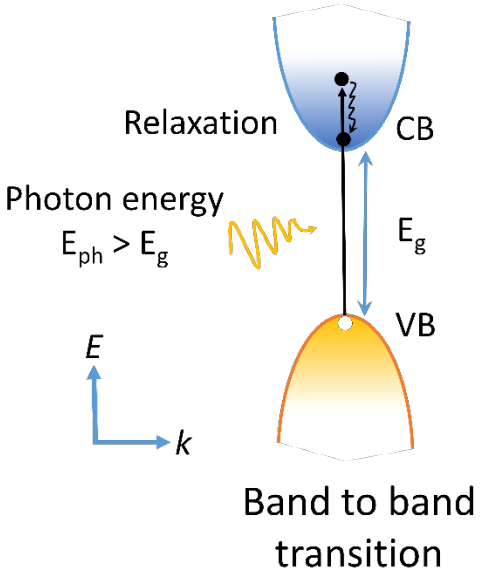

Figure 1.13 Absorption through the band-to-band transition when an incident photon has higher energy than the bandgap.

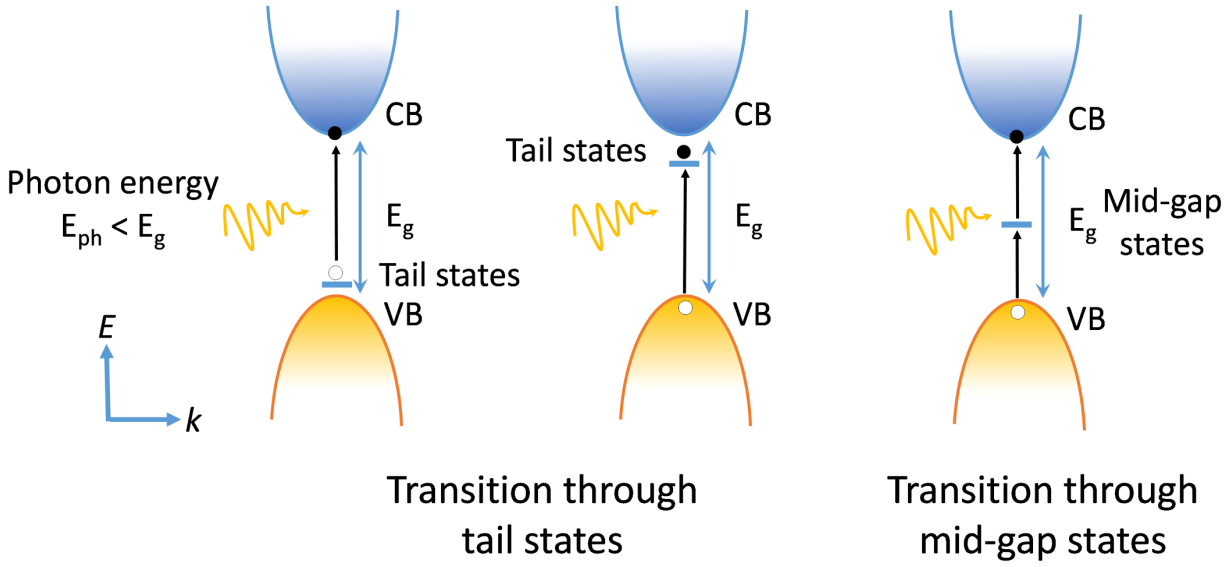

Figure 1.14 Absorption assisted by defect states when an incident photon has lower energy than the bandgap.

These photo-generated electrons and holes are bound together with an attractive Coulomb force. These pairs of bound electrons and holes are referred to as excitons and the binding energy is called the exciton binding energy. The exciton binding energy is a function of the dielectric constant of the material and can be expressed by the equation:

$$E_b = \frac{\mu e^4}{2\hbar^2 \varepsilon^2} \qquad \textbf{Equation 1.11}$$

where, E_b is the exciton binding energy, μ is the effective mass of an electron, ε is the dielectric constant of the semiconductor material, e is the charge of an electron, and $\hbar = \frac{h}{2\pi}$, where h is the Planck constant. According to **Equation 1.11**, the higher the dielectric constant the lower the Coulomb attraction force between the electron-hole pair and the lower the exciton binding energy. For $MAPbI_3$, E_b has been estimated to be ~10 meV at room temperature.[33, 34] If E_b is lower than the thermal energy (which is 26 meV at room temperature, calculated from k_BT; where k_B is the

Boltzmann constant and T is the temperature), then the photo-generated electron-hole pairs exist as free electrons and holes.

The next step is the transport of the free charge carriers through the perovskite absorber layer toward the respective transport layers. This process can happen either by diffusion or drift induced by the built-in electrical field. When charge transport is driven by the gradient in concentration of the charge carriers, then this is diffusion-based transport. If the process is driven by an internal electric field it is drift-based transport. Usually, for a solar cell power is generated at the maximum power point when the electric field inside the device is small. Therefore, the transport of charge carriers is dominated by diffusion. For diffusion, the collection efficiency of the carriers is dependent on diffusion length of the charge carriers which can be expressed by:

$$L = \sqrt{D\tau} \qquad \textbf{Equation 1.12}$$

where D is the diffusion coefficient and τ is the lifetime of the excited carrier.

The diffusion coefficient can be written as follows:

$$D = \frac{\mu \mathrm{k_B} T}{e} \qquad \textbf{Equation 1.13}$$

where μ is the charge carrier mobility, k_B is the Boltzmann constant, T is the temperature, and e is the charge of an electron. The longer the diffusion length, the greater the probability of charge collection. For efficient charge collection the diffusion length (L) must be much larger than the thickness of the active layer.

Lead halide perovskites usually have long diffusion lengths and high carrier mobilities.[35-37] For example, the diffusion length and hole mobility of a $MAPbI_3$ single crystal are 175 ± 25 μm and 164 ± 25 cm^2 V^{-1} s^{-1}, respectively.[35] This is because lead halide perovskites have strong spin-orbit coupling in the electronic band structure resulting from the presence of heavy atoms such as Pb.[38,

[39] This strong spin-orbit coupling leads to a reduction of the bandgap and modifies the band structure. The transport of charge carriers is directly related to the band structure of the material via their effective masses.

In the final step, the charge carriers are collected by electrodes into an external circuit. For the collection of electrons, the semiconductor must have a higher work function than the electrode. On the other hand, the holes must be collected in an electrode that has a higher work function than the semiconductor. Therefore, for effective charge collection and high performance a proper choice of electrodes is required along with the additional selective transport layers. The selective transport layer that helps in transporting only electrons from the perovskite layer to the electrode is called the electron-transport layer (ETL). The hole-transport layer (HTL) selectively collects holes and blocks the movement of electrons to the other electrode.

Even though the device architecture is rapidly being optimized and new materials are being developed for high performance PSCs, the PCE of PSCs is still far from the theoretical value calculated by the Schottky-Queisser limit. This is because the performance of PSCs is strongly influenced by recombination losses inside the device. Recombination reduces the number of charge carriers that contribute to the photocurrent. Recombination occurs when an excited electron in the conduction band recombines with a hole in the valence band to return to the ground state. It can be of two types: radiative and non-radiative. Radiative recombination occurs when energy is released in the form of photons as a result of the recombination process. On the other hand, the non-radiative recombination process releases energy in the form of phonons. There are three major recombination mechanisms: band-to-band recombination, trap assisted recombination (Shockley-Read-Hall (SRH) recombination) and Auger recombination as shown in **Figure 1.15**.

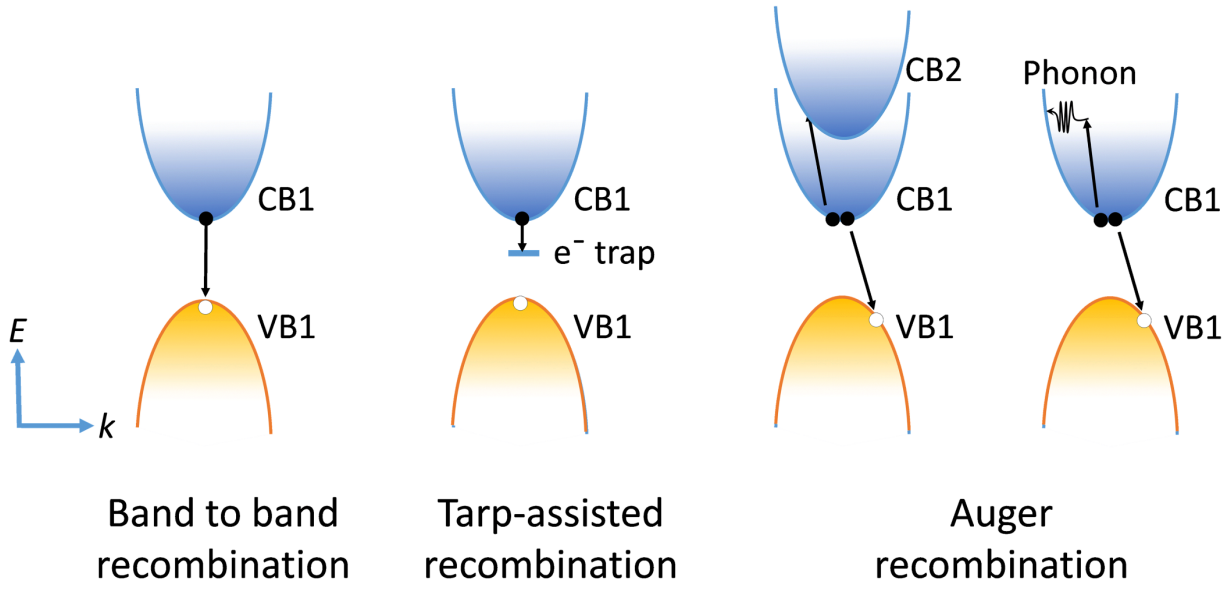

Figure 1.15 Schematic illustration of all three-recombination process in PSC (**a**) band-to-band recombination involving a direct recombination between electron and hole from band-to-band, (**b**) trap-assisted recombination involving capture of either electron or hole in the trap state and (**c**) Auger recombination involving transfer of energy of an electron (or hole) to other charge carrier to allow non-radiative recombination either with electron (or hole).

1.2.3.2. Principles of the Heterojunction Interface

Perovskite solar cells consist of several layers including a perovskite absorber layer (intrinsic semiconductor) which is sandwiched between an n-type ETL and a p-type HTL. The n-type ETL and p-type HTL are each connected to an electrode. The interfaces of each junction have a major impact on the photovoltaic performance of these cells. At a heterojunction, when two different semiconductors are put in contact their Fermi levels are aligned by a phenomenon called band bending. The intrinsic carriers present in materials start to flow across the contact in order to establish an equilibrium. Thus, the unification of the Fermi levels happens on both sides. **Figure 1.16** represents a model of p-i-n junction of PSCs under forward bias. Absorption of light by the

perovskite leads to the generation of free electron and hole pairs. These electron and hole pairs are separated by the electric field across the junction, leading to current flow in the external circuit.

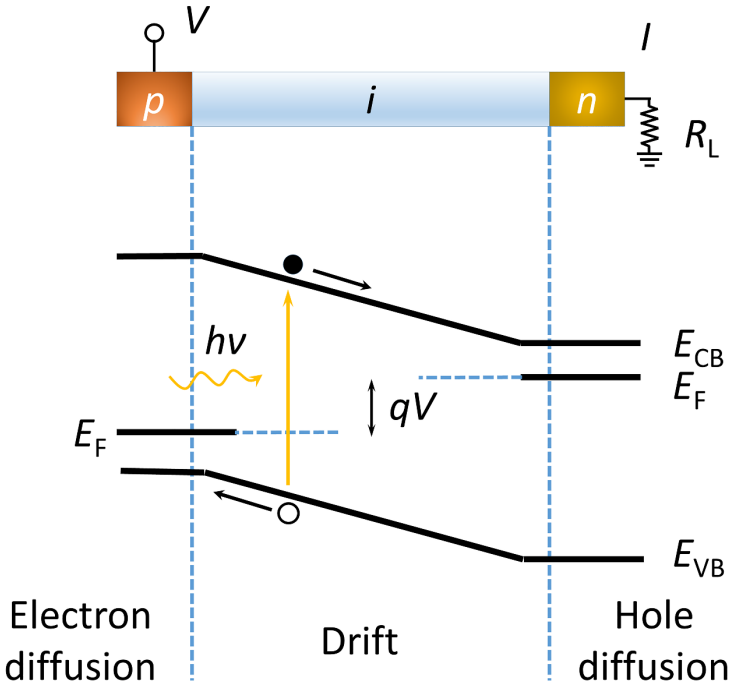

Figure 1.16 Illustration of the operation of a p-i-n diode, showing a cross-section, the energy band diagram under forward bias, and the carrier generation characteristics. V is the applied bias, I is the current, R_L is the load resistance, and V_{bi} is the built-in potential, E_F is the quasi-Fermi level of the respective semiconductors.

Under open-circuit conditions ($V = V_{oc}$), the applied bias is very close to the built-in potential (V_{bi}) and the net current is zero as the dark current balances out the photogenerated current. When the electrodes are connected (under short-circuit conditions ($V = 0$)), the current starts to flow. The band diagram at open-circuit and short-circuit are presented in **Figure 1.17**.

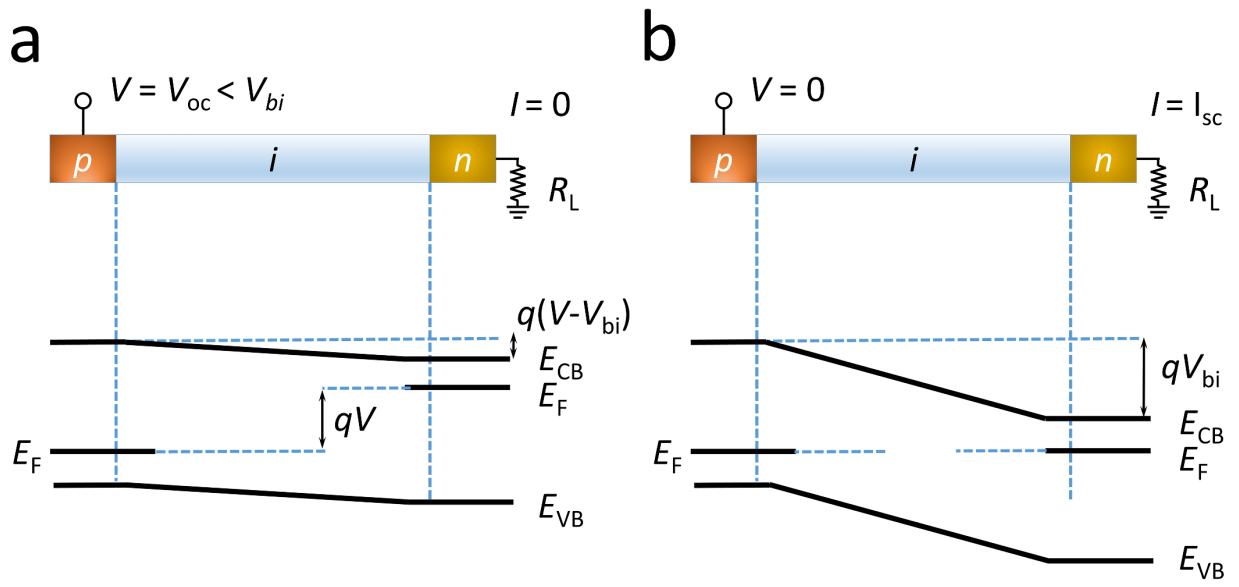

Figure 1.17 Illustration of the operation of a p-i-n diode under open (**a**) and short-circuit (**b**) conditions. V is the applied bias, I is the current, R_L is the load resistance, and V_{bi} is the built-in potential.

1.2.3.3. Solar Cell Architectures

The device configuration of a PSC greatly affects the performance of the device. It can direct the morphology and growth of the perovskite crystallites, and is important for efficient charge carrier extraction. Additionally, it can affect the stability of the PSC. PSCs can be fabricated in two major ways: regular (n-i-p) and inverted (p-i-n) structures. This depends upon which transport (electron/hole) material is on the substrate. PSCs can also be classified into two categories (mesoscopic and planar) depending on whether they have a mesoporous layer or all planar layers. PSCs even without electron or/and hole transporting layers have also been reported. PSC structural variations are presented graphically in **Figure 1.18**.

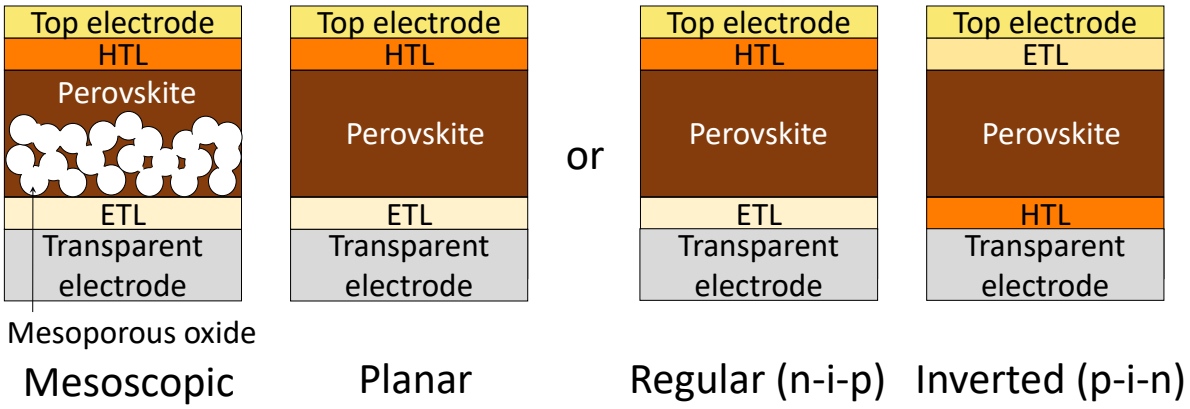

Figure 1.18 PSCs architectures: illustration of different types of PSCs; left based on presence of mesoscopic layer mesoscopic and planar structures; and right based on arrangement of charge transport layers regular (n-i-p) and inverted (p-i-n) structures.

1.2.3.4. Evolution of Device Structures

$MAPbI_3$ was first employed as a dye in a dye-sensitized solar cell where a thin layer of the perovskite was deposited on a mesoporous TiO_2 ETL (PCE 3.8% in 2009).[40] The solar cell lasted for only a few minutes as a liquid electrolyte was used. When the liquid electrolyte was removed and the perovskite was put between a solid HTL (spiro-OMeTAD) and a mesoscopic TiO_2 scaffold (as ETL) the stability drastically improved and over 10% PCE was achieved.[41] This initial advancement in PSCs gained attention rapidly and soon led to the development of other PSC device configurations.[42-44] As a result simpler planar architectures evolved by replacing the mesoscopic scaffold by a planar layer. Planar n-i-p and p-i-n architectures both gained popularity quickly.[45, 46] To date, the highest PCE of 25.2% was achieved by using a mesoporous architecture.[7] Planar n-i-p and p-i-n devices have record PCEs of 23.6%[47] and 21.0%[48] respectively. Although mesoporous PSCs can achieve better performances than planar structures, the mesoporous layer must be thin (less than 300 nm).[49] In addition, planar devices can be fabricated at room temperature, whereas higher temperatures are required for the mesoporous structure.[50]

1.2.3.5. Hysteresis

The current-voltage characteristics (*J-V* curves) of PSCs often show an anomalous hysteresis behavior, when PSCs are scanned in different directions i.e., forward scan (voltage swept from short-circuit to open-circuit) and reverse scan (voltage swept from open-circuit to short-circuit) (**Figure 1.19**).[51-54] The extent of hysteresis in PSCs often depends on scan rate,[52, 55] light-soaking conditions,[52] and applied bias.[51] This hysteretic behavior sometimes leads to inaccurate reporting of efficiencies for PSCs. The origin of this unusual behavior has been ascribed to several factors including ion migration, and charge trapping or detrapping.[53, 54, 56] However, the major contributor to hysteresis of PSCs is ion migration.[53, 57] Different factors such as perovskite grain boundaries, the capacitive behavior of perovskites, intrinsic trap states, and internal electrical field modulation are responsible for ion migration, which in turn results in the hysteresis behavior.[22, 53, 54, 58] This hysteretic behavior in PSCs was first reported by Snaith et al. in 2014.[51] The hysteresis mainly depends on the device architecture (planar or mesoporous, p-i-n or n-i-p) and the choice of interfacial layers.[53, 54, 59] For example, regular planar PSCs which use TiO_2 as the ETL and spiro-OMeTAD as the HTL show pronounced hysteresis compared to both inverted and mesoscopic solar cells.[59] This is due to the high capacitance of TiO_2 and spiro-OMeTAD which leads to charge accumulation at the ETL/perovskite and perovskite/HTL interfaces. Choosing different low capacitance materials, such as PCBM and PEDOT:PSS or NiO_x, can decrease or remove the hysteresis.[59] Recently, several hysteresis free PSCs have been developed.[22, 54, 60, 61]

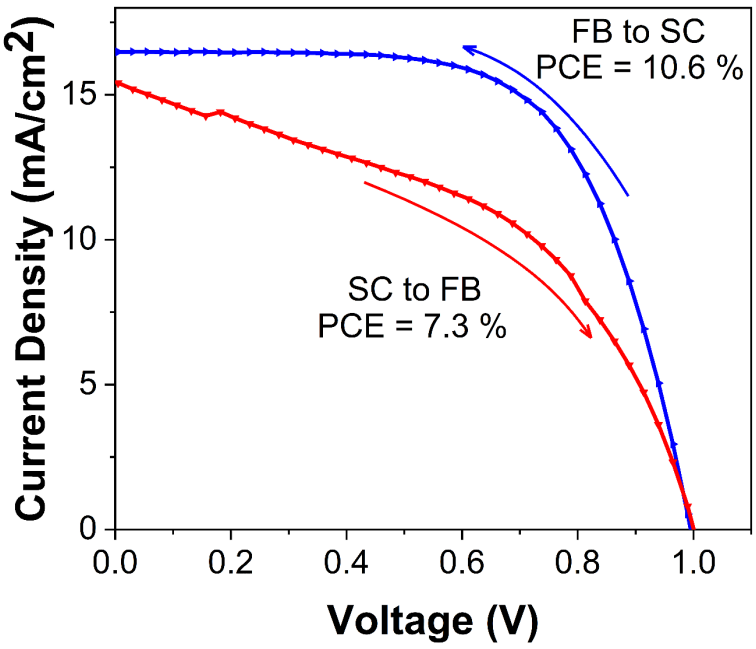

Figure 1.19 Hysteresis in current-voltage measurement of a PSC measured under 1 sun (AM 1.5 G) illumination.

1.3. Stability of PSCs

At present, PSCs are emerging as one of the most promising next generation photovoltaic technologies with a record laboratory-based PCE over 25%.[7] In addition to their high performance and cheap starting materials, their projected energy payback time is much shorter than that of silicon-based devices.[62, 63] However, their long-term stability and the toxicity of lead are two formidable obstacles for commercialization.[64-66] In order to compete with silicon solar cells, PSCs must guarantee a stable power output under outdoor operating conditions in relatively harsh environments for a period of ~ 25 years. Unfortunately, PSCs suffer from inherently poor stability.[64-66] Environmental factors such as humidity, heat, light, and oxygen cause serious damage to PSCs.[64-66] Therefore, performance deterioration and/or material degradation problems must be addressed for the commercial success of PSCs.

1.3.1. Humidity

Humidity has a profound effect on the performance and stability of PSCs. During perovskite film formation, a low level of humidity helps to improve the morphology of the perovskite layer.[67] This can lead to improved device performance. However, long exposure or high relative humidity can lead to serious damage in PSCs. The detrimental effect of humidity on $MAPbI_3$ is well-studied.[64, 68-70] Due to the hygroscopic nature of $MAPbI_3$, even a small amount of humidity can have detrimental effects on the devices and may lead to premature device failure.[69, 71] Two main mechanisms have been proposed to explain the humidity-induced decomposition of $MAPbI_3$. According to the first mechanism, water simply acts as a catalyst by accelerating the thermodynamic degradation of $MAPbI_3$. This pathway leads to the formation of PbI_2 and gaseous byproducts such as MAI or (methylamine and HI) at room temperature.[72-74] As the decomposed products are gaseous this is an irreversible pathway.

$$MAPbI_3 \xrightarrow{\boldsymbol{humidity}} PbI_2 + MAI \qquad \textbf{Scheme 1.1}$$

Or

$$MAPbI_3 \xrightarrow{\boldsymbol{humidity}} CH_2NH_2 + HI \qquad \textbf{Scheme 1.2}$$

The second degradation mechanism proposes a pathway that involves the formation of hydrates.[68-70, 74] At high RH (70-90% RH), water molecules penetrate the $MAPbI_3$ crystal and they form hydrogen bonds with the MA cations. This process leads to the formation of the metastable monohydrate phase ($MAPbI_3 \cdot H_2O$) (**Figure 1.20**).[70, 75] The formation of the monohydrate is reversible as upon drying it can revert back to the perovskite structure. After complete decomposition PbI_2 is formed as one of the major decomposition products. At very high RH

(>95%), the water molecules can cause the irreversible degradation of the perovskite structure by dissolving the MA cation.[70]

$MAPbI_3 + H_2O \rightleftharpoons [MAPbI_3 \cdot H_2O]$ **Scheme 1.3**

$[MAPbI_3 \cdot H_2O](s) + H_2O(l) \rightarrow MAI(aq) + PbI_2(s) + 2H_2O(l)$ **Scheme 1.4**

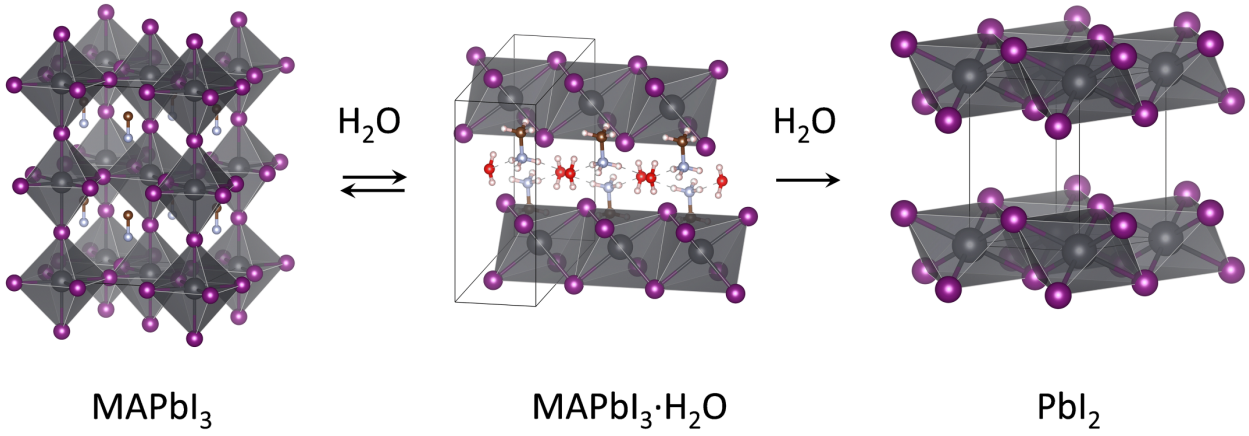

Figure 1.20 Decomposition of $MAPbI_3$ perovskite proceeds via hydration to $MAPbI_3 \cdot H_2O$, followed by the formation of PbI_2 in presence of humidity.

1.3.2. Heat

Heat is another major concern for the longevity of PSCs as the temperature can reach as high as 85 °C in extreme conditions during operation in direct sunlight.[76] Additionally, modules can experience temperature extremes ranging from −40 to +85 °C depending on the environmental conditions. Usually, $MAPbI_3$ is stable well over the operational temperature, though it breaks down around 200 °C.[77, 78] However, when it is incorporated in a device it degrades much faster at relatively low temperature. A study by Yong et al. showed that when $MAPbI_3$ is deposited onto a ZnO based ETL, it decomposes even at 100 °C.[79] In addition, humidity also helps in the thermal decomposition of $MAPbI_3$.

According to several studies based on x-ray diffraction, $MAPbI_3$ degrades to PbI_2 via intermediates when annealed over 100 °C for a prolonged time.[80-82] This results in a visual change in color from a dark brown perovskite film to a light yellow PbI_2-rich film. This transformation leads to a deterioration in device performance as PbI_2 is not photoactive due to its unfavorable bandgap. Additionally, charge transport in PbI_2-based cells is much slower than that in PSCs.[83] Later on, numerous studies claimed that $MAPbI_3$ is more susceptible to thermal decomposition because of the MA cation which leads to the formation of volatile decomposition byproducts.[84] It usually decomposes through a release of gases via sublimation or assisted chemical reaction as follows:[77, 78, 85-87]

$$MAPbI_3(s) \xrightarrow{\boldsymbol{heat}} HI(g) + CH_3NH_2(g) + PbI_2(s) \qquad \textbf{Scheme 1.5}$$

$$MAPbI_3(s) \xrightarrow{\boldsymbol{heat}} CH_3I(g) + NH_3(g) + PbI_2(s) \qquad \textbf{Scheme 1.6}$$

At relatively lower temperature (80 − 144 °C) and under partial vacuum, $MAPbI_3$ decomposes to CH_3NH_2 and HI following a kinetically favored pathway (**Scheme 1.5**).[77, 78, 85] This is a partially reversible process. On the other hand, at high temperature (~ 300 °C) and atmospheric pressure, $MAPbI_3$ decomposes through a thermodynamically favored pathway which leads to the release of CH_3I and NH_3 as gaseous byproducts (**Scheme 1.6**).[86] This decomposition is an irreversible process.

1.3.3. Light

In order to even be considered as a possible photovoltaic technology, a solar cell must be stable under light. Although many studies have now demonstrated the stability of encapsulated PSCs over hundreds of hours of illumination, there is a substantial amount of work describing photoinduced changes to the perovskite structure and PSC performance.[41, 88-98] One important

example is the light soaking that has often been found to be beneficial for device performance;[99-102] however, under long term irradiation, both reversible[103-106] and irreversible[107, 108] degradation has been observed. This has been variously ascribed to the formation of light-activated trap states,[103, 109] photoinduced ion segregation,[104, 109, 110] photoinduced atom/ion migration,[142] and photodecomposition.[96, 98]

White light exposure for a few hours in vacuum decomposes $MAPbI_3$ into PbI_2 and metallic Pb resulting in an obvious color change from dark brown to gray.[111] According to several studies, $MAPbI_3$ decomposes into PbI_2 and other gaseous components.[95, 105, 107, 111] Upon longer exposure, PbI_2 further decomposed into metallic Pb. Even though most of the studies claimed PbI_2 and metallic Pb as the solid byproducts, there is debate on the identity of the gaseous decomposition products.[95, 105, 107, 111] According to Xu et al.[107] and others[95, 112] the gaseous decomposed products are NH_3, HI, and I_2 with a hydrocarbonaceous species left on the surface (**Scheme 1.7**), while Tang et al.[111] and others[105] suggest the volatile components could be CH_3NH_2, HI, and I_2 (**Scheme 1.8**). Therefore, the photodecompostion of $MAPbI_3$ can be summarized as follows:

$$MAPbI_3(s) \xrightarrow{light} \text{Organic residue(s)} + NH_3(g) + HI(g) + PbI_2(s) \qquad \textbf{Scheme 1.7}$$

$$MAPbI_3(s) \xrightarrow{light} CH_3NH_2(g) + HI(g) + PbI_2(s) \qquad \textbf{Scheme 1.8}$$

$$PbI_2(s) \xrightarrow{light} Pb(s) + I_2(g) \qquad \textbf{Scheme 1.9}$$

1.3.4. Light and Air (Oxygen, Humidity)

Several studies have revealed that the presence of oxygen and/or humidity accelerates the photodecomposition of PSCs relative to a vacuum or inert atmosphere.[113, 114] Under continuous illumination in air, $MAPbI_3$ films photobleach and the color changes from black to transparent[111]

or yellow[114, 115] within just a few hours. Due to photoexcitation of $MAPbI_3$ and subsequent electron transfer to an oxygen molecule, superoxide is formed at the surface of the $MAPbI_3$ film. The superoxide reacts with $MAPbI_3$ and forms PbI_2 and other gaseous species (CH_3NH_2 and I_2).[115]

$$MAPbI_3 \xrightarrow{h\nu \geq Eg} MAPbI_3^* \qquad \textbf{Scheme 1.10}$$

$$MAPbI_3^* + O_2 \rightarrow MAPbI_3^+ + O_2^{\cdot -} \qquad \textbf{Scheme 1.11}$$

$$4\ MAPbI_3 + O_2^{\cdot -} \rightarrow 4\ CH_3NH_2 + 4\ PbI_2 + 2\ I_2 + 2\ H_2O \qquad \textbf{Scheme 1.12}$$

Upon longer exposure, PbI_2 further reacts with air to form lead salts like PbO, $PbCO_3$, and $Pb(OH)_2$.[111, 115]

After continuous illumination in air $TiO_2/MAPbI_3$ based devices experience a severe degradation in device performance.[114, 116, 117] Further investigation suggested that the photoexcitation of $MAPbI_3$ leads to generation of electron and hole pairs. Transfer of the photoelectron from the conduction band of $MAPbI_3$ to molecular oxygen again produces a reactive superoxide anion, which then in turn attacks the perovskite, resulting in both deprotonation of the MA cation and oxidation of iodide to iodine. This leads to a significant reduction in photocurrent to device failure.

1.3.5. Other Factors

Several other factors such as ion/atom migration, mechanical stress, applied bias, and choice of ETM, HTM and electrode also play a significant role in the decomposition of PSCs. In PSCs, high performing organic HTMs such as spiro-OMeTAD are typically used along with dopants like lithium bis(trifluoromethane)sulfonamide (Li-TFSI) and 4-*tert*-butylpyridine (TBP). Li-TFSI is very hygroscopic; therefore, PSCs employing this additive tend to suffer from rapid moisture-induced degradation.[68, 118] Additionally, diffusion of Li^+ into the perovskite layer causes hysteresis.[51, 119] During heating cycles, low boiling TBP can evaporate at temperatures as low as

85 °C, causing the formation of voids and a decrease in PCE.[120, 121] Additionally, the poor barrier properties of spiro-OMeTAD aids in the diffusion of ions and atoms from the perovskite layer to the electrode and vice versa. For example, heat, moisture, light or bias induced migration of iodide ions from the perovskite layer to the top metal electrode leads to the formation of metal iodide salts and the corrosion of the top electrode.[122, 123] Metal electrodes such as gold can also diffuse through the spiro-OMeTAD layer to the perovskite layer, leading to a decrease in PCE.[124, 125]

Due to their different compositional variations, lead halide perovskites offer flexibility and tunability of the bandgap. Therefore, the bandgap of a mixed $APb(I_xBr_{1-x})_3$ (where A is MA, FA or Cs) perovskite can be varied by controlling the ratio of I/Br. This can improve device performance and stability. However, increasing the Br content does not necessarily always produce PSCs with higher V_{OC}'s, as expected from their higher bandgap.[18, 126-128] During light exposure, $APb(I_xBr_{1-x})_3$ undergoes a reversible phase segregation into I and Br rich domains.[66, 129-131] Therefore, mixed perovskites tend to have reduced photostability. This light-induced phenomenon was first reported by Hoke et al in 2015.[109] However, this phenomenon does not typically occur when the Br content is lower than 20% in the mixed perovskites. However, this phenomenon is particularly concerning for the application of perovskite tandem solar cells where a bandgap of 1.7-1.8 eV is desirable.

In addition to the light-activated movement of I^- and Br^-, heat and humidity are also responsible for the migration of these ions. A similar light-activated phenomenon has been observed in mixed cation perovskite compositions.[25, 26] This causes a decrease in device performance.

1.4. Strategies to Improve Moisture Stability

As device performance has improved and exceeded 25% (which is better than many other PV technologies), the goal of the perovskite research field has shifted towards increasing longevity. The undeniable role of moisture in the PSC decomposition process has led to intensive research focused on improving the lifetime of PSCs. Even though for commercial applications PSCs will likely be encapsulated, the stabilization of each layer is still essential, as otherwise even a small pinhole could result in total device failure. Even with perfect seals, moisture and oxygen trapped during device fabrication or sealing can increase ion mobility leading to a decline in device performance. Therefore, extensive research is ongoing to stabilize each component of the PSC. From the first PSC in which liquid electrolyte was used, which was only stable for few minutes, to today, where PSCs have achieved over 1000 h operational lifetime, significant improvements in device engineering and materials developments are continually being made.

1.4.1. Perovskite Materials

The prototypical lead halide perovskite, $MAPbI_3$, is highly moisture sensitive. It starts decomposing as soon as it comes in contact with moisture. Therefore, replacing it with more stable perovskite compositions is one of the obvious routes to improve stability. Replacing the iodide with the smaller bromide ions improves the moisture resistance. This was first demonstrated by Noh et al.[126] They observed that the partially substituted $MAPb(Br_xI_{1-x})_3$ was more resistant to moisture than pure $MAPbI_3$. The stability of the devices improved as the bromide content was increased. In a separate study, Buin et al. demonstrated that amongst pure $MAPbX_3$ (where X = I, Br and Cl) compositions, $MAPbBr_3$ and $MAPbCl_3$ were more stable than $MAPbI_3$ in ambient humidity.[132] Substituting I^- with SCN^- is also reported to enhance moisture stability due to a

stronger interaction between Pb^{2+} and SCN^- than Pb^{2+} and I^-.[133, 134] This stronger interaction makes it difficult to form the hydrate phase in the perovskite crystal.

Another effective strategy is to replace or modify the more volatile and reactive MA cation with more robust FA or Cs cations. However, pure $FAPbI_3$ and $CsPbI_3$ suffer from phase stability issues at operational temperatures, which is even worse in the presence of moisture. However, mixed perovskite compositions can solve this problem. For example, when Cs is doped into $FAPbI_3$ the resulting $Cs_{0.1}FA_{0.9}PbI_3$ perovskite becomes more moisture resistant with improved device stability, as demonstrated by Park et al.[135] This fact was further supported by subsequent studies.[136, 137] Similarly, partial replacement of MA with FA improves the moisture stability.[138] Due to resonance stabilization of FA, the positive charge on FA is more declocalized leading to a weaker interaction between the FA cation and water.[139, 140] On the contrary, a strong interaction between the oxygen of a water molecule the hydrogen of the MA cation leads to the decomposition of $MAPbI_3$ via hydrate formation. Later on, another complex perovskite formulation ($Cs_{0.05}MA_{0.16}FA_{0.79}PbI_{2.49}Br_{0.51}$) became popular due to its combination of improved device performance, lifetime, and reproducibility.[141]

When the small hygroscopic MA cation is replaced with bulkier hydrophobic organic cations (such as an aliphatic or aromatic alkylammonium) it results in a reduction in dimensionality from a 3D perovskite to a 2D structure which consist of single (or multiple) inorganic sheets sandwiched between organic spacers. This also results in superior moisture stability which prevents hydrate formation.[142-144] In 2014 Karunadasa et al. reported the first application of 2D halide perovskites as a promising material with better moisture stability. However, the PCE was relatively low due to the reduced dimensionality and wider bandgap.[142] Later, Mohite and co-authors improved the PCE to over 10% by using a 2D Ruddlesden–Popper layered perovskite, $(BA)_2(MA)_{n-1}Pb_nI_{3n+1}$

(where BA = *n*-butylammonium).[145] This has led to increased interest in 2D layered perovskite materials over the past few years.[146-148] Most recently, 2D/3D perovskites (a mixture of 2D and 3D perovskite phases) have emerged as a class of excellent photovoltaic materials with long-term stability. Broadly, three different routes have been developed to synthesize 2D/3D perovskites: mixed directly into the bulk 3D structure (**Figure 1.21a**), deposited at one interface, and coated onto the grains (**Figure 1.21c**). The first approach takes advantage of quasi-2D perovskites where phenylethylammonium (PEA) layers are systematically incorporated into every *n* integer layers of the bulk 3D $MAPbI_3$ perovskite (**Figure 1.21a**).[149] Quasi-2D perovskites have enhanced moisture stability like 2D perovskites, and the excellent optoelectronic properties of 3D perovskites. By fine-tuning *n* (*n* = 60), a record PCE of 15.3% was achieved. The 2D perovskite acts as a moisture barrier protecting the inner 3D structure, thus enhancing the longevity of these perovskite materials. In the second approach, Grancini et al. synthesized an ultra-stable 2D/3D $(HOOC(CH_2)_4NH_3)_2PbI_4/MAPbI_3$ perovskite composition by adding a few percent of aminovaleric acid iodide (AVAI) in the perovskite precursor solution.[150] The resulting 2D/3D perovskite, in combination with a 1-μm-thick carbon electrode and protective glass covering (**Figure 1.21b**) resulted in devices with lifetimes of over one year under 1 sun at 55 °C in ambient atmosphere. In addition, the 2D perovskite coating helped to improve the morphology by guiding the growth of the 3D perovskite. The third route utilizes 2D perovskite crystallites to passivate the moisture-sensitive grain boundaries of a 3D perovskite.[151-153] This also helps to improve crystallinity and reduce defects in the crystal. Using this approach, Wang et al. were able to obtain 17.5% PCE solar cells with enhanced stability in the ambient environment.[151]

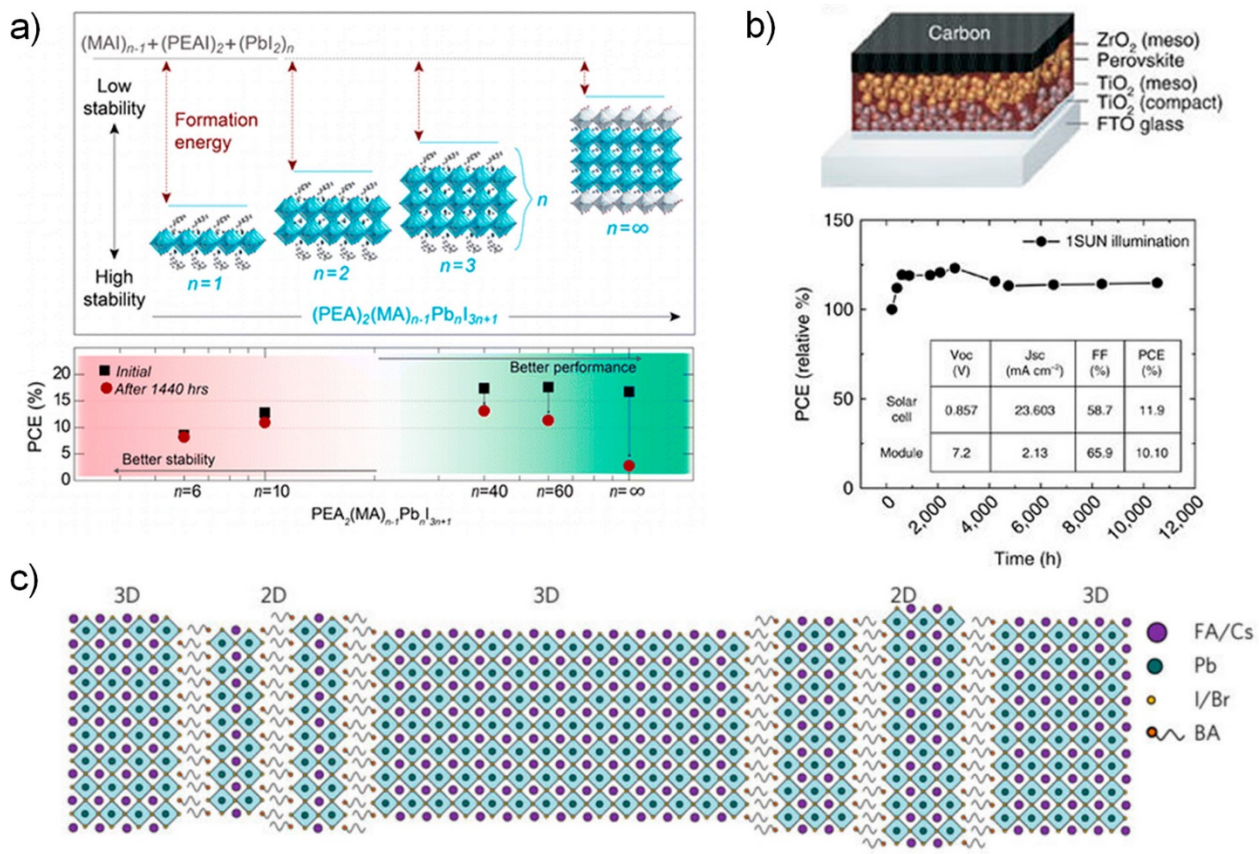

Figure 1.21 Strategies to produce perovskites with reduced dimensionality (2D/3D perovskites): (**a**) Variation of perovskite dimensionality from 3D to 2D with improved device stability. Reproduced from ref ([149]). Copyright 2016 American Chemical Society. (**b**) Device architecture used by Grancini et al. to achieve employing a 2D/3D perovskite with 1 year stability under 1 sun illumination in an ambient atmosphere. Reprinted with permission from ref ([150]). Copyright 2017 Springer Nature, under a Creative Commons 4.0 License. (**c**) Schematic showing 2D perovskite that resides at the grain boundaries of the bulk 3D perovskite. Reprinted with permission from ref ([151]). Copyright 2017 Springer Nature.

In the early stage of perovskite decomposition, water molecules infiltrate the perovskite layer through the gaps between grains. Decomposition, therefore, starts at the grain boundaries and progresses to the grain interior. Therefore, passivating the grain boundaries is one of the effective ways to minimize moisture-induced degradation. Additionally, perovskite layers with larger grains

and fewer grain boundaries are desirable as larger grains have lower surface area/volume ratios and fewer defects.[154] This not only helps to improve the moisture resistance[155] but also increases device performance.[156, 157] Several research articles have been published with different passivation agents, such as polymers,[158, 159] fullerenes and their derivatives,[160] and other organic compounds[161-163] which demonstrate the utility of this approach. For example, de Carvalho et al. used tetraethyl orthosilicate (TEOS) in the precursor solution to passivate the perovskite grains. Devices modified with TEOS were able to retain 85% of their performance after 1200 h under 1 sun in ambient atmosphere.[162] Another good example was demonstrated by Bi et al.[164] They introduced poly(methyl methacrylate) (PMMA) into a chlorobenzene/toluene mixture (which was used as an antisolvent to facilitate fast crystallization process) to prepare the perovskite film. Similarly, passivating grain boundaries with polydimethylsiloxane enhanced the long-term stability of the perovskite.[163] Adding hydrophobic PEA cations [165, 166] and other long-chain cations such as n-butylammonium,[165] 1,1,1-trifluoro-ethylammonium,[167] and oleic acid[168] into the perovskite precursor solution also leads to improved moisture stability.[165-168] By using the crosslinking agent alkylphosphonic acid ω-ammonium chloride (4-ABPACl), Li et al. improved the quality of the surface of $MAPbI_3$.[169] The 4-ABPACl acts as a crosslinking agent between neighbouring grains in the perovskite structure via strong hydrogen bonding of the $–PO(OH)_2$ and $–NH_3^+$ terminal groups to the perovskite surface. Therefore, 4-ABPACl-modified devices have improved lifetime in a 55% RH environment compared to control $MAPbI_3$ PSCs.

1.4.2. Hole-transport Materials (HTMs)

The HTL plays a major role in device function by selectively transporting holes to the electrode. In a “standard” n-i-p structure, the HTL lies between the perovskite absorber and the top electrode.

If it is made hydrophobic, it can also serve as an effective vapor barrier between the perovskite and its environment. Additionally, it can also block the undesired movement of ionic or molecular species among the layers in PSCs. Among the most common HTMs, semi-crystalline and hydrophobic P3HT serves as one of the best vapor barriers for PSCs.[169, 170] Due to the use of a large amount of hygroscopic Li-dopant in two other high-performance HTMs, 2,2′,7,7′-tetrakis[*N*,*N*-di(4-methoxyphenyl)amino]-9,9′-spirobifluorene (spiro-OMeTAD) and poly[bis(4-phenyl)(2,4,6-trimethylphenyl)amine] (PTAA), PSCs decompose much faster.[171] Therefore, researchers are constantly looking for new hydrophobic HTMs[172-174] or HTMs with tailored energy levels and inherently good charge transport characteristics where additional doping is not required.[175-179] One promising example employed an HTL made of polymer-functionalized single-walled carbon nanotubes (SWCNTs) in a PMMA matrix.[118] The PMMA layer was an effective moisture barrier and allowed the PSCs to withstand direct exposure to running water for a short period of time. One example of a dopant free HTM was reported by Kim et al.[180] They have shown that at 75% RH in the dark and at room temperature their HTM based on benzo[1,2-*b*:4,5:*b*′]dithiophene and 2,1,3-benzothiadiazole was able to protect the perovskite absorber for 1400 h compared to their control PSCs based on spiro-OMeTAD (900 h, 0% PCE). This improved stability of the PSCs is attributed to the hydrophobic HTM and avoiding the use of deliquescent and hygroscopic dopants. Similarly, Jiang et al. designed a dopant-free hydrophobic HTM based on CuPc-OBu (a derivative of copper (II) phthalocyanine (CuPc)) for PSCs which had a PCE of 17.6%.[181] It was found that after exposing the CuPc-OBu PSCs to 85% RH for 120 h, the devices retained 84% of their initial efficiency which was significantly better than their control PSCs where they used Li-doped spiro-OMeTAD as HTM (retained 21% of their initial PCE).

In another approach, Xu and co-workers synthesized a dopant-free polymeric HTM (*N*4,*N*4′-di(naphthalen-1-yl)-*N*4,*N*4′-bis(4-vinylphenyl)biphenyl-4,4′-diamine) (VNBP) via thermal crosslinking.[182] Devices made using VNPB achieved a steady-state PCE of 16.5% when coupled with MoO_3. The VNBP-MoO_3 double layer protected the perovskite underneath when exposed to 70% RH for 30 days. This moisture resistance was attributed to the excellent barrier properties of the crosslinked double-layer HTL.

Inorganic HTMs like NiO_x,[183-185] copper gallium oxide ($CuGaO_2$),[186] and copper chromium oxide ($CuCrO_2$)[187] have gained popularity for producing more stable devices with high PCEs. For example, Cao et al. demonstrated the excellent stability of NiO_x/CuSCN based PSCs.[185] The NiO_x formed a dense and compact HTL and the PSCs did not show any loss of device performance, even after exposure to 50–60% RH for 4 months without encapsulation. Another excellent metal oxide HTM is $CuGaO_2$. Zhang et al. used $CuGaO_2$ nanoplates as the HTM and achieved a PCE of 18.51% with long-term stability.[186] In addition, $CuGaO_2$ NPs based devices showed improved stability compared to spiro-OMeTAD-based PSCs when aged at 40% RH.[187] After aging in air over 60 days, the $CuCrO_2$-based device retained 83% of its original PCE, whereas the PCE of the spiro-OMeTAD-based PSCs decreased to 24% of its initial value. An overview of PSCs with different HTMs and their effect in improving device stability is summarized in **Table 1.1**.

Table 1.1: A survey of HTMs used in PSCs to improve the long-term stability of PSCs with relevant parameters such as relative humidity, atmosphere, illumination, and UV irradiation. The figures of merit are the initial power-conversion efficiency, the rate of decreasing efficiency (in %/100 h), the total decrease in efficiency, as well as the decline in efficiency of the respective control system.

Reference	HTL	Humidity (RH) (%)	Other conditions	Time (h)	Initial PCE (%)	Total decrease (%)	Control HTL	Control degradation (%)
[118]	SWNT-PMMA	50% in air	80 °C	96	15.3	0.0	spiro-OMeTAD	100.0
[175]	TTF-1	40% in air	−	500	10.0	20.0	spiro-OMeTAD	60.0
[180]	RCP	75% in air	−	1400	17.3	0.0	spiro-OMeTAD	100.0
[174]	SAF-OMe	30% in air	−	240	15.2	39.0	spiro-OMeTAD	55.0
[181]	CuPc-OBu	85% RH	−	120	17.6	26.0	spiro-OMeTAD	79.0
[182]	VNBP-MoO_3	70% RH	−	480	16.5	−	spiro-OMeTAD	0.0
[179]	Z1011	50% RH in air	light 100 (mW cm^{-2})	200	16.3	0.0	spiro-OMeTAD	100.0
[188]	P3HT-WBH	85% RH	−	1008	22.7	20.0	P3HT	0.0
[184]	Cu:NiO_x	air	−	240	15.0	10.0	PEDOT:PSS	70.0
[185]	NiO_x-CuSCN	50-60% in air	−	2880	17.2	0.0	spiro-OMeTAD	35.0
[186]	$CuGaO_2$	30-55% in air	−	720	18.5	0.0	spiro-OMeTAD	100.0
[187]	$CuCrO_2$	> 40% in air	−	1440	16.7	17.0	spiro-OMeTAD	86.0

1.4.3. Electron-transport Materials (ETMs)

Similar to HTMs, hydrophobic and modified ETMs can be used as a secondary protection layer for the PSCs in addition to their primary function as an effective electron transporter. In the common n-i-p type architecture, the ETL lies between the perovskite absorber and the glass substrate. The glass substrate being impenetrable to moisture, the ETL is not the route of moisture

ingress in unencapsulated cells. However, the choice of ETM can still have a pronounced impact on device stability.[189] Several studies have indicated that mesoscopic structures ETLs have better moisture stability than planar ETLs.[73, 189, 190] The relatively thick mesoporous layer better encapsulates the perovskite crystallites, thus protecting them from moisture ingress. In the inverted p-i-n architecture, the ETL lies on the top of the perovskite layer. Therefore, it can potentially serve as a barrier layer for water vapor. Therefore, the stability of p-i-n PSCs can dramatically improve with the proper choice of ETM. For example, depositing a dense and smooth ZnO (roughness of <2 nm and a particle size of <10 nm) ETL on top of the perovskite improved the moisture stability of the PSCs many-fold compared to PCBM based PSCs.[191] Another good example was demonstrated by Jen and co-workers who used the hydrothermal method to prepare highly crystalline SnO_2 nanoclusters (NCs) as an ETL.[192] Due to their high degree of crystallinity, SnO_2 NCs in the PSCs achieved 18.8% PCE with a remarkable stability. The devices were able to retain over 90% of their initial efficiency when stored in ambient air with >70% RH for 30 days. Other examples of potential barrier ETMs with high performance are CeO_x,[193] Zn_2SnO_4,[194] and $Ti(Nb)O_x$.[89]

1.4.4. Electrodes

The top electrode, being the topmost layer of the device stack, can potentially be used as a protective barrier if made of hydrophobic and stable materials. Metals, including gold, can lead to degradation due to ion migration and eventually corrode, resulting in complete device failure.[122, 125] Carbon-based electrodes lead to more moisture resistant PSCs as they are hydrophobic and less susceptible to corrosion. Additionally, carbon is earth-abundant and highly cost-effective. Therefore, carbon based electrodes are one of the best choices for a top contact layer. Several

studies have demonstrated the impressive stability of PSCs when carbon electrodes were used.[195-198] The stability of different carbon-based top contacts is summarized in **Table 1.2**. Mei et al.[195] and Hu et al.[199] achieved an impressive stability of over 1 year of storage in 54% RH ambient air and 1000 h under 1 sun in ambient air by using a combination of a double layer of mesoporous TiO_2 and ZrO_2 as a scaffold, infiltrated with $(5\text{-AVA})_x(MA)_{1-x}PbI_3$ [5-ammoniumvaleric acid (5-AVA)] and a micron-thick carbon electrode. This system showed impressive stability when tested outdoors in Jeddah, Saudi Arabia, for 168 hours[200] and Wuhan, China, for 720 hours.[199] Metal oxides are chemically robust and form effective protective coatings, therefore, use of conductive metal oxides significantly improves the moisture stability of PSCs (**Table 1.2**).[201-203] For example, Kaltenbrunner et al. used a combination metal and metal oxide electrode (Cr_2O_3/Cr/Au) which led to improved device stability.[203] The chromium oxide–chromium interlayer acts as a buffer between the gold electrode and the $MAPbI_3$ layer, effectively protecting the gold electrode from chemical etching caused by I^- liberated from the $MAPbI_3$ layer.

Table 1.2: Different top contact layer of PSCs and their corresponding stability in humid environments.

Reference	Electrode	Humidity (RH) (%)	Other conditions	Time (h)	Initial PCE (%)	Total decrease (%)
[195]	carbon	54% in air	sunlight	> 1000	12.8	0.0
[196]	carbon	30% in air	–	288	11.6	10.0
[197]	carbon	40% in air	60 °C	1000	14.9	20.0
[198]	carbon	in air	–	480	13.5	5.0
[203]	Cr_2O_3/Cr/Au	–	–	–	12.0	–
[201]	SnO_x/ultrathin Ag/SnO_x	50% in air	–	4500	11.0	19.0

1.4.5. Additional Interfacial Layers

Another way to increase the lifetime of PSCs is to add additional interfacial layers. These extra layers strengthen the moisture resistance of the overall device stack. There are several examples of this strategy in the literature, and a few of them are discussed in this section (**Table 1.3**). The addition of an alumina (Al_2O_3) buffer layer between the spiro-OMeTAD HTL and the metal electrode has been shown to improve device stability.[73, 204, 205] Similarly, Luther et al. added MoO_x between the HTL and the Al electrode which improved the device stability under ambient conditions.[206] They hypothesized that a thin layer of aluminum oxide formed at the MoO_x–Al interface, which was responsible for the increase in lifetime. Arora et al. introduced a conductive reduced graphene oxide (rGO) layer at the interface of the CuSCN HTL and the Au electrode.[207] The hydrophobic rGO layer improved the PSCs lifetime by effectively blocking metal diffusion and moisture ingress. Another method is the addition of an organic hydrophobic layer in

the device stack to resist moisture ingress.[168, 208, 209] However, the addition of these insulators decreases charge transport thus decreasing the overall PCE. For inverted device architectures, inserting a layer of chemically-stable inorganic metal oxide or nonreactive metal between PCBM and the electrode dramatically improves stability without affecting the device performance.[92, 210-213]

Table 1.3: Different passivation layers reported to improve moisture resistance of PSCs.

Reference	Interfacial layer	Humidity (RH) (%)	Other conditions	Time (h)	Initial PCE (%)	Total decrease (%)	Control degradation (%)
[204]	Al_2O_3	50% in air	−	576	12.9	10.0	100.0
[205]	ALD Al_2O_3	40−70% in air	−	1680	18.0	30-40	88.0
[206]	MoO_x/Al	51.5 ± 1.5%	light 100 (mW cm^{-2})	24	9.8	39.0	100.0
[207]	reduced graphene oxide (rGO)	not maintained	light 100 (mW cm^{-2}) at 60 °C	1000	20.5	5.0	100.0
[208]	alkylalkoxysilane	45% in air	−	600	13.7	10	30.0
[209]	hydrophobic thiols	45% in air	−	250	12	25	100.0
[168]	oleic acid	76% in air	−	672	9.1	improved 8.0%	83.0
[210]	CeO_x	30% in air	−	720	18.7	0.0	100.0
[211]	aluminum-doped zinc oxide (AZO)/ALD SnO_2	50% in air	−	400	12.8	0.0	100.0
[92]	ALD-AZO/Al_2O_3	20-60% in air	light 100 (mW cm^{-2})	500	18.8	0.5	60.0% in 326 h
[212]	Bi	50% in air	85 °C	6000	18.0	22.0	100.0
[213]	carbon quantum dots	50% in air	85 °C	500	17.0	2.0	20.0

1.5. Experimental Techniques

As mentioned earlier, PSCs have the potential for a future breakthrough in the field of photovoltaics. However, in order to make that happen device longevity is the key. Scientists are working on different ways to improve the longevity of perovskite devices. However, in order to do that, it is necessary to find out which parts are the weak links in device stack and how they handle/interact with the environmental stress. Therefore, having comprehensive and in-depth knowledge about how the PSCs decompose is crucial. Several techniques are being used to study the decomposition process. This thesis also uses different techniques such as UV/vis spectroscopy, pXRD, AFM, SEM, and grazing incidence wide angle x-ray scattering (GIWAXS). Among them, the theory behind GIWAXS is discussed in the following section in details for building a better understanding of this technique as it has been used extensively in **Chapter 4**.

1.5.1.GIWAXS

1.5.1.1. Theory

X-ray Diffraction

In solid, the distance between two atoms is on the order of a few Ångstroms. Therefore, electromagnetic waves in the range of 1-100 Å wavelength (x-ray) have to be used to probe the structural arrangement of atoms and molecules in materials. When an incoming x-ray interacts with an atom it gets scattered by the electron cloud of the atom. When x-rays are scattered by multiple atoms, the scattered x-rays interact with each other resulting in constructive and destructive interference. The constructive interference leads to the formation of a characteristic pattern called a diffraction pattern and the phenomenon is called diffraction. This pattern depends on the arrangement of the atoms in the material. The intensity of the diffraction peaks depends on: (i) the electron density

of the elements present in the material. Heavier elements scatter x-rays more strongly than lighter elements. (ii) The structure of the substance; i.e., the number of planes (corresponding to each peak) present within the material.

This diffraction of x-rays from a crystalline material can be expressed by Bragg's law (**Equation 1.14**). When two incoming x-rays of wavelength λ are scattered by atoms in a lattice with a spacing of d, according to Bragg equation:

$$2d \sin\theta = n\lambda \qquad \textbf{Equation 1.14}$$

where θ is the incident angle of the incoming x-ray with respect to the lattice plane and n is an integer. This equation can be used to determine crystallographic information for crystalline materials. For example, if the incident angle θ is known, then the d-spacing of a set of lattice planes can be calculated (**Figure 1.22**). The d-spacing is the distance between the lattice planes of atoms that give rise to diffraction peaks. Each peak in a diffractogram results from a corresponding d-spacing. Therefore, a complete diffraction pattern of the material can be obtained. Usually, crystalline materials have their unique characteristic diffraction patterns. This can be used to differentiate different crystalline materials, making XRD a very powerful tool for solid-state structural analysis.

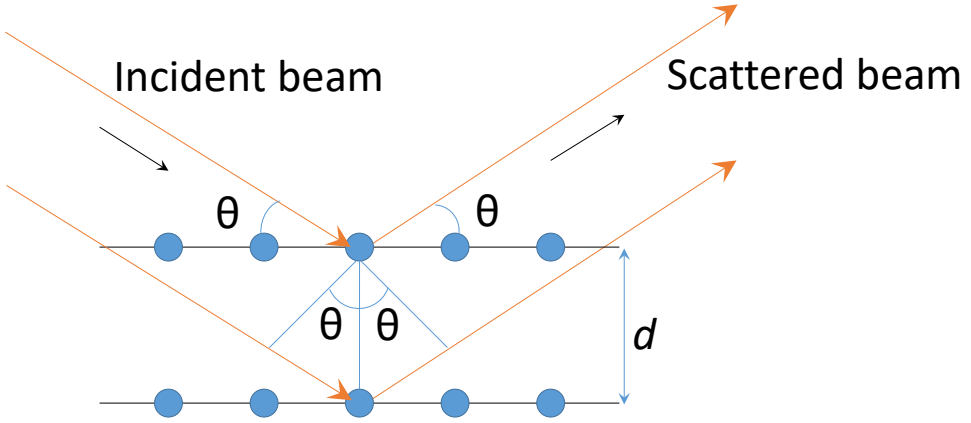

Figure 1.22 Bragg's law: A two-dimensional crystal lattice and a set of imaginary planes is represented by the grid. The diffracted x-rays exhibit constructive interference when the distance between paths of the incident x-rays and scattered x-rays differs by an integer number of wavelength ($n\lambda$).

Bragg's law can also be written in terms of the x-ray wave vectors. An incident x-ray photon with wave vector $\boldsymbol{k}_i$ is scattered by the sample; the scattered photon now has a new wave vector $\boldsymbol{k}_f$. Therefore, the scattering vector can be defined as:

$$\vec{\boldsymbol{q}} = \overrightarrow{\boldsymbol{k_f}} - \overrightarrow{\boldsymbol{k_i}} \qquad \textbf{Equation 1.15}$$

In a diffraction pattern, the x-axis is either the diffraction angle in degrees (2θ) or the scattering vector (q in Å^{-1}). The relationship between θ and q can be expressed as:

$$|\vec{\boldsymbol{q}}| = q = \frac{4\pi}{\lambda}\sin\theta \qquad \textbf{Equation 1.16}$$

where:

$$|\overrightarrow{\boldsymbol{k_i}}| = \frac{2\pi}{\lambda} \qquad \textbf{Equation 1.17}$$

or,

$$2\theta = 2\sin^{-1}\left(\frac{\lambda q}{4\pi}\right) \qquad \textbf{Equation 1.18}$$

where θ is the incident angle and 2θ is the Bragg angle.

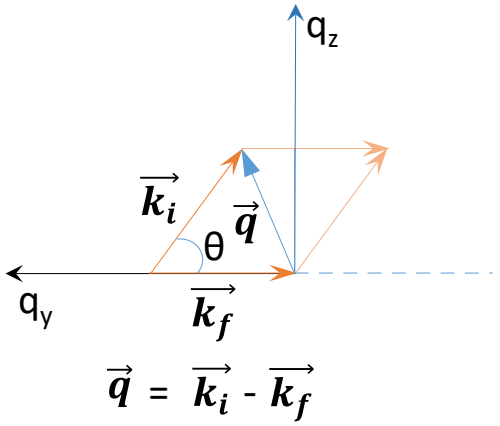

Figure 1.23 Scattering vector $\vec{q}$ and its relation with wave vectors.

If the interaction between the x-ray and the sample is elastic, then no energy is gained or lost in the scattering process. Then, $|\vec{k_f}| = |\vec{k_i}|$. Therefore, the scattering vector must lie on the surface of a sphere of radius $\frac{2\pi}{\lambda}$. This sphere is called the Ewald sphere or sphere of reflection. In reciprocal space, the reciprocal lattice points correspond to the values of momentum transfer where the Bragg diffraction condition is satisfied. Therefore, for diffraction to occur the scattering vector must be equal to a reciprocal lattice vector. Geometrically this implies that diffraction will occur only for reciprocal lattice points that lie on the surface of the Ewald sphere.

The analysis of materials using x-ray diffraction is a powerful characterization technique for solid-state materials. Single crystal XRD provides a complete characterization of the solid-state structure of a material; however, for fields like photovoltaics, the characterization of polycrystalline thin films is generally required. Therefore, powder XRD (pXRD) is used to characterize powders and thin films. Single crystal structures can be used as references to analyze the pXRD data. pXRD can provide bulk information about the crystalline phases present in a

sample. However, information about amorphous phases cannot be collected from pXRD. In addition, pXRD peaks can be broad, which sometimes makes it hard to resolve overlapping peaks. This peak broadening is related to crystallite size and strain. The peak broadening due to size of the crystallites can be calculated by using the Scherrer equation (**Equation 1.19**):

$$\tau = \frac{k\lambda}{\beta \cos\theta} \qquad \textbf{Equation 1.19}$$

where τ is the mean size of coherently scattering domains, k is the shape factor, λ is the x-ray wavelength, β is the full width at half maximum of the diffraction peak, and θ is the Bragg angle. Other factors responsible for peak broadening are related to instrumental conditions which include the beam spot size and divergence, sample size, and the resolution of the detector.

1.5.1.2. GIWAXS

GIWAXS is a variation of pXRD. The major differences between these two techniques are: (i) in pXRD the x-ray beam hits the sample at a higher angle, whereas in GIWAXS the x-ray beam hits the surface of the sample at a very shallow angle (0.1 - 3°). This increases the path length of the x-ray beam resulting in an increase in signal to noise ratio. (ii) GIWAXS is a two-dimensional x-ray diffraction (XRD^2) technique which uses a two-dimensional (2D) area detector. The data recorded by the 2D detector are represented in reciprocal space and defined by the scattering vector q.

The GIWAXS experiments for this thesis were carried out using at the Hard X-ray MicroAnalysis (HXMA) beamline of the Canadian Light Source (CLS), a synchrotron radiation source. A synchrotron is a type of particle accelerator in which the accelerating particle beam travels in a cyclic closed-loop path. When charged particles like electrons are forced to change direction they emit electromagnetic radiation. In a synchrotron facility, pulses of electrons are

generated by passing very high voltage (~200,000 volts) through a heated electron gun made of tungsten-oxide. The electrons are then accelerated (electron energy ~ 250 MeV) by a linear particle accelerator. Once injected, the pulses of electrons are accelerated around a booster ring to increase their energy to ~ 2900 MeV. Then the electrons are transferred to the storage ring where their path is bent by powerful magnets. This causes the electrons to emit photons as synchrotron light which is collected by the beamlines and used for specific experiments. At the CLS, insertion devices (HXMA uses a 63 pole superconducting wiggler) are used to further increase the brightness of the light. Even though the storage ring is under very high vacuum (~10^{-11} Torr), the ring current decreases over time. Therefore, the injection of electrons at regular intervals is required to keep the ring current stable. Usually, the intensity and energy distribution of the light depends on the synchrotron operating energy (order of few GeV) and ring current (in 100's of mA range). The operating energy and ring current at the CLS is generally 2.9 GeV and 140-230 mA, respectively.

At the HXMA beamline, the synchrotron light passes through the optics hutch before it gets delivered to the end station for use. The optical hutch consists of several optical instruments including apertures that block the scattered beam, filters that remove lower and higher energy photons, and a monochromator which selects the light of only one wavelength. Then the selected wavelengths of x-rays are focused by the mirrors in the optics hutch and the beam size is set through a vertical and horizontal slit and sent to the end station. When low energy x-rays are used additional flight tubes and a sample chamber with either a helium or vacuum atmosphere is required to decrease scattering caused by air.

In this thesis, the perovskite thin films were characterized using an energy of 17.99 keV (Zr K edge, $\lambda \approx 0.6889$ Å). To collect the diffraction pattern a MAR 165 CCD area detector was used which was placed ~15 cm away from the sample. For the GIWAXS experiments, a custom built

gas-tight sample chamber was mounted to an 8 circle psi diffractometer (**Figure 1.24**). The sample was placed at the origin of the laboratory $\boldsymbol{L} = [\hat{\boldsymbol{l}}_{\boldsymbol{x}} \quad \hat{\boldsymbol{l}}_{\boldsymbol{y}} \quad \hat{\boldsymbol{l}}_{\boldsymbol{z}}]$ and sample $\boldsymbol{S} = [\hat{\boldsymbol{s}}_{\boldsymbol{x}} \quad \hat{\boldsymbol{s}}_{\boldsymbol{y}} \quad \hat{\boldsymbol{s}}_{\boldsymbol{z}}]$ coordinate systems. For accurate positioning of the sample in the path of the incident x-ray beam (coming from y-axis direction), with the desired angle of incidence, the sample stage and the diffractometer have several motors. The sample height can be adjusted by controlling the movement of the sample stage along the z-axis (z transition). To align the sample with respect to the incident beam and to define the angle of incidence, eta is used (**Figure 1.24**). For additional control of rotation in and out of the xy plane (i.e., roll), delta and phi are used. Similarly, for yaw (moving in xy plane) mu and nu is used. The x-ray penetration depth within the perovskite film depends on the incident angle of the incoming beam (for a fixed energy x-ray). When the incident angle (α_i) is below the critical angle (α_c) the beam is fully reflected from the film. Therefore, the x-rays only probe the first few nanometers of the film surface. In order to measure the bulk of the film, the incident angle must be above the critical angle ($\alpha_i > \alpha_c$). For the purpose of this thesis, the incident angle (α_i) was set to 1.5° which is above the critical angle. Therefore, the bulk of the perovskite films was probed.

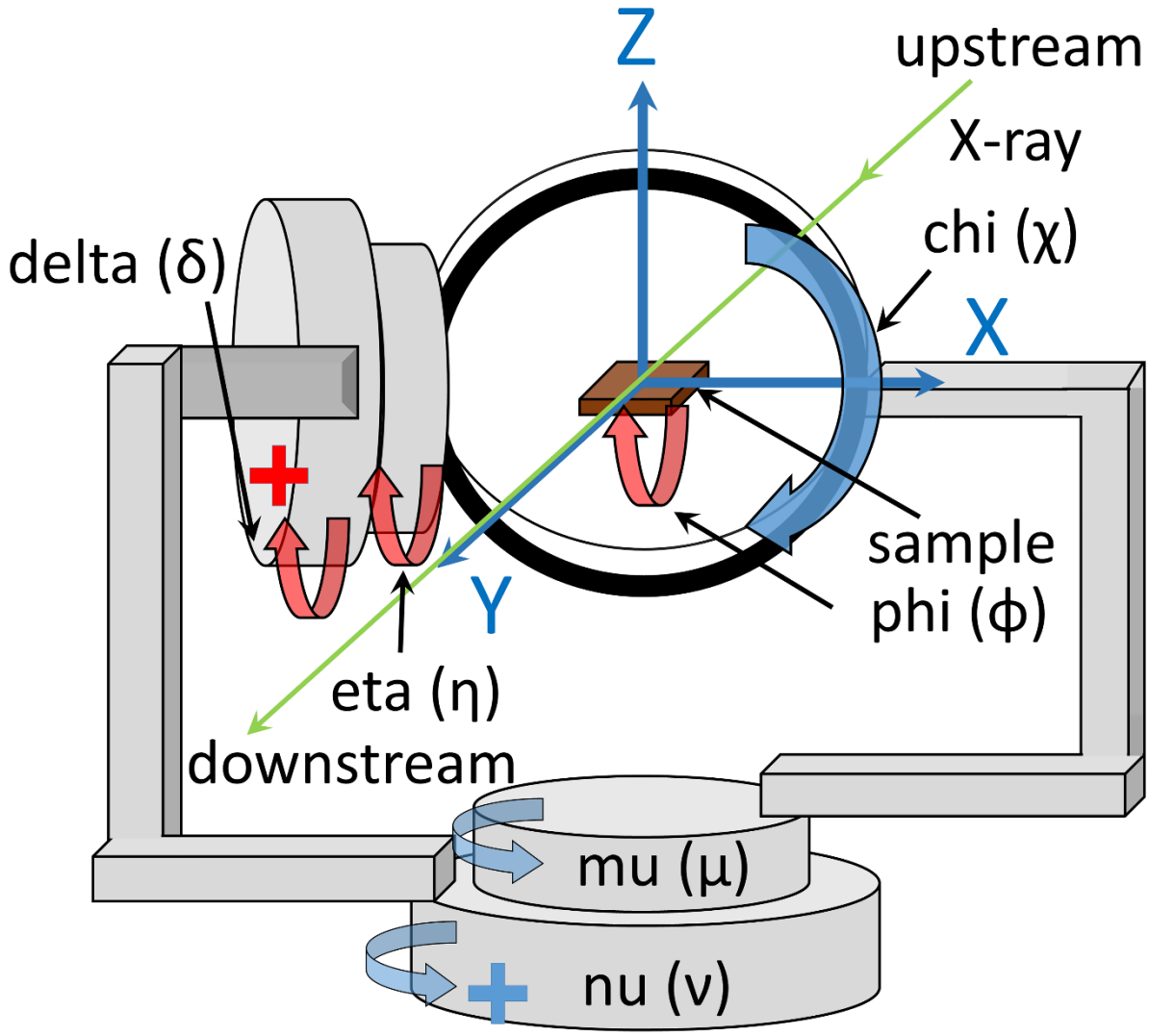

Figure 1.24 An illustration of the diffractometer used in the GIWAXS experiment at the beamline of CLS.

Prior to data processing, calibrations were performed to extract the sample-detector distance by using the Matlab based software GIXSGUI (written and distributed by Zhang Jiang)[214] and Datasqueeze. For calibration, standard diffraction patterns of silver behenate or lanthanum

hexaboride are collected. The diffraction patterns of these standards are known with accuracy. Then, with the help of the GIXSGUI and Datasqueeze the calibration is performed.

The raw data from the 2D area detector consists of a two-dimensional matrix of scattered intensities which is saved as an image file (**Figure 1.25a**). Therefore, for data interpretation the image coordinates need to be converted into scattering vector coordinates. The advantage of using scattering vector (as opposed to 2θ) is that it is independent of the wavelength of incident light and depends only on the d-spacing of the material (**Equation 1.20**). Therefore, the scattering vector geometry is particularly relevant for the synchrotron diffraction experiments.

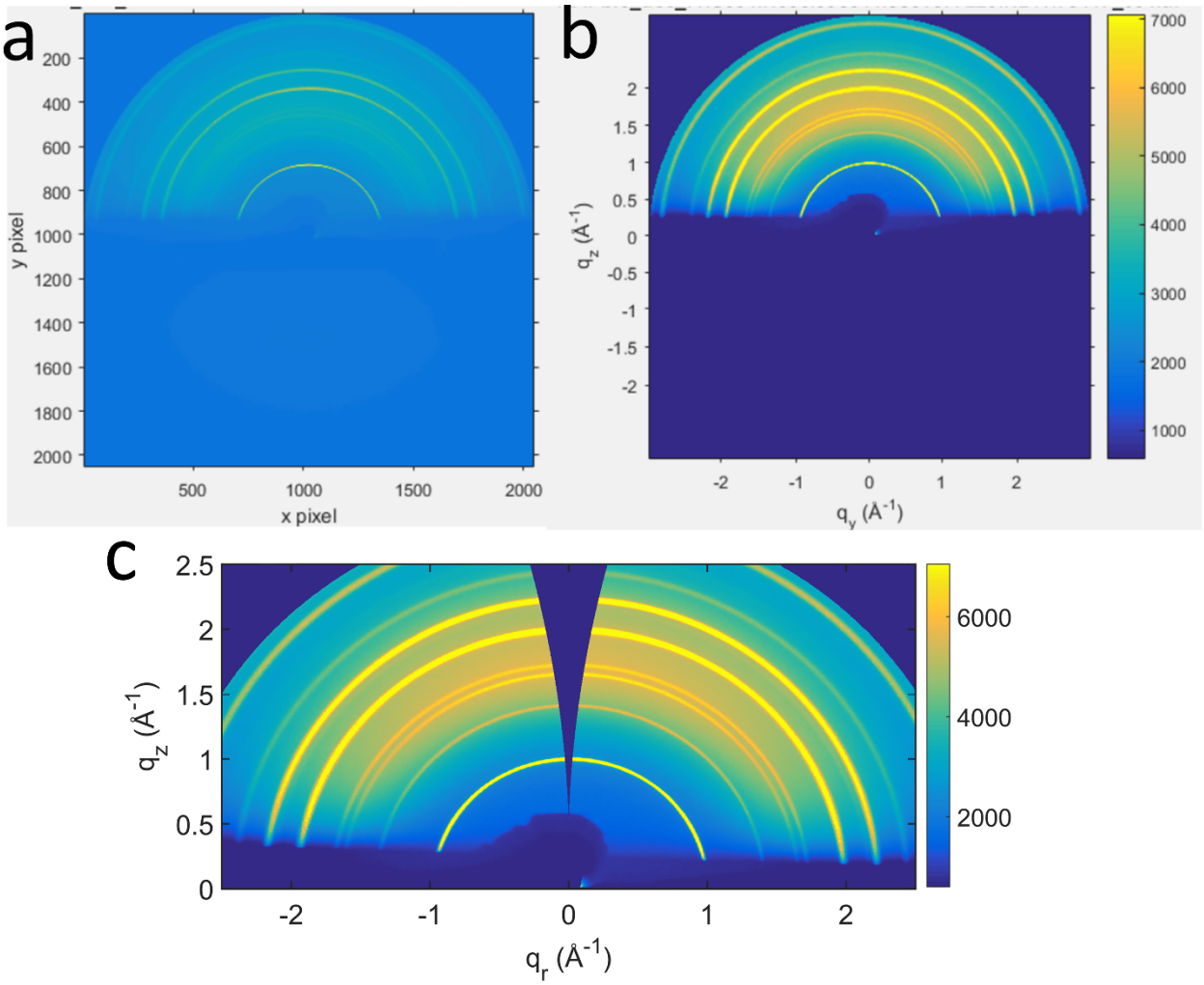

Figure 1.25 Data processing: (**a**) raw diffraction pattern as collected by a 2D detector, (**b**) the same diffraction pattern after reshaping with respect to q_z and q_r, (**c**) the same diffraction pattern after reshaping and accounted for the missing wedge along the q_z.

In grazing-incidence geometry, the true q_z axis is not being probed. This is because the signal observed on the 2D area detector comes from the intersection of the Ewald sphere with the reciprocal-space peaks, and the Ewald sphere curves away from the q_z axis. This results in a missing wedge along q_z in the detector image as shown in **Figure 1.25c**.

$$q = \frac{2\pi}{d} \qquad \textbf{Equation 1.20}$$

The scattering vector $\boldsymbol{qS}$ is tridimensional, thus it can be reduced into its component vectors, $\boldsymbol{q_x}$, $\boldsymbol{q_y}$, and $\boldsymbol{q_z}$. When considering the GIWAXS patterns in 2D Cartesian coordinates, the $\boldsymbol{q_x}$ and $\boldsymbol{q_y}$ vectors are in the plane of the substrate (xy plane); they can be represented by $\boldsymbol{q_r}$. The relationship of $\boldsymbol{q_r}$ to $\boldsymbol{q_x}$ and $\boldsymbol{q_y}$ is defined by **Equation 1.22** (**Figure 1.26**):

$$q_r = \sqrt{(q_x^2 + q_y^2)} \qquad \textbf{Equation 1.21}$$

$$\chi = \frac{\pi}{2} - \tan^{-1}\frac{q_z}{q_r} \qquad \textbf{Equation 1.22}$$

where q is the absolute value of the scattering vector and χ is the azimuthal angle.

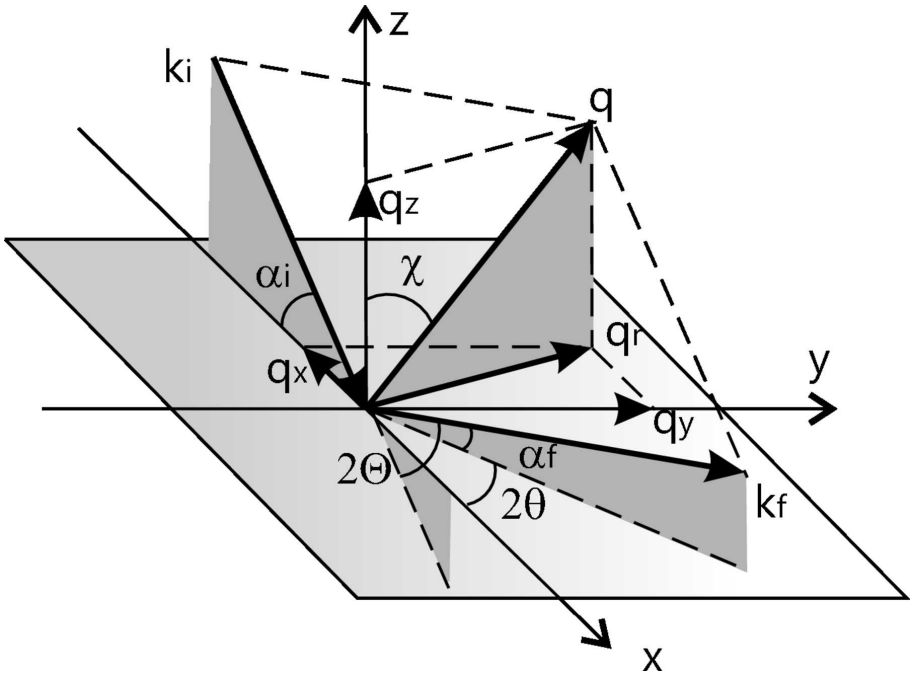

Figure 1.26 Schematic diagram of grazing-incidence scattering geometry in the sample reference frame. Reproduced with permission of the International Union of Crystallography from reference [214].

In the GIWAXS diffraction pattern, an isotropic distribution of crystallites leads to a ring-like diffraction pattern with equal intensity across q_z and q_r (**Figure 1.27a**). However, if there is a

preferential orientation of the crystallites, the diffraction pattern has reduced intensity at specific parts of the diffraction ring (**Figure 1.27b**). Depending upon the preferential orientation of the lattice planes the intensity increases or decrease along q_z or q_r (parallel or perpendicular to the substrate). For example, for a highly crystalline film with particular lattice planes crystallites oriented parallel to the sample surface, the scattering intensity is greater along the q_z axis (**Figure 1.27c**).

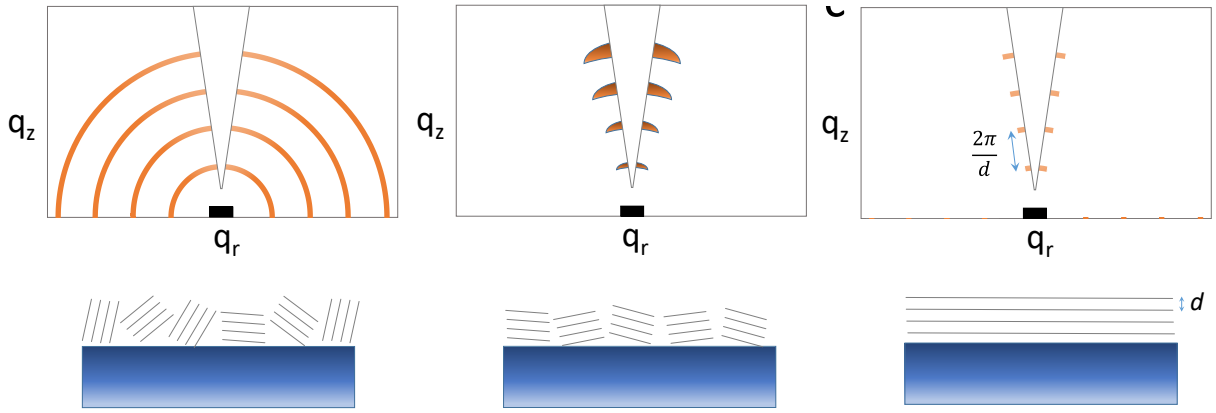

Figure 1.27 Illustration of film crystallinity and the corresponding GIWAXS patterns of: (**a**) crystallites with isotropic distribution, (**b**) crystallites with out-of-plane preferential orientation, (**c**) crystallites with highly oriented out-of-plane preferential orientation.

1.5.1.3. GIWAXS as a Tool to Study Lead Halide Perovskites

GIWAXS has been used to study different crystalline materials in the photovoltaic field.[215-219] One of the well-studied examples is semicrystalline P3HT and its preferential orientation.[216, 220-223] In the field of PSCs, GIWAXS has been used to study either the decomposition mechanism[68, 224] or to follow the film formation mechanism.[80, 82, 225-229] In addition to perovskite layers, it has also been used to probe different layers of the perovskite device stack.[207, 215, 230, 231] Early studies were conducted by Tan and coworkers where they monitored the perovskite crystallization process and film formation during thermal annealing.[80] Here, they utilized in situ GIWAXS to monitor the

formation mechanism of $MAPbCl_xI_{3-x}$ on a mesoporous Al_2O_3 scaffold from different precursor solutions. During their studies, they found that an unknown intermediate phase formed within a few minutes of casting which then disappeared to form a pure perovskite phase. However, over-annealing of the perovskite film led to the decomposition of the perovskite phase by forming PbI_2. In a follow-up study, Saliba et al. used GIWAXS to fine-tune the annealing conditions by analyzing the film morphology after different thermal annealing conditions.[225] They found that short rapid annealing at 130 °C resulted in larger micron-sized perovskite domains resulting in better performing devices for planar PSCs.

Realizing the potential of GIWAXS, Yang et al. performed a series of in situ experiments to monitor the changes in $MAPbI_3$ films when subjected to harsh environmental conditions.[68] In their first paper, they subjected $MAPbI_3$ to humid atmosphere (98% RH at 22 °C) while collecting diffraction data.[68] According to their study, $MAPbI_3$ decomposes to PbI_2 via an intermediate hydrate phase. In a follow-up study, they used GIWAXS for screening better ETMs among different metal oxide supports: planar TiO_2, mesoporous TiO_2, or mesoporous Al_2O_3.[189] Here, they used GIWAXS as a tool to follow the degradation kinetics and compare the stability of the various ETMs/$MAPbI_3$ bilayers. The mesoscopic scaffolds, due to better encapsulation can delay the formation of the monohydrate phase, and were better able to protect the perovskite films. In another work, they took advantage of in situ GIWAXS to probe the instability of ZnO/$MAPbI_3$ films when heated at 100 °C in air.[79] Due to the presence of surface hydroxyl groups on the ZnO surface, the $MAPbI_3$ decomposed faster than calcinated ZnO.

More complicated operando measurements have, GIWAXS is proven to be a useful tool to study how structural changes affect device performance.[224, 226, 232] For example, Schelhas et al. used operando GIWAXS to probe the effect of the tetragonal-to-cubic phase transition on $MAPbI_3$-

based PSCs.[232] They found that $MAPbI_3$ PSCs have a high degree of tolerance to the phase change as no significant change in PCE was observed. This kind of operando experiment was even used to monitor the change in PCE of PSCs during the formation and crystallization process of the perovskite.[226] Another excellent example of an operando GIWAXS experiment was carried out by Fransishyn et al. in a humid atmosphere.[224] Their results showed that the choice of the electrode is important for PSC stability. Due to humidity-induced iodide ion migration, silver electrodes corrode much faster than gold electrodes. Furthermore, their work revealed that at high humidity, high temperature leads to the suppression of both intermediates and byproducts.

1.6. Thesis Objectives

The major challenge for the PSC field is long-term stability. The goal of this thesis is to address this issue and to improve the longevity of PSCs. This is discussed over the course of three chapters. This thesis describes how different hydrophobic HTMs were synthesized, modified and applied in solar devices to improve their lifetime, and how different lead halide perovskite compositions were screened for their moisture resistance, with the goal of finding a stable composition to improve device lifetime.

The HTL is one of the major components of a PSC and is critically important to device performance. The most common HTMs used in high performance PSCs are spiro-OMeTAD and PTAA, but these HTMs leave the devices more susceptible to moisture. Therefore, new hydrophobic HTMs are needed to improve stability. P3HT is one of the HTMs which is proven to help protect the perovskite. **Chapter 2** describes how new polythiophene-based HTMs were synthesized by modifying the side chains of P3HT with different alkyloxy groups. This resulted in

a range of HTMs with different degrees of hydrophobicity. The effect of the different side chains is discussed in terms of their ability to protect thin films of $MAPbI_3$.

In **Chapter 3**, a new HTL for PSCs was used to solve the problem of moisture stability. **Chapter 2** revealed that fluorinated polythiophines could improve the perovskite lifetime significantly, but the device performance was poor. Therefore, a new HTL was prepared – a poly(3-hexylthiophene) nanowire network in a PMMA matrix. Stability tests on different devices (with both silver and gold electrodes) were carried out at high humidity.

Ultimately, even with good barrier layers, without having a robust perovskite composition it is impossible to fully solve the issue of device stability. There are many possible compositions that use cations like MA, FA and Cs, and anions such as I, Br, and Cl. These compositions have different chemical stabilities. **Chapter 4** discusses screening these perovskite compositions for their moisture-resistance using in situ UV-visible spectroscopy. The Chapter also discusses the decomposition mechanisms of different perovskite compositions as revealed by in situ GIWAXS experiments.

Finally, **Chapter 5** gives a comprehensive overview of the work described in this thesis. This chapter places the contribution of this thesis in the context of PSC field. It also provides future plans and suggestions for further research that could advance the field of PSCs.

2. Hydrophobic Polythiophene Hole-transport Layers to Address the Moisture-induced Decomposition Problem of Perovskite Solar Cells

2.1. Introduction

As discussed in **Section 1.3** and **1.4**, the moisture sensitivity of $MAPbI_3$ leads to decomposition; therefore, physical protection of $MAPbI_3$ can lead to better stability for PSCs. Several approaches have been used to improve PSC stability such as device encapsulation, changing the perovskite composition, and the addition of interfacial layers and have been discussed in detail in **Section 1.4**. One of the most interesting strategies is to take advantage of the layers that are already a part of the device architecture such as the top electrode, ETLs, or HTLs. Hydrophobic carbon-based top electrodes or mesoscopic alumina or titania scaffolds have successfully been used to help stabilize the devices (discussed in detail in the **Section 1.4**). However, one of the most popular strategies is to use an interfacial layer that can act as both a water vapor barrier and a HTL. In the conventional PSC architecture, the HTL lies directly on top of the perovskite layer. The work discussed in this chapter uses HTL to stabilize the PSC.

In the literature different hydrophobic HTMs have been synthesized and used to produce PSCs with longer lifetime. The most commonly used HTMs are spiro-OMeTAD, PTAA, and P3HT. Among these HTLs, P3HT has proven to be an effective vapor barrier.[68, 170] A study conducted by Yang et al. on $MAPbI_3$/HTMs bilayers at 98% relative humidity with these three HTMs showed that the spiro-OMeTAD-coated film degraded more rapidly than the films coated with the other two HTMs.[65] The film (with spiro-OMeTAD) degradation was even faster than the bare perovskite

film without any HTM. The P3HT-coated film had the highest stability followed by the PTAA-coated film. Their in situ UV-visible decomposition kinetics studies even showed a delay in the onset of decomposition for the P3HT-coated $MAPbI_3$ film. This suggests that the P3HT coating is able to resist moisture ingress for a few hours (**Figure 2.1a**).

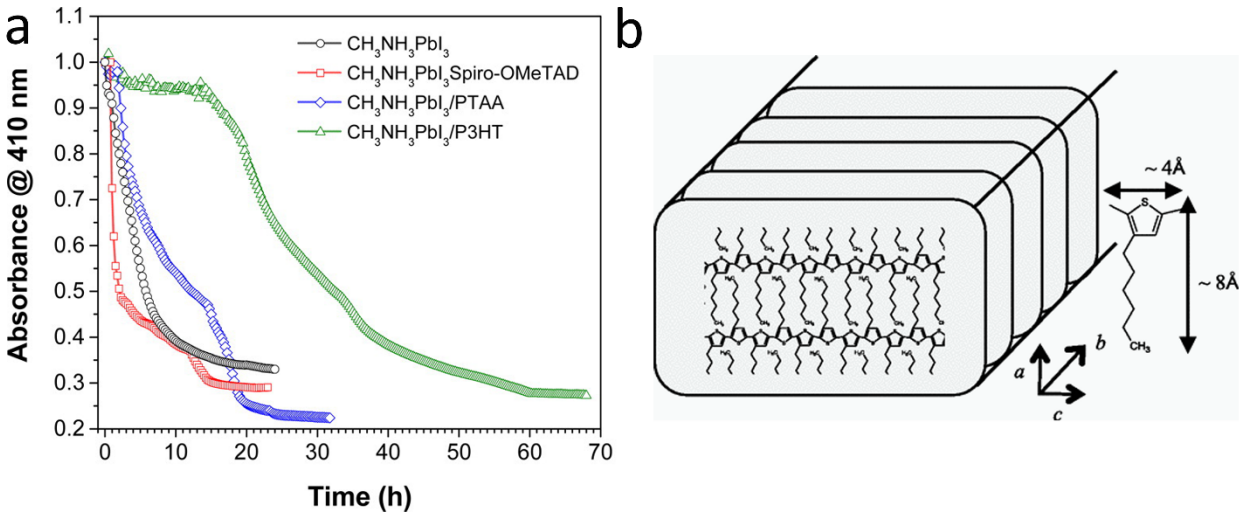

Figure 2.1 (**a**) Normalized absorbance at 410 nm as a function of time for $MAPbI_3$ (open circles), $MAPbI_3$/spiro-OMeTAD (open squares), $MAPbI_3$/PTAA (open diamonds), and $MAPbI_3$/P3HT (open triangles) films exposed to a 98 ± 2% RH environment at 22.8 ± 0.5 °C. Reproduced with permission of the American Chemical Society from reference ([68]). (**b**) Schematic diagram of dense, crystalline regioregular P3HT. The lamellae of polymer chains in the ac plane are stacking to the b axis, which corresponds to the longitudinal axis of nanofibers, by π - π interaction. Reproduced with permission of the American Physical Society from reference ([233]).

This observation can be rationalized in terms of the ability of the HTM to form a uniform, pinhole free, dense film on top of the perovskite layer. The formation and decomposition of the perovskite film involves large volume changes which eventually leads to an increase in mechanical stress on HTMs.[234] Spiro-OMeTAD is a small molecule and it has a nonplanar twisted geometry. It cannot form a dense, regular film. Due to its poor mechanical properties it can easily develop cracks. Moisture can easily penetrate it, making the perovskite underneath vulnerable to

decomposition. In addition, a large amount of hygroscopic lithium salt is used as a dopant to improve the conductivity of spiro-OMeTAD. This helps absorb more moisture, thus contributing to the poor protection ability of spiro-OMeTAD. Even though PTAA is a polymer, due to its lower molecular weight ($M_n \sim$ 7-10 kDa) and lack of efficient packing it cannot form dense, pinhole free films. So, moisture can go through it. On the other hand, regioregular P3HT can form dense, pinhole free, crystalline film due to interdigitation of the regioregular alkyl chains and π-π stacking of the thiophene backbones (**Figure 2.1b**).[233] This efficient packing of P3HT helps to provide better protection to the underlying $MAPbI_3$ layer.

Given that P3HT increases the stability of the $MAPbI_3$ layer, here I have used a similar polythiophene-based system which has perfluorinated alkyl chains (P3OFHT) instead of hexyl chains (**Figure 2.2**). Perfluorinated alkyl derivatives are usually more hydrophobic than normal hydrocarbons. [235] [236] Therefore, this new perfluorinated polythiophene P3OFHT should be more hydrophobic than P3HT. Thus it has the potential to improve the longevity of the $MAPbI_3$ based PSCs. In order to study the effect of installing hydrophobic perfluorinated side chains in the polythiophene system thoroughly, four different polythiophenes of varying hydrophobicity were synthesized with different side chains. The side chains range from hydrophilic (triethylene glycol methyl ether), through standard hydrocarbons (hexyloxy, dodecyloxy), to extremely hydrophobic (highly fluorinated hexyloxy) (**Figure 2.2**). All four polymers (alongside commercially available P3HT) were evaluated for their ability to act as HTLs in PSCs and also for their ability to reduce the rate of moisture ingress into the underlying perovskite layer. In situ UV–vis spectroscopy was used to evaluate the stability of the different HTM/$MAPbI_3$ bilayers.

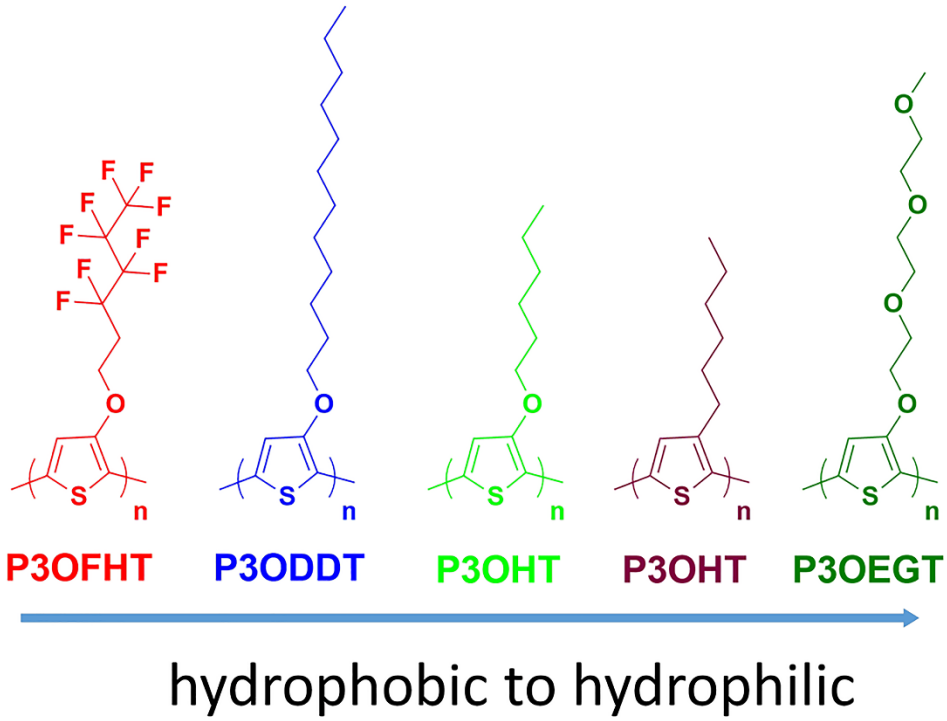

Figure 2.2 Structures of the poly(3-alkoxythiophene) HTLs, arranged in order from hydrophobic to hydrophilic (left to right, respectively).

Section 2.2 and **Section 2.3.** were adopted with permission from Kundu S.; and Kelly T. L. *Can. J. Chem*. **2019**, 97, 435-441. Copyright 2019 Canadian Science Publishing.[237]

2.2. Experimental Section

2.2.1.Materials

All solvents were analytical grade and were purchased from Fisher Chemicals and used as received, except where noted below. All other reagents were used as received, without further purification. All reactions were carried out under an argon atmosphere using standard Schlenk techniques, unless otherwise stated. Toluene, DMF, and THF were dried over activated 3 Å molecular sieves and stored under nitrogen. 3-Methoxythiophene, 1H,1H,2H,2H-perfluorohexan-1-ol, 1-dodecanol, 1-hexanol, 2-(2- (2-methoxyethoxy)ethoxy)ethanol, *p*-toluenesulfonic acid

monohydrate, copper(I) chloride, sodium metal, 1,3-dibromo-5,5-dimethylhydantoin, [1,3-bis(diphenylphosphino)propane]dichloronickel(II), lead(II) iodide (99%), methylamine (37% in absolute ethanol), hydriodic acid (57% in H_2O), TBP (96%) and Li-TFSI (99%) were purchased from Sigma-Aldrich. Zinc acetate dihydrate was purchased from Alfa Aesar. 3-Bromothiophene was purchased from Matrix Scientific. P3HT (electronic grade, $M_w \sim 50$ kDa) was purchased from Rieke Metals Inc. ITO-coated glass (R_s = 20 $\Omega \cdot sq^{-1}$) substrates were purchased from Delta Technologies, Ltd. Ag pellets (99.99%) were purchased from Kurt J. Lesker.

2.2.2. Synthesis

2.2.2.1. Synthesis of 3-((3,3,4,4,5,5,6,6,6-Nonafluorohexyl)oxy)thiophene (**1**)

3-((3,3,4,4,5,5,6,6,6-nonafluorohexyl)oxy)thiophene **(1)** was synthesized according to previously reported procedure.[238] 3-Methoxythiophene (1.70 mL, 17.5 mmol) was placed in a 100 mL two-necked round bottom flask and dissolved in 15 mL dry toluene. To it, 3,3,4,4,5,5,6,6,6-nonafluorohexan-1-ol (5.81 mL, 35.0 mmol) was added, followed by addition of *p*-toluenesulfonic acid (0.33 g, 1.80 mmol). Then the reaction mixture was heated at reflux under argon atmosphere for 24 hours. After the completion of the reaction, checked by TLC, 50 mL DCM was added to the reaction mixture and it was transferred to a 125 mL separating funnel and washed with distilled water (30 mL × 2). The organic layer was dried over anhydrous magnesium sulfate and concentrated to dryness. The crude product was purified by column chromatography using hexane as eluent to give a colorless liquid **1** (30 %).

Yield 1.81 g, 5.25 mmol, 30%

^{1}H NMR (500 MHz, $CDCl_3$, δ ppm): 7.24-7.19 (m, 1H), 6.75-6.74 (m, 1H), 6.3.-6.29 (m, 1H), 4.25 (t, J = 6.53 Hz, 2H), 2.65-2.57 (m, 2H).

2.2.2.2. Representative Synthesis of 3-(Alkoxy)thiophenes (**2**-**4**)

3-Hexyloxythiophene **(3)** was synthesized by following the literature procedure.[239] First, sodium hexoxide was prepared in situ by slowly adding dry 1-hexanol (75 mL) and sodium (147 mmol, 3.38 gm). After the complete disappearance of Na, dry DMF (20 mL) was added to the reaction mixture as a co-solvent. Then 3-bromothiophene (6.89 mL, 73.6 mmol) was slowly added to the reaction mixture followed by catalytic amount of copper (I) chloride (1.09 g, 11.0 mmol). The reaction mixture was allowed to stir continually for 0.5 hours at 110 °C under argon. After the reaction was completed, checked by TLC, the reaction mixture was poured into water and extracted with diethyl ether and concentrated under vacuum. The products were purified by fractional distillation in order to yield 85% of 3-hexyloxythiophene (**3**).

Yield 11.53 g, 62.56 mmol, 85%

^{1}H NMR (500 MHz, $CDCl_3$, δ ppm): 7.16 (dd, 1H), 6.75 (dd, 1H), 6.22 (dd, 1H), 3.94 (t, J = 6.53 Hz, 2H), 1.80-1.74 (m, 2H), 1.36-1.31 (m, 6H), 0.92-0.89 (m, 3H).

3-dodecyloxythiophene (**2**) and 3-(2-(2-(2-methoxyethoxy)ethoxy)ethoxy)thiophene (**4**) were prepared following same procedure using 1-dodecanol, 2-(2-(2-methoxyethoxy)ethoxy)ethanol) respectively.

3-dodecyloxythiophene (**2**)

Yield 17.58 g, 65.50 mmol, 89%

^{1}H NMR (500 MHz, $CDCl_3$, δ ppm): 7.20 (dd, 1H), 6.80 (dd, 1H), 6.27 (dd, 1H), 3.97 (m, J = 6.53 Hz, 2H), 1.85-1.80 (m, 2H), 1.37-1.34 (m, 18H), 0.99-0.95 (m, 3H).

3-(2-(2-(2-methoxyethoxy)ethoxy)ethoxy)thiophene (**4**)

Yield 14.86 g, 60.35 mmol, 82%

^{1}H NMR (500 MHz, $CDCl_3$, δ ppm): 7.16 (dd, 1H), 6.77 (dd, 1H), 6.26 (dd, 1H), 4.12 (t, J = 4.7 Hz, 2H), 3.84 (t, J = 4.9 Hz, 2H), 3.74-3.72 (m, 2H), 3.79-3.65 (m, 4H), 3.56-3.54 (m, 2H), 3.38 (s, 3H).

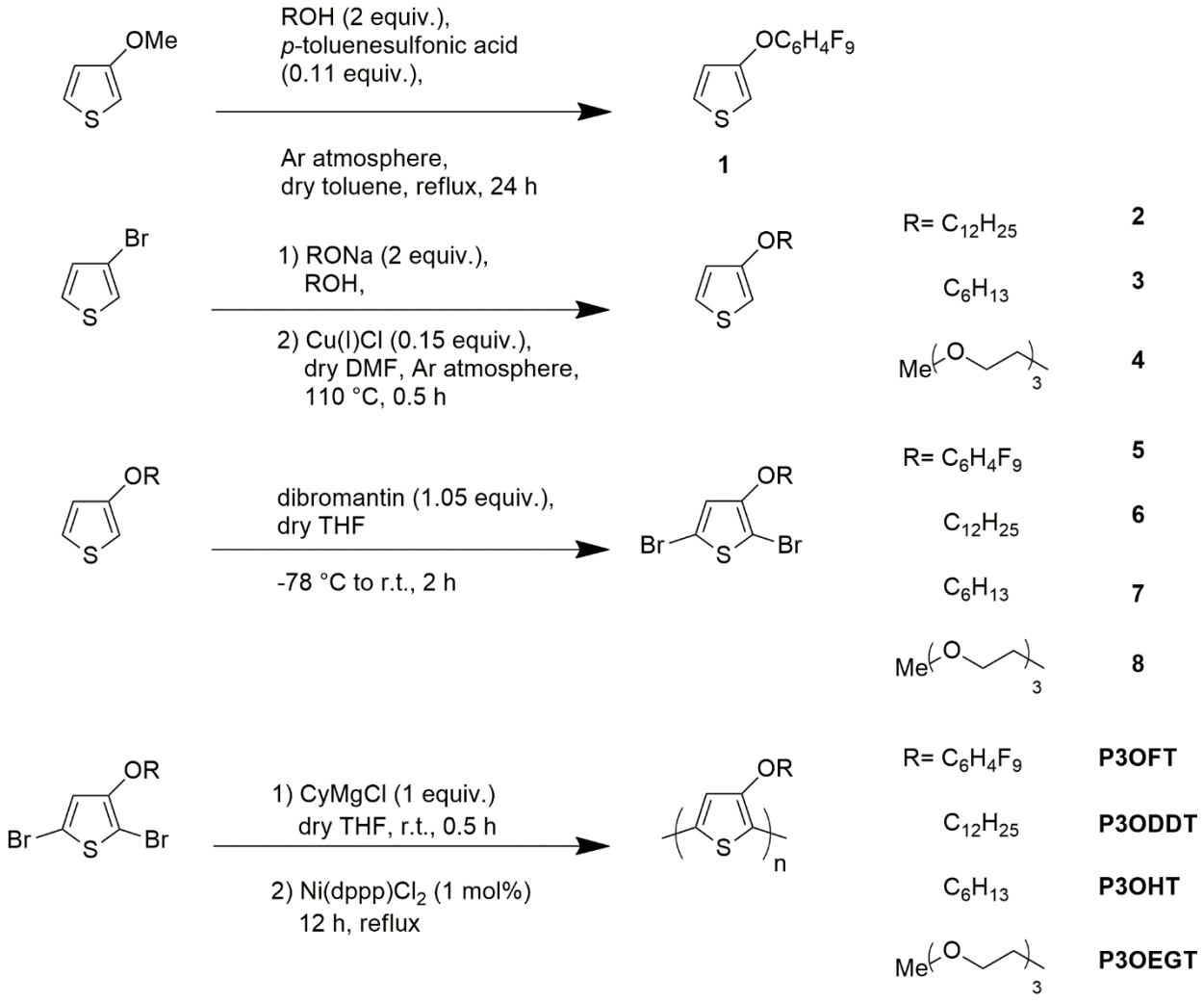

Scheme 2.1 Synthesis of poly(3-alkoxythiophenes).

2.2.2.3. Representative Synthesis of 2,5-Dibromo-3-alkoxythiophene (**5**-**8**)

Bromination of 3-alkyoxythiophene was performed using dibromatin as a brominating agent by following the literature procedure.[240] First, 3-hexyloxythioplene (**3**) (3.15 g, 17.0 mmol) was dissolved in 50 mL of anhydrous THF. Then the reaction mixture was cooled to -78 °C. To it, 1,3-dibromo-5,5-dimethylhydantoin (5.35 g, 18.7 mmol) was added and then the reaction mixture was stirred for 0.5 hours at -78 °C under argon atmosphere. Then the low-temperature bath was removed and the reaction was continued for another 2 h at room temperature. After the reaction was complete, as monitored by TLC, the solvent was removed by rotary evaporation. Then, the residue was transferred into a filter paper and washed several times with hexanes. The filtrate was concentrated at reduced pressure. The product was purified by column chromatography using hexanes as an eluent to yield 85-90%. In order to prevent any radicle side reactions activated charcoal was added and finally the product was stored at 0 °C in dark for future use.

2,5-dibromo-3-((3,3,4,4,5,5,6,6,6-nonafluorohexyl)oxy)thiophene (**5**)

Yield 7.28 g, 14.45 mmol, 85%

^{1}H NMR (500 MHz, $CDCl_3$, δ ppm): 6.75 (s, 1H), 4.25 (t, J = 6.53 Hz, 2H), 2.65-2.57 (m, 2H).

2,5-dibromo-3-dodecyloxythiophene (**6**)

Yield 6.52 g, 15.30 mmol, 90%

^{1}H NMR (500 MHz, $CDCl_3$, δ ppm): 6.78 (s, 1H), 4.01 (m, J = 6.53 Hz, 2H), 1.79-1.48 (m, 2H), 1.48-1.30 (m, 18H), 0.93-0.89 (m, 3H).

2,5-dibromo-3-hexyloxythiophene (**7**)

Yield 5.22 g, 15.30 mmol, 90%

^{1}H NMR (500 MHz, $CDCl_3$, δ ppm): 6.76 (s, 1H), 3.99 (t, J = 6.60 Hz, 2H), 1.76-1.70 (m, 2H), 1.46-1.42 (m, 6H), 0.92-0.89 (m, 3H).

2,5-dibromo-3-(2-(2-(2-methoxyethoxy)ethoxy)ethoxy)thiophene (**8**)

Yield 5.84 g, 14.45 mmol, 85%

^{1}H NMR (500 MHz, $CDCl_3$, δ ppm): 6.79 (s, 1H), 4.15 (t, J = 3.9 Hz, 2H), 3.79 (t, J = 4.0 Hz, 2H), 3.72-3.71 (m, 2H), 3.67-3.64 (m, 4H), 3.56-3.54 (m, 2H), 3.38 (s, 3H).

2.2.2.4. Representative Synthesis of Poly(3-alkoxythiophenes) (**9**-**12**) by Grignard Metathesis (GRIM)

The GRIM polymerization was done by following the reported procedure by McCullough.[240] First cyclohexylmagnesium chloride solution (2.59 mL, 2M) was slowly added to 2,5-dibromo-3-hexyloxythiophene **(7)** (1.76 g, 5.17 mmol) in dry THF (50 mL) under argon atmosphere. The reaction mixture was allowed to stir continuously for 0.5 hours after which a catalytic amount of $Ni(dppp)Cl_2$ (42 mg, 0.078 mmol) previously dissolved in anhydrous THF (2 mL) was added via syringe. The reaction mixture was stirred continuously at gentle reflux under argon atmosphere for 24 hours. Then the polymer was precipitated by the addition of 200 mL methanol and purified by Soxhlet extraction by using methanol, hexanes, and chloroform in sequence. The chloroform fraction was concentrated and then was dried over high vacuum to give the desired polymer (P3OHT).

Poly(3-((3,3,4,4,5,5,6,6,6-nonafluorohexyl)oxy)thiophene) (P3OFHT) Yield 0.256 g

^{1}H NMR (600 MHz, $CDCl_3$, δ ppm): 6.91-6.85 (s), 4.43-4.41 (t), 2.71 (m)

Poly(3-dodecyloxythiophene) (P3ODDT) Yield 0.402 g

^{1}H NMR (600 MHz, $CDCl_3$, δ ppm): 6.93 (s), 4.19 (m), 1.91 (m), 1.70 (m), 1.57 (m), 1.27 (m), 0.89 (s)

Poly(3-hexyloxythiophene) **(**P3OHT**)** Yield 0.351 g

^{1}H NMR (600 MHz, $CDCl_3$, δ ppm): 6.86 (s), 4.09-3.97 (m), 1.85-1.76 (m), 1.58-1.26 (m), 0.94-0.87 (m)

Poly(3-(2-(2-(2-methoxyethoxy)ethoxy)ethoxy)thiophene) (P3OEGT) Yield 0.324 g

^{1}H NMR (600 MHz, $CDCl_3$, δ ppm): 6.96 (s), 4.33-3.31 (m)

2.2.2.5. Synthesis of ZnO Nanoparticles

ZnO nanoparticles were synthesized by previously reported procedures.[241, 242] Zinc acetate dihydrate (2.95 g, 13.4 mmol) was first dissolved in methanol (125 mL) at 70 °C followed by the addition of a solution of KOH (1.48 g, 23 mmol) in methanol (65 mL) over a period of 10-15 minutes. The reaction mixture was allowed to stir continuously at 65 °C for an additional 2.5 h. The reaction mixture was allowed to cool down to room temperature and the precipitate was washed twice with methanol (2 × 50 mL). Finally, chloroform (10 mL), n-butanol (50 ml) and methanol (5 ml) were added to prepare a translucent dispersion of ZnO nanoparticles (~ 6 mg/mL). The solution was filtered using a 0.45 μm PVDF syringe filter prior to use.

2.2.2.6. Synthesis of Methylammonium Iodide

Methylammonium iodide was synthesized according to literature procedures.[41, 243] First, a solution of methylamine (30 mL, 37% in EtOH) was added to 200 mL of ethanol and cooled to 0 °C, followed by the dropwise addition of hydriodic acid (30 mL). The reaction mixture was allowed to stir continually at 0 °C for 2 h. The product was recovered by removing the solvent on a rotary

evaporator at 50 °C for 1 h. It was washed with diethyl ether (3 × 50 mL), dissolved in ethanol (50 mL), and reprecipitated in diethyl ether to obtain crystalline methylammonium iodide. The powder was dried under high vacuum for 1 day at 65 °C.

2.2.3. Solar Cell Fabrication

Solar cells were fabricated by following previously reported procedures (**Figure 2.3**).[244] ITO-coated glass substrates were cleaned by sequentially sonicating them for 20 min in 2% Extran 300 detergent, acetone, and isopropanol followed by drying in an oven at 120 °C for 2 h. A thin ZnO nanoparticle layer was deposited by spin-coating onto the substrate at 3000 rpm for 30 s from a solution of 6 mg·mL^{-1} in *n*-butanol. This procedure was repeated three times in order to produce a uniform film. To form the methylammonium lead iodide perovskite layer a two-step sequential method was adopted. First, a thin layer of lead iodide was spin-coated on top of ZnO layer at 3000 rpm for 15 s from a lead iodide solution (dissolved in *N*,*N*-dimethylformamide at a concentration of 460 mg·mL^{-1}). Then the substrate was dipped into a solution of CH_3NH_3I in 2-propanol (10 mg·mL^{-1}) for 3 minutes. The substrate was spin-dried at 3000 rpm for 25 s. For the deposition of different HTLs, five solutions containing five different polymers were prepared. All HTLs were deposited using the same spin conditions (spin-coated at 1000 rpm for 25 s). A solution of Li-TFSI (28 mg Li-TFSI/1 mL acetonitrile) was used as a dopant to improve the conductivity of the polymer layers. All polymer HTLs were prepared by dissolving appropriate amount of polymers (P3OFHT (10 mg·mL^{-1}, LiTFSI 6.66 μL, TBP 3.33 μL), P3ODDT (15 mg·mL^{-1}, LiTFSI 13 μL, TBP 7.5 μL), P3OHT (10 mg·mL^{-1}, LiTFSI 6.66 μL, TBP 3.33 μL), P3HT (20 mg·mL^{-1}, LiTFSI 6.66 μL, TBP 3.33 μL), P3OEGT (15 mg·mL^{-1}, LiTFSI 6.66 μL, TBP 3.33 μL)) in 1 mL of chlorobenzene overnight. For only P3OFHT based devices,, an additional layer of molybdenum oxide (~ 5 nm

thick) was deposited by thermal evaporation at a base pressure of 2×10^{-6} mbar. Finally, a silver electrode was deposited by thermal evaporation at a base pressure of 2×10^{-6} mbar.

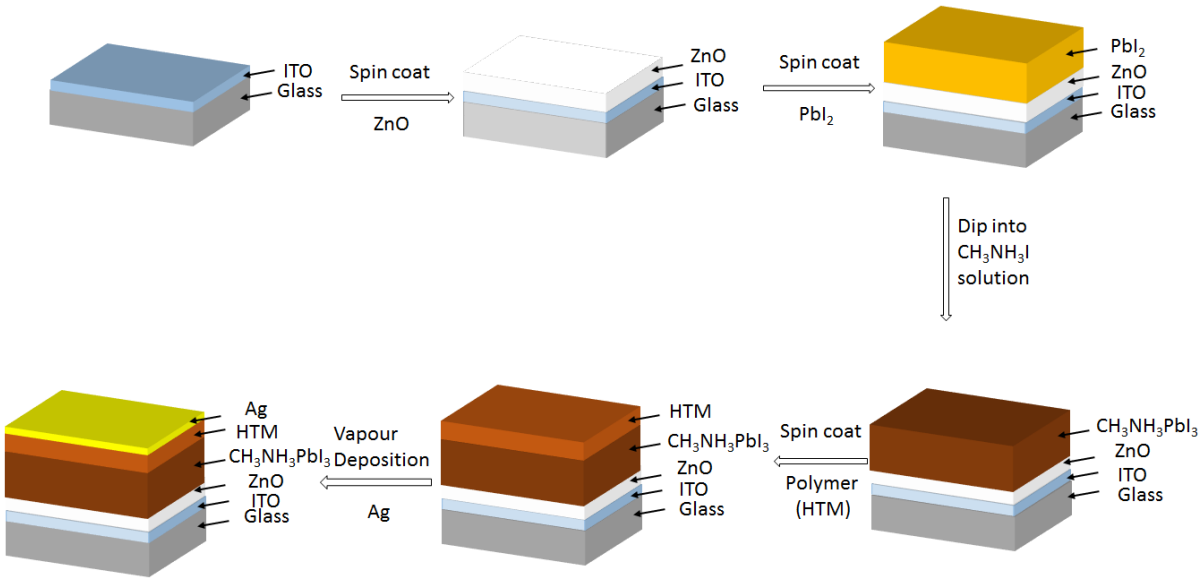

Figure 2.3 Schematic of fabrication of solar cells.

2.2.4. Characterization:

2.2.4.1. ^{1}H NMR and ^{13}C NMR

NMR spectra were recorded using a Bruker Avance 500 MHz and 600 MHz spectrometers.

2.2.4.2. UV-visible Spectroscopy

UV-visible spectra were obtained using a Cary 6000i UV-Visible spectrophotometer in $CHCl_3$ and on solid-state films.

2.2.4.3. Powder X-ray Diffraction

Powder x-ray diffraction measurements were carried out on a PANalytical Empyrean diffractometer configured using a cobalt (λ = 1.79 Å) x-ray source. The data were collected with a 0.0469° step size (2θ). pXRD was performed on a PANalytical Empyrean diffractometer configured with.

2.2.4.4. Scanning Electron Microscopy

Scanning electron microscopy was carried out on a Hitachi SU8010 microscope operating at a 1.0−5.0 kV landing voltage under high vacuum.

2.2.4.5. Gel Permeation Chromatography (GPC)

Molecular weights of the polymers were acquired by triple detection gel permeation chromatography (GPC) using a Viscotek 350 HT-GPC system (Malvern) using tetrahydrofuran as the eluent at 1.0 mL min^{-1} flow rate. The instrument is equipped with an autosampler (Model 430 Vortex), a degasser (model 7510), two pumps (model 1122), 7 and 90° light-scattering detectors, refractometer, and viscometer. Three types of GPC columns (three main columns: Plgel 10 mm MIXED-B LS 300 × 7.5 mm; one guard column: 10 mm GUARD 50 × 7.5 mm; Agilent Technologies) were used to cover the range of M_w of 500 to 10 000 000 $g \cdot mol^{-1}$. To prepare the samples, first the polymers were dissolved in THF with stirring overnight, and then filtered through 0.45 mm PTFE syringe filters just before GPC analysis. The apparent molecular weights and dispersities ($Đ = M_w/M_n$) were calculated with a calibration based on linear polystyrene standards.

2.2.4.6. Solar Cell Characterization

The performance of the devices was measured using a Keithley 2400 source-measure unit and a 450 W Class AAA solar simulator equipped with an AM1.5G filter (Sol3A, Oriel Instruments) inside a nitrogen filled glovebox (<0.1 ppm O_2 and H_2O). The illumination intensity was adjusted to 100 $mW \cdot cm^{-2}$ as determined by a standard silicon reference cell (91150V, Oriel Instruments). A non-reflective metal mask was used to define the effective area of the device to be 0.0708 cm^2.

2.2.4.7. Water Vapor Stability Tests

A stream of nitrogen carrier gas was bubbled through water in order to generate a stream of saturated (99 ± 1% relative humidity (RH)) water vapor. This flowed into a custom-built sample holder (for in situ absorbance spectroscopy, **Figure 2.4**) The RH and temperature were measured downstream of the sample chamber by an RH-USB humidity sensor (Omega).

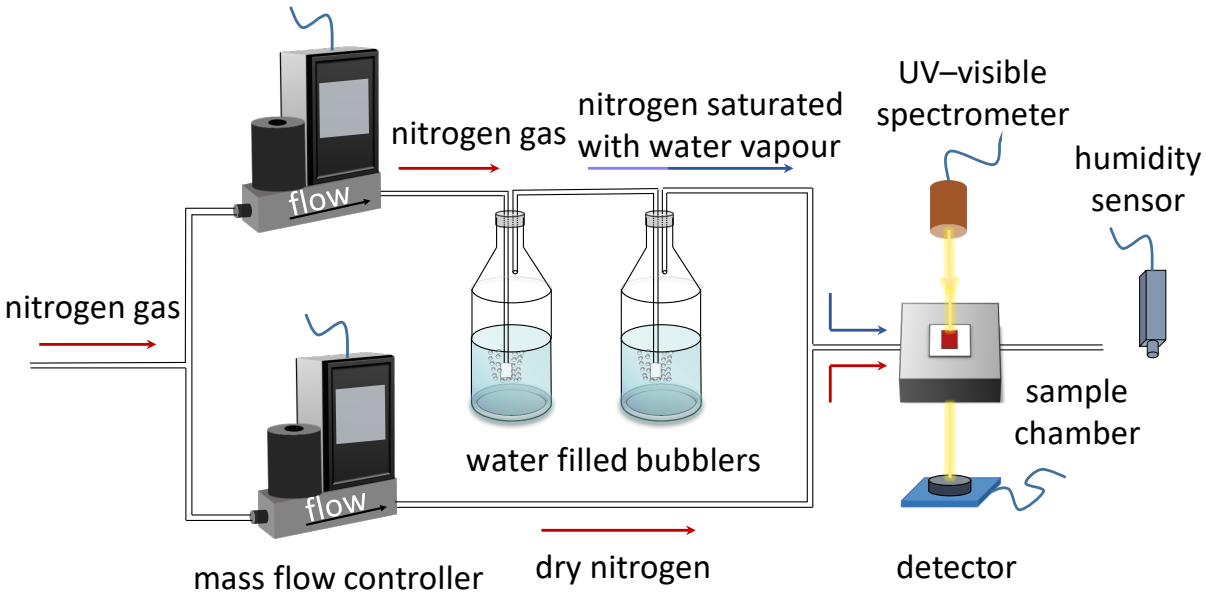

Figure 2.4 Schematic illustration of the RH control setup for in situ UV/vis spectroscopy.

2.3. Results and Discussion

2.3.1.Synthesis and Properties of the Polymers

To determine what effect the hydrophobicity of the HTL has on the moisture resistance of the perovskite layer, I synthesized four different poly(3-alkoxythiophenes) with side chains of varying hydrophobicity. The four polymers synthesized for this study were as follows: poly(3-(3′,3′,4′,4′,5′,5′,6′,6′,6′-nonafluorohexyl-1′-oxy)thiophene) (P3OFHT), poly(3-dodecyloxythiophene) (P3ODDT), poly(3-hexyloxythiophene) (P3OHT), and poly(3-(2-(2-(2-

methoxyethoxy)ethoxy)ethoxy)thiophene) (P3OEGT) (**Figure 2.2**). Commercially sourced P3HT was used as a comparator. Of the polymers studied, P3OFHT is reported here for the first time; the others have been reported previously for applications in organic solar cells and (or) organic thin film transistors.[108, 240, 245, 246] An alkyl-exchange reaction was used to prepare the most hydrophobic monomer, 3-(3′,3′,4′,4′,5′,5′,6′,6′,6′-nonafluorohexyl-1′-oxy)thiophene (**1**); 3-methoxythiophene and 1H,1H,2H,2H-perfluorohexan-1-ol were combined in the presence of a catalytic amount *p*-toluenesulfonic acid in dry toluene to yield **1** (**Scheme 2.1**). In contrast, the synthesis of monomers **2–4** started from commercially available 3-bromothiophene, which was reacted with the appropriate sodium alkoxide in the presence of a catalytic amount of copper(I) chloride. This second approach is higher yielding but uses a large excess of the appropriate alcohol as both a reagent and the co-solvent; the high cost of 1H,1H,2H,2H-perfluorohexan-1-ol made this approach impractical for the synthesis of **1**. The various 3-alkoxythiophenes (**1–4**) were then brominated at the 2- and 5-positions using dibromatin as the brominating agent to yield **5–8**.

The desired poly(3-alkoxythiophenes) were then synthesized from the corresponding 2,5-dibromo-3-alkoxythiophenes (**5–8**) using a Grignard metathesis (GRIM) polymerization. The GRIM method, originally reported by McCullough and coworkers, is one of the most effective methods for producing poly(3-alkylthiophenes) with a high degree of regioregularity and good molecular weights.[43] In this case, cyclohexylmagnesium chloride was used as the Grignard reagent and Ni(dppp)Cl_2 was used as the metal catalyst (**Scheme 2.1**). The resulting polymers were purified by Soxhlet extraction using methanol and hexanes to remove residual metal salts and oligomeric impurities, respectively; the polymers were then extracted into chloroform.

The molecular weights of the chloroform-soluble fractions were then characterized by gel permeation chromatography (GPC). The dodecyloxy-substituted polymer (P3ODDT) had the

highest molecular weight, with M_n = 16.6 kDa (**Table 2.1**), corresponding to a number-average degree of polymerization (X_n) of 62. Both the hexyloxy-substituted polymer (P3OHT) and the fluorinated hexyloxy-substituted polymer (P3OFHT) had more modest number-average molecular weights of 6.4 kDa (X_n = 35) and 7.6 kDa (X_n = 22), respectively. The higher molecular weight of P3ODDT may be due to the longer alkyl chain imparting better solubility to the growing polymer chain in the polymerization solvent (THF), allowing it to grow for a longer period before precipitating from the reaction mixture. In marked contrast, the oligo(ethylene glycol)-substituted polymer (P3OEGT) was not soluble enough in THF (GPC solvent) to allow its molecular weight to be measured accurately. Regardless of any differences in molecular weight, P3ODDT, P3OHT, and P3OFHT all had very similar dispersities ($Đ$) of 1.3–1.4 due to the quasi-living nature of the GRIM polymerization. The values are in good agreement with those reported for similar polymer systems in the literature (**Table 2.1**).[247, 248]

Table 2.1: Tabulated data for different polymers with different parameters like contact angle, molecular weight and absorbance.

HTMs	M_n (kDa)	M_w (kDa)	$Đ$	Contact angle (degrees)	λ_{max} (nm)
P3OFT	7.6	10.3	1.3	135	495
P3ODDT	16.6	23.4	1.4	119	560
P3OHT	6.4	8.9	1.4	109	620
P3HT	50	−	−	103	445
P3OEGT	−	−	−	37	575

In addition to molecular weight, polymer regioregularity is one of the most important structural parameters governing the optoelectronic properties of 3-substituted polythiophenes. Two repeat units can couple in three different ways: head to tail (HT), head to head (HH), and tail to tail (TT). This, in turn, gives rise to four different triads: HT–HT, HT–HH, HT–TT, and TT–HT. The GRIM polymerization heavily favors HT couplings for steric reasons,[249, 250] but the degree of regioregularity depends on the specific system and reaction conditions employed.[249] This can be evaluated by analyzing the ^{1}H NMR spectra of the polymers, where each triad gives rise to a unique signal in the aromatic region (~δ 6.9 ppm) that corresponds to the hydrogen at the 4-position of the thiophene ring.[240, 250, 251] The ^{1}H NMR spectrum of the commercially supplied sample of P3HT (**Figure 2.5-2.6**) has a single sharp peak at δ 6.98 ppm, consistent with highly regioregular, HT-P3HT.[252] Much smaller peaks at δ 7.00 ppm, δ 7.02 ppm, and δ 7.05 ppm are due to the TT–HT, HT–HH, and TT–HH triads, respectively.[251] The clear triplet corresponding to the α-methylene protons at δ 2.8 ppm is further evidence of the high degree of regioregularity in this polymer sample. In marked contrast, the ^{1}H NMR spectrum of P3OFHT shows a broad peak with multiple

components in the range of δ 6.8–7.0 ppm, suggesting that the sample is essentially regiorandom (**Figure 2.7-2.8**). P3ODDT appeared to be the most regioregular of the polymers synthesized, with a single, relatively sharp peak at δ 6.9 ppm (**Figure 2.9-2.10**); this may be due to the longer dodecyloxy chain imparting more stringent steric requirements during the polymerization, leading to a higher overall degree of HT coupling. P3OHT appeared to have more intermediate regioregularity, with clear evidence of shouldering in the peak at δ 6.85 ppm (**Figure 2.11-2.12**), while due to the low solubility of P3OEGT, the aromatic signal was too weak to provide meaningful structural data (**Figure 2.13-2.14**). The imperfect regioregularity synthesized here is consistent with previous reports of poly(3-alkoxythiophenes) synthesized via the GRIM polymerization;[248] whether through nickel–oxygen interactions or through reduced steric requirements of the 3-alkoxy substituents, the poly(3-alkoxythiophenes) appear to be more regio-irregular than analogous poly(3-alkylthiophene) systems.

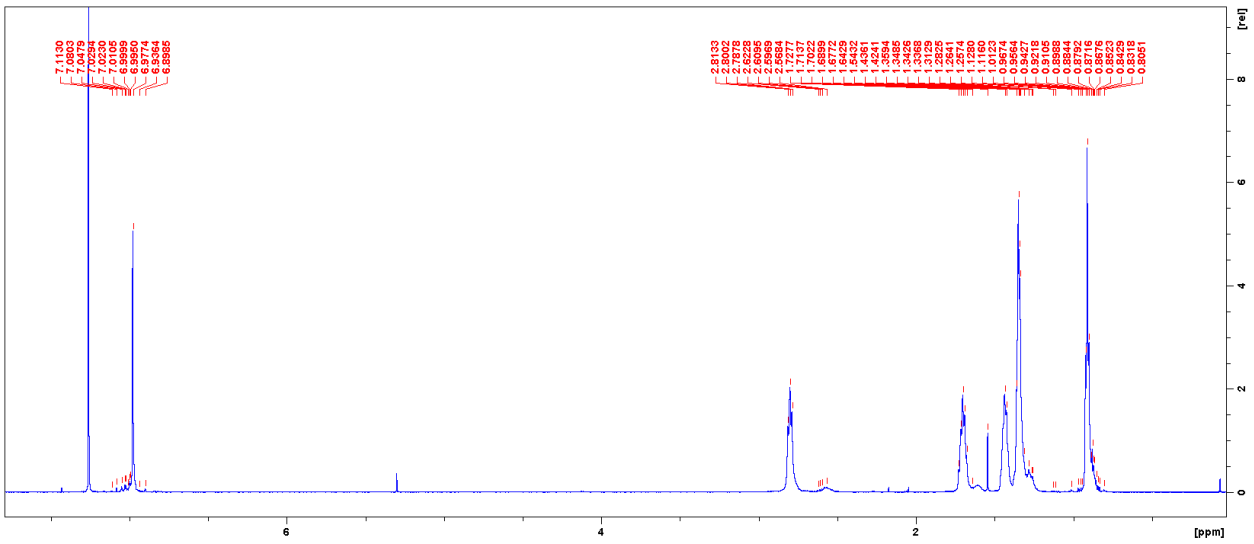

Figure 2.5 ^{1}H NMR of P3HT in $CDCl_3$.

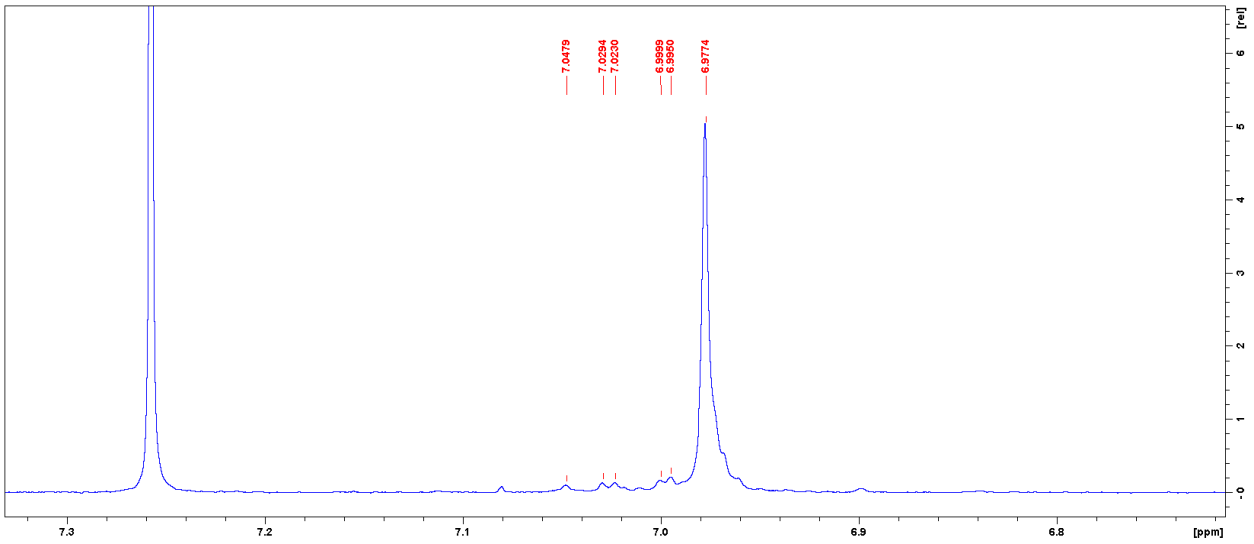

Figure 2.6 ^{1}H NMR of α-methylene protons in the 3-position of the P3HT in $CDCl_3$.

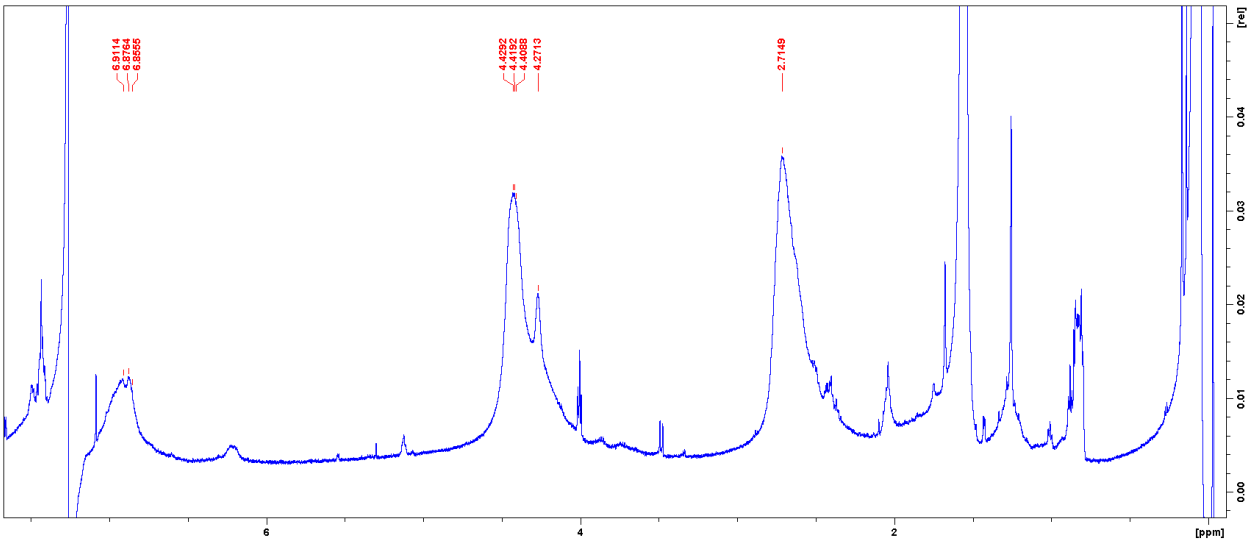

Figure 2.7 ^{1}H NMR of P3OFHT in $CDCl_3$.

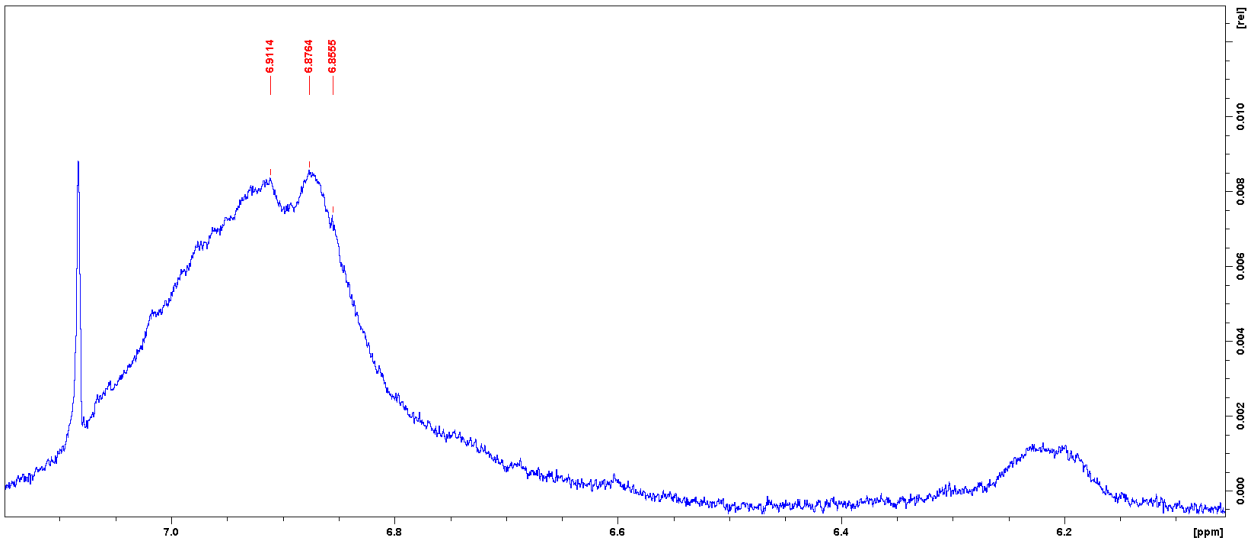

Figure 2.8 [1]HNMR of α-methylene protons in the 3-position of the P3OFHT in $CDCl_3$.

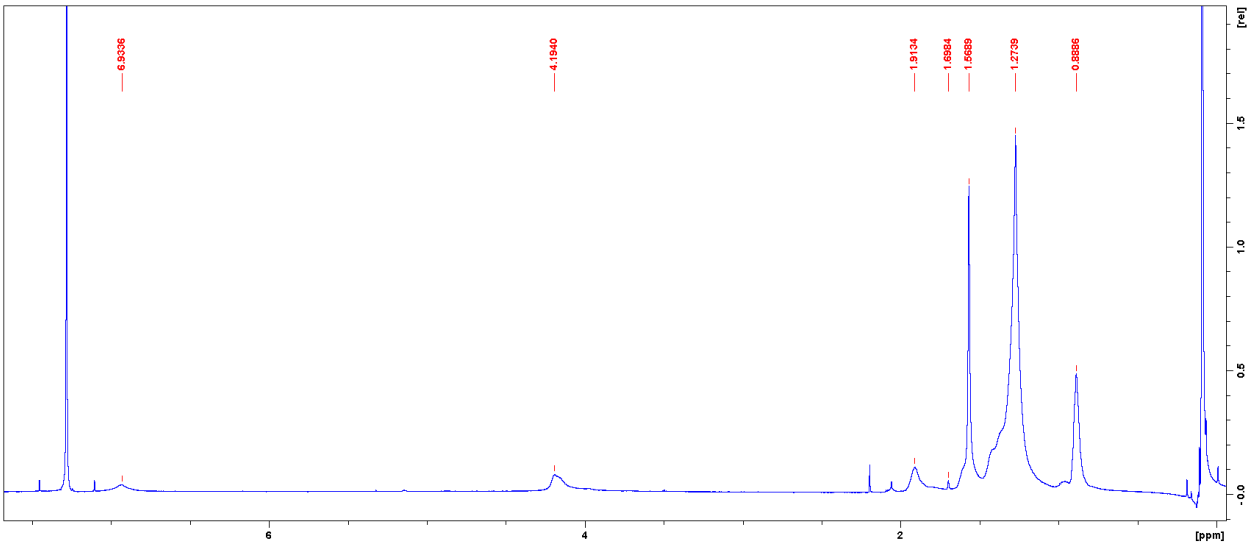

Figure 2.9 [1]H NMR of P3ODDT in $CDCl_3$.

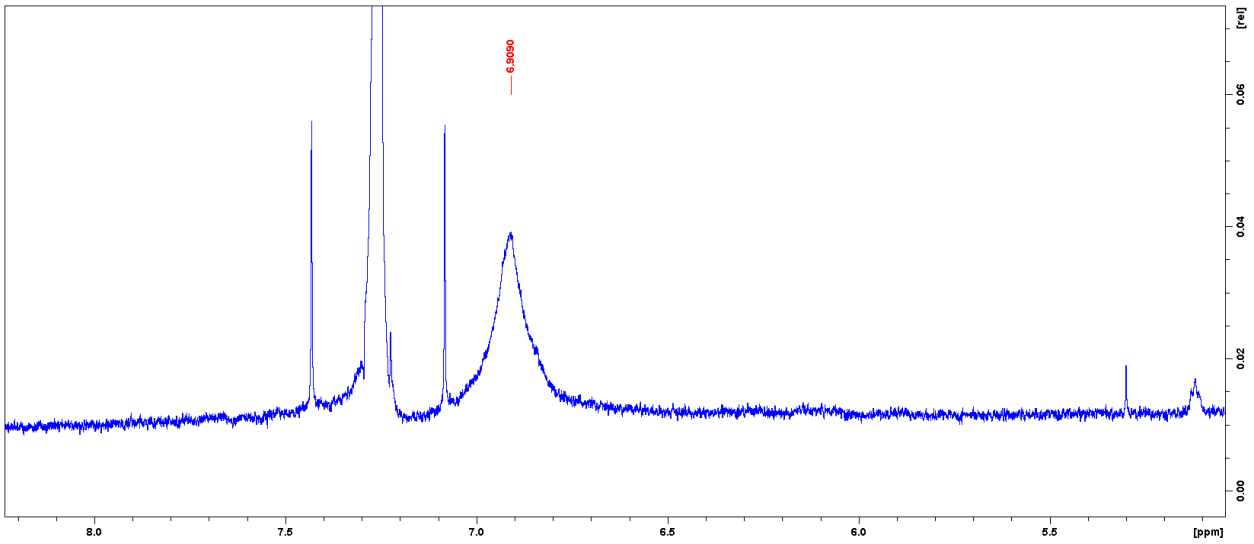

Figure 2.10 ^{1}H NMR of α-methylene protons in the 3-position of the P3ODDT in $CDCl_3$.

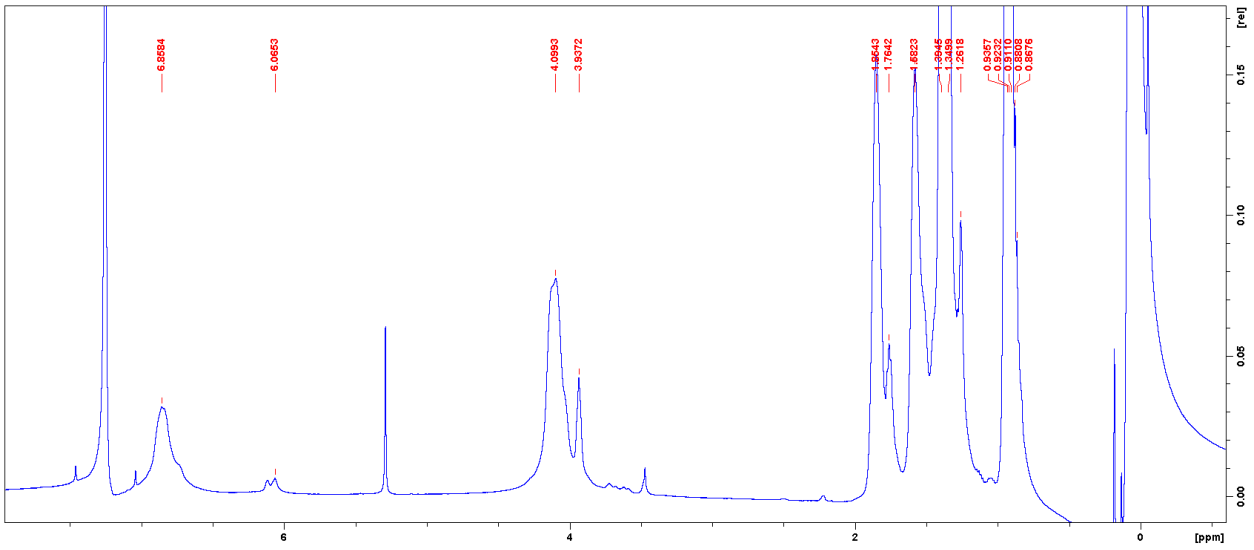

Figure 2.11 ^{1}H NMR of P3OHT in $CDCl_3$.

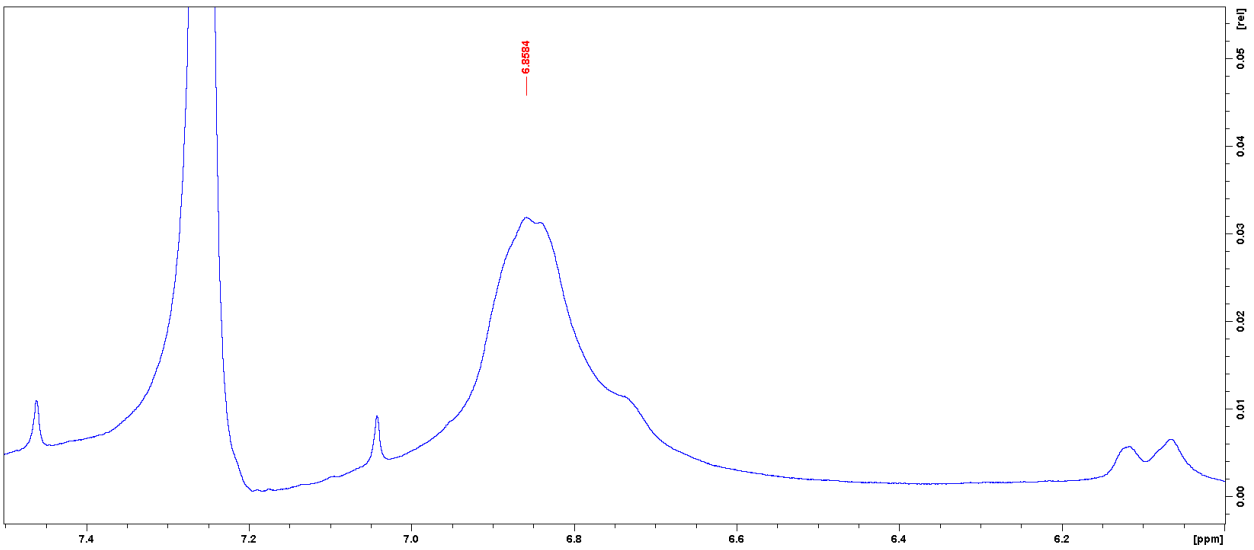

Figure 2.12 [1]H NMR of α-methylene protons in the 3-position of the P3OHT in $CDCl_3$.

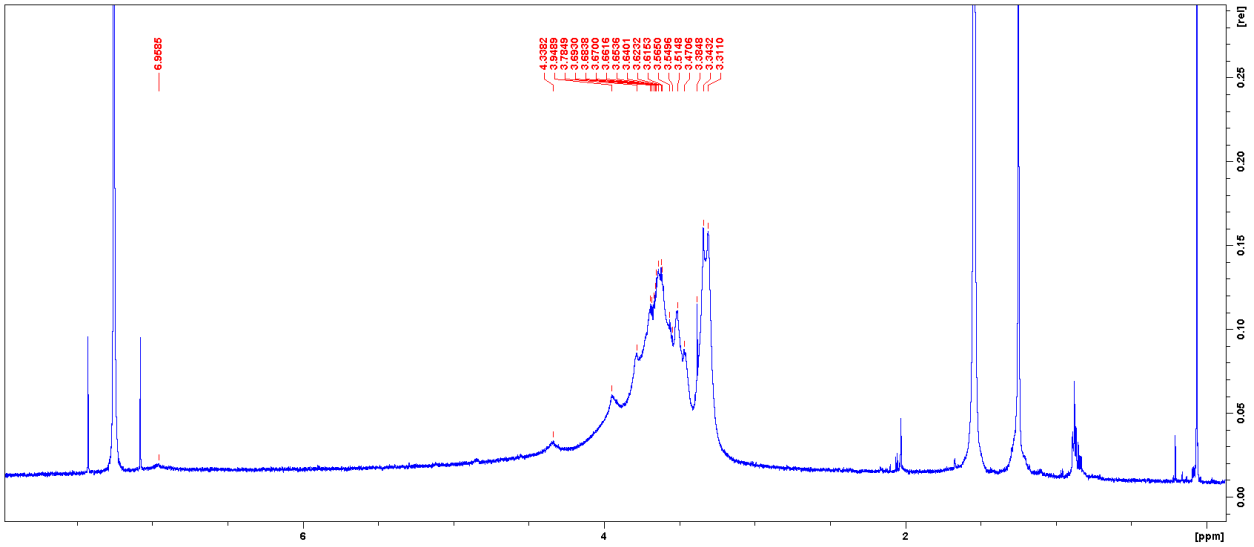

Figure 2.13 [1]H NMR of P3OEGT in $CDCl_3$.

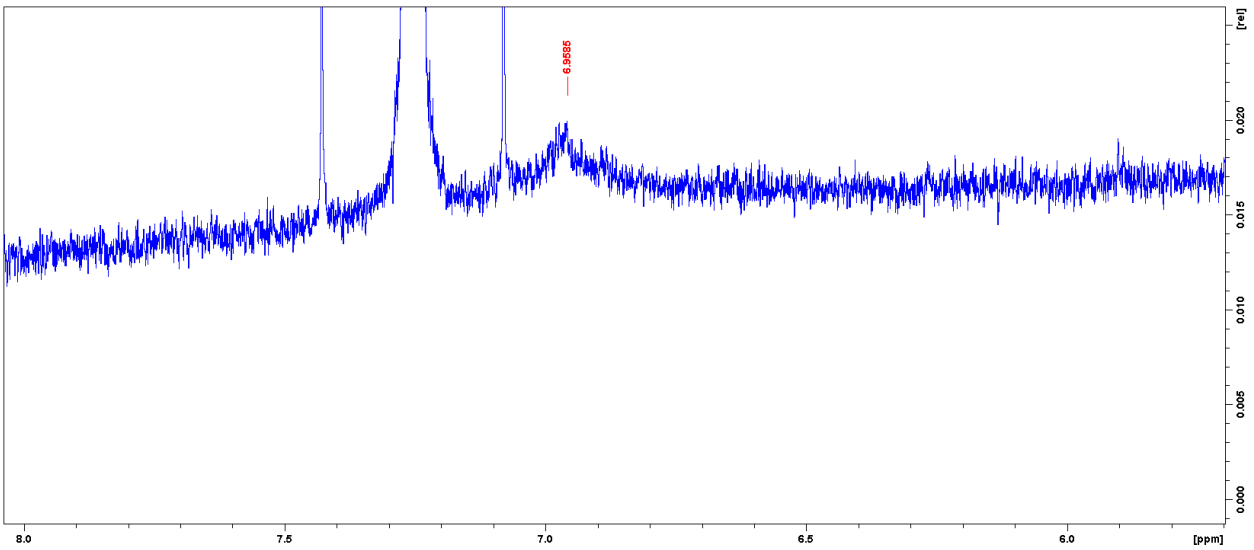

Figure 2.14 ^{1}H NMR of α-methylene protons in the 3-position of the P3OEGT in $CDCl_3$.

Next, the optical absorption spectra of the polymers were measured in chloroform solution (**Figure 2.15**), and wavelengths of the absorption maxima (λ_{max}) are listed in **Table 2.1**. The spectra are all dominated by a single, broad peak between 400 and 700 nm, which is ascribed to the $\pi \rightarrow \pi^*$ transition of the polythiophene backbone. Compared with P3HT (λ_{max} = 445 nm), all of the poly(3-alkoxythiophenes) have red-shifted absorption bands. This is caused by a combination of two factors: one is the more coplanar conformation of poly(3-alkoxythiophenes), owing to the smaller size of the oxygen atom at the 3-position (relative to the methylene group in poly(3-alkylthiophenes)); the other is the electronic influence of the electron-donating alkoxy group.[247, 253] Of the polymers synthesized in this study, P3OFHT displayed the smallest red-shift relative to P3HT and had the shortest λ_{max} (495 nm). In contrast, P3ODDT and P3OEGT had more substantially red-shifted absorption bands (λ_{max} = 560 and 575 nm, respectively), whereas P3OHT had the lowest energy $\pi \rightarrow \pi^*$ transition (λ_{max} = 620 nm). Electronically, all four polymers are expected to be quite similar; each polymer has the same ethylene spacer between the oxy-substituted thiophene ring and the remainder of the side chain, limiting electronic perturbations to

the polymer backbone. We therefore ascribe the differences in the optical absorption spectra to differences in regioregularity and the steric constraints imparted by the various side chains. The heavily fluorinated polymer (P3OFHT) had the shortest λ_{max}, which is entirely consistent with the regiorandom nature of the polymer backbone; HH couplings inevitably result in substantial torsion between adjacent thiophene rings, reducing the effective conjugation length. By the same argument, the more regioregular nature of P3ODDT results in a more red-shifted absorption band. However, it is harder to explain the pronounced red-shift of P3OHT using only regiochemical arguments, because there is clear evidence of regio-irregularity in the ^{1}H NMR spectrum (**Figure 2.12**). One possibility is the partial aggregation of the polymer in solution, which would be expected to red-shift the absorption band; this is supported by the nonzero baseline at long wavelengths (~800 nm), which may result from light scattering from small aggregates in solution. Because a similar nonzero baseline is observed in the P3OEGT spectrum and the polymer has a low solubility in chloroform, the red-shift observed for this polymer may also be due to aggregation.

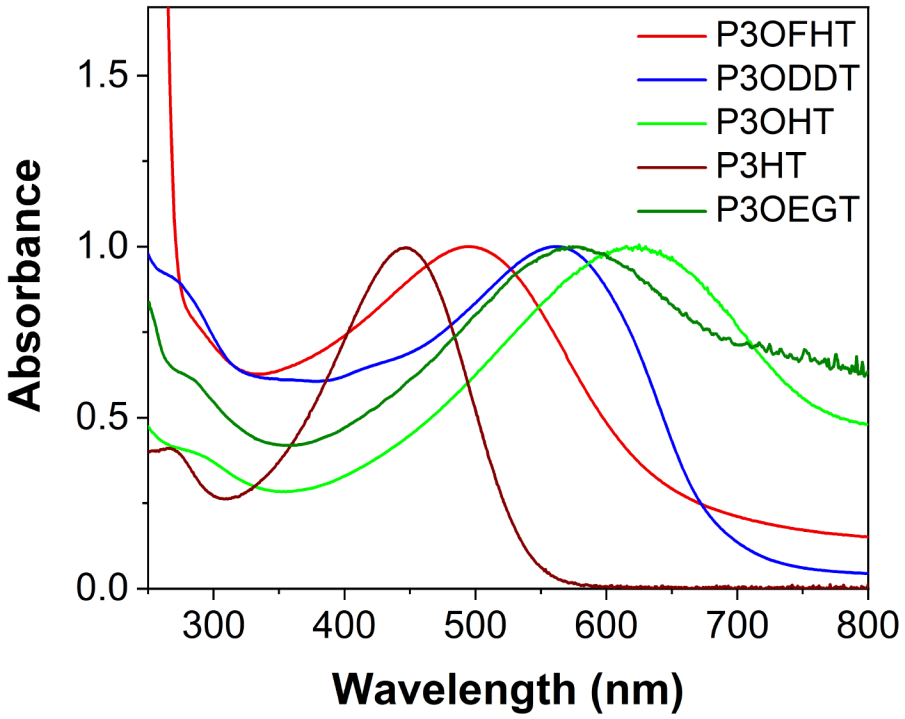

Figure 2.15 Normalized absorbance of different polymers in $CHCl_3$ solutions.

2.3.2. Device Performance

Although P3HT is well known to be an effective HTL in PSCs, we first needed to ascertain whether the poly(3-alkoxythiophenes) synthesized as part of this study would function in devices. To test this, we built a series of devices based on an ITO/ZnO/$MAPbI_3$/HTL/Ag device architecture, as shown in **Figure 2.16**. With this cell design, the polymeric HTL lies between the perovskite layer and the outside environment, helping to protect it from moisture ingress.

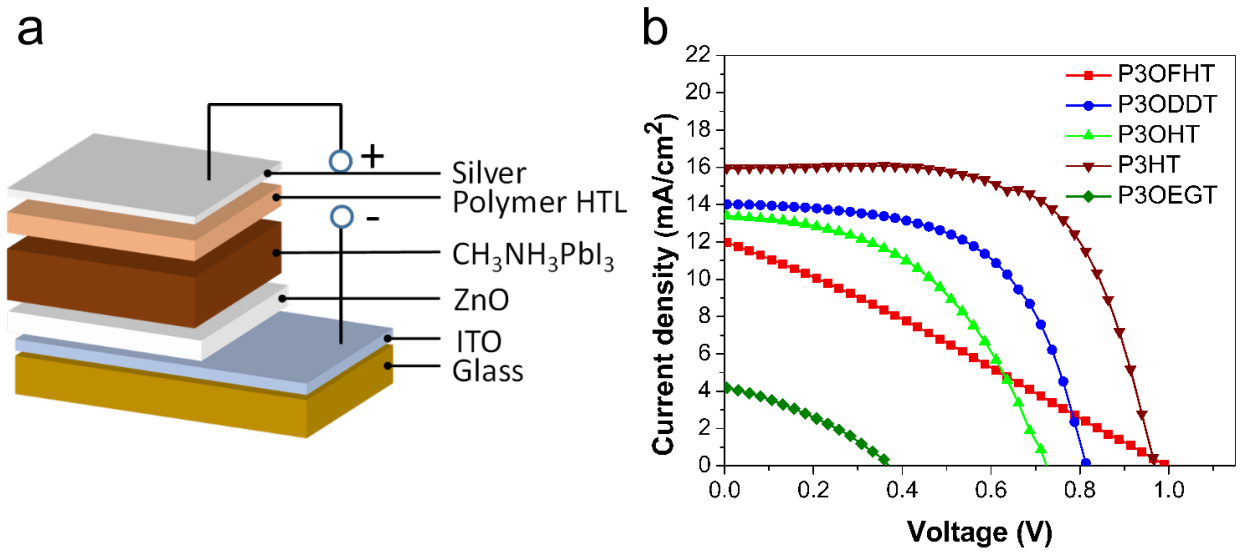

Figure 2.16 (**a**) Schematic of the PSC architecture used in this work; (**b**) *J-V* curves of the highest performing devices with different polymer HTLs.

After testing the cells, it was obvious that the P3HT-based devices outperformed those cells based on the poly(3-alkoxythiophenes). The P3HT cells had an average power conversion efficiency (PCE) of 9.4% ± 0.3% (**Figure 2.17**; **Table 2.2**), with the best-performing cell having a PCE of 10.2% (**Figure 2.17b**). The superior performance of the P3HT-based devices was primarily due to their higher short-circuit current densities (J_{SC} = 16 ± 1 mA/cm^2) and fill factors (FF = 64% ± 2%) compared with the poly(3-alkoxythiophenes) (**Figure 2.17**). Among the synthesized polymers, P3ODDT and P3OHT were the most successful as HTLs. P3ODDT-based devices had an average PCE of 5.1% ± 0.5%, whereas P3OHT-based cells had average PCEs of 4.3% ± 0.4%. Although these devices did not perform as well as those based on commercial P3HT, they had reasonable FF (~50%), J_{SC} (>12 mA/cm^2), and V_{OC} (>0.7 V), indicating that the PSCs were fully functional. In contrast, the devices based on both the fluorinated and oligo(ethylene glycol)-substituted polythiophenes displayed poor performance. The P3OFHT-

based devices were only able to achieve a 3.3% PCE at best, whereas the P3OEGT-based cells were essentially non-functional, with an average PCE of 0.4%. In both cases, this was due to the extremely low FFs (<35%), with the P3OEGT PSCs also suffering from very poor J_{SC} and V_{OC}.

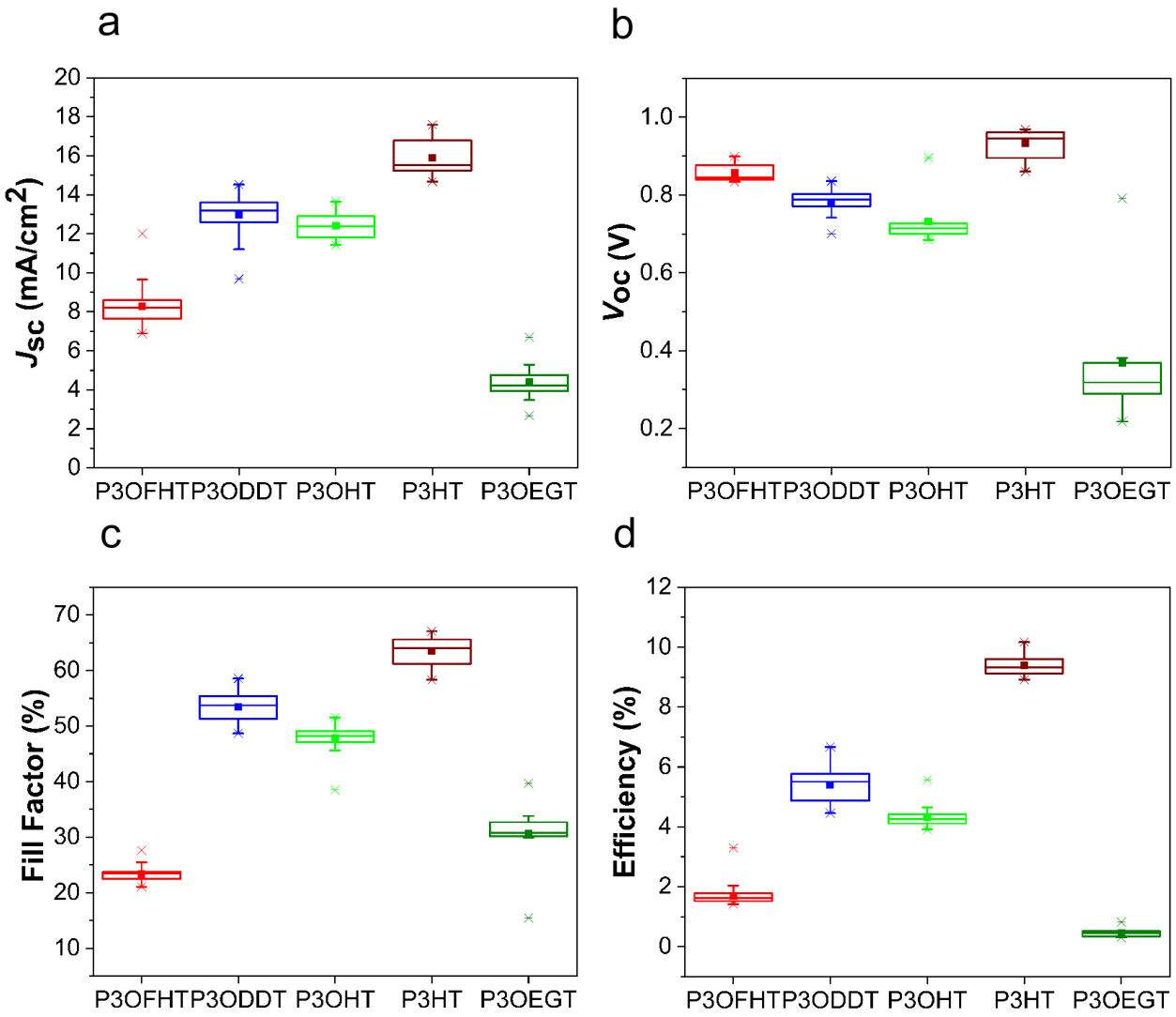

Figure 2.17 Box and whisker plots of device parameters for PSCs with different polymer HTLs: (**a**) short-circuit current density, (**b**) open-circuit voltage, (**c**) fill factor, and (**d**) power conversion efficiency. The solid square denotes the mean, the horizontal line denotes the median, the box boundaries mark the 25th and 75th percentiles, the whiskers mark 1.5 × the interquartile range, and the crosses denote maximum and minimum values.

Table 2.2: Average device performance parameters for ITO/ZnO/$MAPbI_3$/HTLs/Ag devices with different HTMs. The associated uncertainties represent plus-or-minus one standard deviation from the mean.

HTMs	V_{OC} (V)	J_{SC} (mA/cm^2)	Fill Factor (%)	Avg. Efficiency (%)	Best Effecency (%)
P3OFT	0.87 ± 0.04	8.3 ± 1	23 ± 1	1.7 ± 0.3	3.3
P3ODDT	0.78 ± 0.03	13.0 ± 1	53 ± 2	5.1 ± 0.5	6.7
P3OHT	0.73 ± 0.05	12.4 ± 0.6	48 ± 2	4.3 ± 0.4	4.7
P3HT	0.93 ± 0.03	15.9 ± 1	64 ± 2	9.4 ± 0.3	10.2
P3OEGT	0.30 ± 0.05	4.0 ± 0.8	33 ± 3	0.4 ± 0.9	0.5

The relative performance of the various HTLs can be understood in terms of their structural properties. The trend in device performance (P3HT > P3ODDT > P3OHT > P3OFHT > P3OEGT) mirrors the trends observed in polymer regioregularity and molecular weight (and in the case of P3OEGT, solubility). Previous studies have shown that the hole mobility of P3HT scales dramatically with molecular weight (M_w);[254] the M_w of the commercial P3HT sample is ~50 kDa, which is over twice that of the P3ODDT polymer (M_w = 23.4 kDa). This readily explains the better performance of the P3HT HTLs, even though both polymers had a high degree of regioregularity. P3OHT had both a lower M_w (8.9 kDa) and a lower degree of regioregularity than P3ODDT and P3HT, and the PCE was correspondingly lower (4.3% ± 0.4%) as a result. Similarly, the regiorandom nature of P3OFHT clearly affected its ability to work as a HTL, and the PCE drops to 1.7% ± 0.3%. This decline in PCE can be related back to the hole mobility of the HTL; the more regio-irregular HTLs produce devices with higher series resistances (e.g., P3OFHT, R_S = 119 Ω cm^2) compared with P3HT (R_S = 10 Ω cm^2) (**Figure 2.16b**). The extremely poor performance of

the P3OEGT-based devices (PCE = 0.4% ± 0.1%) is mainly due to the low solubility of the polymer, which makes it difficult to coat homogeneous, pinhole-free films. As can be seen from the *J–V* curve (**Figure 2.16b**), in addition to a high series resistance, the P3OEGT-based cells suffer from a low shunt resistance. The combination severely curtails the FF. Each of the devices displayed roughly the same amount of hysteresis in their *J–V* curves (**Figure 2.18**).

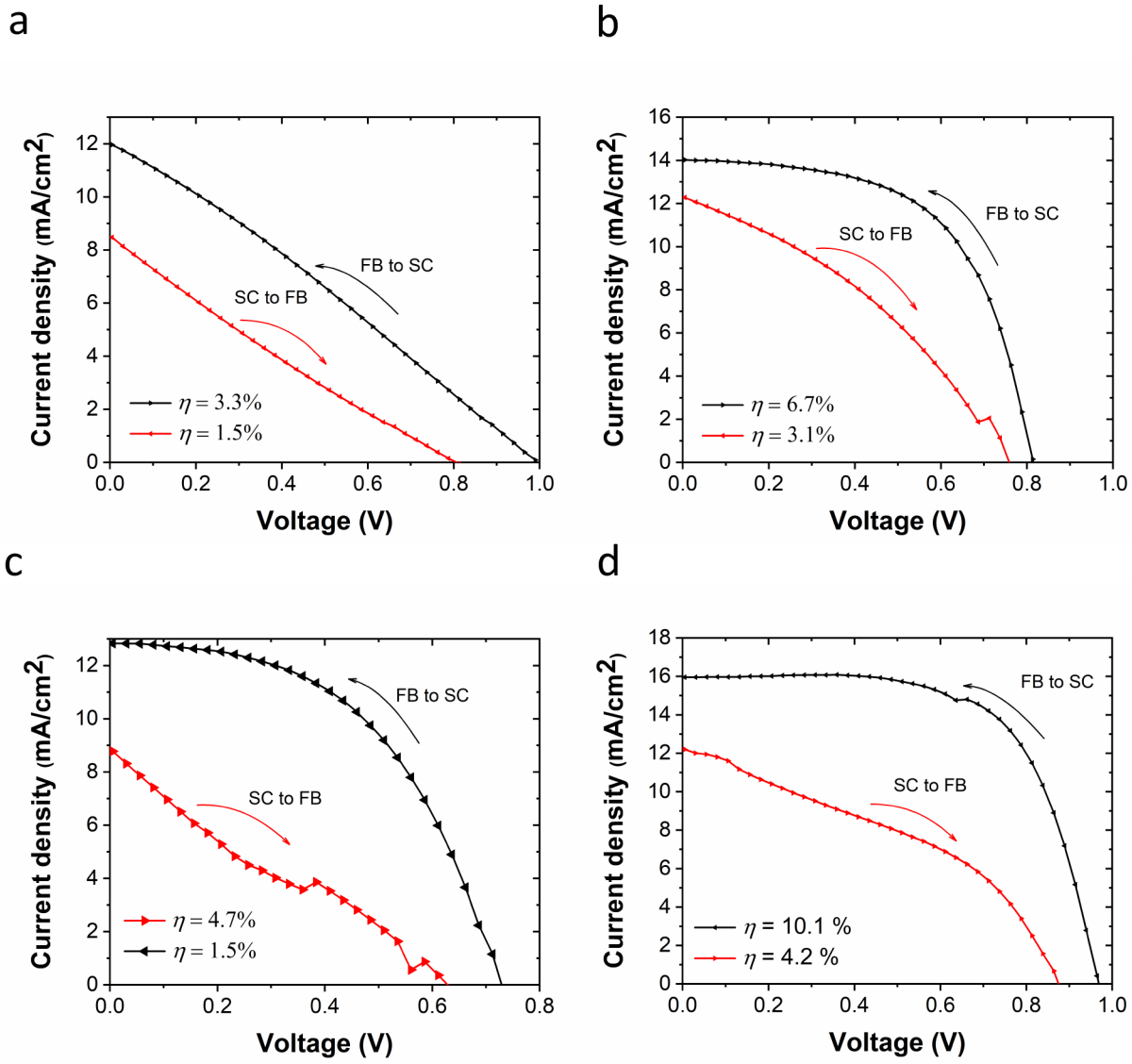

Figure 2.18 *J-V* curves in both scan directions for devices with various HTLs: (**a**) P3OFHT, (**b**) P3ODDT, (**c**) P3OHT, (**d**) P3HT. *J-V* curves were measured at a scan rate of 0.83 $V \cdot s^{-1}$.

2.3.3. Effect of Different Side Chains on Film Stability

The primary goal of this study was to determine whether changing the hydrophobicity of the HTMs would affect its ability to act as a vapor barrier and stabilize the underlying perovskite film. We therefore first measured the water contact angle on thin films of each of the polymers, which

were deposited on glass substrates (**Figure 2.19**; **Table 2.1**). Due to the presence of the highly fluorinated side chains, P3OFHT was the most hydrophobic polymer tested, with a water contact angle of 135°. This was followed by those polymers with hydrocarbon side chains, with P3ODDT, P3OHT, and P3HT having contact angles of 119°, 109°, and 103°, respectively. On the other hand, the oligo(ethylene glycol) chains of P3OEGT rendered the resulting polymer film quite hydrophilic, with a water contact angle of only 37°. Unsurprisingly, the hydrophobicity of the films depends strongly on the identity of the polymer side chain.

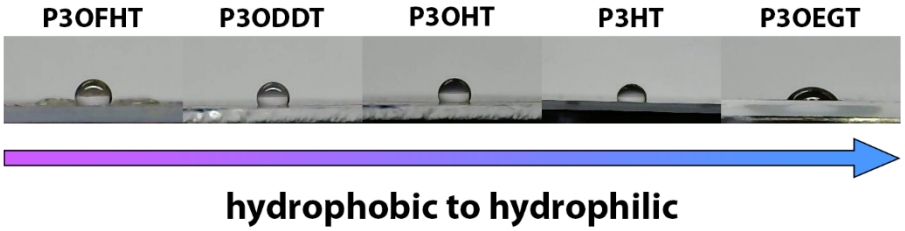

Figure 2.19 Water contact angle for different polymers.

We then deposited the various HTLs onto $MAPbI_3$ films to probe their ability to act as water vapor barriers. The samples were placed in an in situ UV–vis sample holder and subjected to a flow of nitrogen gas with a fixed RH of 98% ± 2%;[14, 43] absorbance spectra were acquired every 15 min (**Figure 2.20a** and **Figure 2.21**). The normalized absorbance at 410 nm (a wavelength at which $MAPbI_3$ absorbs strongly) is plotted as a function of time (**Figure 2.21b**). As expected, bare films of $MAPbI_3$ decompose very rapidly. Defining $\tau_{1/2}$ as the time required for the absorbance to drop to one-half of its initial value, we find that uncoated $MAPbI_3$ has a $\tau_{1/2}$ of only 1.7 h, and the decomposition is nearly complete after 3 h. Coated perovskite films (regardless of which polymer HTL was used) all decomposed more slowly, although the rate of decomposition depended strongly on the identity of the polymer coating. The hydrophilic P3OEGT coating was a very poor vapor barrier, extending the $\tau_{1/2}$ to only 6.8 h. In contrast, the more hydrophobic polythiophenes

were all much more resistant to moisture ingress. P3HT-coated films had a short (~3 h) induction period prior to significant decomposition, and the overall decomposition rate appeared to be substantially slower ($\tau_{1/2} \approx 14.6$ h). The P3OHT ($\tau_{1/2} \approx 45.5$ h) and P3ODDT ($\tau_{1/2} \approx 13.5$ h) coated films displayed similar behavior; both had induction periods prior to moisture breakthrough, and both did a better job of protecting the perovskite than the hydrophilic P3OEGT. The better performance of P3OHT as a barrier layer may be due to its solid state packing efficiency;[252, 255] long dodecyl chains are known to disrupt the efficient solid state packing observed with shorter alkyl chains (e.g., P3HT), and a less densely packed film would be expected to increase its permeability to water vapor. Most significantly, the highly fluorinated side chains of P3OFHT provided the greatest moisture resistance. Even after 70 h of exposure to a high humidity environment, the P3OFHT-coated perovskite film retained 76% of its initial absorbance. Based on a linear extrapolation of the curve in **Figure 2.21b**, we calculated a $\tau_{1/2}$ of ~160 h. This is an order of magnitude slower decomposition than was observed for P3HT-coated films and nearly two orders of magnitude slower than uncoated perovskite films. The results clearly show that the hydrophobicity of the HTL affects its ability to act as a moisture vapor barrier and that fluorinated HTLs can provide a high level of protection to the underlying perovskite film.

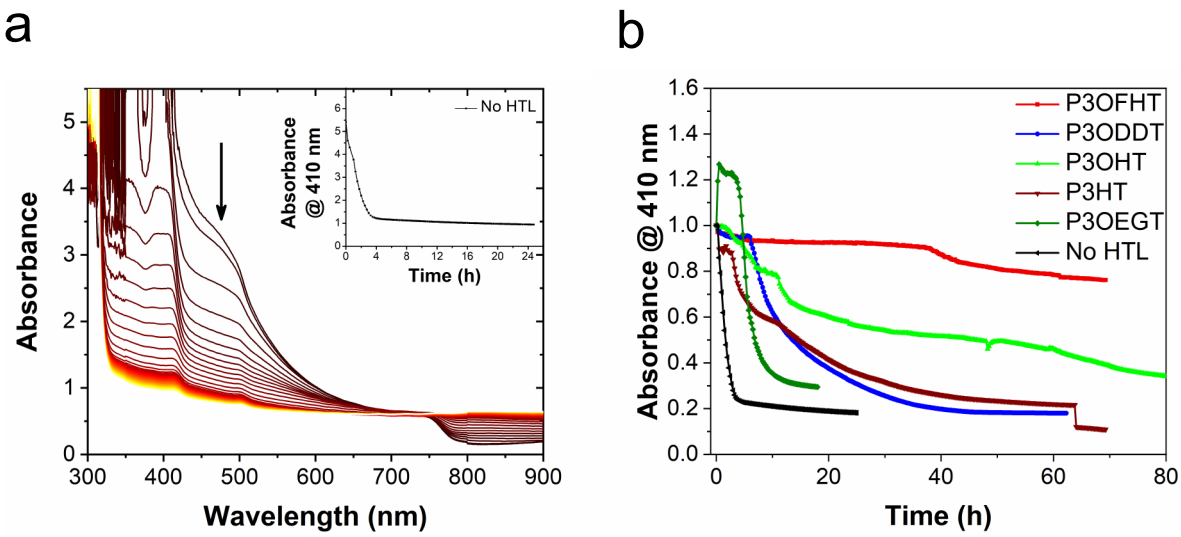

Figure 2.20 (**a**) Absorption spectra of a $MAPbI_3$ film in a high RH (98% ± 2%) environment; spectra were acquired at 15 min intervals and the inset shows the absorbance at 410 nm as a function of time; (**b**) normalized absorbance at 410 nm as a function of time for $MAPbI_3$ films with different polymer coatings.

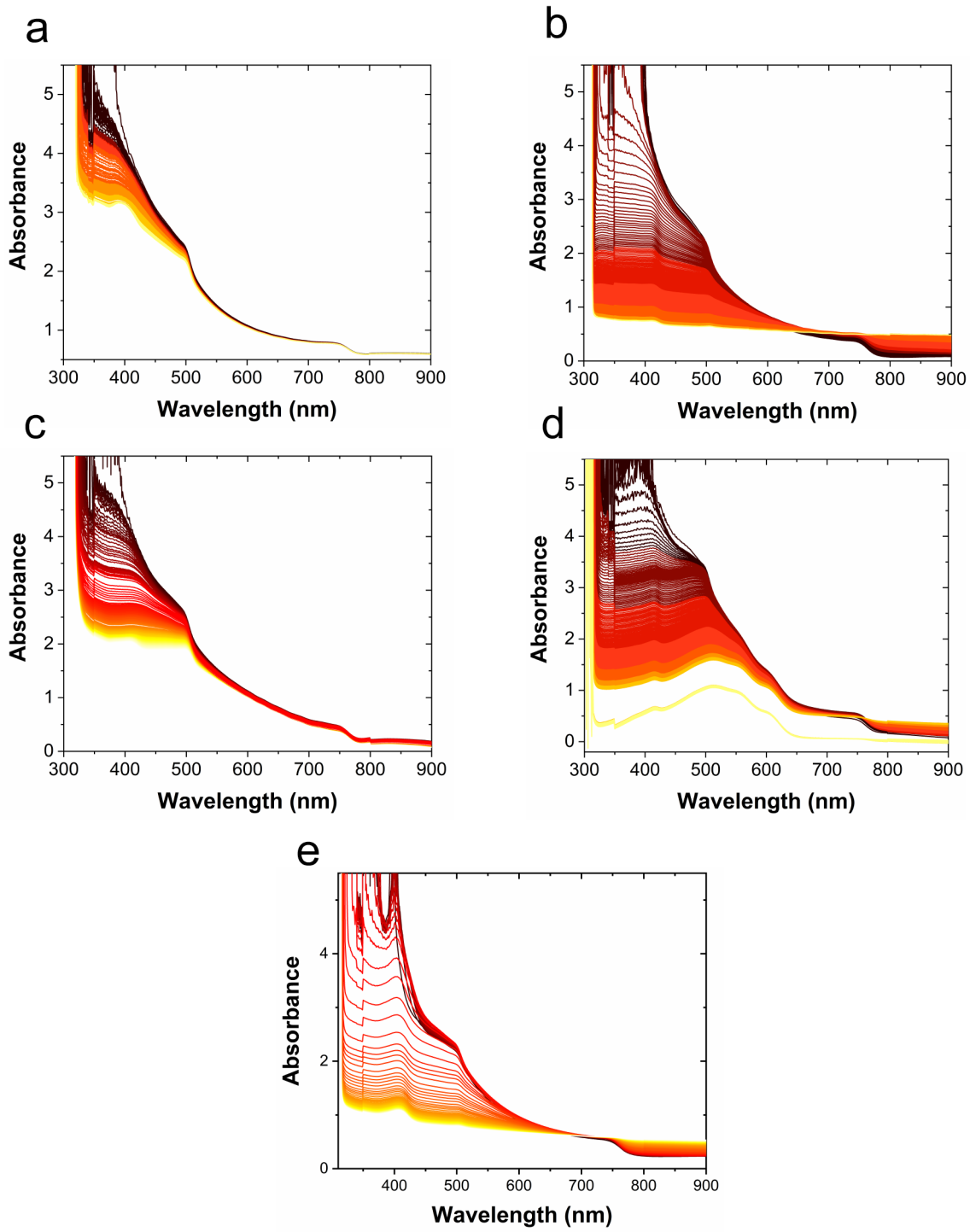

Figure 2.21 UV/vis absorption spectra of glass/$MAPbI_3$/HTL films in a RH = 98 ± 2% environment, acquired at 15 min intervals: (**a**) P3OFHT, (**b**) P3ODDT, (**c**) P3OHT, (**d**) P3HT, and (**e**) P3OEGT.

2.4. Conclusions

In this chapter, the synthesis of a new polythiophene base HTM was discussed. The potential of using poly(3-alkoxythiophenes) as both HTLs and vapor barriers to prevent perovskite decomposition and extend the lifetime of PSCs were explored. The moisture-blocking ability of the various poly(3-alkoxythiophenes) studied appears to be correlated to both the hydrophobicity of the polymer and its solid state packing efficiency, with highly fluorinated polymers providing an impressive level of protection to the underlying perovskite. Practically, however, the efficiency of the P3OFHT-based devices was low, primarily because a lack of regioregularity and low molecular weight limited the hole mobility of the polymer. The findings suggest that if fluorinated polythiophenes can be prepared with a high degree of regioregularity and in high molecular weights, then they will be able to function well in the role of a barrier HTL. Alternatively, substituting other polymeric HTLs with perfluorinated side chains may be an effective strategy to improve the moisture resistance of perovskite devices. The synthesis of such a polymer, which combines a high hole mobility with effective barrier properties, would be an important step toward the production of long-lived, environmentally stable PSCs.

3. Improving the Moisture Stability of Perovskite Solar Cells by Using PMMA/P3HT Based Hole-transport Layers

3.1. Introduction

Hydrophobic thiophene based polymers such as P3HT and its perfluorinated analog (P3OFHT) can have a profound impact on the lifetime of PSCs, as shown in the previous chapter (**Chapter 2**). The work discussed in this chapter is a continuation of the previous approach.

The previous project uses highly hydrophobic P3OFHT as a HTL which improved the moisture stability of the underlying $MAPbI_3$ layer compared to P3HT. However, the performance of this polymeric HTM in the device was very poor due to the poor hole mobility of the polymer. A PCE of 10.2 % was achieved by the champion P3HT based device (control), whereas the champion P3OFHT based device could only achieve a PCE of 3.3%. The real application of a photovoltaic technology depends upon three major factors: photovoltaic performance, stability of the devices and the production cost. Therefore, even though the P3OFHT improves the device lifetime significantly, poor performance of this polymer as a HTM limits any further exploration. On the other hand, P3HT as a HTM performs well in PSCs. P3HT-coated PSCs have also good device stability.[68] Therefore, designing new P3HT based HTMs is a promising strategy to improve the moisture stability of the PSCs. Hence, a new project was designed that used a PMMA/P3HT based polymer blend as the HTM.

To protect $MAPbI_3$ from liquid and vapor phase water the top layer should be a good moisture barrier. A good moisture barrier layer should be densely packed, hydrophobic and should have low

vapor permeability. In that respect, P3HT and PMMA both are suitable candidates. The hexyl side chains of P3HT make it hydrophobic and the π-π interaction of the polythiophene backbone helps it to form a uniform densely packed film. In addition, it is commercially available with high molecular weight (>50 kDa). It is highly soluble in common organic solvents (e.g. chloroform, chlorobenzene). Both of these factors are required to form films with good mechanical properties. Similarly, because of a very high molecular weight (>350 kDa) and high solubility of PMMA in organic solvents, it forms densely packed water resistive films with good mechanical properties. Owing to the good mechanical properties of PMMA, a HTL made of polymer-functionalized single-walled carbon nanotubes (SWCNTs) in a PMMA matrix demonstrated substantially improved device stability (**Figure 3.1a**).[118] Even after exposing the PSCs to a running stream of water for 1 minute the devices did not show any sign of degradation (**Figure 3.1b**). However, one of the main drawbacks of this approach is a lack of scalability; the purification and functionalization of SWCNTs is extremely challenging synthetically, substantially increasing cost. Additionally, lack of reproducibility of this approach makes it very challenging in real life applications.

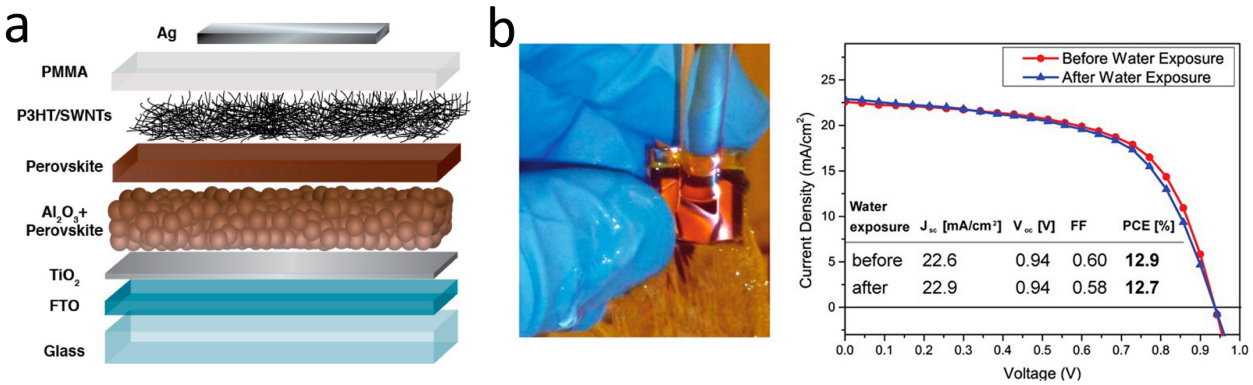

Figure 3.1 (**a**) Schematic architecture of the investigated device consisting of sequential layers of FTO as transparent electrode, a TiO_2 compact layer, a mesostructured layer of Al_2O_3 coated with

$MAPbI_{3-x}Cl_x$ and the hole-transporting structure composed of a P3HT/SWNT layer in-filled with a PMMA matrix. (**b**) A photograph of a complete perovskite solar cell employing a SWNT hole-extraction layer placed under a flowing tap with the active layer on the top side of the glass directly under the water flow (left-hand side). Current density–voltage plots measured under AM1.5 simulated sunlight of 100 $mW \cdot cm^{-2}$ irradiance of the same perovskite solar cell before and after being placed under the running water for 1 minute. Reproduced with permission of the American Chemical Society from reference ([118]).

Therefore, a HTL composed of a P3HT nanowire framework suspended in a PMMA matrix was employed. This type of PMMA/P3HT composite has been previously used in organic electronic applications to improve air stability and for its mechanical strength.[256-259] Here it was exploited as a potential vapor barrier between the external environment and the perovskite active layer (**Figure 3.2**). A thin compact layer of P3HT efficiently collects holes from the perovskite, while the P3HT nanowire framework provides a percolation pathway for holes to effectively reach the metal top electrode. Meanwhile, the dense PMMA matrix blocks the ingress of water into the device, leading to devices whose lifetime is improved by an order of magnitude relative to P3HT controls.

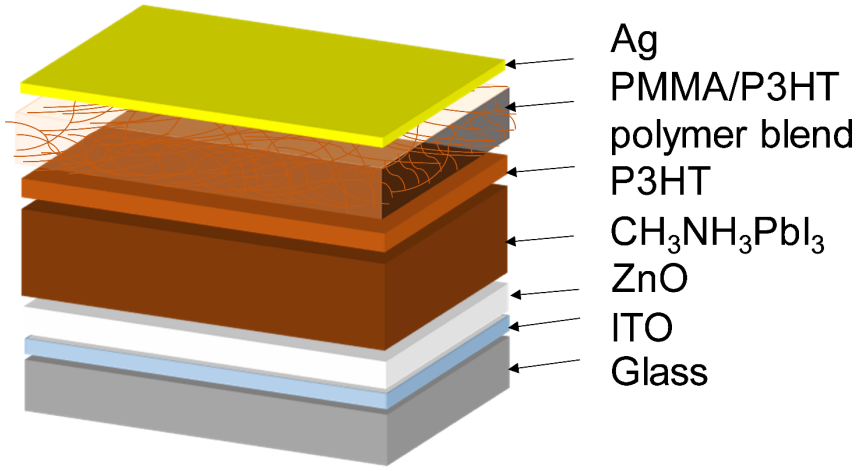

Figure 3.2 Schematic of the device architecture used in this study. The HTL consists of a thin, compact layer of P3HT, followed by a thicker layer of P3HT nanowires suspended in a PMMA matrix.

Section 3.2 and **Section 3.3.** were adopted with permission from Kundu S.; and Kelly T. L. *Mater. Chem. Front*. **2018**, 2, 81-89. Copyright 2018 The Royal Society of Chemistry and the Chinese Chemical Society.[260]

3.2. Experimental Section

3.2.1. Materials

ITO-coated glass (R_S = 20 Ω·sq^{-1}) substrates were purchased from Delta Technologies. P3HT (electronic grade, M_w ~ 50 kDa) and zinc acetate dihydrate were purchased from Rieke Metals Inc., and Alfa Aesar, respectively. Ag (99.99%) and Au pellets (99.99%) were purchased from Kurt J. Lesker. PMMA (M_w ~ 350 kDa), lead(II) iodide (99%), methylamine (37% in absolute ethanol), hydriodic acid (57% in H_2O), TBP (96%) and Li-TFSI (99%) were purchased from Sigma-Aldrich. All solvents were purchased from Fisher Scientific. All chemicals were used without any further purification.

3.2.2. Characterization

3.2.2.1. UV-visible Spectroscopy

A Cary 6000i spectrophotometer was used to record UV-vis spectra.

3.2.2.2. Powder X-ray Diffraction

pXRD measurements were carried out on a PANalytical Empyrean diffractometer configured using a cobalt x-ray source (Co K_α, λ = 1.79 Å). The data were collected with a 0.0469° step size (2θ).

3.2.2.3. Scanning Electron Microscopy

Scanning electron microscopy was carried out on a Hitachi SU8010 microscope operating at a 1.0−5.0 kV landing voltage.

3.2.2.4. Atomic Force Microscopy

AFM measurements were performed using a Dimensions Hybrid Nanoscope system (Veeco Metrology Group) under tapping mode in air.

3.2.3. P3HT Nanowire Synthesis

PMMA/P3HT polymer blends were prepared using previously reported procedures.[257, 261] P3HT and PMMA were added to a solvent mixture of chloroform/anisole (50:50 v/v) in order to achieve a total polymer concentration of 10 mg·mL^{-1}. Four different samples were prepared, with PMMA to P3HT ratios (w/w) varying from 80:20 to 95:5. Then the mixture was placed on a programmable hot plate to dissolve at 70 °C overnight with continuous stirring. The solution was then gradually cooled to room temperature at 20 °C·h^{-1} without stirring. The color of the solution changed from transparent red to dark brown, indicating the formation of P3HT nanowires. The solution was left undisturbed for 3 days before use.

ZnO nanoparticles and methylammonium iodide were synthesized following the procedures described in the section **2.2.2.**

3.2.4. Solar Cell Fabrication

Solar cells were fabricated by following previously reported procedures.[67, 242] ITO-coated glass substrates were cleaned by sequentially sonicating them for 20 min in 2% Extran 300 detergent, acetone and isopropanol followed by drying in an oven at 120 °C for 2 h. Then a thin ZnO nanoparticle layer was spin coated onto the substrate at 3,000 rpm for 30 s from a solution of 6 $mg \cdot mL^{-1}$ in *n*-butanol. In order to produce a uniform film, the procedure was repeated three times. By using thermal evaporation, a thin layer of PbI_2 (~ 150 nm) was deposited at a base pressure of 2×10^{-6} mbar. Then the substrate was dipped into a solution of CH_3NH_3I in 2-propanol (10 $mg \cdot mL^{-1}$) for 3 minutes, inside a glove-bag maintained at a relative humidity of ~ 40%. The substrate was spin-dried at 3,000 rpm for 25 s and then was kept for additional 10 minutes inside the bag. For control samples, a layer of P3HT was deposited by spin coating (1,000 rpm for 30 s) from a solution containing 20 mg of P3HT, 1 mL of chlorobenzene, 3.4 μL of TBP, and 6.8 μL of a Li-TFSI solution (28 mg Li-TFSI/1 mL acetonitrile). For the PMMA/P3HT-based devices, first a thin layer of P3HT was deposited by spin coating (2,000 rpm for 30 s) from a solution containing 20 mg of P3HT, 1 mL of chlorobenzene, 10 μL of TBP, and 20.4 μL of the same Li-TFSI solution. Then the PMMA/P3HT blend was deposited by spin coating using a two-step spinning protocol (500 rpm for 10 s; 2,500 rpm for 20 s). To produce different thicknesses of PMMA/P3HT layers, the spin speed of the second step was varied. Finally, either a silver or gold electrode was deposited by thermal evaporation at a base pressure of 2×10^{-6} mbar.

3.2.5. Solar Cell Characterization

The performance of the devices was measured using a Keithley 2400 source-measure unit and a 450 W Class AAA solar simulator equipped with an AM1.5G filter (Sol3A, Oriel Instruments) inside a nitrogen filled glovebox (<0.1 ppm O_2 and H_2O). The illumination intensity was adjusted to 100 $mW \cdot cm^{-2}$ as determined by a standard silicon reference cell (91150V, Oriel Instruments). A non-reflective metal mask was used to define the effective area of the device to be 0.0708 cm^2.

3.2.6. Liquid Water Stability Tests

Enough water was added to the top of a substrate to completely cover the surface (0.5 – 1.0 mL), and was left to stand for 1 minute. The devices were then blown dry in a stream of air, and reintroduced into the glovebox prior to testing.

3.2.7. Water Vapor Stability Tests

A stream of nitrogen carrier gas was bubbled through water in order to generate a stream of saturated (99 ± 1% relative humidity (RH)) water vapor. This flowed into either a custom-built sample holder (for in situ absorbance spectroscopy, **Figure 3.3**) or a gas-tight sample chamber (for device lifetime measurements, **Figure 3.4**). The RH and temperature were measured downstream of the sample chamber by an RH-USB humidity sensor (Omega). Devices were reintroduced into the glovebox prior to each measurement of their performance.

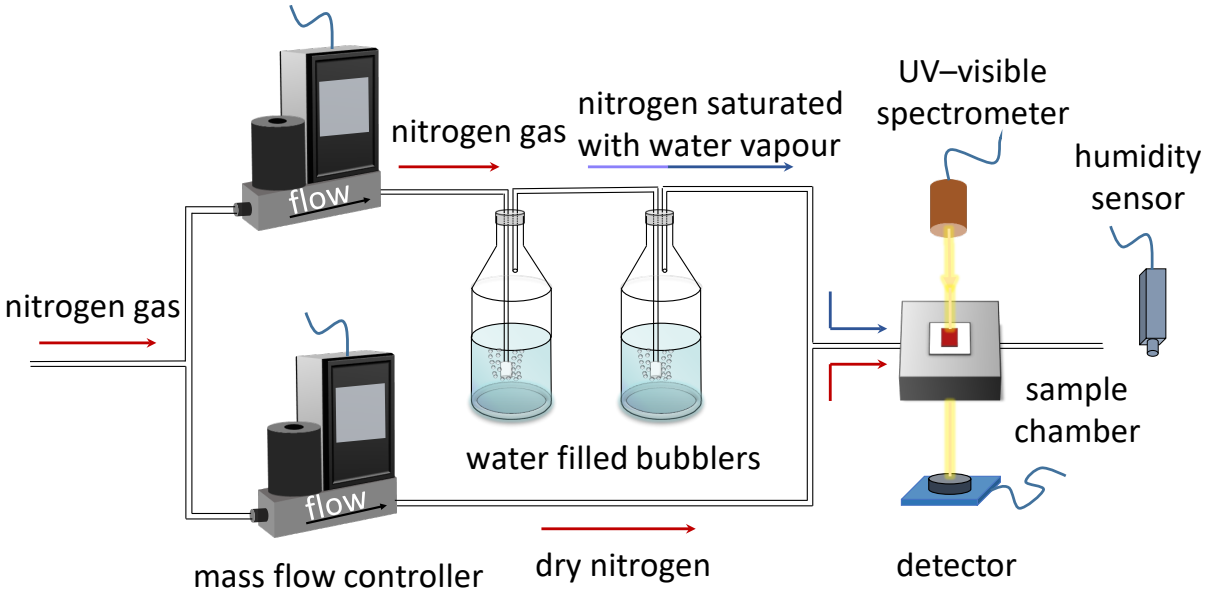

Figure 3.3 Schematic illustration of the RH control setup for in situ UV/vis spectroscopy.

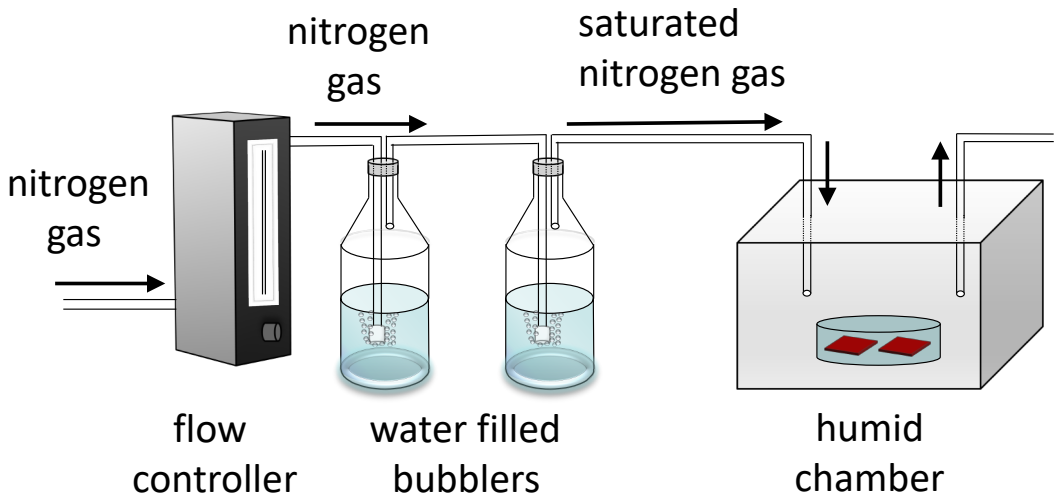

Figure 3.4 Schematic illustration of the RH control setup for measuring device lifetime.

3.3. Results and Discussion

3.3.1. Device Design

The device architecture used in the current study is shown in **Figure 3.2**. I deposit the $MAPbI_3$ absorber directly onto a compact ZnO ETL in a planar heterojunction design, as reported elsewhere. [67, 242] Onto this I deposit either a simple P3HT HTL (as a control), or a thin layer of P3HT, followed by a layer of P3HT nanowires in a PMMA matrix. The thin, compact P3HT layer is to ensure efficient hole-extraction from the perovskite absorber; from there, the P3HT nanowire network provides a percolation pathway to the top electrode (either Ag or Au). The rationale behind the PMMA matrix is that it serves to prevent moisture ingress into the perovskite layer, thereby improving device stability. However, since the PMMA matrix is insulating, the hole-transporting characteristics of P3HT need to be carefully balanced against the protective properties of PMMA. I therefore prepared devices with four different PMMA/P3HT ratios: 95 : 5, 90 : 10, 85 : 15, and 80 : 20. I then investigated the effect of HTL composition on the layer morphology, device performance, and device lifetime.

3.3.2.PMMA/P3HT Film Morphology

In order for the PMMA/P3HT blend to work as a HTL, the P3HT must self-assemble into an interconnected nanowire network, through which holes can percolate from the P3HT collection layer to the metal electrode; as such, the morphology of the HTL is critical. AFM was used to assess the nanostructure of the four different PMMA/P3HT films on glass substrates (**Figure 3.5**). Promisingly, even at the lowest P3HT loading (95 : 5 PMMA/P3HT), the appearance of nanowire-like structures can be observed in an otherwise smooth film (**Figure 3.5a**), with nanowire widths of ~10–20 nm. As the amount of P3HT in the blend is increased, the nanowire structure becomes

more pronounced; the morphology of the 90 : 10 PMMA/P3HT sample appears to consist of the desired interconnected nanowire network, although this is also accompanied by an overall increase in surface roughness (**Figure 3.5b**). The increase in surface roughness continues as the P3HT fraction is increased, with the 85 : 15 and 80 : 20 PMMA/P3HT films appearing to display less structured, but overall rougher, morphologies (**Figure 3.5c-d**). At the highest P3HT loading, there is relatively little evidence of polymer nanowires, and the AFM image is consistent with simple phase separation into PMMA- and P3HT-rich domains.

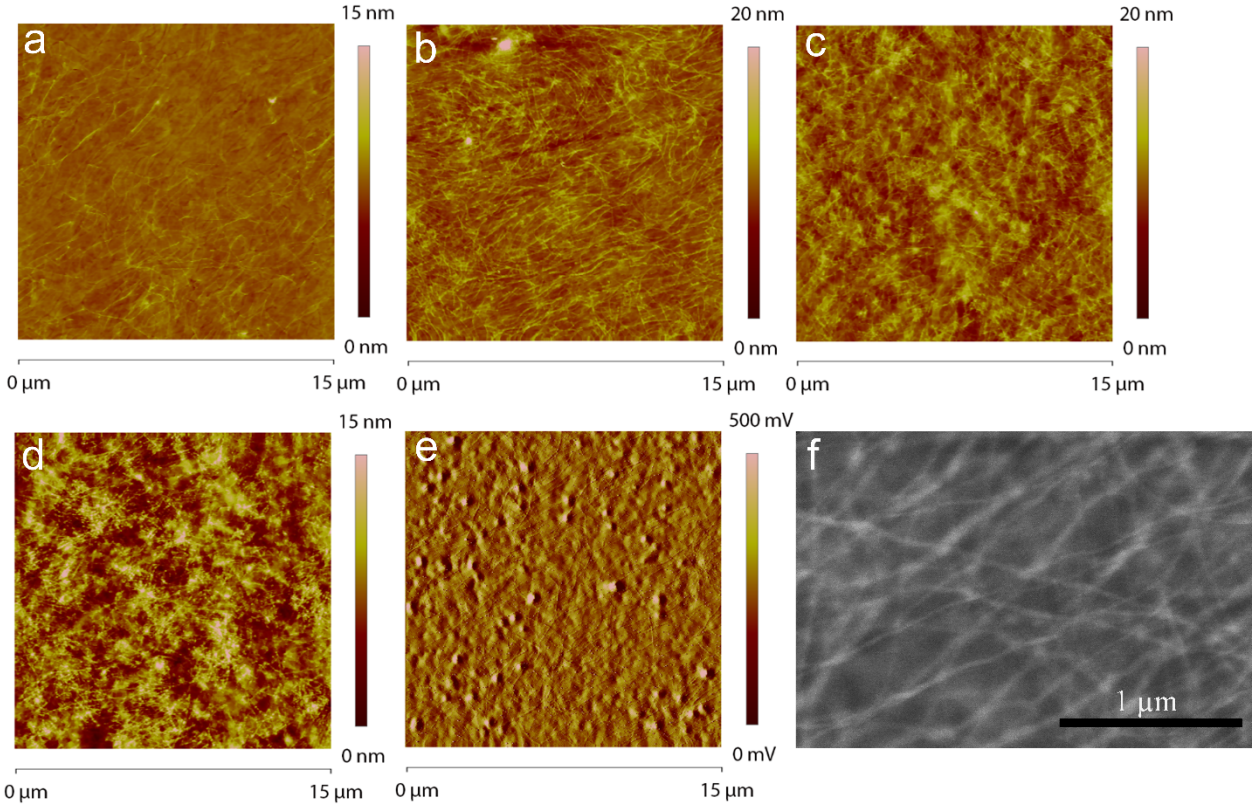

Figure 3.5 AFM images (height image) of PMMA/P3HT thin films on glass substrates, with varying PMMA/P3HT ratios: (**a**) 95 : 5; (**b**) 90 : 10; (**c**) 85 : 15; (**d**) 80 : 20. (**e**) AFM image (phase image) and (**f**) SEM image of 85 : 15 PMMA/P3HT films deposited on SiO_2/ZnO/$MAPbI_3$/P3HT substrates.

PSCs were then fabricated using the four different PMMA/P3HT blends, using a ITO/ZnO/$MAPbI_3$/P3HT/PMMA:P3HT/Ag architecture (**Figure 3.2**). AFM was used to image the surface of the HTL (in areas lacking a metal top electrode). The rough surface of the underlying perovskite can still be seen in the AFM height images (**Figure 3.6**), suggesting conformal coverage by the HTL; the P3HT nanowires are also still visible in the AFM phase images, indicating that the nanowire morphology is maintained on the perovskite-coated substrate (**Figure 3.5e** and **Figure 3.6**). SEM imaging validates these observations (**Figure 3.5f**); at moderately high accelerating voltages, and with low *Z* samples, SEM is sensitive to sub-surface morphology, and the embedded P3HT nanowires can be clearly observed in the PMMA/P3HT film.

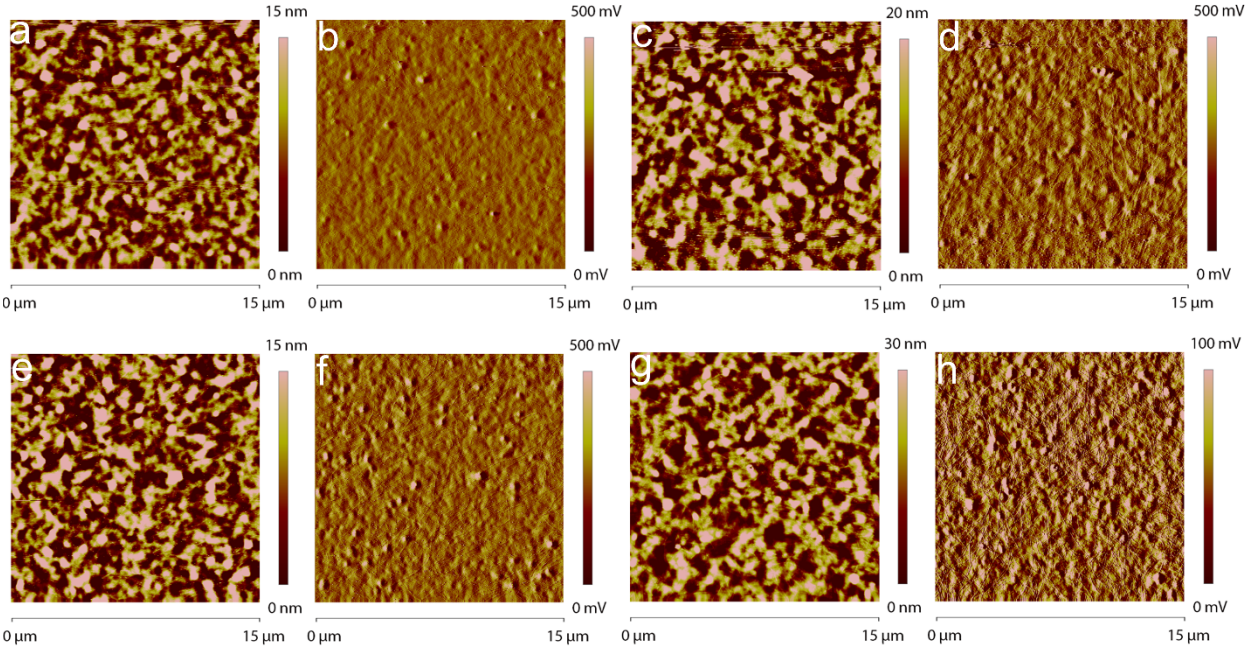

Figure 3.6 AFM images of PMMA/P3HT thin films on SiO_2/ZnO/$MAPbI_3$/P3HT substrates with different PMMA/P3HT ratios: (**a**) 95:5, height image; (**b**) 95:5, phase image; (**c**) 90:10, height image; (**d**) 90:10, phase image; (**e**) 85:15, height image; (**f**) 85:15, phase image; (**g**) 80:20, height image; (**h**) 80:20, phase image.

3.3.3. Device Performance

Having established that the PMMA/P3HT HTLs had the desired nanowire morphology, we then evaluated their performance in PSCs, as compared to conventional P3HT HTLs. The devices based on pure P3HT HTLs had an average PCE of 9.1 ± 0.9%, with the champion device having a PCE of 11.0%, which is consistent with previous literature reports.[67, 234, 262-264] Although this is lower than the efficiency of devices based on Li-TFSI-doped spiro-OMeTAD, numerous studies have now shown that spiro-OMeTAD HTLs can lead to relatively short device lifetimes, whereas P3HT-based cells often show less rapid decomposition.[68, 118] In comparison with the P3HT-only control devices, PSCs based on the PMMA/P3HT HTLs had device characteristics that were highly dependent on the PMMA/P3HT ratio (**Figure 3.6**). When only a small amount of P3HT was added to the HTL (95 : 5 PMMA/P3HT), the devices performed quite poorly (best PCE of 5.6%); this is almost entirely due to a high series resistance (**Figure 3.7e**), which limits both the fill factor and the short-circuit current density. This likely indicates poor connectivity between the P3HT nanowires; with no percolation pathway for holes, the PMMA matrix effectively limits the efficiency with which holes can be extracted. However, for the 90 : 10 PMMA/P3HT ratio, the interconnected nature of the nanowire array (**Figure 3.5b**) provides for efficient hole transport, even through the PMMA matrix. As a result, these devices performed almost equivalently to the P3HT controls (PCE = 8.1 ± 0.9% *vs.* 9.1 ± 0.9% for the controls). As the P3HT concentration is increased further, the two polymers begin to phase separate more coarsely (**Figure 3.5c** and **d**), resulting in a slow increase in series resistance and a concomitant decrease in FF and J_{SC}. In order to quantify the effect of hysteresis in our devices, we measured the *J–V* curves in both scan directions. For all devices, including both the P3HT controls and the PMMA/P3HT HTLs, the

device efficiency was relatively independent of scan direction, indicating little hysteresis (**Figure 3.8**).

Table 3.1: Average device performance parameters for ITO/ZnO/$MAPbI_3$/HTLs/Ag devices. The associated uncertainties represent plus-or-minus one standard deviation from the mean.

HTLs	**# of devices**	**V_{OC} (V)**	**J_{SC} (mA/cm^2)**	**Fill Factor (%)**	**PCE (%)**	**Best Efficiency (%)**
PMMA/P3HT 80:20	60	0.89 ± 0.06	16 ± 1	48 ± 5	6.8 ± 0.7	8.4
PMMA/P3HT 85:15	60	0.92 ± 0.04	16 ± 1	49 ± 5	7.5 ± 0.9	9.3
PMMA/P3HT 90:10	60	0.92 ± 0.06	16 ± 1	53 ± 6	8.1 ± 0.9	10.6
PMMA/P3HT 95:5	40	0.89 ± 0.04	11 ± 2	41 ± 5	4.2 ± 0.6	5.4
P3HT	30	0.97 ± 0.03	15.8 ± 0.8	62 ± 5	9.1 ± 0.9	11.0

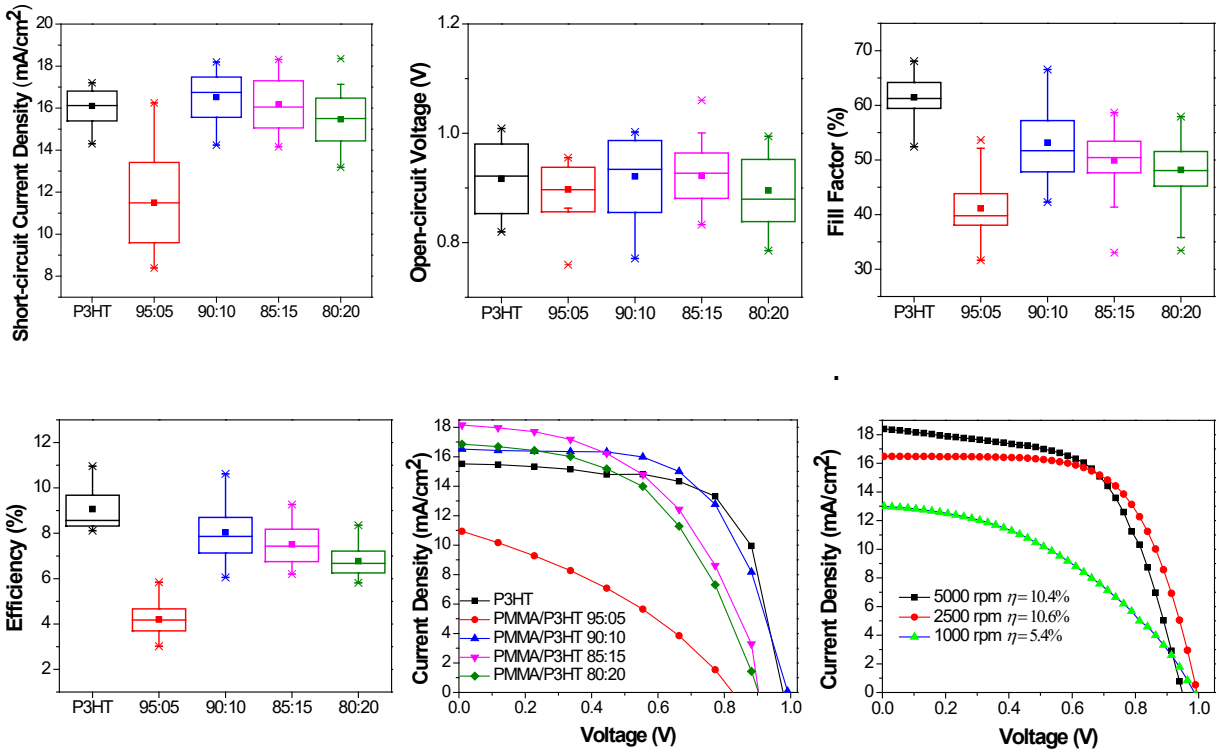

Figure 3.7 Cell performance parameters for devices made with varying HTLs: (**a**) J_{SC}; (**b**) V_{OC}; (**c**) FF; (**d**) PCE. The crosses denote the 1st and 99th percentiles; the bars denote the maximum and minimum values; the box boundaries mark the 25th and 75th percentiles; the horizontal line denotes the median; the solid square denotes the mean. (**e**) *J–V* curve of the champion devices with the various HTLs, measured at a scan rate of 0.1 $V \cdot s^{-1}$. (**f**) *J–V* curves for devices made with 90 : 10 PMMA/P3HT HTLs, deposited at different spin speeds.

Since one of the primary functions of the PMMA/P3HT HTL is to provide an internal vapor barrier within the device stack, thicker layers would presumably impart better protection to the underlying perovskite; however, this comes at the cost of increased series resistance. For a fixed PMMA/P3HT ratio (90 : 10), the HTL was deposited at three different spin speeds (1000, 2500, and 5000 rpm), providing three different layer thicknesses. The PCEs of the champion devices from this study were 5.4, 10.6 and 10.4%, respectively (**Figure 3.7f**). For the thickest HTL, the

increase in series resistance (combined with a loss of shunt resistance) severely limits the cell performance; however, at 2500 rpm provide the best combination of a relatively low series resistance and a thicker vapor barrier, and these fabrication conditions were chosen for the subsequent stability studies.

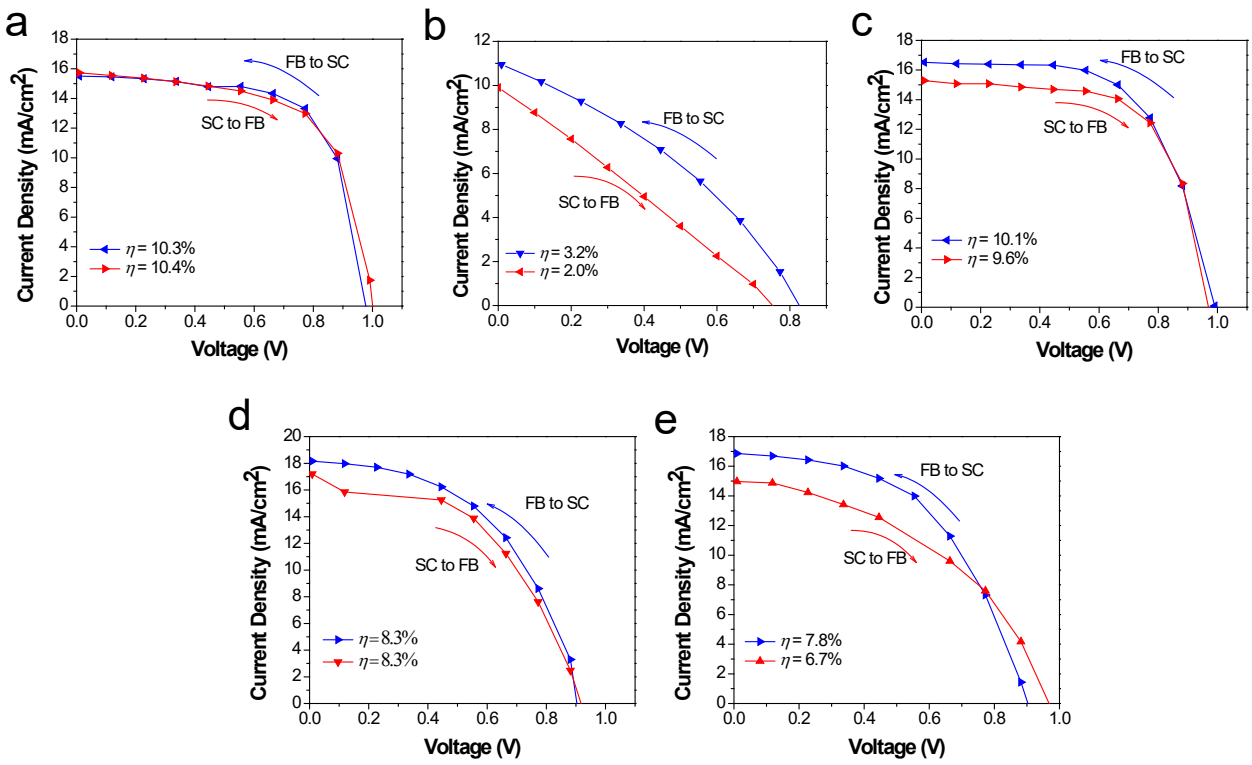

Figure 3.8 *J-V* curves in both scan directions for devices with various HTLs: (**a**) P3HT; (**b**) 95:5 (**c**) 90:10, (**d**) 85:15, (**e**) 80:20 PMMA/P3HT. *J-V* curves were measured at a scan rate of 0.1 $V \cdot s^{-1}$.

3.3.4.Effect of Liquid Water on Device Performance

The deleterious effects of water on $MAPbI_3$ have been well-established; liquid water rapidly destroys these materials by dissolution of MAI, leaving behind residual PbI_2. Due to the excellent film forming properties and overall hydrophobicity (water contact angle = 103°)[261] of the PMMA/P3HT layer, it is expected to form a water-impermeable coating over the $MAPbI_3$. In order to study the resistance of our devices to liquid water, both our PMMA/P3HT-based and control

devices (P3HT-only) were exposed to liquid water for 1 minute. Within a few seconds, the control sample had begun to degrade, and after 15 s it had completely decomposed, as evidenced by a color change from dark brown to yellow (**Figure 3.9**). In contrast, devices with PMMA/P3HT HTLs were unaffected (**Figure 3.9**). Both UV/vis spectroscopy (**Figure 3.10**) and powder x-ray diffraction (**Figure 3.11**) support this conclusion, with no change observed in either the absorption spectra or the diffraction patterns. The photovoltaic performance of the devices was also evaluated, both before and after water exposure (**Figure 3.12**). Unsurprisingly, the P3HT-only control devices short-circuited after water exposure, and were virtually non-functional. In contrast, there was virtually no change in performance for any of the PMMA/P3HT-based devices. This is highly encouraging, as it suggests that even if the encapsulation on a commercial cell or module were to degrade, it may not immediately lead to catastrophic device failure.

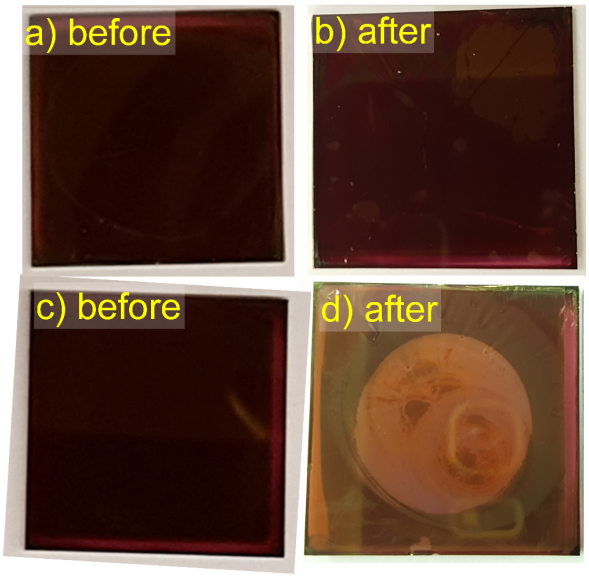

Figure 3.9 Photographs of polymer-coated perovskite films exposed to liquid water for 1 minute: (**a**) 90:10 PMMA/P3HT-coated, before; (**b**) 90:10 PMMA/P3HT-coated, after; (**c**) P3HT-coated, before; (**d**) P3HT-coated, after.

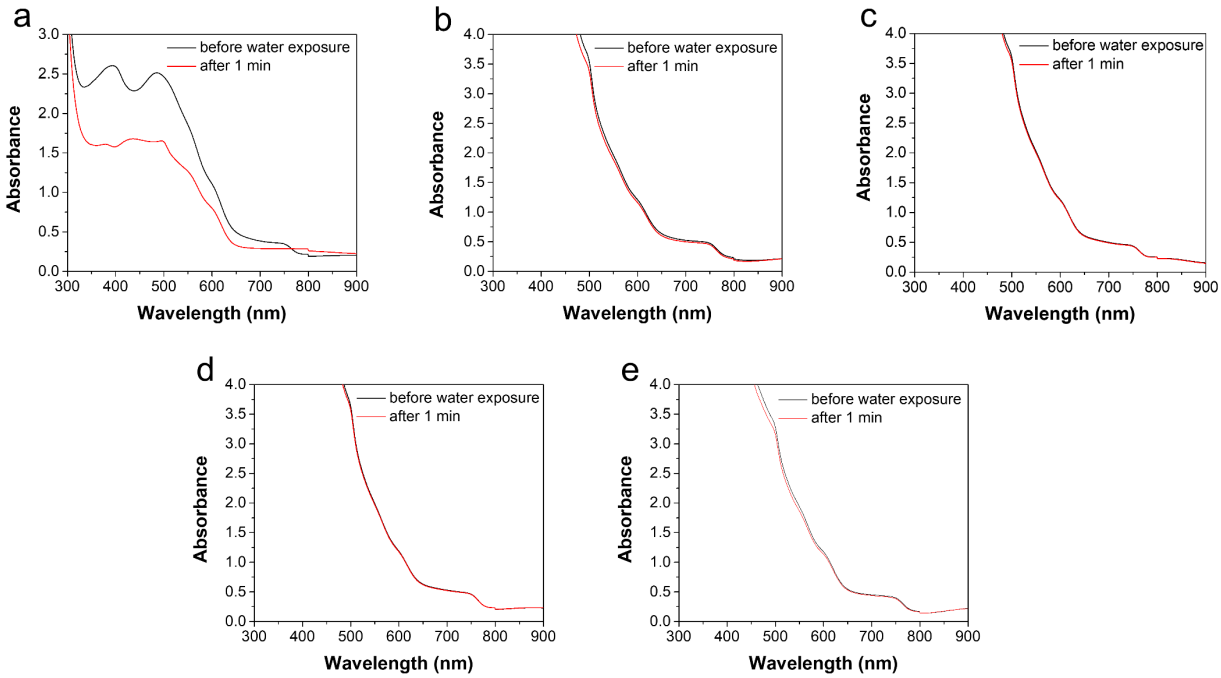

Figure 3.10 Absorption spectra of polymer-coated perovskite films, before and after exposure to liquid water for 1 minute: (**a**) P3HT; (**b**) 95:5, (**c**) 90:10, (**d**) 85:15, and (**e**) 80:20 PMMA/P3HT.

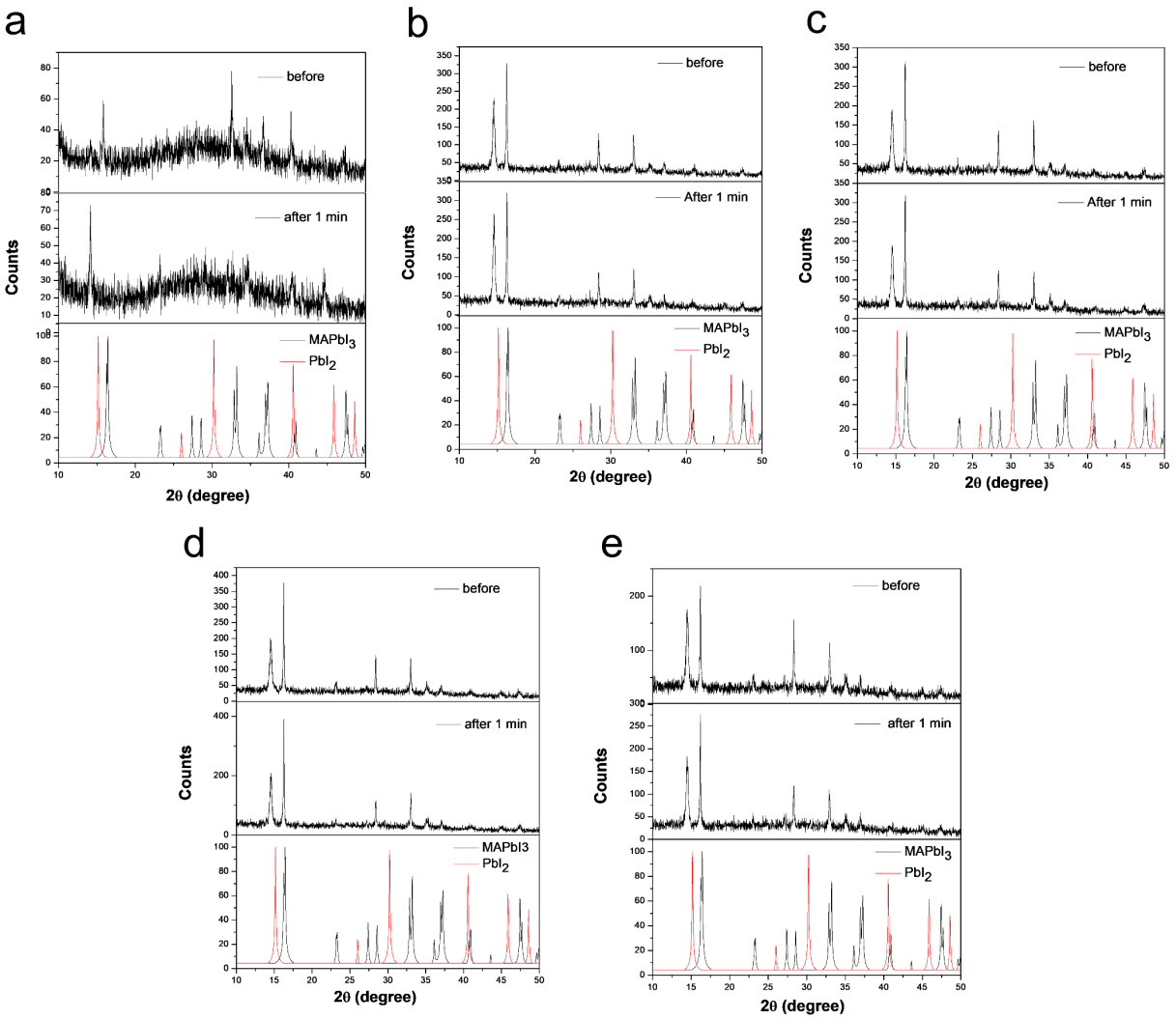

Figure 3.11 pXRD patterns of polymer-coated perovskite films, before and after exposure to liquid water for 1 minute: (**a**) P3HT; (**b**) 95:5, (**c**) 90:10, (**d**) 85:15, and (**e**) 80:20 PMMA/P3HT.

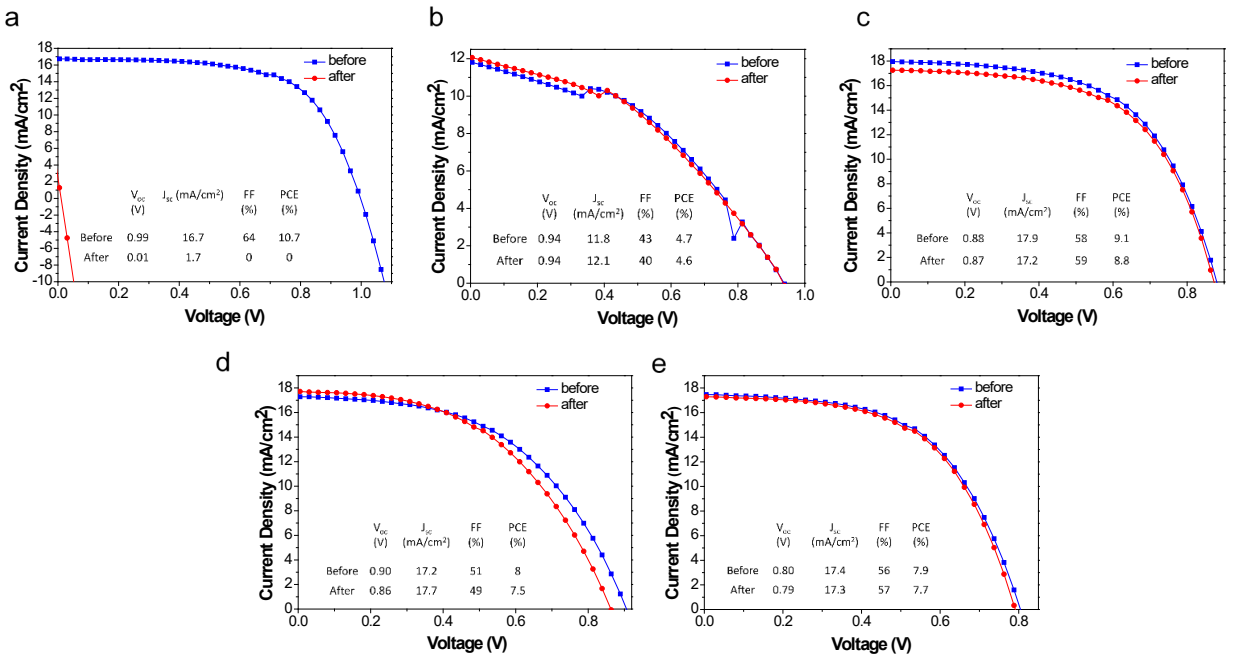

Figure 3.12 *J-V* curves for devices with various HTLs, measured before and after exposure to liquid water for 1 minute: (**a**) P3HT-only; (**b**) 95:5, (**c**) 90:10, (**d**) 85:15, (**e**) 80:20 PMMA/P3HT. Scans were performed at a scan rate of 0.83 $V \cdot s^{-1}$ from forward bias to short-circuit.

3.3.5. Effect of Water Vapor on Device Performance

Although the penetration of liquid water into the device stack leads to the most rapid cell degradation, its high surface tension makes it relatively facile to exclude from the cell; in contrast, vapor-phase water is much more insidious, and even good barrier plastics have a non-zero moisture vapor transmission rate. Therefore, in order to better evaluate the performance of our PMMA/P3HT barrier HTL, we exposed our devices to various RH environments, and measured their performance as a function of time.

As an initial test, we stored our devices in ambient air at 21–23 °C and 35–45% RH, and measured their photovoltaic performance at one day intervals (**Figure 3.13**). Even under these relatively mild conditions (room temperature and moderate RH), all of the P3HT control devices

failed within 24 h. In contrast, the cells with PMMA/P3HT-based HTLs degraded much more slowly; after 96 h, all PMMA/P3HT-based devices retained ~50% of their initial efficiency. While the devices with 80 : 20 and 85 : 15 PMMA/P3HT ratios had completely failed after 120 h, devices with higher PMMA ratios (90 : 10 and 95 : 05) were still functional, retaining ~30–40% of their initial efficiency.

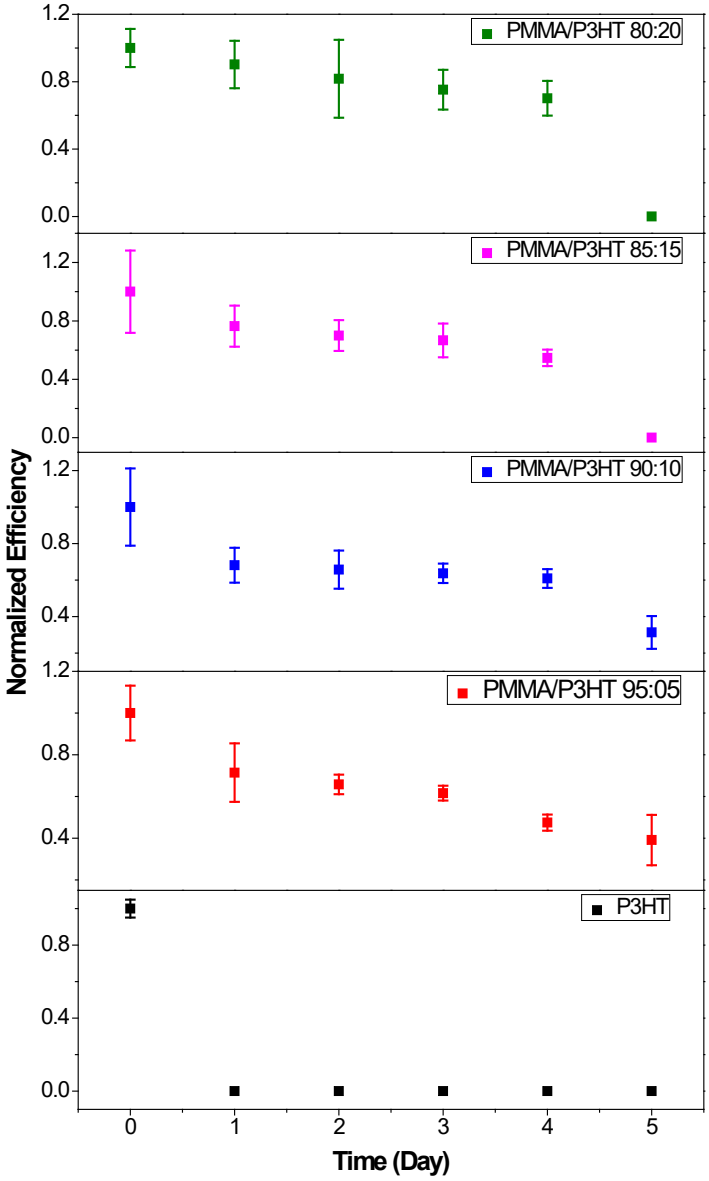

Figure 3.13 Normalized power conversion efficiency as a function of time for perovskite solar cells with silver electrodes, stored in a 35-45% RH environment. Error bars denote plus-or-minus one standard deviation from the mean.

The rapid cell failure observed for the P3HT control samples is ascribed to halide ion migration from the $MAPbI_3$ layer to the silver electrode; the iodide ions help facilitate the oxidation of the electrode, leading to cell failure.[123, 265] UV/vis spectroscopy and SEM were used to support this conclusion. The UV/vis spectra of the control devices showed that the band edge feature at 760

nm disappears upon aging, indicating decomposition of $MAPbI_3$ (**Figure 3.14**). A basic visual inspection of the device also shows that the silver electrodes of the control devices were discoloured and corroded (**Figure 3.15**), which can also be observed by comparing SEM images of the electrodes before and after aging (**Figure 3.16 -3.17**). High magnification SEM images show pronounced corrosion at the edges of the silver electrodes, with the appearance of cracks and non-metallic byproducts (as indicated by a change in electron contrast and an increase in charging). In contrast, the PMMA/P3HT devices all show only a minor decrease in absorbance across the UV/vis spectrum (**Figure 3.14**), and the silver electrodes remain shiny and metallic even after six days of aging (**Figure 3.15**), even under microscopic analysis (**Figure 3.16-3.17**). The PMMA may serve two functions here: (i) to prevent the ingress of water vapor into the perovskite layer, thereby reducing the mobility of iodide ions; and (ii), to block mobile iodide ions from leaving the perovskite layer and reaching the silver electrode. The better barrier properties of PMMA as compared to P3HT may be related to its molecular weight (350 kDa for PMMA, *vs.* 50 kDa for P3HT) or its more polar functional groups, which better bind water and/or iodide ions, slowing their transit through the layer.

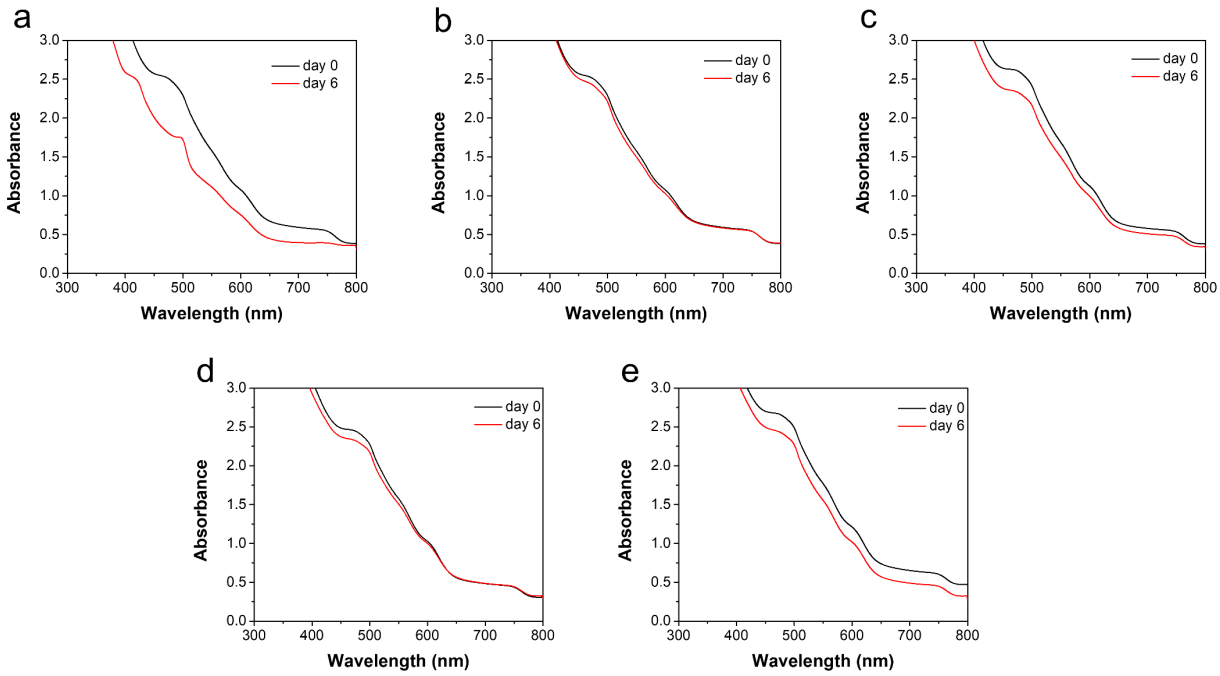

Figure 3.14 Absorption spectra of perovskite solar cells with various HTLs before and after aging in air (RH = 35 – 45%): (**a**) P3HT; (**b**) 95:5, (**c**) 90:10, (**d**) 85:15, and (**e**) 80:20 PMMA/P3HT.

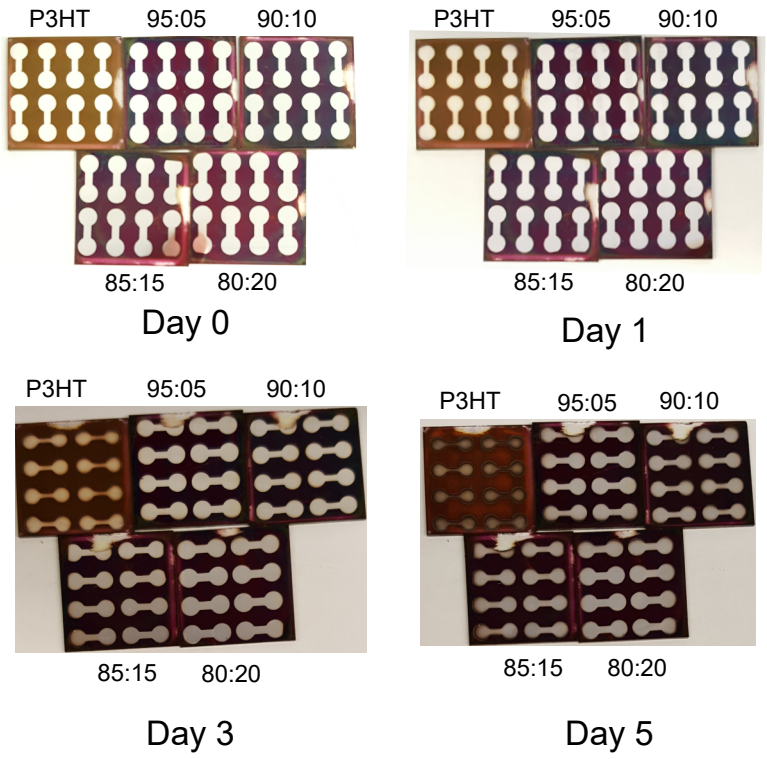

Figure 3.15 Photographs of the ITO/ZnO/$MAPbI_3$/HTLs/Ag devices after aging in air; the corrosion of the silver electrode in the P3HT control samples is easily apparent.

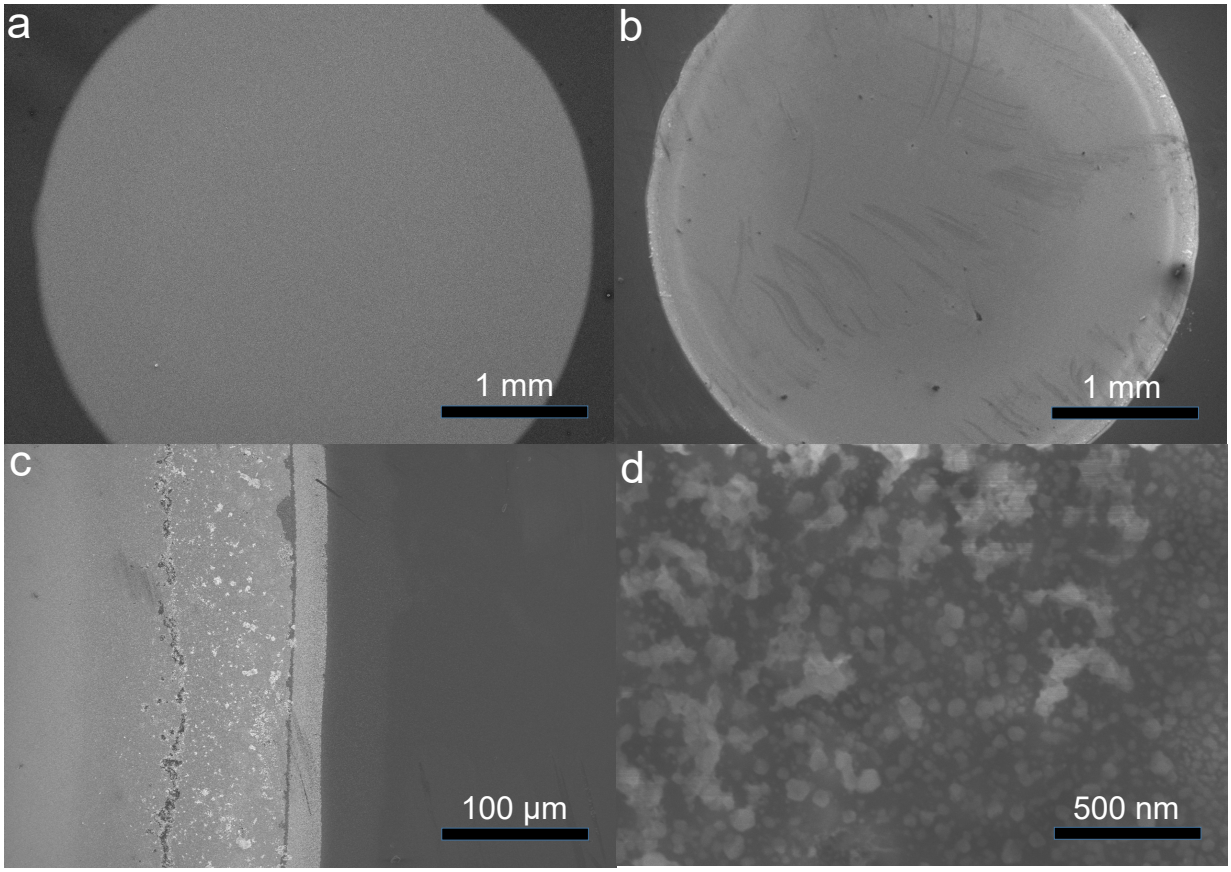

Figure 3.16 SEM images of the silver electrode of a P3HT control device: (**a**) as prepared, and (**b-d**) after 6 days of aging in air; (**c**) and (**d**) are higher magnification images of the electrode edge.

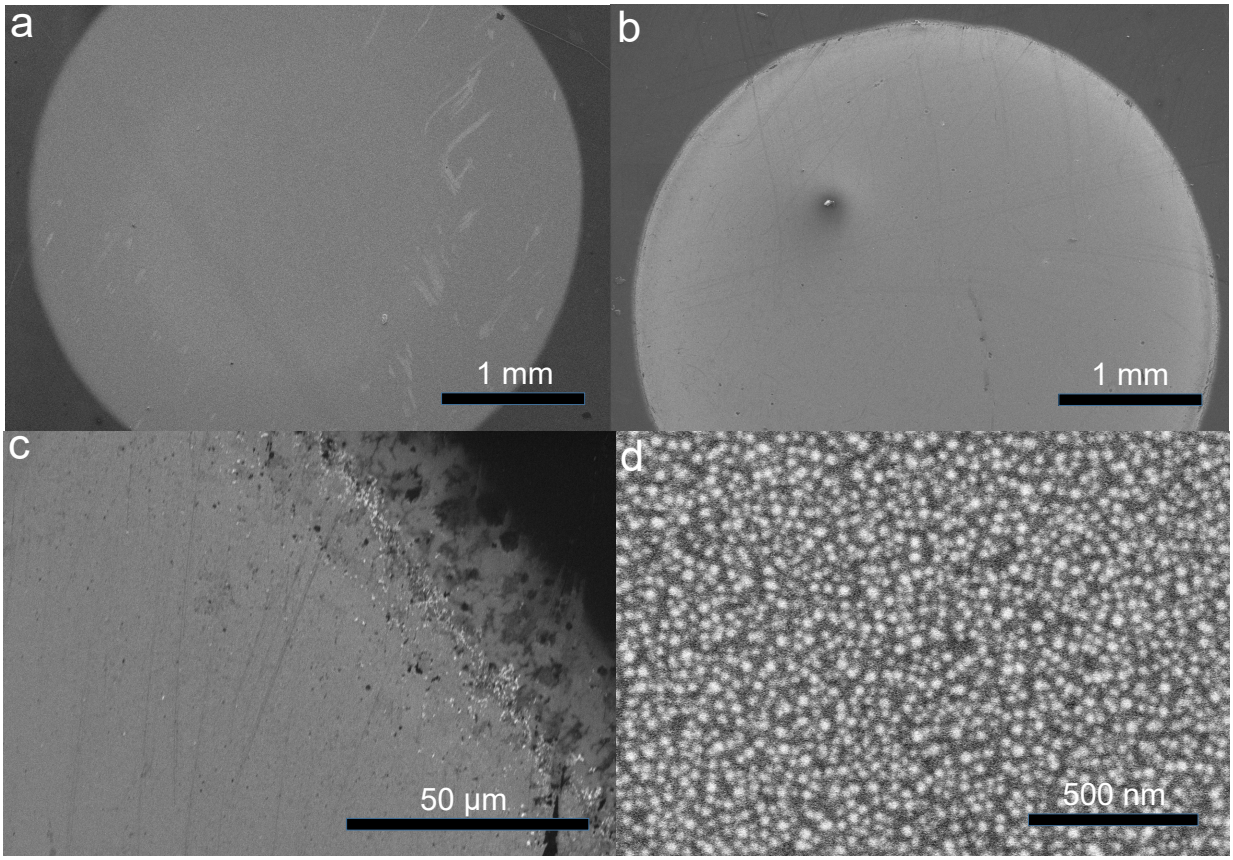

Figure 3.17 SEM images of the silver electrode of a 95:5 PMMA/P3HT device: (**a**) as prepared, (**b-d**) after 6 days of aging in air; (**c**) and (**d**) are higher magnification images of the electrode edge.

Although a RH of ~40% is typical of indoor conditions, modules deployed in the field will encounter a much wider range of water concentrations. We therefore carried out a more rigorous study where we subjected our devices to a 99 ± 1% RH environment. For this study, we flowed nitrogen carrier gas through a series of water-filled bubblers, producing a stream of saturated water vapor; this was then connected to the inlet of an air-tight sample chamber, while a RH sensor was connected to the outlet in order to validate the humidity inside the chamber (**Figure 3.4**). Since the silver electrode was identified as a critical component in the device degradation process, we carried out the study on devices built using both silver and gold electrodes.

As expected, the devices with silver electrodes decomposed at an accelerated rate in the 99% RH environment; the P3HT control devices retained only a third of their initial performance after 30 minutes of exposure, and completely short-circuited after 1 hour (**Figure 3.18a**). Again, those devices incorporating a PMMA/P3HT barrier layer displayed enhanced lifetimes; with an 80 : 20 PMMA/P3HT ratio, the devices lasted for ~2.5–3 h before failure, a five-fold increase in lifetime; with increasing PMMA loadings, the improvements are even more marked. The 90 : 10 PMMA/P3HT devices (which also displayed the best PCEs), retained ~40% of their initial performance after 6 h of exposure to saturated water vapor. This represents over an order of magnitude increase in lifetime relative to the P3HT-only controls, and highlights the performance of the PMMA/P3HT HTL as an effective vapor barrier.

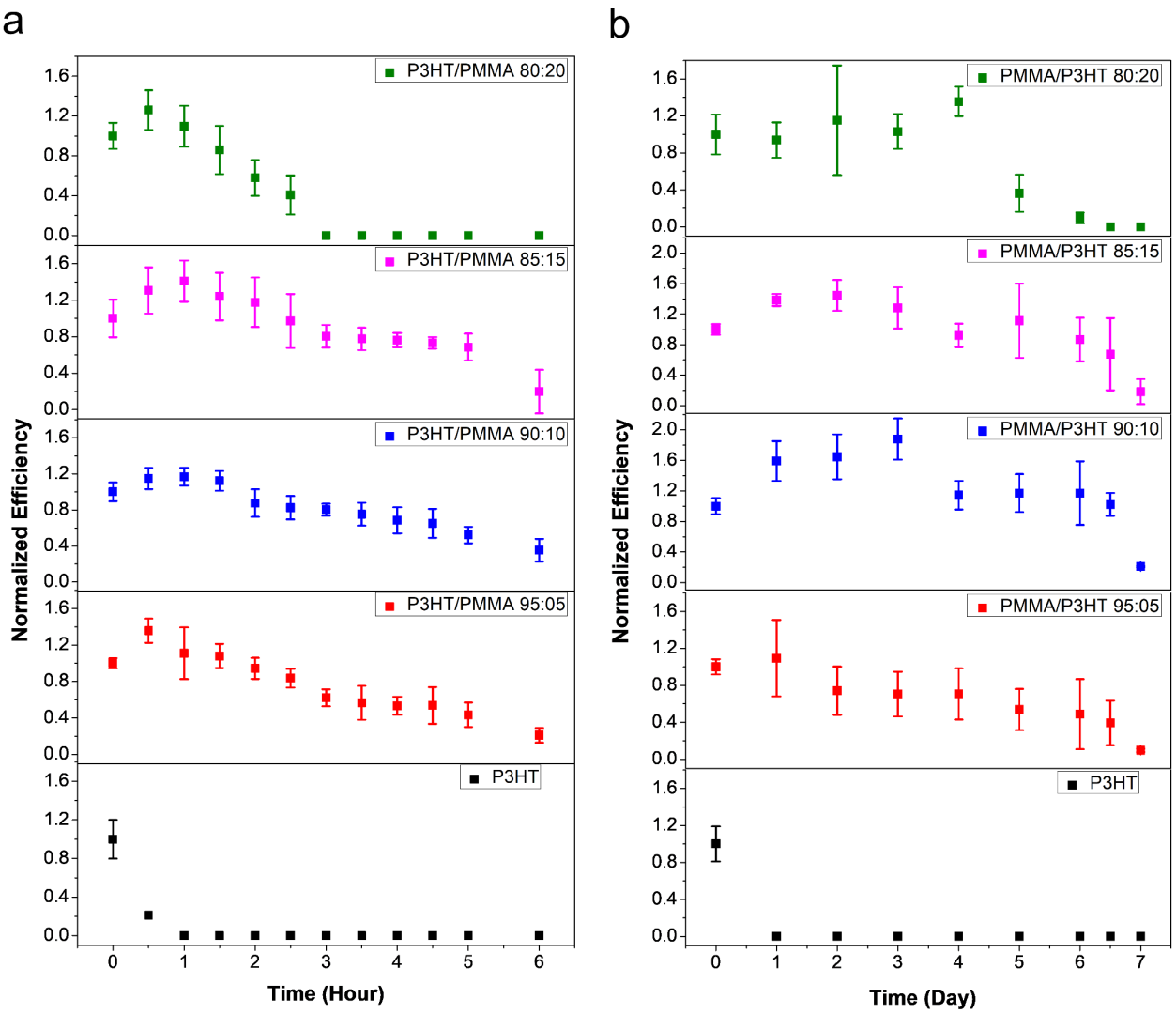

Figure 3.18 Normalized power conversion efficiency as a function of time for perovskite solar cells with (**a**) silver electrodes and (**b**) gold electrodes, stored in a 99 ± 1% RH environment. Error bars denote plus-or-minus one standard deviation from the mean.

Switching the top electrode from silver to gold provided a notable increase in device lifetime, and allowed a longer-term study to be carried out (**Figure 3.18b**). Again, the devices based on P3HT controls degraded relatively quickly, with all devices shorting after <24 h of exposure. In contrast, the cells incorporating vapor barrier HTLs survived for ~1 week in the 99% RH atmosphere. Again, the 80 : 20 PMMA/P3HT ratio provided the least resistance to water vapor,

with cells failing after 4–5 days of exposure. This may be due to the more coarsely phase-separated morphology of these films (**Figure 3.6d**); presumably, the large P3HT domains break up the more smooth, conformal, and less permeable PMMA coating, allowing for greater levels of moisture permeation. As the PMMA loading is increased, the devices last longer, with some of the best results obtained with a 90 : 10 PMMA/P3HT ratio. In this case, over the first few days of testing, we actually observed an increase in device performance, primarily due to an increase in photocurrent and fill factor. Our previous work has noted that non-zero RH levels during the perovskite deposition process can actually increase device performance due to better connectivity between individual crystalline grains;[67] in this case, low levels of moisture may actually be solvent-annealing the perovskite layer, resulting in improved performance. However, after 4 days the PCE had returned to its initial value, and after 7 days, the device performance had dropped by >60%. This nonetheless represents a roughly 10-fold improvement in device lifetime over the P3HT-only control devices, consistent with the data derived from devices with silver electrodes.

3.3.6. In Situ UV/vis Spectroscopy

Ultimately, the potential of these vapor barrier HTLs is governed by the ability of PMMA to prevent moisture ingress and perovskite degradation. In order to separate this from other electrical effects present in devices (*e.g.*, electrode corrosion), we carried out an in situ UV/vis spectroscopy study on perovskite thin films capped with either pure P3HT, pure PMMA, or P3HT/PMMA barrier layers. The films were exposed to a 98 ± 2% RH environment, and absorbance spectra acquired every 15 min. The absorbance at 410 nm is then plotted as a function of time (**Figure 3.19**). From the data, it can be concluded that $MAPbI_3$ is extremely sensitive to water vapor, with uncoated samples decomposing in <6 h, consistent with our previous work.[68] P3HT provides a

small amount of additional protection, with films decomposing in <1 day. The improved barrier properties of PMMA are also clearly apparent from the data, with the PMMA-coated samples only showing appreciable signs of decomposition after >100 h of exposure to 98% RH. The PMMA/P3HT-coated samples all provide intermediate levels of protection, with the performance of the 90 : 10 PMMA/P3HT ratio being very comparable to pure PMMA films. One other key difference between the uncoated film and the coated samples is the appearance of a step-wise decomposition process in the coated samples. This may be due to pinhole formation in the barrier film. As water vapor penetrates the barrier layer, it leads to the rapid decomposition of the $MAPbI_3$ beneath it; as another pinhole forms, another section of the perovskite film decomposes, leading to the observed step-wise decomposition profile.

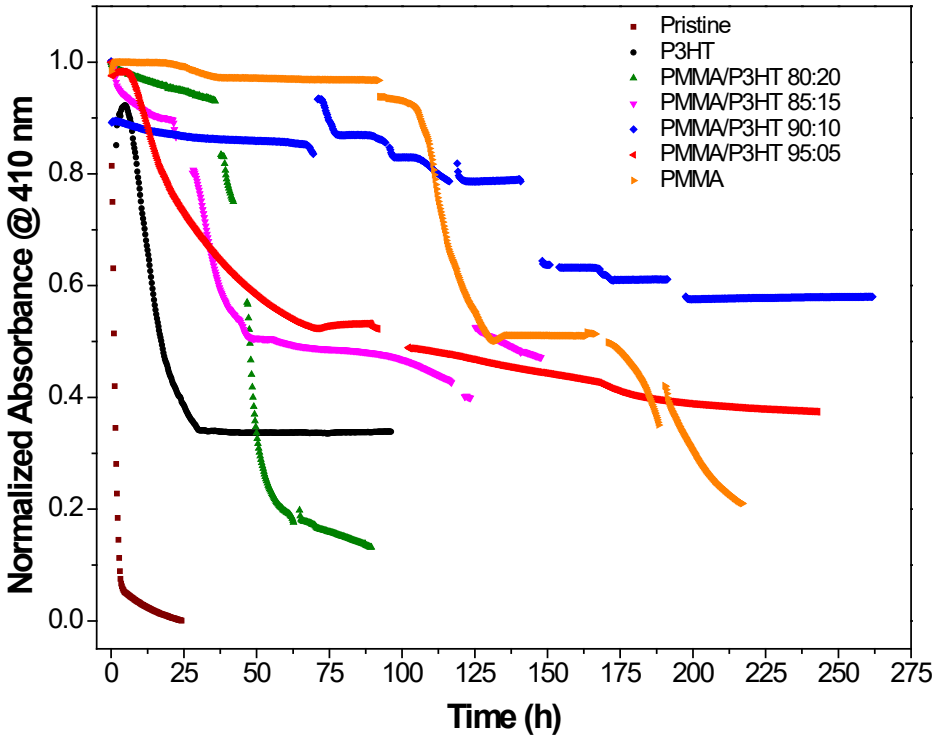

Figure 3.19 Normalized absorbance at 410 nm as a function of time for polymer-coated perovskite films exposed to a 99 ± 1% RH environment.

3.4. Conclusions

This chapter demonstrated a simple, scalable strategy to improve the moisture resistance and device lifetime of PSCs. P3HT nanowires can provide a hole-transport pathway between the $MAPbI_3$ absorber and the top electrode, with performance nearly equivalent to that of a compact P3HT layer; by embedding the nanowires in a PMMA matrix, the HTL then additionally serves as a barrier to both liquid and vapor phase water. Measurements in a 99% RH environment show that optimized PMMA/P3HT HTLs (using a 90 : 10 PMMA/P3HT ratio) can improve the lifetime of PSCs by roughly one order of magnitude, even in the absence of any additional encapsulation. These test conditions are much more aggressive than those typically encountered in the literature (often 30–40% RH), highlighting the ability of the PMMA/P3HT barrier layers to withstand even very damp environments.

4. Moisture-induced Decomposition Mechanisms of Lead Halide Perovskites: an in Situ Absorption Spectroscopy and X-ray Scattering Study

4.1. Introduction

The archetypal hybrid perovskite $MAPbI_3$ is inherently moisture sensitive. Owing to the low formation energy of $MAPbI_3$, stress factors such as moisture, heat, light have a profound effect on its stability. Even the presence of a small amount of moisture is enough to alter the composition of $MAPbI_3$ perovskite crystals and accelerate the decomposition process. Therefore, additional actions should be taken in order to minimize the contact of $MAPbI_3$ with atmospheric moisture. There are a couple of ways to protect the $MAPbI_3$ layer from moisture exposure. One approach is to apply physical barrier layers between $MAPbI_3$ and the environment so that moisture cannot come in contact with the perovskite layer. The previous chapters (**Chapter 2** and **3**) discussed this approach. Another approach is to replace $MAPbI_3$ with more stable perovskite compositions.

Having different A-site cations like MA, FA and Cs and anions (X) such as I, Br, and Cl, hybrid organic inorganic lead iodide perovskites ($APbX_3$) can have several compositions. Each composition is chemically different. Therefore, each has a different reactivity and affinity towards water. For example, among $MAPbX_3$ (where X = I, Br, and Cl) $MAPbCl_3$ and $MAPbBr_3$ are more stable than $MAPbI_3$ in ambient humidity.[132] The partial replacement of I by Br improves the moisture stability of the resulting $MAPbBr_xI_{3-x}$ composition.[126] Similarly, replacing the MA cation and FA cation with the inorganic Cs cation increases the moisture stability.[135-137, 266]

Recently, $FAPbI_3$ has gained popularity over other pure compositions although its instability remains problematic.[26, 267] Previous studies have revealed that doping with a small amount of Cs can improve its stability.[135, 136] According to Lee et al., $Cs_{0.1}FA_{0.9}PbI_3$ based devices have higher stability (in 40-50 % RH) and slightly better performance than pure $FAPbI_3$.[135] However, there is no study related to the decomposition rates or the decomposition mechanisms. Hence, $Cs_{0.1}FA_{0.9}PbI_3$ will be one of the important mixed compositions for this study. After the work by Saliba et al., $Cs_{0.1}MA_{0.15}FA_{0.75}Pb(Br_{0.15}I_{0.85})_3$ gained popularity and has been used in high performance devices.[141] Hence, $Cs_{0.1}MA_{0.15}FA_{0.75}Pb(Br_{0.15}I_{0.85})_3$ will be another important composition in this study.

Several studies have reported trends in the moisture stability of lead halide perovskites; however, a comprehensive understanding of the moisture stability of the various perovskite compositions is missing. In addition, the decomposition mechanisms of these perovskites are poorly understood. Comparing the different studies done in different labs is also hard, as there are huge geographical and seasonal variations between locations. Most of these experiments are conducted at room temperature and under "ambient" conditions without having any tight control over the environment. Therefore, the results of these experiments are uncertain, incomparable, and often conflicting. This makes it extremely difficult to draw meaningful comparisons between these experiments carried out in different laboratories, which in turn limits insight into the degradation process. In order to provide meaningful insight into the decomposition mechanism it is necessary to conduct experiments which are comparable and reproducible with tight control over the environmental conditions.

This chapter discusses the results of a quantitative investigation of the moisture-induced degradation of eight different perovskite compositions by in situ studies. In situ methodologies are

important and necessary tools to study these degradation processes as they provide continuous, reliable, and real-time data. They can provide crucial information on the transient stages of a degradation mechanism, and help to detect metastable phases which could otherwise be missed by non-continuous, ex situ studies. We have carefully studied the decomposition rates of different perovskite compositions by using in situ absorption spectroscopy in an environmental chamber where the RH was carefully controlled. By in situ GIWAXS, we were able to monitor changes in the perovskite crystallinity and phase which enabled us to gain important insights into the intrinsic moisture instability of different perovskite compositions. Our studies have revealed that the degradation of lead halide perovskites at high RH is a more complex process than is typically thought.

4.2. Experimental Section

4.2.1. Materials

Lead(II) iodide (99%), lead(II) bromide (98%), and cesium iodide were purchased from Sigma Aldrich. Cesium bromide was purchased from Alfa Aesar. All the materials were used as received. *N*,*N*-Dimethylformamide, dimethyl sulfoxide, chlorobenzene was purchased from Fisher scientific and was dried and stored over molecular sieves 3Å inside a nitrogen-filled glove box.

MAI, FAI, MABr, FABr were synthesized in the lab following standard procedures.[18, 268]

4.2.2.Film Formation

All films were deposited on 1 inch × 1 inch glass substrates that had been cleaned by sequentially sonicating in dilute Extran 300 detergent, acetone, and isopropanol for 20 min. The substrates were stored in isopropanol. Before film deposition the substrates were blown dry in a jet of nitrogen.

Perovskite precursor solutions were prepared by completely dissolving the starting materials and filtering the solution through a 0.45 μm syringe filter. All films were prepared inside a glove box in an inert atmosphere (<5 ppm of O_2 and <1 ppm of H_2O)

$MAPbI_3$. The $MAPbI_3$ perovskite films were prepared from perovskite precursor solution by completely dissolving 1 mmol PbI_2 and 1 mmol methylammonium iodide (MAI) in 1 mL of 4:1 DMF/DMSO. Then the solution was spun at 1000 rpm for 10 s followed by 4000 rpm for 20 s. 150 μL of chlorobenzene was dripped onto the surface 9 s prior to the end of the program. Then the film was annealed at 65 °C for 1 minute and 100 °C for 3 minutes.

$FAPbI_3$. To prepare $FAPbI_3$ films, first 1 mmol PbI_2 and 1 mmol formamidinium iodide (FAI) were dissolved in 1 mL of 4:1 DMF/DMSO. The solution was spin-coated at 1000 rpm for 10 s followed by 4000 rpm for 20 s. 150 μL of chlorobenzene was dripped onto the surface 7 s prior to the end of the program. The films were annealed at 50 °C for 3 minutes and 150 °C for 5 minutes.

$CsPbI_3$. 1 mmol CsI and 1 mmol PbI_2 were dissolved in 1 mL of 7:3 DMF/DMSO. The solution was spun at 1000 rpm for 10 s followed by 4000 rpm for 20 s. 150 μL of chlorobenzene was dripped onto the surface 7 s prior to the end of the program. The resulting films were annealed at 50 °C for 3 minutes and at 350 °C for 5 minutes.

$Cs_{0.1}FA_{0.9}PbI_3$. For $Cs_{0.1}FA_{0.9}PbI_3$, the precursor solution was prepared by dissolving CsI (25.9 mg, 0.1 mmol), FAI (154.8 mg, 0.9 mmol), and PbI_2 (461 mg, 1 mmol) in 1 mL of 4:1 DMF/DMSO. $Cs_{0.1}FA_{0.9}PbI_3$ films were prepared by following the same procedure as $FAPbI_3$.

$Cs_{0.1}MA_{0.15}FA_{0.75}Pb(Br_{0.15}I_{0.85})_3$. $Cs_{0.1}MA_{0.15}FA_{0.75}Pb(Br_{0.15}I_{0.85})_3$ films were prepared by dissolving CsI (25.9 mg, 0.1 mmol), MAI (23.8 mg, 0.15 mmol), FAI (129 mg, 0.75 mmol), $PbBr_2$ (55 mg, 0.15 mmol), and PbI_2 (391.9 mg, 0.85 mmol) in 1 mL 4:1 DMF/DMSO solution. Then the solution was spun at 1000 rpm for 10 s followed by 4000 rpm for 20 s. 150 μL of chlorobenzene

was dripped onto the surface 7 s prior to the end of the program. The films were annealed at 100 °C for 90 minutes.

$MAPbBr_3$ and $FAPbBr_3$. $MAPbBr_3$ and $FAPbBr_3$ were prepared from 1 M $PbBr_2$ and 1 M MABr or FABr solution in 4:1 DMF/DMSO followed by spin-coating at 1000 rpm for 10 s followed by 4000 rpm for 20 s. 150 μL of chlorobenzene was dripped onto the surface 12 s prior to the end of the program. $MAPbBr_3$ and $FAPbBr_3$ films were annealed at 100 °C for 10 minutes and 150 °C for 10 minutes respectively.

$CsPbBr_3$. To deposit $CsPbBr_3$ films a two steps deposition technique was adopted. First, $PbBr_2$ films were deposited from a 1.2 M $PbBr_2$ solution dissolved in DMF by spin-coating at 3000 rpm for 15 s. The films were annealed at 75 °C for 30 minutes. Then the resulting $PbBr_2$ films were dipped into a 17 mg/mL CsBr in ethanol solution at 70 °C for 10 minutes. The films were then annealed at 250 °C for 30 minutes.

4.2.3. Characterization

4.2.3.1. UV/vis Spectroscopy

A stream of nitrogen carrier gas was bubbled through water in order to generate a stream of saturated (97 ± 3% RH) water vapor which was then flowed into a custom-built sample holder placed inside a Cary 6000i spectrophotometer. The RH and temperature were measured downstream of the sample chamber by an RH-USB humidity sensor (Omega). Spectra were collected at 15 minute intervals.

4.2.3.2. GIWAXS

In situ GIWAXS measurements were performed at the Hard X-ray MicroAnalysis (HXMA) beamline of the Canadian Light Source. An energy of 17.998 keV (λ = 0.6888 Å) was selected

using a Si(111) monochromator. The diffraction patterns were collected on a SX165 CCD camera (Rayonix) using an acquisition time of 1-10 s as suitable for different samples. The sample-to-detector distance (239 mm) was calibrated using a LaB_6 powder standard. For in situ experiments, devices were mounted in a custom-built gas-tight sample chamber. Nitrogen carrier gas was connected to a series of mass flow controllers (Alicat MC-5SLPM-D) and water-filled bubblers, and the output of this system connected to the sample chamber (**Figure 4.1**). The RH inside the chamber was controlled by varying the relative flow rates of dry nitrogen and nitrogen saturated with water vapor, and was validated by a flange-mounted humidity sensor (RH-USB, Omega). The RH was maintained 90 ± 5%. GIWAXS patterns were acquired every 30-180 s depending upon the samples.

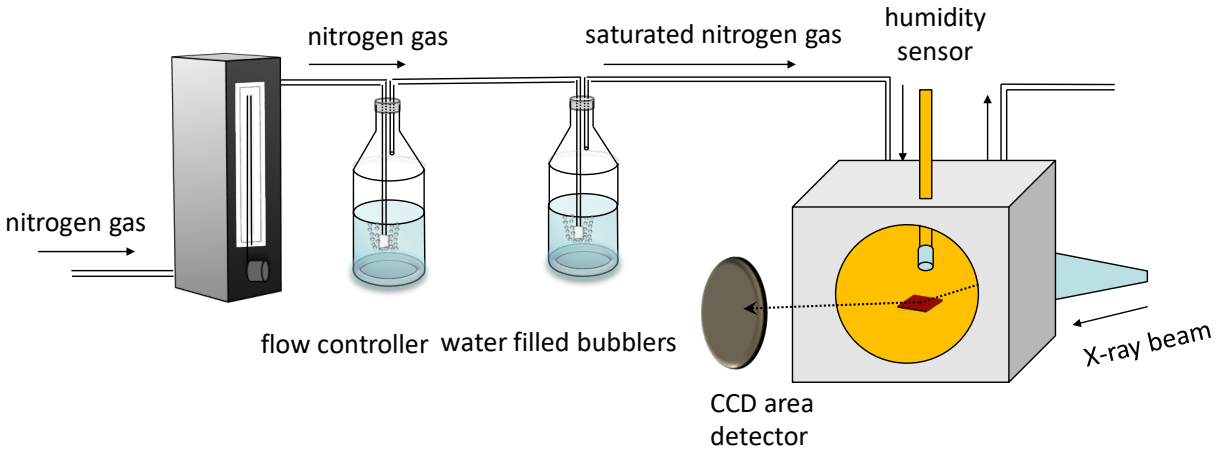

Figure 4.1 Schematic illustration of the RH control setup to control the chamber humidity.

4.2.3.3. Data Processing

The 2D GIWAXS patterns were processed using the GIXSGUI[214] and Datasqueeze software packages; the patterns were calibrated in Datasqueeze, solid angle corrections applied, and the data reshaped to account for the missing wedge along q_z. Azimuthally-integrated scattering intensities were calculated using the Datasqueeze 3.0 software package; data were azimuthally-integrated

between $-75° \leq \chi \leq 75°$ and 0.3 $Å^{-1} \leq q \leq 2.9$ $Å^{-1}$ in 0.002 $Å^{-1}$ increments. The diffuse background (primarily due to scattering from the glass substrate) was subtracted by fitting to a spline curve.

4.2.3.4. Powder X-ray Diffraction

pXRD was performed on a PANalytical Empyrean diffractometer configured with cobalt (λ = 1.79 Å) x-ray source.

4.3. Results and Discussion

This chapter discusses the decomposition rates and degradation mechanisms of the different perovskite compositions listed in **Figure 4.2**. These include the pure iodides ($MAPbI_3$, $FAPbI_3$, and $CsPbI_3$), pure bromides ($MAPbBr_3$, $FAPbBr_3$, and $CsPbBr_3$) and the mixed perovskite compositions $Cs_{0.1}FA_{0.9}PbI_3$ and $Cs_{0.1}MA_{0.15}FA_{0.75}Pb(Br_{0.15}I_{0.85})_3$. All decomposition studies were carried out on perovskite films made on bare glass substrates.

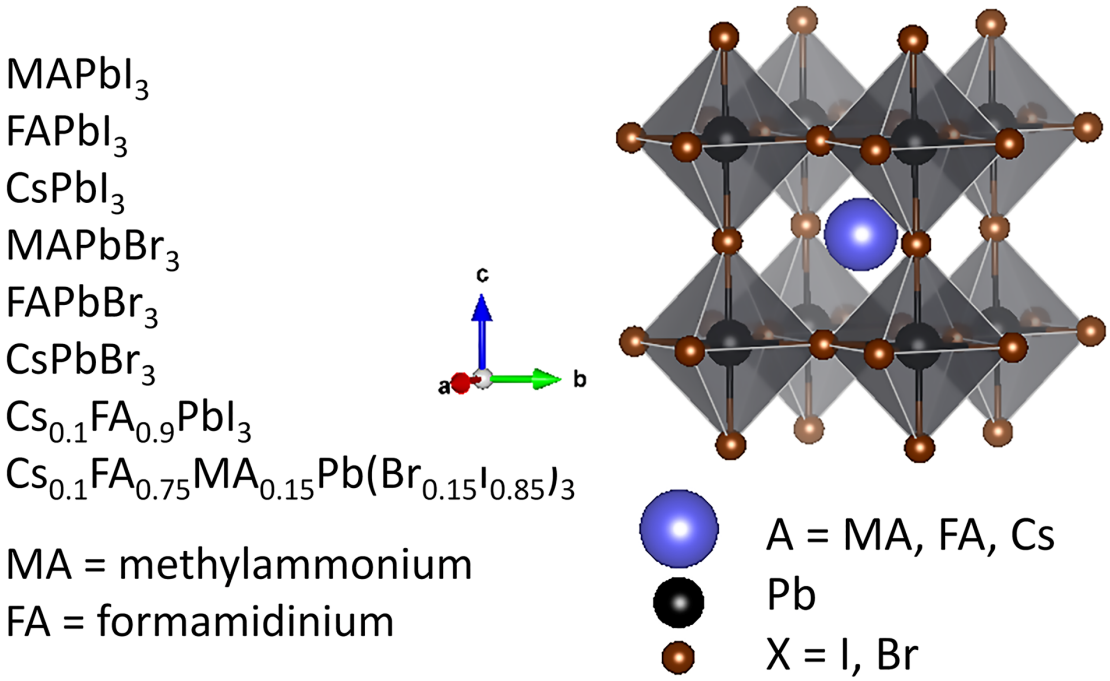

Figure 4.2 Representation of a cubic lead perovskite ($APbX_3$) unit cell and a list of the perovskite compositions studied.

4.3.1. Decomposition Rates of Different Perovskite Compositions

In order to compare and analyze the decomposition rates of different perovskite compositions, in situ UV-visible spectroscopy was used (**Figure 4.3a**).[68, 260] The samples (**Figure 4.3b**) were placed inside a custom-built UV–vis sample holder. Nitrogen gas was allowed to flow at a certain rate (0.25 SLPM) through two mass flow controllers, one of which was connected to two water bubblers. The flow rates were adjusted in such a way so as to produce gas with a fixed RH of 95 ± 5%. The humidity and temperature of the waste gas were measured downstream using a humidity sensor. Absorbance spectra were acquired every 15 min. A representative dataset for $MAPbI_3$ is shown in **Figure 4.3c**. All other spectra are shown in **Figure 4.4**. The normalized absorbance at 500 nm (a wavelength at which all of the perovskites absorb strongly) is plotted as a function of time (**Figure 4.3d**). As the films degrade, the absorbance at 500 nm decreases. The rate of

decomposition is strongly dependent on the composition. Among the different compositions, the iodides appear to be the least stable, followed by the mixed compositions. The bromides tend to be more stable, with $MAPbBr_3$ and $FAPbBr_3$ lasting longer than a week at > 95% RH. Note that the initial absorption spectra of the perovskite films (at t = 0 h) (**Figure 4.4**) are consistent with the literature; the iodides have optical bandgaps near 750-850 nm and the bromides have bandgaps near ~550 nm.[14, 17, 18]

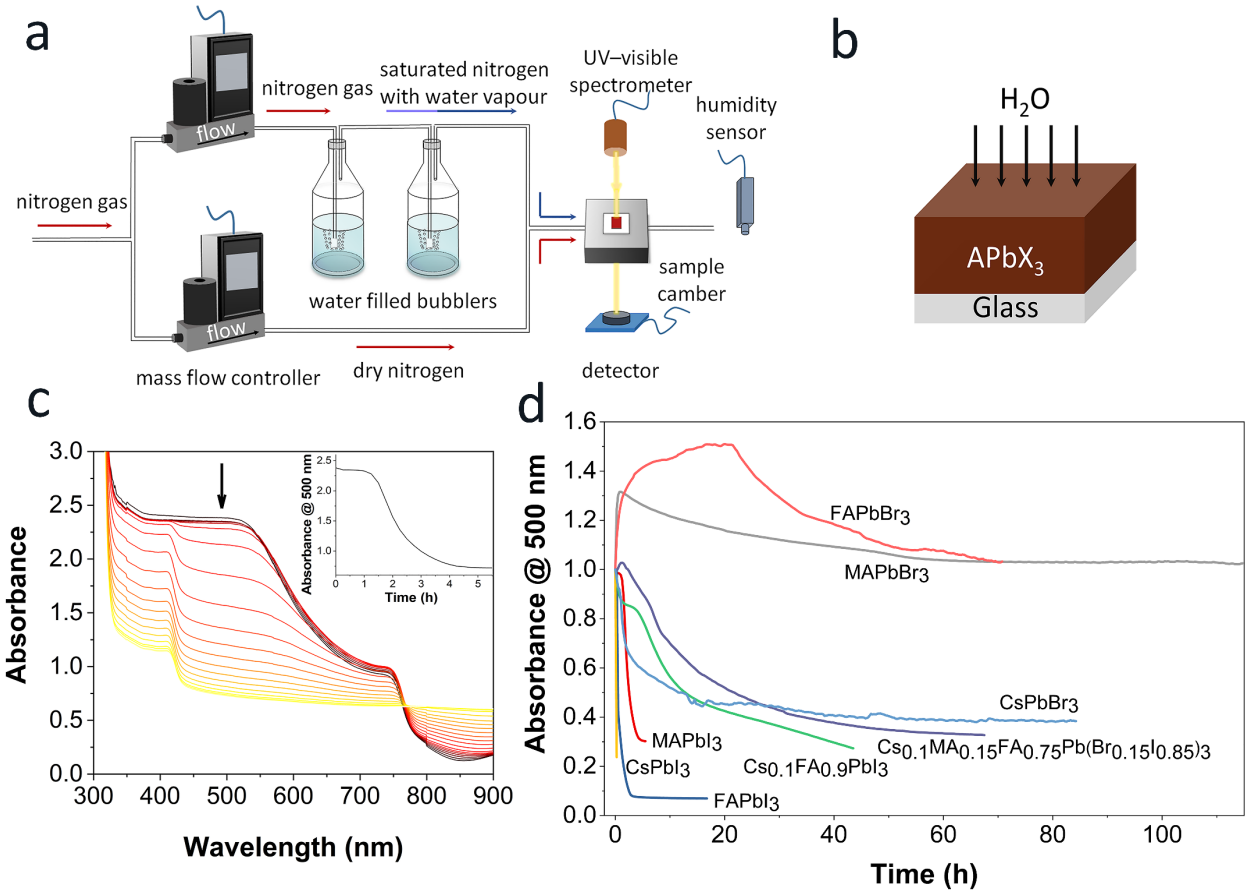

Figure 4.3 (**a**) Schematic representation of experimental setup; (**b**) a schematic representation of the films used for this experiment; (**c**) UV–vis spectra of a $MAPbI_3$ film exposed to flowing N_2 gas with RH = 95 ± 5%, data acquired at 15 min intervals; (**d**) Normalized absorbance at 500 nm as a function of time for perovskite films with different compositions.

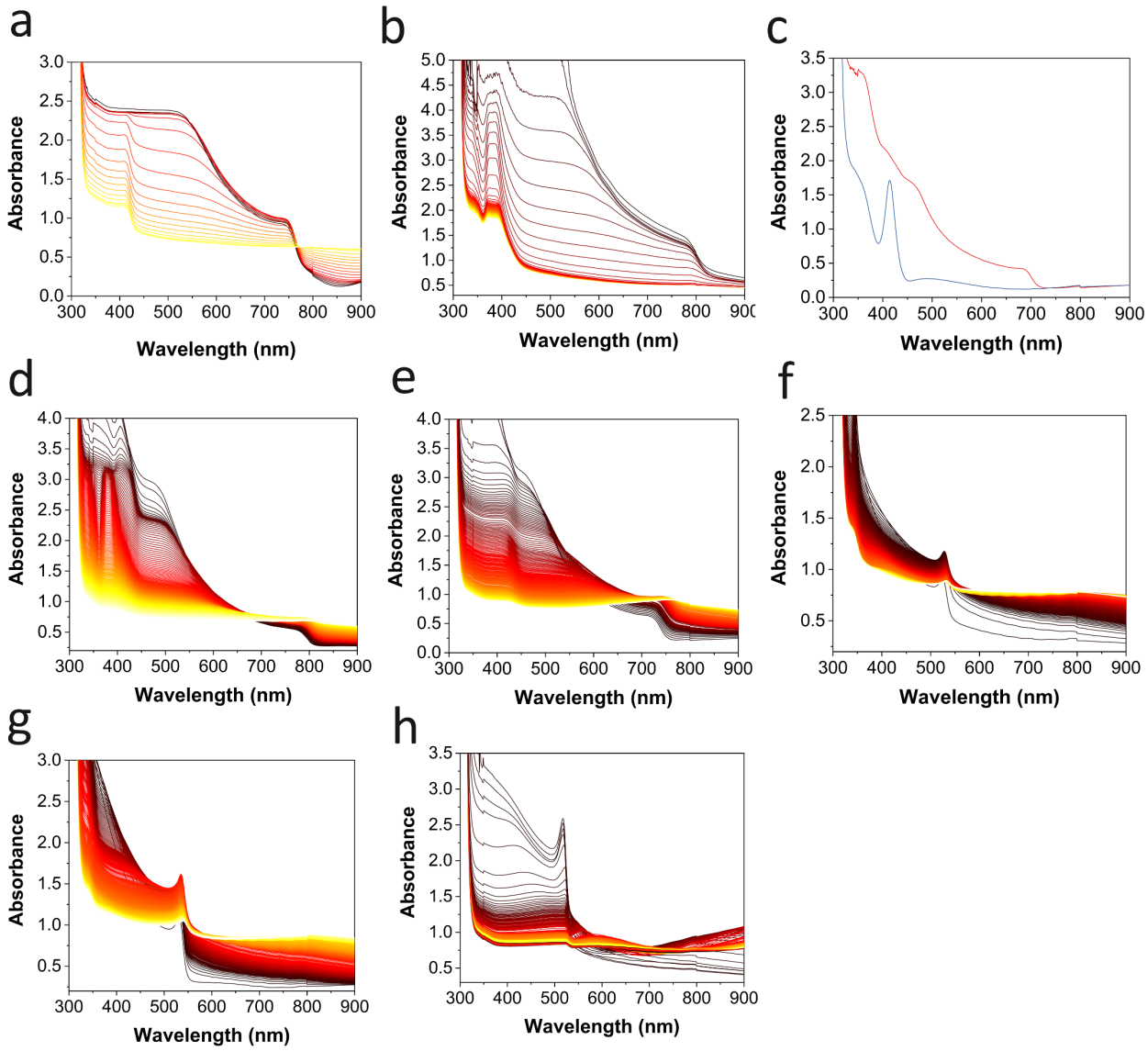

Figure 4.4 UV-vis spectra, acquired at 15 min intervals, of a perovskite thin films exposed to high humidity RH = 95 ± 5%; (**a**) $MAPbI_3$, (**b**) $FAPbI_3$, (**c**) $CsPbI_3$, (**d**) $Cs_{0.1}FA_{0.9}PbI_3$, (**e**) $Cs_{0.1}MA_{0.15}FA_{0.75}Pb(Br_{0.15}I_{0.85})_3$, (**f**) $MAPbBr_3$, (**g**) $FAPbBr_3$, (**h**) $CsPbBr_3$.

In order to quantitatively analyze the rate of decomposition of the perovskite films, the term $\tau_{1/2}$ was defined as the time at which the absorbance of the film becomes half of the initial value. Among the different iodide compositions, $CsPbI_3$ (here, it refers to the black perovskite phase, α-

$CsPbI_3$) is the least stable with a $\tau_{1/2}$ of 0.13 h (**Figure 4.3d**). As soon as it came into contact with moisture it decomposed rapidly. $FAPbI_3$ (i.e. black α-$FAPbI_3$) was more resistant towards moisture-induced decomposition than $CsPbI_3$. The $\tau_{1/2}$ was found to be ca. 0.33 h (**Figure 4.3d**). Among the iodides, $MAPbI_3$ had the slowest decomposition rate with a $\tau_{1/2}$ of 1.8 h (**Figure 4.3d**).

In contrast to pure iodides, the mixed compositions have superior moisture stability. For example, when a small fraction of FA is replaced by Cs ($Cs_{0.1}FA_{0.9}PbI_3$), the stability increases, with $\tau_{1/2} \approx 6$ h (**Figure 4.3d**). Incorporating Cs also helps to stabilize the alpha phase, making it more resistant towards phase change.[269] The stability improves further if bromide is incorporated in the mixed composition. This is evident from the fact that $Cs_{0.1}MA_{0.15}FA_{0.75}Pb(Br_{0.15}I_{0.85})_3$ has a higher $\tau_{1/2}$ value ($\tau_{1/2} \approx 10$ h) (**Figure 4.3d**) than $Cs_{0.1}FA_{0.9}PbI_3$ ($\tau_{1/2} \approx 6$ h).

Among the pure bromide compositions, $CsPbBr_3$ is the least stable with a measured $\tau_{1/2} \approx 2$ h (**Figure 4.3d**). The decomposition rate is similar to the decomposition rate of $MAPbI_3$ ($\tau_{1/2} \approx 1.8$ h). The decomposition kinetics of $MAPbBr_3$ and $FAPbBr_3$ were very similar (**Figure 4.3d**). For $FAPbBr_3$, within a few hours the absorbance at 350-550 nm started to increase (**Figure 4.3d**). This could be an indication of a solvent annealing effect. As moisture penetrates the film, small crystallites join together to form larger ones. At t = 16.75 h, the absorbance below the band edge (350-550 nm) also changed while the band edge remains almost at 550 nm (**Figure 4.5a**). A significant increase in the absorbance post-band edge at 600-850 nm was observed. This could be due to an increase in Mie scattering from larger crystallites. At longer times the absorbance slowly decreases, indicating a slow degradation process. At t = 71 h, the absorbance at 350-550 nm had decreased significantly, whereas the absorbance at 600-900 nm had increased significantly (**Figure 4.5a**). A similar trend was also observed for $MAPbBr_3$. The absorbance increased until t = 0.75 h and then it started to decrease slowly with time (**Figure 4.5b**). At t = 114.75 h, the absorbance at

350-550 nm decreased significantly indicating decomposition of $MAPbBr_3$ (**Figure 4.5b**). The post-band edge absorbance at 550-900 nm increased significantly indicating significant amount of Mie scattering (**Figure 4.5b**).

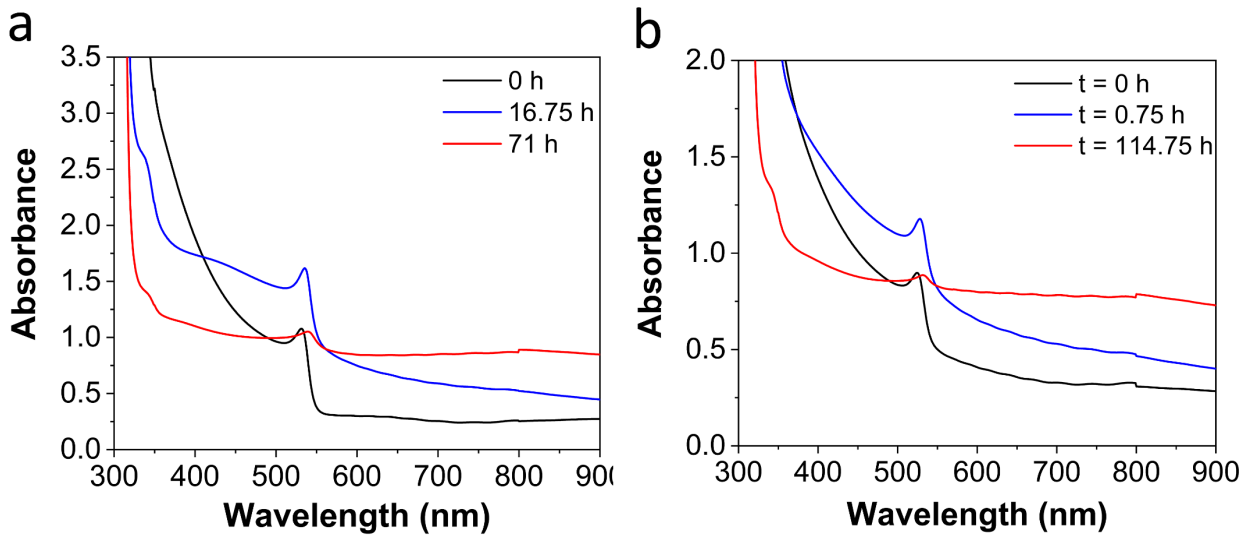

Figure 4.5 (**a**) Absorption spectra of a $FAPbBr_3$ thin film on glass: as-prepared (black line), after exposure to high relative humidity (RH = 95 ± 5%) for 16.75 hours (blue line) and after 71 hours (red line); (**b**) absorption spectra of a $MAPbBr_3$ thin film on glass: as-prepared (black line), after exposure to high relative humidity (RH = 95% ± 5%) for 0.75 hours (blue line) and 114.75 hours (red line).

4.3.2.Degradation Mechanisms of Different Perovskite Compositions

In order to record and analyze the structural and phase changes occurring during perovskite degradation processes, in situ GIWAXS was used. The in situ GIWAXS experimental setup has been previously reported by our group.[224] A custom-built gas tight chamber equipped with a flange-mounted RH sensor and connected to two water bubblers was used. An x-ray flight tube and Kapton window allowed for simultaneous acquisition of GIWAXS data. The RH was controlled by controlling the ratio of dry and wet nitrogen. A high RH (90 ± 5%) was used unless otherwise stated. The flow rate (5 SLPM) was kept constant throughout the experiment. GIWAXS

patterns were acquired at 30-120 s intervals using fast shutters and a 1-10 s acquisition time depending upon the rate of decomposition and scattering intensity. The experiments were carried out at the Hard X-ray MicroAnalysis (HXMA) beamline of the Canadian Light Source. The high x-ray flux of the synchrotron facility and the fast response of a CCD area detector allow better and faster data acquisition in real-time.

4.3.2.1. $MAPbI_3$

The $MAPbI_3$ film was placed inside a sample chamber which was flooded with humid nitrogen (90 ± 5%). The GIWAXS data was acquired in situ every 120 s. The initial diffraction pattern (t = 0 h) of $MAPbI_3$ had peaks at $q \approx 1.0$, 1.4, 1.68, 1.73, 2.02, 2.26, 24.8, 2.87, and 3.02 $Å^{-1}$ (**Figure 4.6**), consistent with reflections from the tetragonal phase of pure $MAPbI_3$ (**Figure 4.7a-b**). As the film was exposed to high humidity, additional diffraction rings began to appear. At t = 0.3 h rings at $q \approx 0.9$ and 2.8 $Å^{-1}$ started to grow which could be assigned to reflections from the (001) and $(2\bar{1}0)$ planes of PbI_2 (**Figure 4.7a-b**). At t = 1.1 h, two prominent peaks were observed at low diffraction angles (ca. $q \approx 0.6$ and 0.74 $Å^{-1}$) (**Figure 4.7b**). These peaks indicate the formation of the monohydrate phase, $MAPbI_3 \cdot H_2O$ by intercalation of water in the $MAPbI_3$ lattice.[70] With time the intensity of the monohydrate peaks increased rapidly, while the perovskite decomposed. After 2.1 h the perovskite peaks almost disappeared leaving the monohydrate and PbI_2 as the major products (**Figure 4.7a-b**). Interestingly, the monohydrate appeared to be one of the major products instead of being a metastable intermediate as previous studies showed.[70, 224]

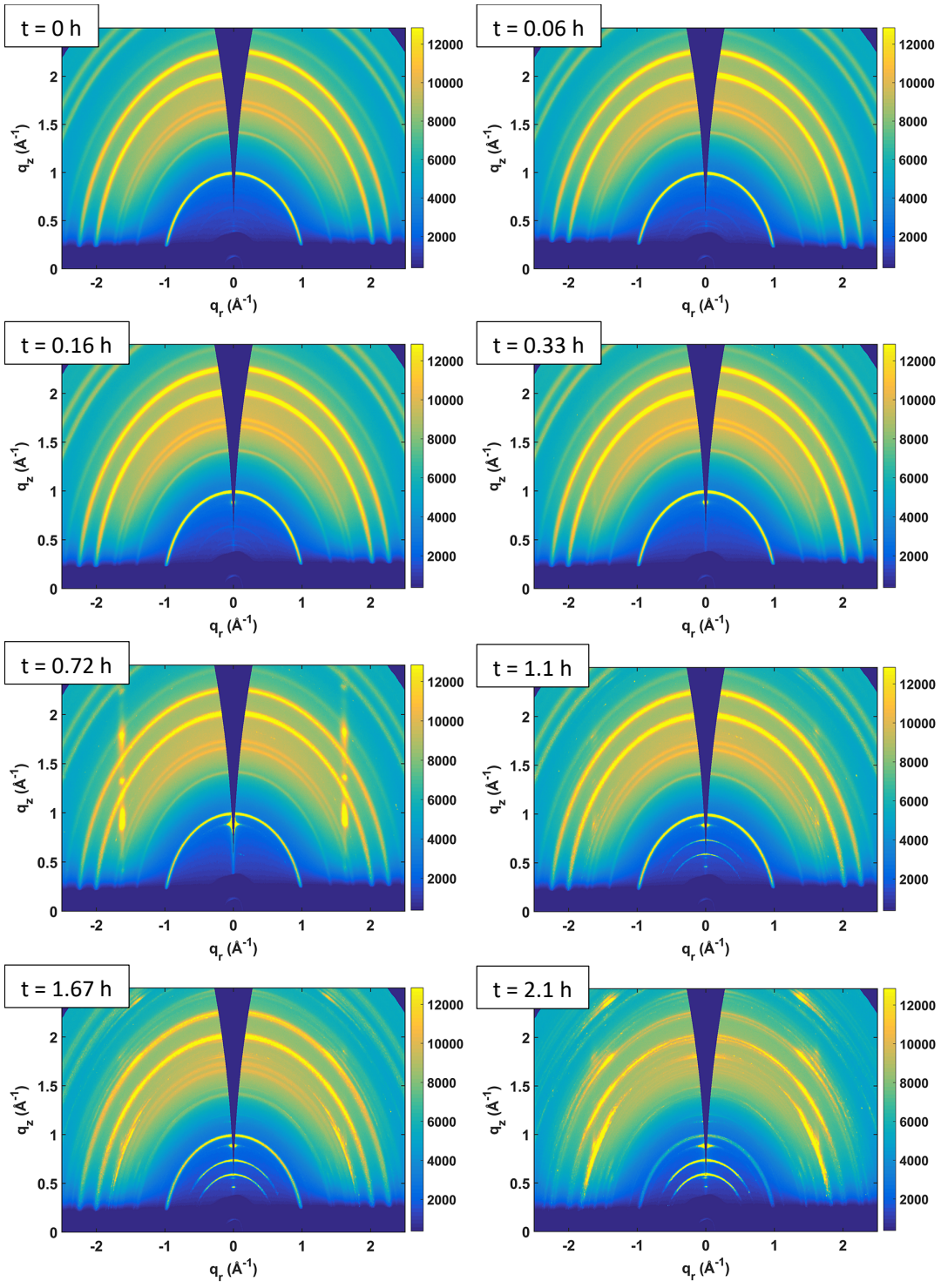

Figure 4.6 2D GIWAXS patterns of $MAPbI_3$ films on glass when exposed to a 90 ± 5% RH environment.

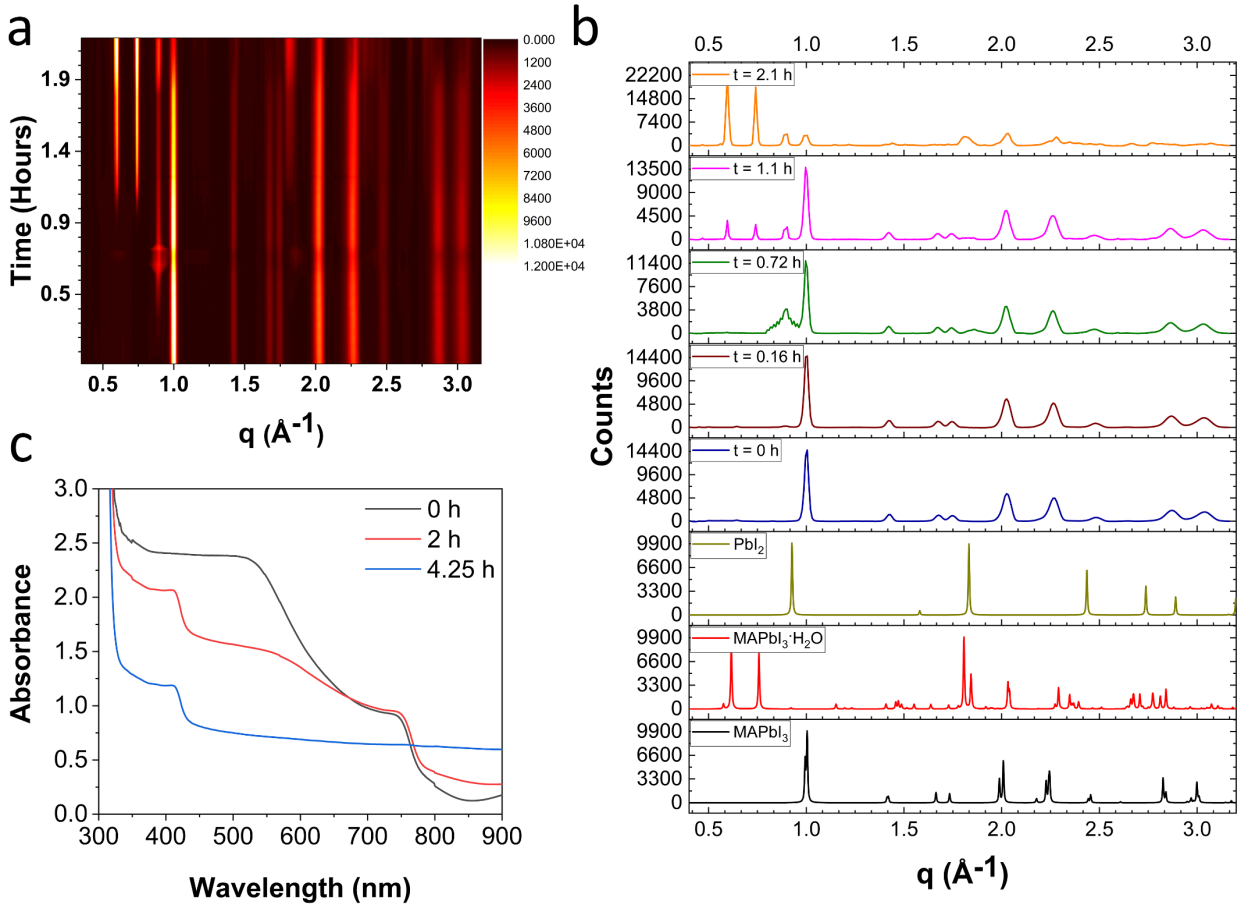

Figure 4.7 Degradation of $MAPbI_3$ film when exposed to 90 ± 5% RH; (**a**) 2D contour plot showing the azimuthally integrated diffraction intensity as a function of both scattering vector (q) and time, (**b**) azimuthally-integrated GIWAXS pattern for $MAPbI_3$ exposed to high humidity (RH 90 ± 5%) at different time compared with predicted pXRD pattern of $MAPbI_3$, $MAPbI_3{\cdot}H_2O$, and PbI_2, and (**c**) absorption spectra of a $MAPbI_3$ thin film on glass: as-prepared (black line), after exposed to high relative humidity (RH = 95%) for 2 hours (red line) or after 4.25 hours (blue line).

This decomposition process can be visualized using a 2D contour plot, which is the azimuthally-integrated diffraction intensity as a function of both scattering vector (q) and time (**Figure 4.7a**).

The in situ UV-visible spectroscopy data supports these conclusions. At t = 2 h, the absorbance had decreased significantly in the 450-760 nm region, while the band edge characteristic was still intact (**Figure 4.7c**). However, the band edge completely disappeared at t = 4.25 h, with a flat

baseline from 450-760 nm (**Figure 4.7c**). The absorbance at 350-450 nm matched the spectrum of PbI_2, indicating PbI_2 as one of the major decomposition products (**Figure 4.7c**).

4.3.2.2. $FAPbI_3$

The $FAPbI_3$ film was placed inside a sample chamber which was flooded with humid nitrogen (90 ± 5%). The GIWAXS data was acquired in situ every 60 s. The initial GIWAXS pattern (at t = 0 h) had peaks at $q \approx$ 1.0, 2.0, 2.3, 2.7, and 3.0 $Å^{-1}$ (**Figure 4.8**). These indicate the pure α-$FAPbI_3$ cubic phase, consistent with reflection from (100), (110), (111), (200), and (210) lattice planes, respectively (**Figure 4.9b**). As soon as humidity was introduced, new rings started to appear. At t = 0.04 h peaks for δ-$FAPbI_3$ and PbI_2 were be observed. The diffraction rings at $q \approx$ 0.84, 1.16, 1.46, 1.62, 1.79, 1.86, 2.15, 2.23, 2.31, 2.44, 2.54, and 2.72 $Å^{-1}$ correspond to δ-$FAPbI_3$ while the rings at $q \approx$ 0.8 and 2.8 $Å^{-1}$ are from PbI_2 (**Figure 4.9b**). With time the intensity of the rings corresponding to the δ-phase increased, whereas a serious drop in the intensity of the α-$FAPbI_3$ rings was observed (**Figure 4.9b**). At t = 0.28 h, α-$FAPbI_3$ mostly converted into δ-$FAPbI_3$ with the formation of a small amount of PbI_2 as one of the decomposed products (**Figure 4.9b**). When black $FAPbI_3$ is subjected to ~ 90% RH it started to decompose faster than $MAPbI_3$, as observed previously by in situ UV-vis spectroscopy. It took only a few minutes to decompose (**Figure 4.9a-b**).

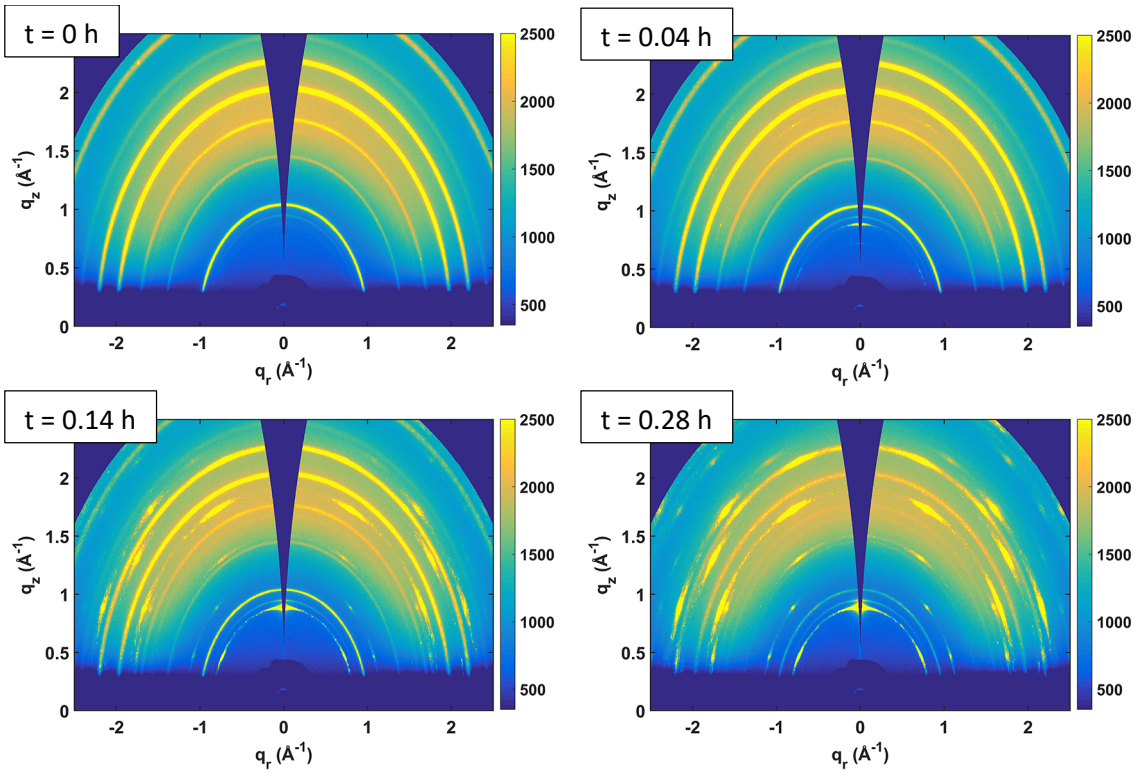

Figure 4.8 2D GIWAXS patterns of $FAPbI_3$ films on glass when exposed to a 90 ± 5% RH environment.

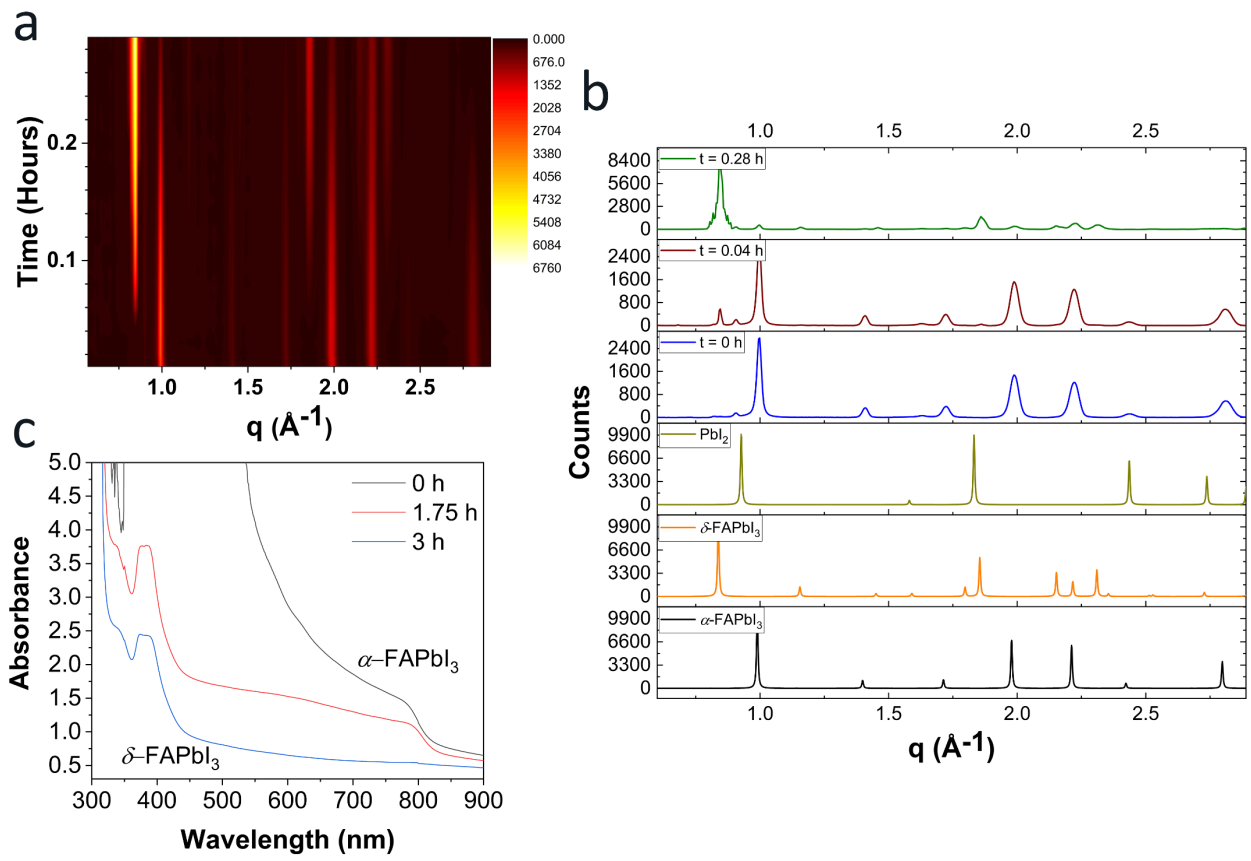

Figure 4.9 Degradation of $FAPbI_3$ film when exposed to 90 ± 5% RH; (**a**) 2D contour plot showing the azimuthally integrated diffraction intensity as a function of both scattering vector (q) and time, (**b**) azimuthally-integrated GIWAXS pattern for $FAPbI_3$ exposed to high humidity (RH = 90 ± 5%) at different time compared with predicted pXRD pattern of α and δ-$FAPbI_3$, and PbI_2, (**c**) absorption spectra of a $FAPbI_3$ thin film on glass: as-prepared (black line), after exposed to high relative humidity (RH ≈ 95%) for 1.75 hours (red line) or after 3 hours (blue line).

Similar observations were found using in situ UV-vis spectroscopy. At t = 0 h, the characteristic absorbance spectrum of α-$FAPbI_3$ can be observed.[136] At intermediate times (t = 1.75 h) the spectrum mostly resembles that of δ-$FAPbI_3$, except it still has the band edge around 800 nm (**Figure 4.9c**). At t = 3 h, the band edge at 800 nm completely disappeared and there is no absorbance between 450-800 nm (**Figure 4.9c**). At this point, only the characteristic absorbance for δ-$FAPbI_3$ could be observed, which matches with the literature.[136]

From the decomposition process it is quite obvious that the black cubic α-$FAPbI_3$ is meta-stable at room temperature. It slowly transforms from the alpha phase to the delta phase to release the inbuilt lattice strain. The lattice strain originates from a higher tolerance factor caused by the larger FA cation.[136] External stimuli like moisture catalyze this phase transfer process by decreasing the activation energy for this phase change. The effect of moisture can possibly be rationalized as following. Frist, moisture infiltrates through the grain boundary of α-$FAPbI_3$. Then it solvates α-$FAPbI_3$ which results in increasing ion diffusion, allowing the lattice to rearrange to relieve strain. When pure α-$FAPbI_3$ is subjected to a humid environment, the phase transfer from $\alpha \rightarrow \delta$ can be observed (**Figure 4.9a**).

4.3.2.3. $CsPbI_3$

The $CsPbI_3$ films were placed inside a sample chamber with high RH (90 ± 5%). GIWAXS data was acquired every 60 s (**Figure 4.10**). As with $FAPbI_3$, a phase change was observed for $CsPbI_3$ as it is subjected to high humidity. The cubic α-$CsPbI_3$ to orthorhombic δ-$CsPbI_3$ transition takes place much faster than that of $FAPbI_3$. The initial diffraction pattern (t = 0 h) had peaks at $q \approx$ 1.0, 1.4, 1.7, 2.0, 2.23, 2.33, 2.5 and 2.85 $Å^{-1}$ for α-$CsPbI_3$ (**Figure 4.11a-b**). In order to make these measurements, the samples were carried from the lab to the CLS and stored outside for hours in a desiccator. The samples also took several minutes to load and to set up the initial scans. It is possible in that time the highly sensitive α-$CsPbI_3$ started to decompose which is reflected in the diffraction pattern. That is why additional rings were observed at $q \approx$ 1.14, 1.47, 1.59, 1.63, 1.78, 1.88, 1.91, 1.97, 2.33, and 2.4 $Å^{-1}$ (**Figure 4.11b**). As soon as the humidity of the chamber was turned on, new rings appeared in the diffraction pattern (**Figure 4.10-11**). The new peaks at $q \approx$

0.71, 0.93, 1.2, 1.21, 1.25, 1.54, 1.6, 1.77, 1.79, 1.81, 1.86, 1.91, 2.19, 2.31, 2.44, 2.64, and 2.84 $Å^{-1}$ appeared at t = 0.02 h which correspond to δ-$CsPbI_3$ (**Figure 4.10-11**).

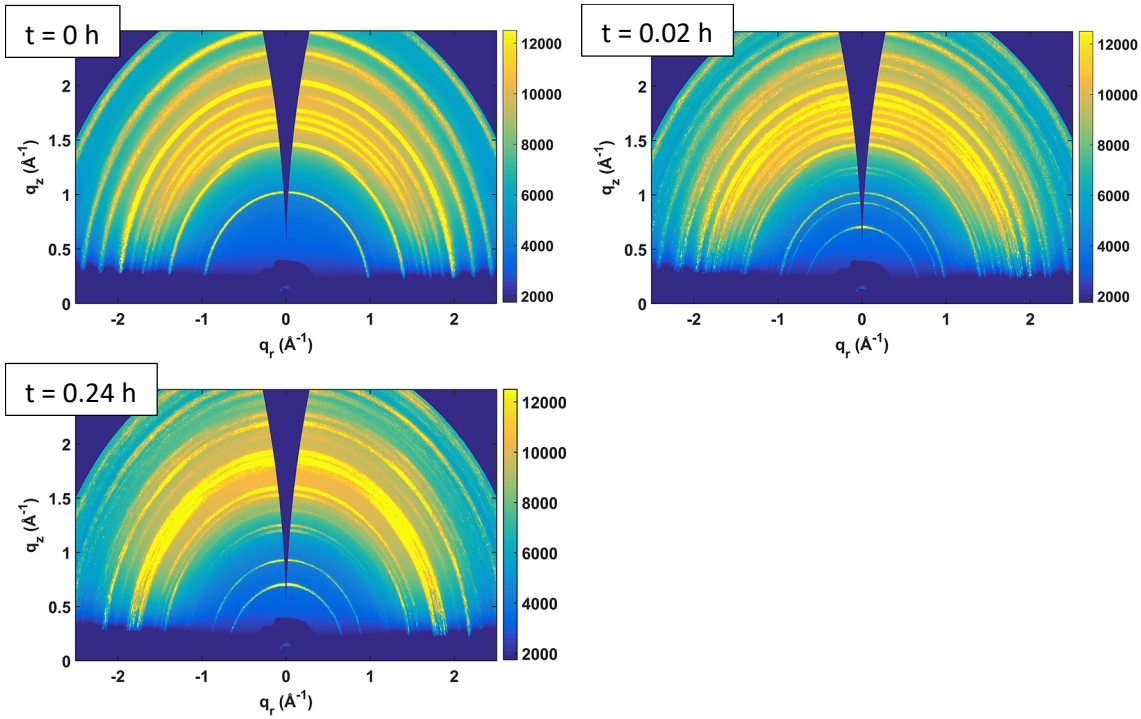

Figure 4.10 2D GIWAXS patterns of $CsPbI_3$ films on glass, after 0 h, 0.02 h, and 0.24 h exposure to a 90 ± 5% RH environment.

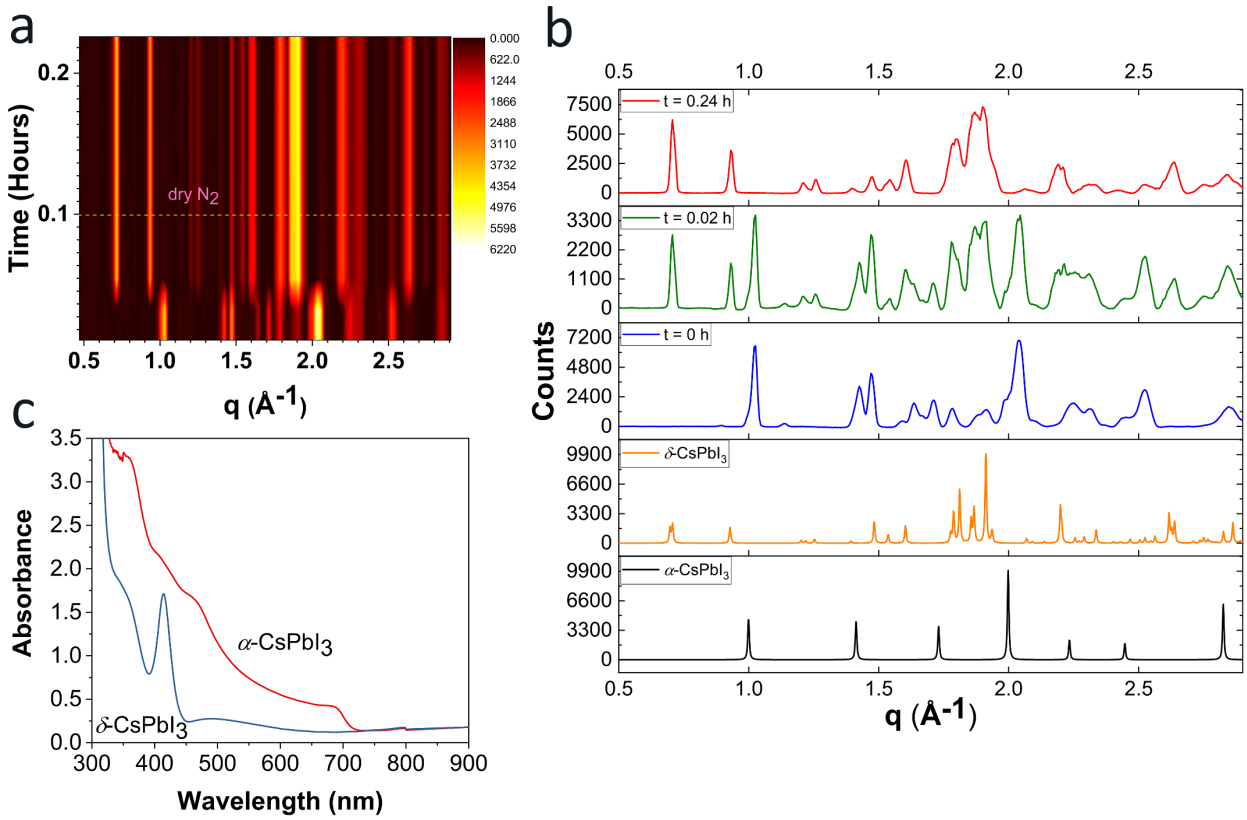

Figure 4.11 Degradation of $CsPbI_3$ film when exposed to 90 ± 5% RH; (**a**) 2D contour plot showing the azimuthally integrated diffraction intensity as a function of both scattering vector (q) and time, (**b**) azimuthally-integrated GIWAXS pattern for $CsPbI_3$ exposed to high humidity (RH 90 ± 5%) at different time compared with predicted pXRD pattern of α and δ-$CsPbI_3$, (**c**) UV-vis spectra, acquired at 15 min intervals, of a $CsPbI_3$ film exposed to high humidity RH = 95 ± 5%; red line as prepared and blue line after 15 minutes.

The rings appeared to be broader indicating the formation of less-ordered powder-like decomposition products (**Figure 4.10**). This $\alpha \rightarrow \delta$ transition took place within a few seconds (**Figure 4.10-11**). Additionally, a trace amount of PbI_2 was found. Mostly the diffraction peaks of PbI_2 overlap with those of δ-$CsPbI_3$, which makes the analysis difficult. The rings at $q \approx 0.93$, 1.86, and 2.44 $Å^{-1}$ match the reflections from PbI_2 (**Figure 4.11b**). Mostly, the ring at $q \approx 2.44$ $Å^{-1}$ stands out as it corresponds to neither the α nor the δ phase of $CsPbI_3$ (**Figure 4.11b**). Within a few

seconds, at t = 0.03 h, the α-$CsPbI_3$ completely disappeared leaving only the δ-$CsPbI_3$, as the major decomposed product accompanied by a trace amount of PbI_2 (**Figure 4.11a**). To study the effect of drying on the decomposition, the chamber was flushed with dry nitrogen for 0.14 h after the decomposition (t = 0.1 h); no change was observed either in the ring intensity or in the diffraction pattern. This suggests that decomposition process is irreversible (**Figure 4.11a**).

To study the moisture-triggered phase transfer process further, an additional experiment was conducted. To eliminate other parameters, first, the chamber was flushed with dry nitrogen for 0.06 h while the GIWAXS pattern of a fresh sample was recorded at 5 s intervals. No change in the diffraction pattern was observed (**Figure 4.12**). When the chamber was flooded with humid nitrogen, within a few seconds (ca. 10 s), the intensity of the δ-$CsPbI_3$ rings started to increase. Within 60 s of turning on the humidity, the α-$CsPbI_3$ completely converted into δ-$CsPbI_3$. This rapid $\alpha \rightarrow \delta$ phase transformation is supported by the in situ UV-vis study (**Figure 4.11c**). The initial absorbance spectrum of α-$CsPbI_3$ matches with the literature.[270] As soon as the humidity was introduced, it decomposed to δ-$CsPbI_3$ which was seen in the next scan (t = 15 minutes).

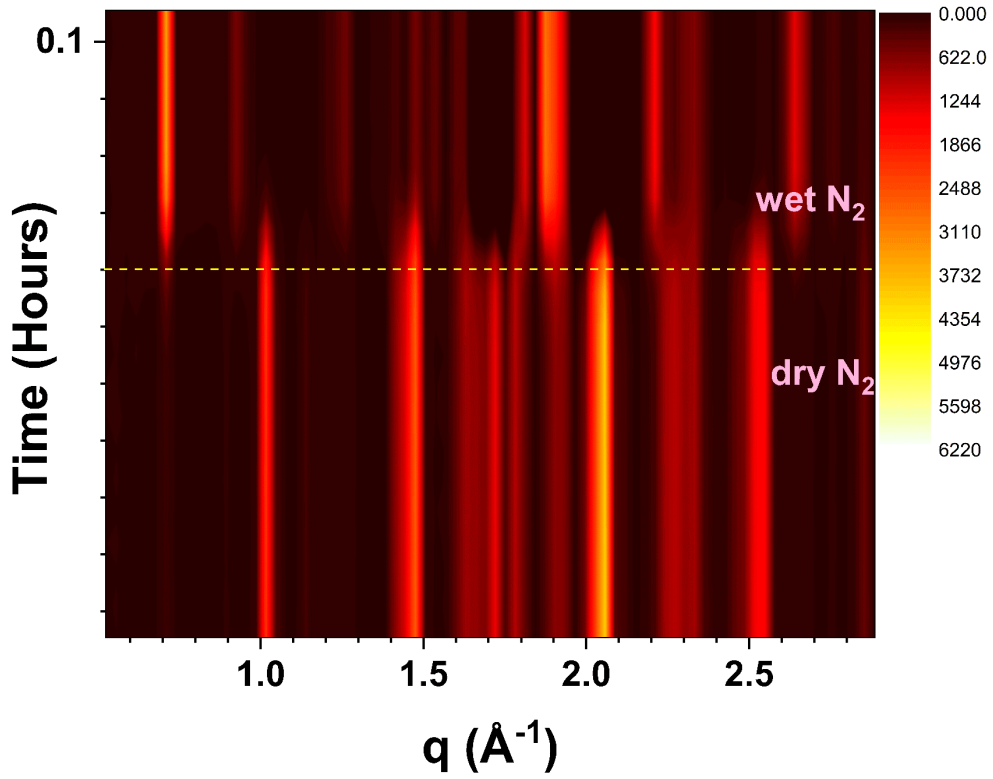

Figure 4.12 2D contour plot showing the azimuthally integrated diffraction intensity as a function of both scattering vector (q) and time of $CsPbI_3$.

4.3.2.4. $Cs_{0.1}FA_{0.9}PbI_3$

The $Cs_{0.1}FA_{0.9}PbI_3$ film was placed inside a sample chamber with high RH (90 ± 5%). The GIWAXS data was acquired in situ every 120 s. The initial pattern (t = 0 h) had peaks at $q \approx 1.0$, 1.42, 1.73, 2.0, 2.24, 2.44, and 2.83 $Å^{-1}$ from α-$Cs_{0.1}FA_{0.9}PbI_3$ (**Figure 4.13-4.14**). As soon as the film came into contact with humid nitrogen (t = 0.037 h), additional peaks started to appear. The peaks at $q \approx 0.93$ and 1.83 $Å^{-1}$ (**Figure 4.13** and **4.14b**) correspond to PbI_2 and the peaks at $q \approx$ 0.56 and 0.68 $Å^{-1}$ may be due to the formation of hydrate phases. With time the amount of PbI_2 kept on increasing. Interestingly, the intensity of the perovskite (α-$Cs_{0.1}FA_{0.9}PbI_3$) increased and reached its highest value at t = 0.558 h. This may be attributed to the solvent annealing effect by water vapor which helps to grow larger size crystallites. At this point minimal amount of perovskite

decomposition had occurred and negligible PbI_2 was present. The results suggest that 0.5 h annealing at high humidity might be actually beneficial for $Cs_{0.1}FA_{0.9}PbI_3$ based PSCs.

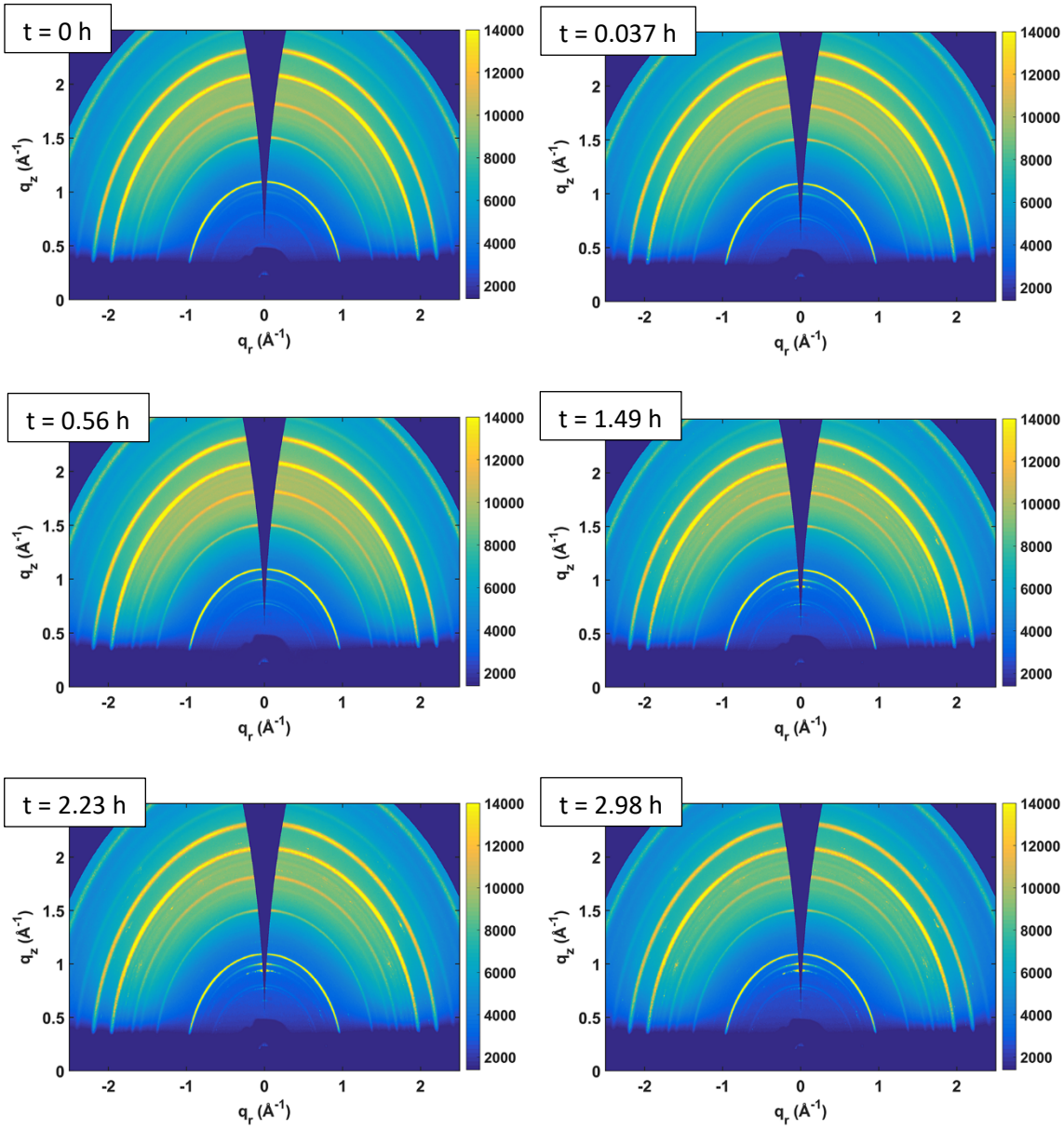

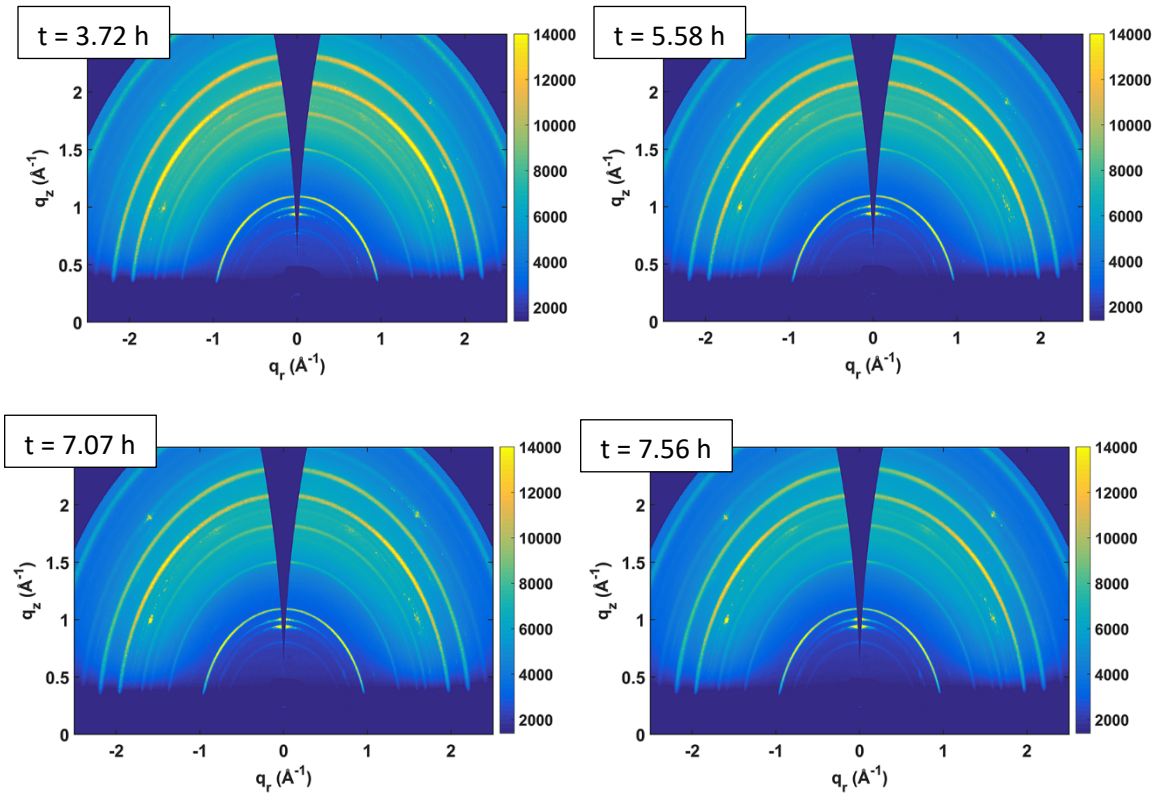

Figure 4.13 2D GIWAXS patterns of $Cs_{0.1}FA_{0.9}PbI_3$ films on glass, after 0 h, 0.037 h, 0.56 h, 1.49 h, 2.23 h, 2.98, 3.72 h, 5.58 h, 7.07 h, and 7.56 h exposure to a 90 ± 5% RH environment.

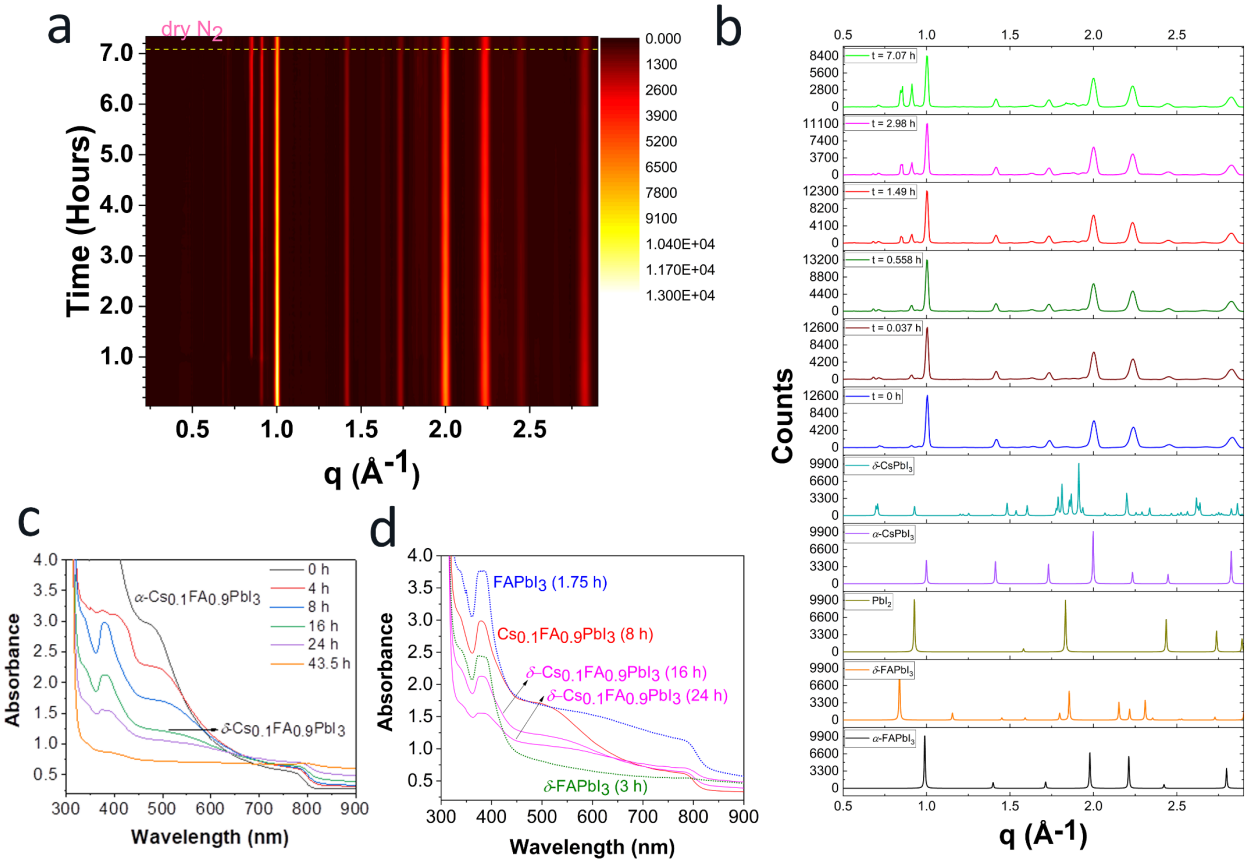

Figure 4.14 Degradation of $Cs_{0.1}FA_{0.9}PbI_3$ film when exposed to 90 ± 5% RH; (**a**) 2D contour plot showing the azimuthally integrated diffraction intensity as a function of both scattering vector (q) and time, (**b**) azimuthally-integrated GIWAXS pattern for $Cs_{0.1}FA_{0.9}PbI_3$ exposed to high humidity (RH 90 ± 5%) at different time compared with predicted pXRD pattern of α and δ-$FAPbI_3$ and α and δ-$CsPbI_3$, and PbI_2, (**c**) absorption spectra of a $Cs_{0.1}FA_{0.9}PbI_3$ thin film on glass: as-prepared (black line), after exposed to high relative humidity (RH ≈ 95%) for 4 hours (red line), after 8 hours (blue line), after 16 hours, (green line) after 24 hours (purple line) and after 43.5 hours (orange line), (**d**) absorption spectra of a $Cs_{0.1}FA_{0.9}PbI_3$ thin film on glass fitted to $FAPbI_3$ (after 1.75 h, blue dotted line) and δ-$FAPbI_3$ (after 3 h, olive dotted line); $Cs_{0.1}FA_{0.9}PbI_3$ thin film after exposed to high relative humidity (RH ≈ 95%) for 8 hours (red solid line), 16 h or 24 h (magenta solid line).

The diffraction peaks ($q \approx 0.85$ Å^{-1}) for δ-$Cs_{0.1}FA_{0.9}PbI_3$ started to appear at $t = 0.558$ h and the intensity kept on increasing (**Figure 4.14b**). However, the intensity of the rings at $q \approx 0.56$ and 0.68 Å^{-1} slowly started to decrease and at $t = 7.07$ h they almost disappeared (**Figure 4.14b**), consistent with our hypothesis of a transient hydrate phase. PbI_2 and δ-$Cs_{0.1}FA_{0.9}PbI_3$ were the major decomposed products of α-$Cs_{0.1}FA_{0.9}PbI_3$.

The chamber was flushed with dry nitrogen for 0.5 h to study the reversibility of the decomposition process. As soon as dry nitrogen was introduced the peaks at lower diffraction angle started to disappear (**Figure 4.15**). After 0.5 h of drying, the peaks at $q \approx 0.56$ and 0.68 Å^{-1} completely disappeared, suggesting the metastable nature of this compound (**Figure 4.13**). The intensity of the PbI_2 and δ-$Cs_{0.1}FA_{0.9}PbI_3$ peaks decreased with an increase in the intensity of the α-$Cs_{0.1}FA_{0.9}PbI_3$ peaks (**Figure 4.15**). This suggests the reversibility of the decomposition process upon drying. In contrast with the decomposition process of $FAPbI_3$, the decomposition mechanism of $Cs_{0.1}FA_{0.9}PbI_3$ is reversible.

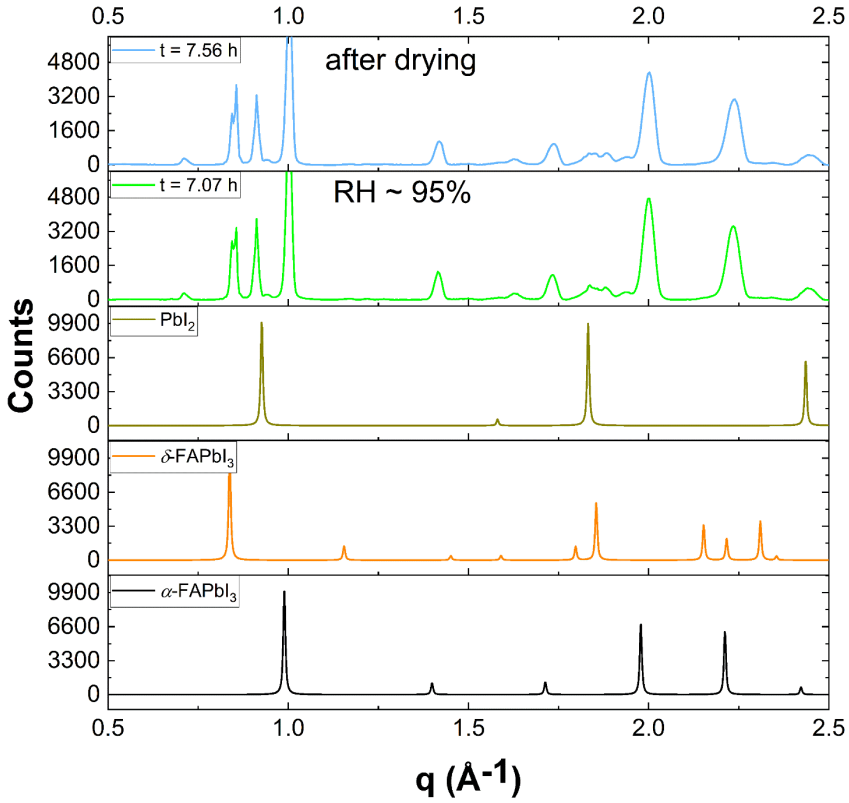

Figure 4.15 Azimuthally-integrated GIWAXS pattern for $Cs_{0.1}FA_{0.9}PbI_3$ at t = 7.07 h and 7.56 h compared with predicted pXRD patterns of α-$FAPbI_3$, δ-$FAPbI_3$, and PbI_2.

The decomposition process of $Cs_{0.1}FA_{0.9}PbI_3$ (mainly $\alpha \rightarrow \delta$ phase transformation) was also supported by in situ UV-vis spectroscopy. The initial absorption spectrum of $Cs_{0.1}FA_{0.9}PbI_3$ matches that of the α-phase. With time the absorption below 450 nm started to change and looked more similar to the δ-phase of $Cs_{0.1}FA_{0.9}PbI_3$ (**Figure 4.14c-d**). The absorbance at t = 16 h closely matches the spectrum of δ-$FAPbI_3$, indicating a complete $\alpha \rightarrow \delta$ transition (**Figure 4.14d**). Upon further exposure to high humidity, the δ-phase decomposed to other products, as evident by a loss of absorbance in the 350-450 region (**Figure 4.14c**). At t = 43.5 h, only a baseline was seen indicating complete decomposition of the δ-phase (**Figure 4.14c**). The mixed $Cs_{0.1}FA_{0.9}PbI_3$

perovskite is more resistant towards moisture compared to pure $FAPbI_3$ and $CsPbI_3$. This is mainly attributed to a decrease in lattice strain.[135]

4.3.2.5. $Cs_{0.1}MA_{0.15}FA_{0.75}Pb(Br_{0.15}I_{0.85})_3$

Among the different perovskite compositions, incorporating three cations (i.e., Cs, MA, FA) in a mixed lead bromide iodide system (for example, $Cs_{0.1}MA_{0.15}FA_{0.75}Pb(Br_{0.15}I_{0.85})_3$) has proven to be most effective at producing high performing devices.[141, 271] As claimed by earlier studies, this type of mixed composition has a longer lifetime.[272] However, when $Cs_{0.1}MA_{0.15}FA_{0.75}Pb(Br_{0.15}I_{0.85})_3$ was subjected to high humidity it started to decompose (**Figure 4.16-4.17**). Initial (t = 0 h) diffraction peaks at $q \approx 1.0$, 1.44, 1.76, 2.02, 2.26, 2.48, and 2.86 $Å^{-1}$ corresponded to the perovskite phase of $Cs_{0.1}MA_{0.15}FA_{0.75}Pb(Br_{0.15}I_{0.85})_3$ (**Figure 4.16-4.17**). Within a few minutes, a peak started to grow at $q \approx 0.82$ $Å^{-1}$, which may correspond to the δ-phase. After 1 h a significant amount of PbI_2 ($q \approx 0.91$ and 1.83 $Å^{-1}$) and δ-phase ($q \approx 0.82$, 1.29, 1.63, 1.89, and 2.55 $Å^{-1}$) can be observed as major decomposition products. Non-uniform diffraction rings appeared at t = 1 h (**Figure 4.16**), suggesting the formation of large crystallites of PbI_2. With time the diffraction from PbI_2 almost disappeared, suggesting PbI_2 formed as an intermediate in the decomposition process (**Figure 4.17**). To check the reversibility of the decomposition process the chamber was purged with dry nitrogen for 0.1 h. This resulted in a significant decrease in the

intensity of the δ-phase while the intensity of the perovskite peaks increased (**Figure 4.18**). This suggests that the decomposition process is at least partially reversible.

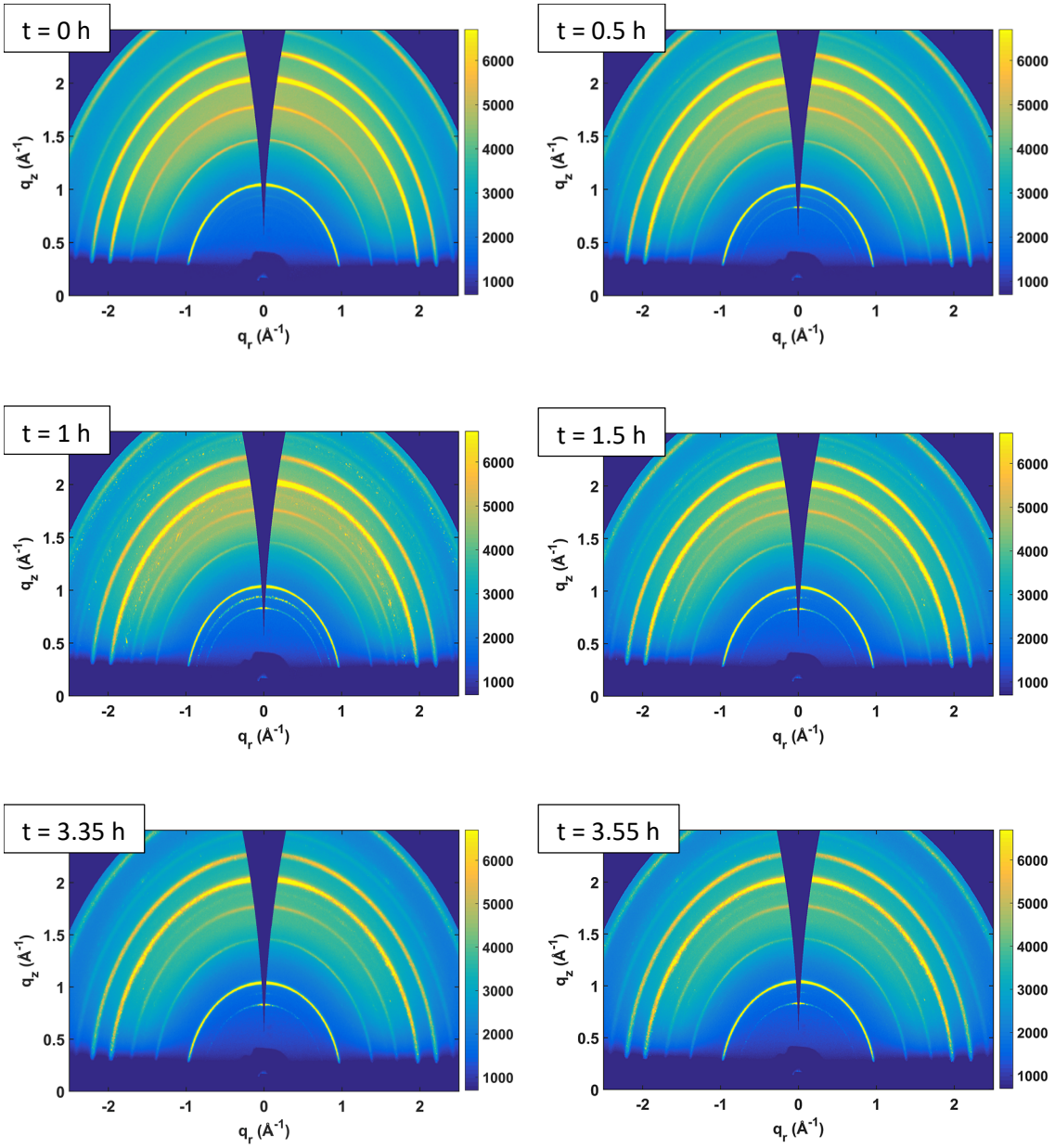

Figure 4.16 2D GIWAXS patterns of $Cs_{0.1}MA_{0.15}FA_{0.75}Pb(Br_{0.15}I_{0.85})_3$ films on glass, at different time when exposed to a 90 ± 5% RH environment.

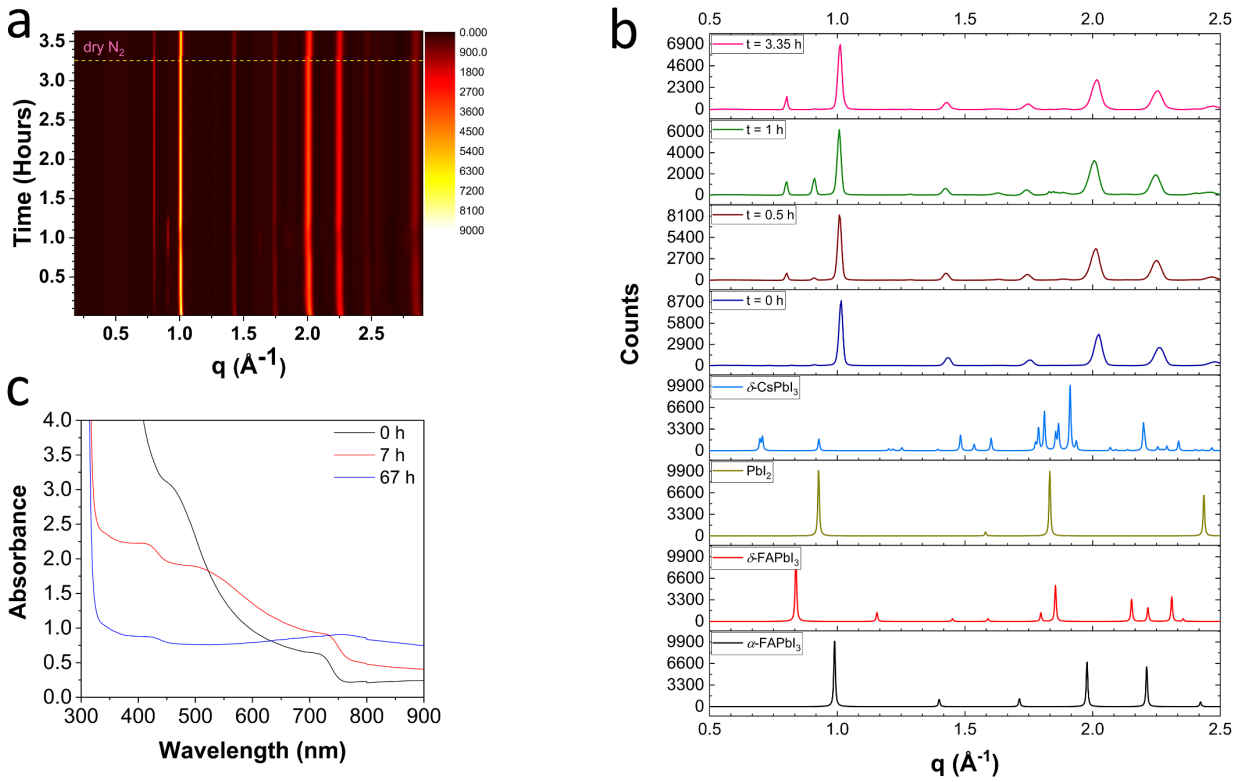

Figure 4.17 Degradation of $Cs_{0.1}MA_{0.15}FA_{0.75}Pb(Br_{0.15}I_{0.85})_3$ film when exposed to 90 ± 5% RH; (**a**) 2D contour plot showing the azimuthally integrated diffraction intensity as a function of both scattering vector (q) and time, (**b**) azimuthally-integrated GIWAXS pattern for $Cs_{0.1}MA_{0.15}FA_{0.75}Pb(Br_{0.15}I_{0.85})_3$ exposed to high humidity (RH 90 ± 5%) at different time compared with predicted pXRD pattern of α and δ-$FAPbI_3$, δ-$CsPbI_3$, and PbI_2, (**c**) UV-vis spectra, acquired at 15 min intervals, at high humidity RH (95 ± 5%); black line as prepared and red line at t = 7 h , and blue line at t = 67 h.

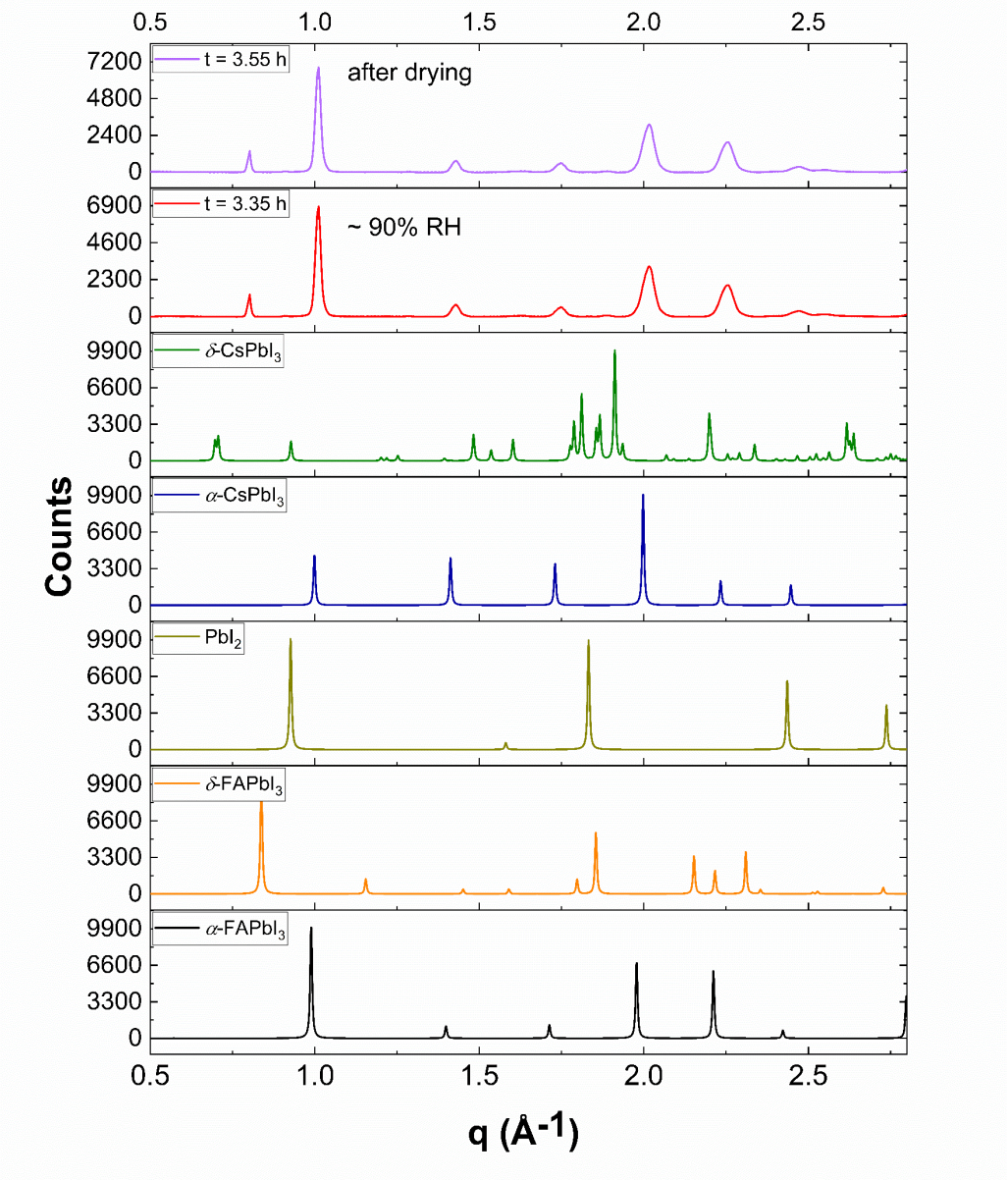

Figure 4.18 Azimuthally-integrated GIWAXS pattern for $Cs_{0.1}MA_{0.15}FA_{0.75}Pb(Br_{0.15}I_{0.85})_3$ at t = 3.25 h and 3.55 h (after drying) compared with predicted pXRD patterns of α-$FAPbI_3$, δ-$FAPbI_3$, PbI_2, and δ-$CsPbI_3$.

When the experiment was repeated with a duplicate sample using the same conditions, a different degradation pathway was observed (**Figure 4.19**). The perovskite formed an intermediate within a few minutes of the introduction of humid nitrogen. At t = 0.18 h peaks appeared at lower

diffraction angles ($q \approx 0.57$ and 0.69 $Å^{-1}$). This might be due to the formation of a hydrate phase, as they do not match with either PbI_2 or the δ-phase (**Figure 4.19**). Then peaks ($q \approx 0.91$ and 1.83 $Å^{-1}$) for PbI_2 started to grow rapidly. At the end of the degradation, PbI_2 was one of the major decomposition product, in contrast to the previously observed pathway (**Figure 4.17**). This decomposition is reversible as after drying the PbI_2 started to convert into the perovskite again (**Figure 4.20**). However, after a certain time (maybe after 1 min) the recovery stopped. No δ-phase was found for this decomposition process which is also supported by UV-vis spectroscopy (**Figure 4.17c**).

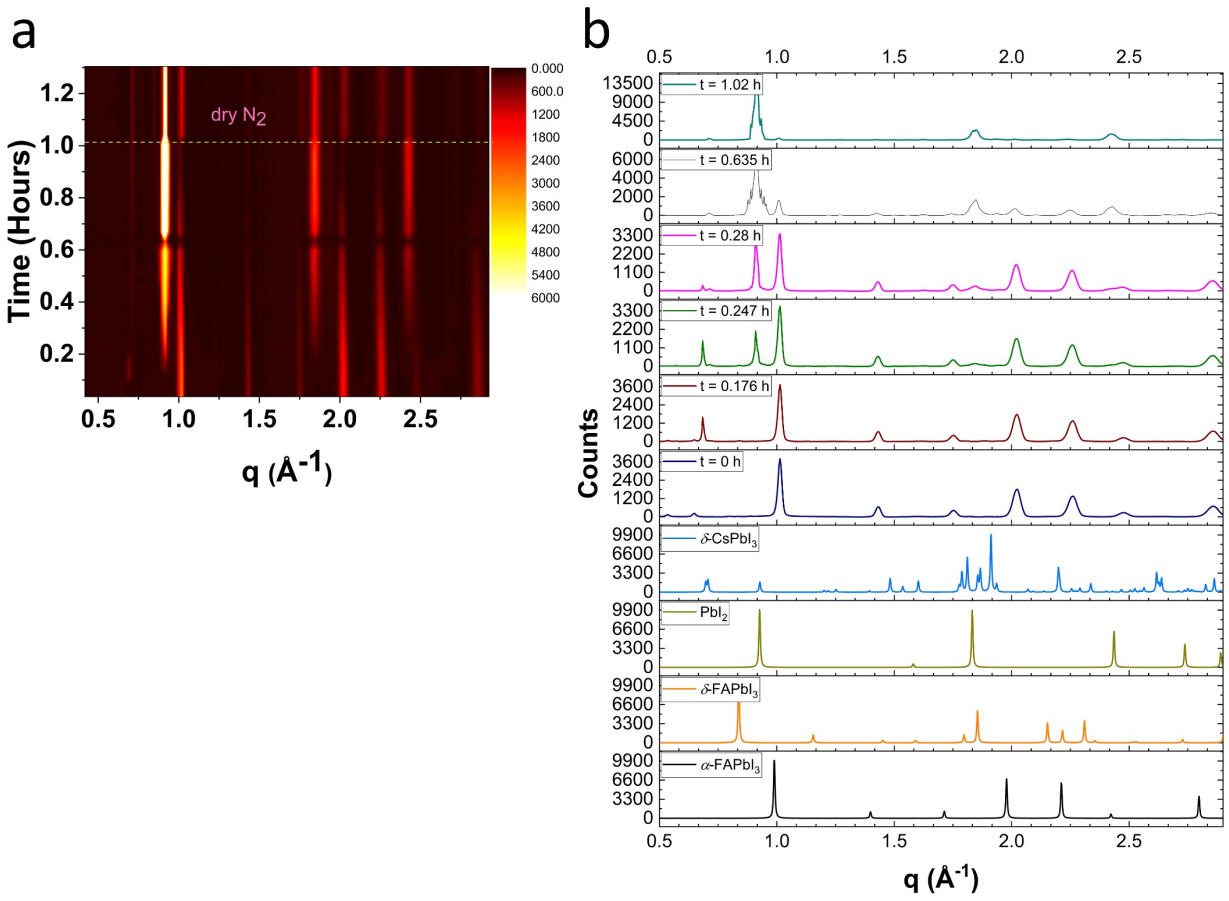

Figure 4.19 (**a**) 2D contour plot showing the azimuthally integrated diffraction intensity as a function of both scattering vector (q) and time $Cs_{0.1}MA_{0.15}FA_{0.75}Pb(Br_{0.15}I_{0.85})_3$ when exposed to 90 ± 5% RH, (**b**) azimuthally-integrated GIWAXS pattern for $FAPbI_3$ exposed to high humidity (RH 90 ± 5%) at different time compared with predicted pXRD pattern of α-$FAPbI_3$, δ-$FAPbI_3$, PbI_2, and δ-$CsPbI_3$.

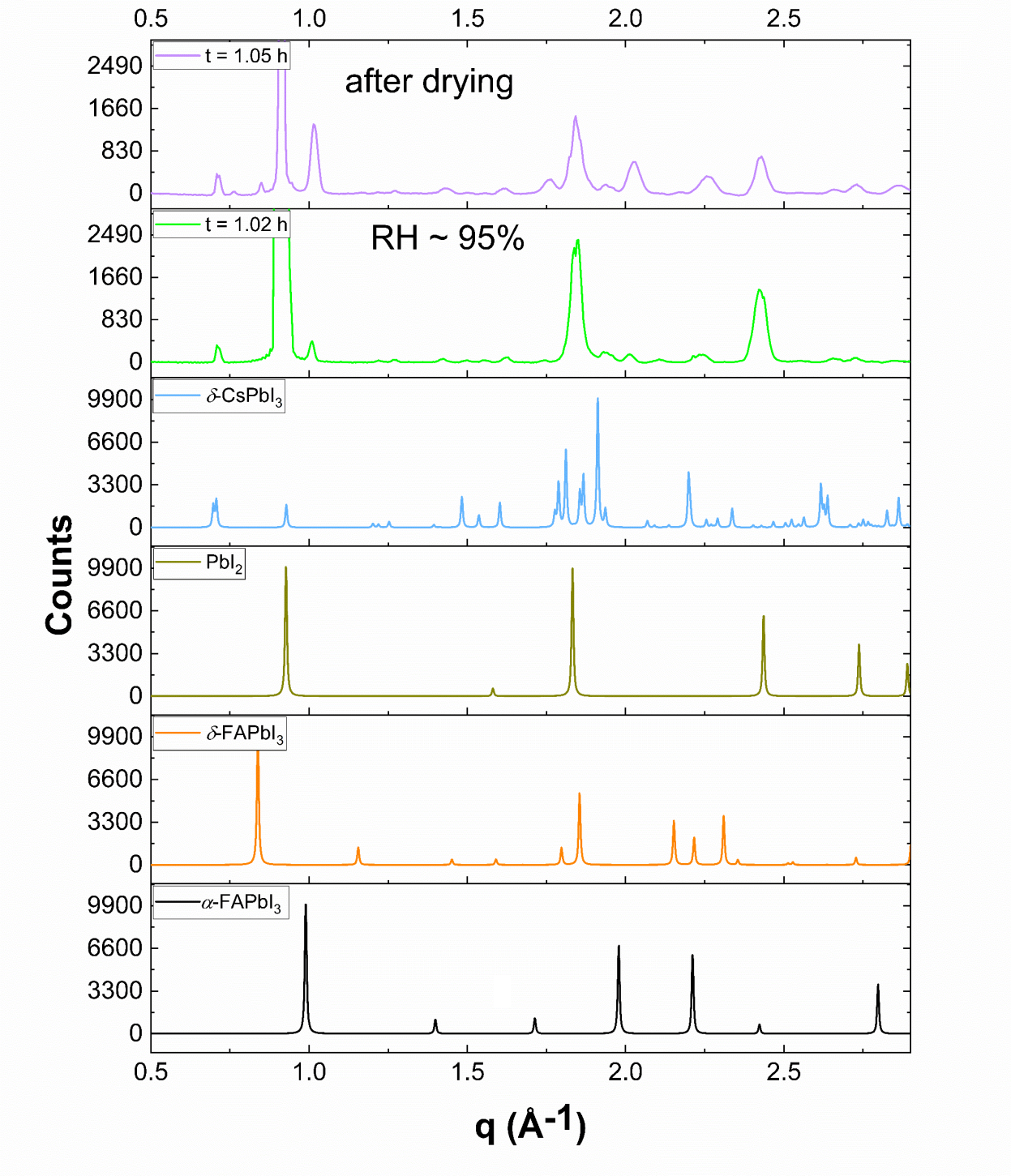

Figure 4.20 Azimuthally-integrated GIWAXS pattern for $Cs_{0.1}MA_{0.15}FA_{0.75}Pb(Br_{0.15}I_{0.85})_3$ at t = 1.02 h and t = 1.05 h compared with predicted pXRD patterns of α-$FAPbI_3$, δ-$FAPbI_3$, PbI_2, and δ-$CsPbI_3$.

4.3.2.6. Comparison of the Degradation Process in $FAPbI_3$, $Cs_{0.1}FA_{0.9}PbI_3$, and $Cs_{0.1}MA_{0.15}FA_{0.75}Pb(Br_{0.15}I_{0.85})_3$

As mentioned earlier, doping $FAPbI_3$ with smaller Cs or MA cations improves its stability. Similarly, replacement of iodide by bromide improves moisture stability. So, the expected stability order would be $FAPbI_3 < Cs_{0.1}FA_{0.9}PbI_3 < Cs_{0.1}MA_{0.15}FA_{0.75}Pb(Br_{0.15}I_{0.85})_3$ which is supported by the in situ UV-vis study at high RH (**Figure 4.21**). This instability is mainly due to in built lattice strain caused by the larger FA cation. As the strain is relieved by alloying with smaller size cations, the reactivity towards water decreases. In a humid environment, water molecules get into the lattice and make the ions more mobile, which decreases the activation energy barrier for the $\alpha \rightarrow \delta$ phase transition. That is why for $FAPbI_3$ the phase change was observed to occur rapidly at high humidity. In contrast, for $Cs_{0.1}MA_{0.15}FA_{0.75}Pb(Br_{0.15}I_{0.85})_3$ very little to no $\alpha \rightarrow \delta$ phase change was observed. It decomposed mainly to PbI_2. For $Cs_{0.1}FA_{0.9}PbI_3$, both the δ-phase and PbI_2 were observed as major decomposition products (**Figure 4.21**).

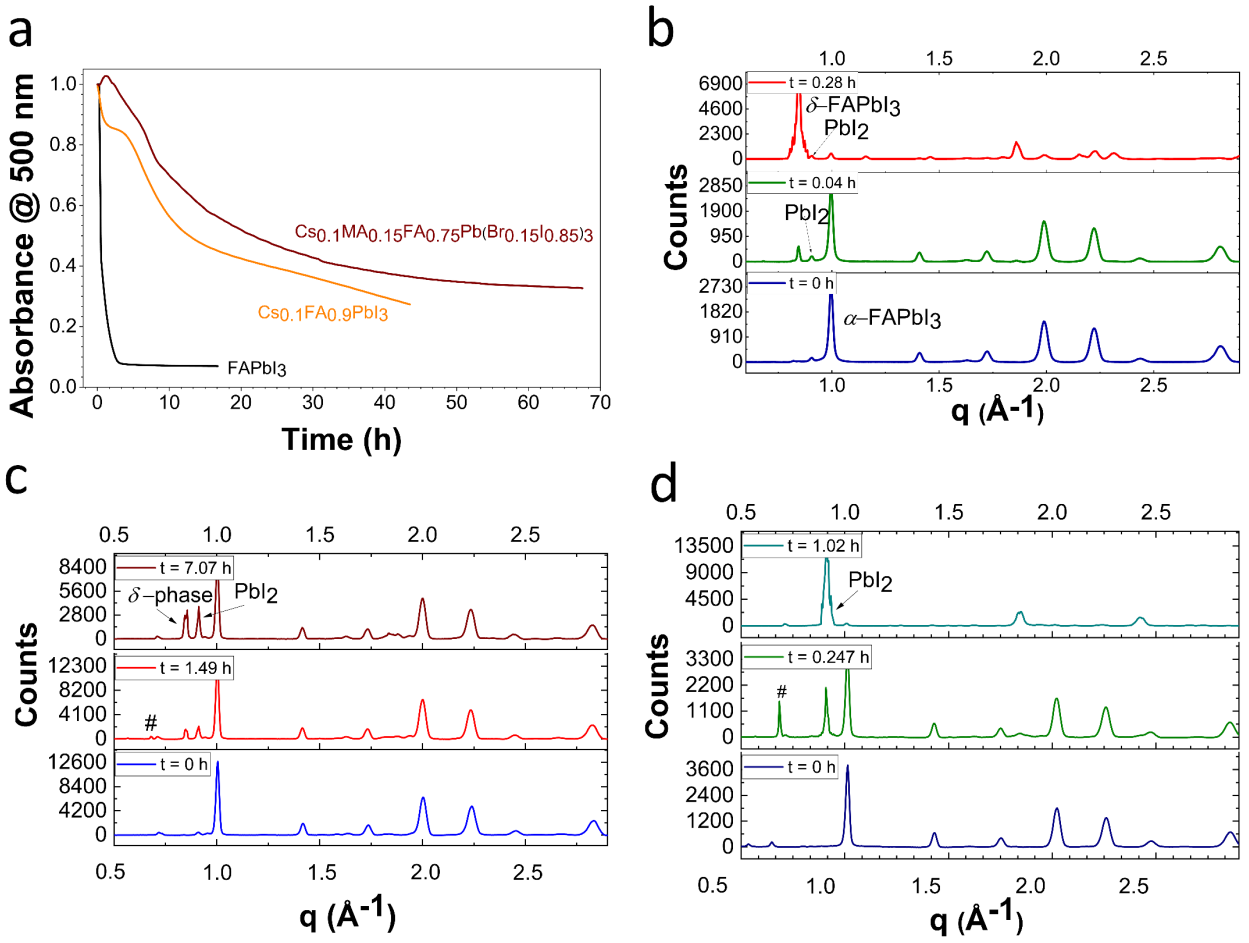

Figure 4.21 Decomposition of $FAPbI_3$, $Cs_{0.1}FA_{0.90}PbI_3$, and $Cs_{0.1}MA_{0.15}FA_{0.75}Pb(Br_{0.15}I_{0.85})_3$; (**a**) Normalized absorbance at 500 nm as a function of time, azimuthally-integrated GIWAXS pattern at 90 ± 5% RH for (**b**) $FAPbI_3$, (**c**) $Cs_{0.1}FA_{0.90}PbI_3$, and (**d**) $Cs_{0.1}MA_{0.15}FA_{0.75}Pb(Br_{0.15}I_{0.85})_3$ respectively.

4.3.2.7. $MAPbBr_3$ and $FAPbBr_3$

Among all the perovskite compositions, $MAPbBr_3$ showed an impressive stability at high RH. Within our limited in situ GIWAXS experimental time, no new diffraction rings were observed. The initial diffraction pattern of $MAPbBr_3$ at $q \approx 1.06$, 1.5, 2.1, 2.36, and 2.59 $Å^{-1}$ is consistent with reflection from the (100), (110), (200) (210), and (211) lattice planes of pure cubic $MAPbBr_3$ (**Figure 4.22-4.23**). After introducing high humidity, over a period of 8 h almost no changes in the

diffraction peaks were observed (**Figure 4.23**). However, with time the intensity the peak slowly decreased. This is mainly attributed to decay of the synchrotron x-ray beam with time (**Figure 4.23**).

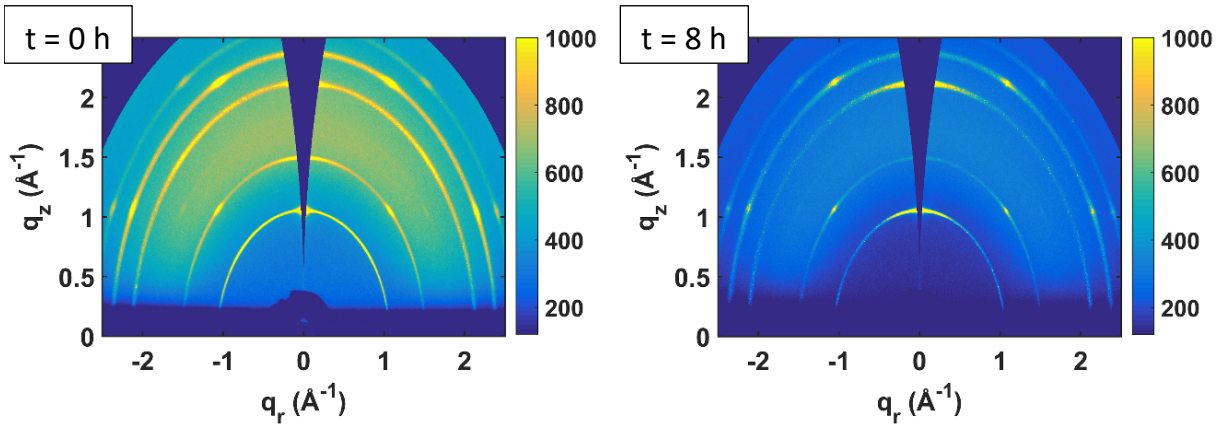

Figure 4.22 2D GIWAXS patterns of $MAPbBr_3$ films on glass, at different time when exposed to a 90 ± 5% RH environment.

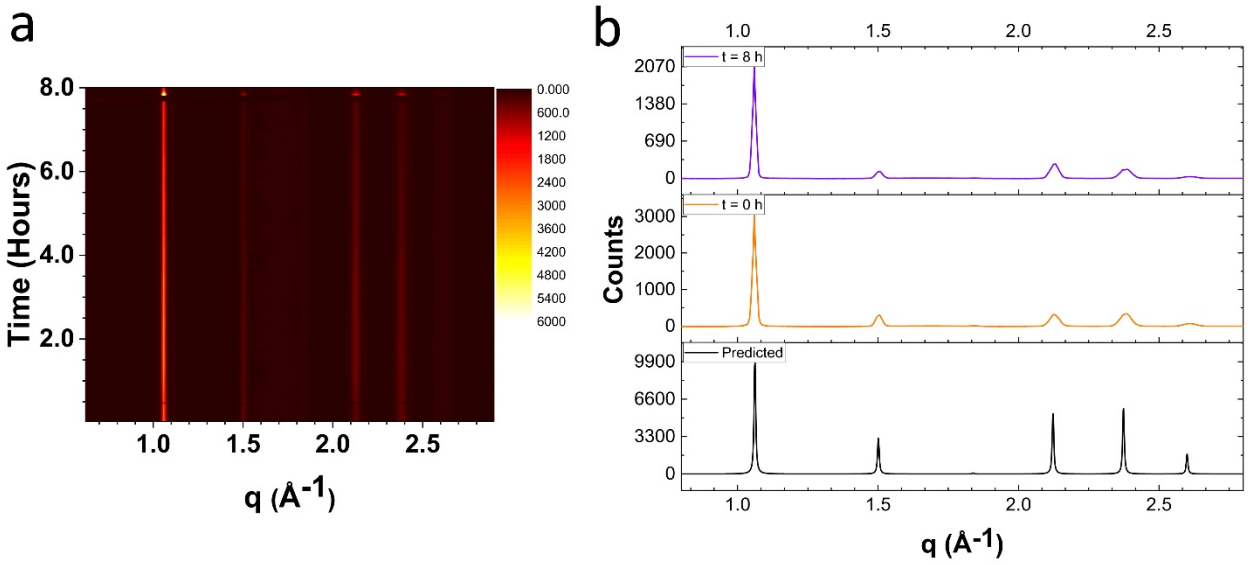

Figure 4.23 (**a**) 2D contour plot showing the azimuthally integrated diffraction intensity as a function of both scattering vector (q) and time for $MAPbBr_3$, (**b**) azimuthally-integrated GIWAXS pattern for $MAPbBr_3$ at t = 0 h, and t = 8 h compared with predicted pXRD pattern.

Like $MAPbBr_3$, $FAPbBr_3$ has good stability towards moisture. The diffraction pattern at t = 0 h ($q \approx$ 1.05, 1.49, 1.83, 2.12, 2.36, and 2.59 $Å^{-1}$) is consistent with reflection from the (100), (110), (111), (200), (210), and (211) lattice planes of pure cubic $FAPbBr_3$ (**Figure 4.24-4.25**). After introducing high humidity, over a period of 8 h almost no changes in the diffraction peaks were observed (**Figure 4.25**).

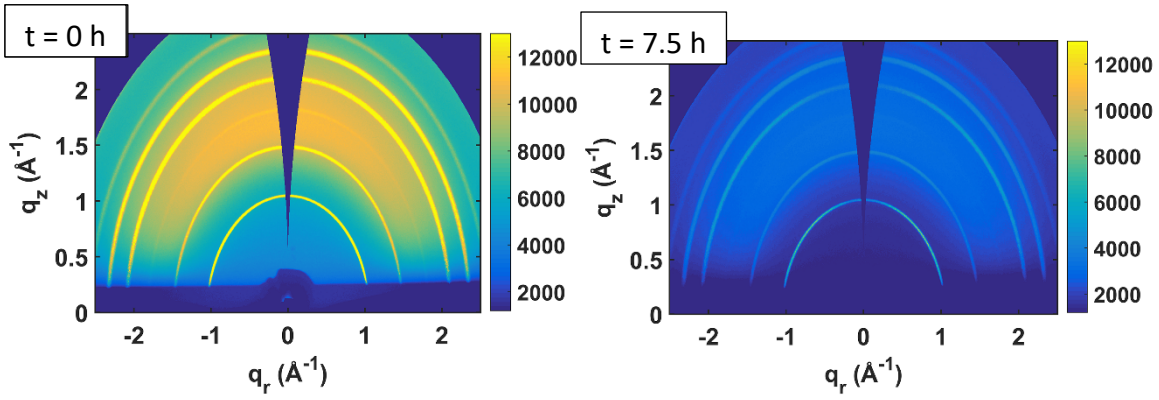

Figure 4.24 2D GIWAXS patterns of $FAPbBr_3$ films on glass, at different time when exposed to a 90 ± 5% RH environment.

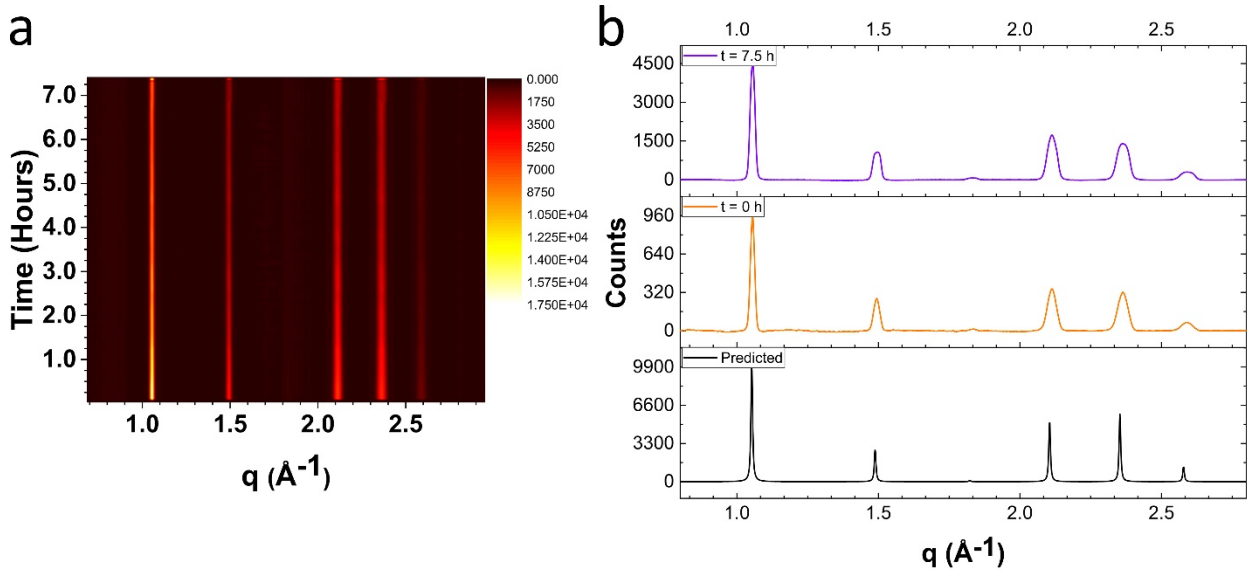

Figure 4.25 (**a**) 2D contour plot showing the azimuthally integrated diffraction intensity as a function of both scattering vector (q) and time for $FAPbBr_3$, (**b**) azimuthally-integrated GIWAXS pattern for $FAPbBr_3$ at t = 0 h, and t = 7.5 h compared with predicted pXRD pattern.

To follow the full decomposition process of $MAPBr_3$ and $FAPBr_3$, ex situ pXRD experiments were carried out at high RH. Due to the solvent annealing effect of water vapor, the intensity of the perovskite peaks increased initially for both $MAPBr_3$ and $FAPBr_3$, then they started to decrease. After 20 days, new peaks appeared at 2θ = 18.6°, 21.6°, 22°, 28.9°, 30.6°, 33.8°, and 37.7° due to partial decomposition of $MAPbBr_3$ into $PbBr_2$ (**Figure 4.26**). Additional peaks with low intensity were found at 2θ = 13.5°, 17.2°, and 19.8° which do not match either $MAPbBr_3$ or $PbBr_2$. These peaks may correspond to the formation of a possible hydrate phase. Upon drying, the intensity of the $PbBr_2$ decreased significantly with a dramatic increase in the intensity of the perovskite peaks which suggests that the decomposition process is partially reversible (**Figure 4.26**). In the case of $FAPbBr_3$, after 20 days new peaks appeared at 2θ = 14.4°, 18.5°, 20.9°, 21.6°, 22°, 24°, 28.4°, 28.9°, 33.4°, and 38.4° which correspond to the diffraction pattern of $PbBr_2$ (**Figure 4.27**). Additionally, peaks appeared at 2θ = 10.4° and 28.4° which may again correspond

to a possible hydrate phase. Upon drying, the intensity of the perovskite peaks increased indicating the reversibility of the decomposition process (**Figure 4.27**).

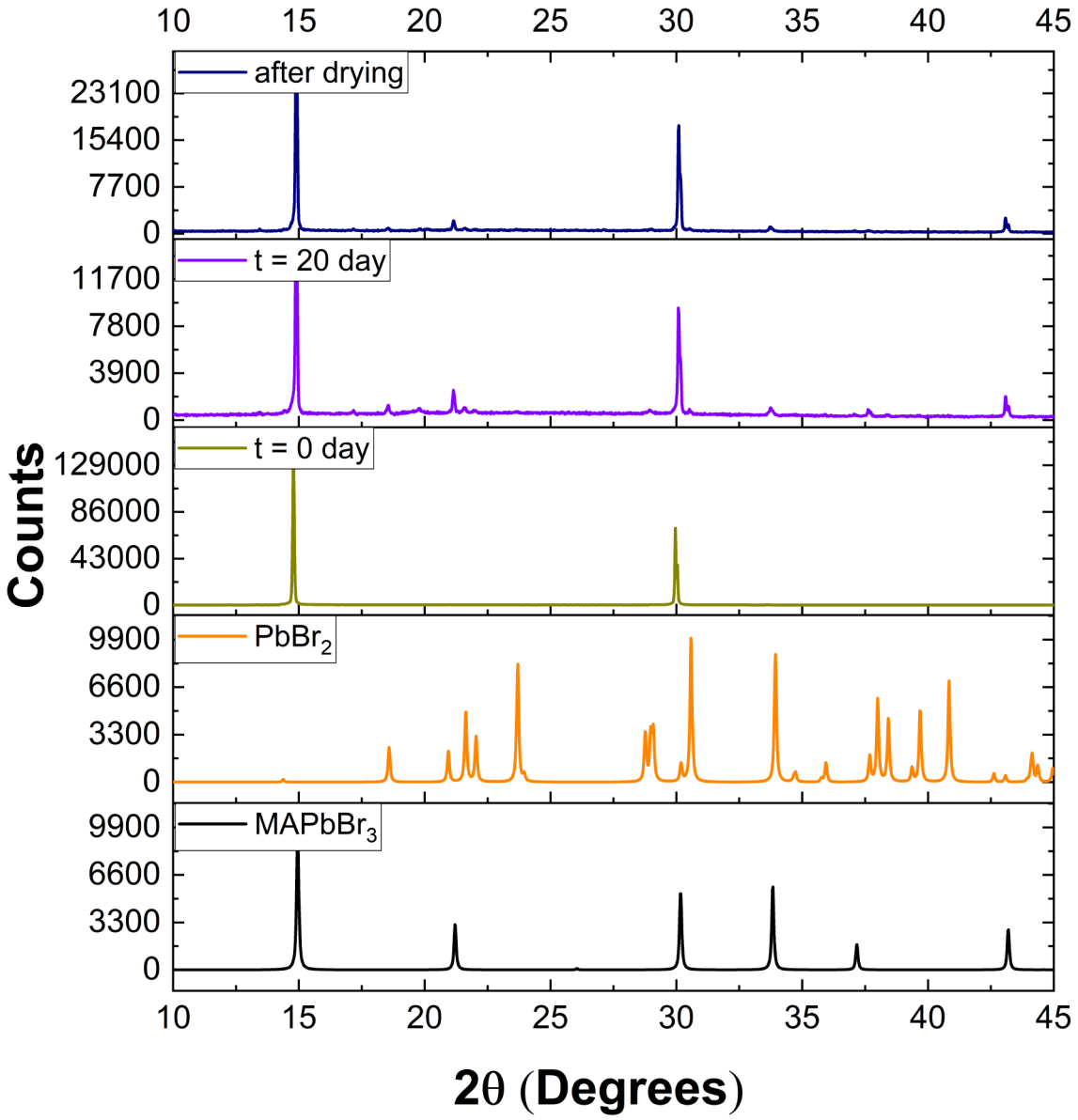

Figure 4.26 pXRD of $MAPbBr_3$ subjected to high humidity (RH 90 ± 5%).

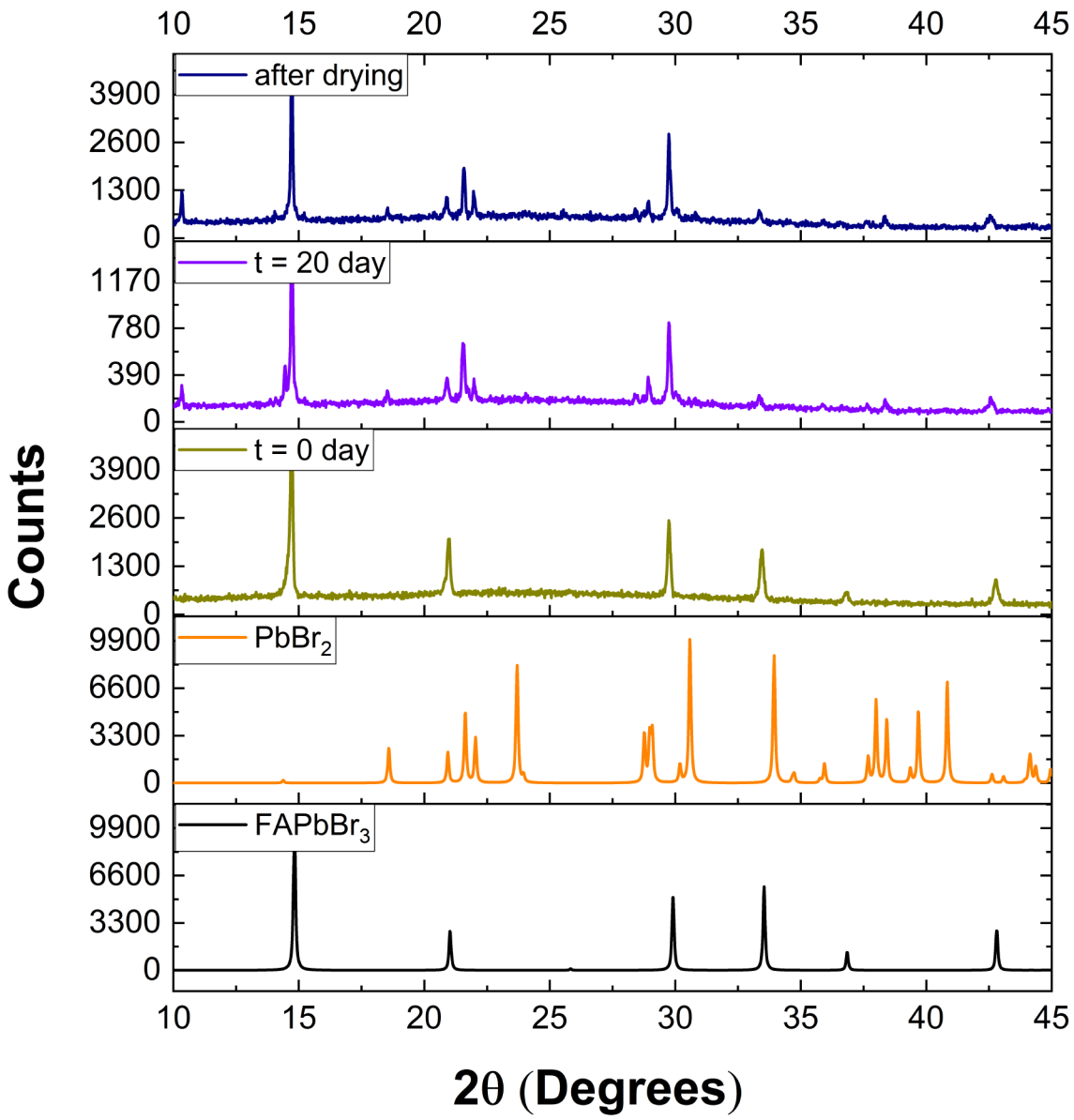

Figure 4.27 pXRD of $FAPbBr_3$ subjected to high humidity (RH 90 ± 5%).

4.3.2.8. $CsPbBr_3$

Compared to other bromides, $CsPbBr_3$ is relatively unstable when subjected to high humidity (**Figure 4.28**). The 2D contour plot (**Figure 4.29**) reflects the decomposition process of $CsPbBr_3$. Whereas $MAPbBr_3$ and $FAPbBr_3$ remained unchanged within the 8 h window of beam-time,

$CsPbBr_3$ went through a reversible transition to Cs_4PbBr_6 and $CsPb_2Br_5$. The initial diffraction pattern (t = 0 h) had peaks at $q \approx$ 1.08, 1.52, 1.71, 1.80, 1.87, 1.95, 2.18, 2.42, and 2.65 $Å^{-1}$ from the orthorhombic phase of $CsPbBr_3$ (**Figure 4.28-4.30**). Additionally, a small amount of Cs_4PbBr_6 ($q \approx$ 0.91 $Å^{-1}$) and $CsPb_2Br_5$ ($q \approx$ 0.84, 1.48, and 2.08 $Å^{-1}$) were present in the initial diffraction pattern. This may be due to the highly moisture sensitive polymorphization of $CsPbBr_3$. A non-uninform diffraction ring due to the presence of large crystallites of $CsPb_2Br_5$ was observed with relatively high intensity at $q \approx$ 2.08 $Å^{-1}$. When the film came into contact with wet nitrogen, within seconds (t = 0.035 h) new peaks started to appear at $q \approx$ 0.9, 1.43, 1.59, 1.80, 1.95, 2.02, and 2.36 $Å^{-1}$ which correspond to Cs_4PbBr_6. Simultaneously, the intensity of the $CsPbBr_3$ peaks started to decrease (**Figure 4.28-4.30**). The peak at $q \approx$ 2.08 $Å^{-1}$ started to disappear and completely disappeared after 0.27 h, indicating the disappearance of $CsPb_2Br_5$. At t = 0.1 h, the intensity of the $CsPbBr_3$ peaks reached a minimum and then started to increase again. At t = 3.8 h, Cs_4PbBr_6 completely disappeared, leaving only pure $CsPbBr_3$. This process appears to be catalyzed by moisture (**Figure 4.29-4.30**). Therefore, annealing at high humidity can be used to help produce pure $CsPbBr_3$. After a few hour $CsPbBr_3$ again started to decompose into Cs_4PbBr_6. With time this process kept happening while the peak intensity of the perovskite phase increased and the peak intensity of Cs_4PbBr_6 decreased. At the end, the diffraction rings appeared to become more non-uniform (**Figure 4.28**) suggesting the formation of larger crystallites. As soon as the chamber was flushed with dry nitrogen, Cs_4PbBr_6 ($q \approx$ 0.9, 0.92, 1.43, 1.83, 1.95, 2.02, and 2.74 $Å^{-1}$) and $CsPb_2Br_5$ ($q \approx$ 2.08 $Å^{-1}$) appeared again (**Figure 4.31**).

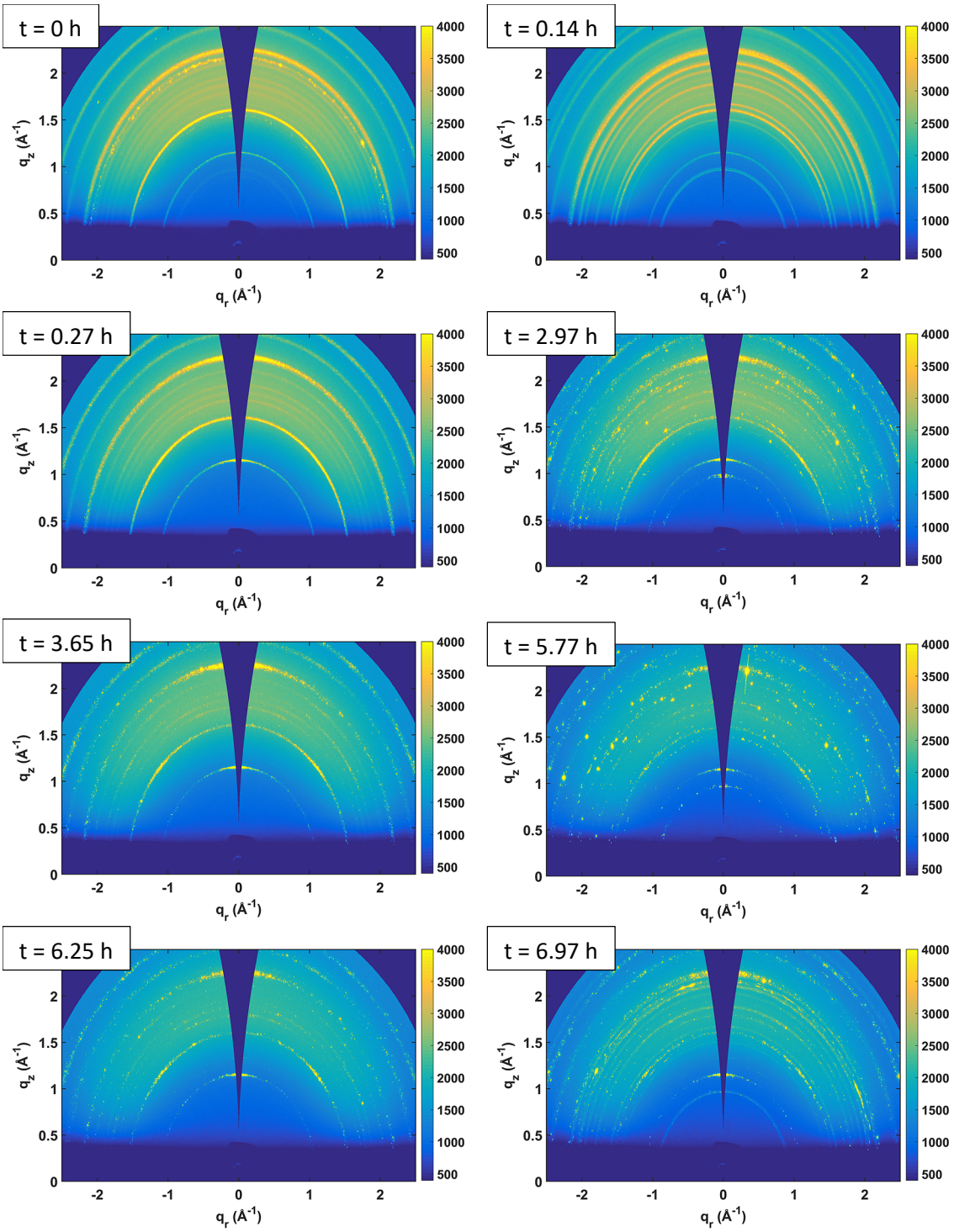

Figure 4.28 2D GIWAXS patterns of $CsPbBr_3$ films on glass, at different time when exposed to 90 ± 5% RH.

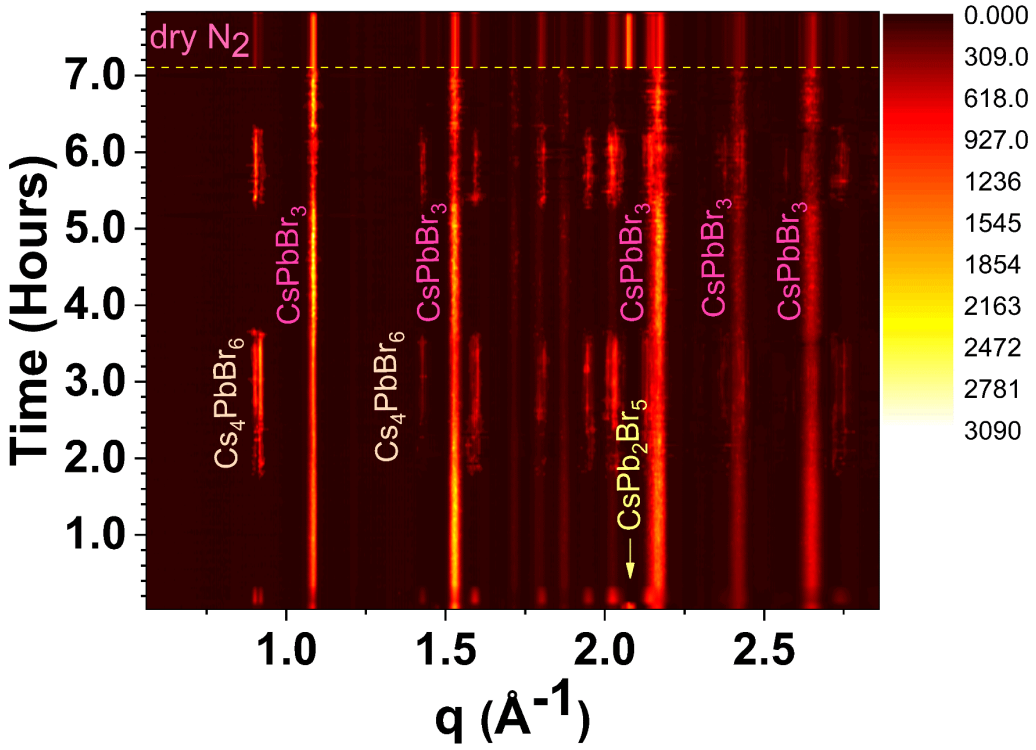

Figure 4.29 2D contour plot showing the azimuthally integrated diffraction intensity as a function of both scattering vector (q) and time of $CsPbBr_3$.

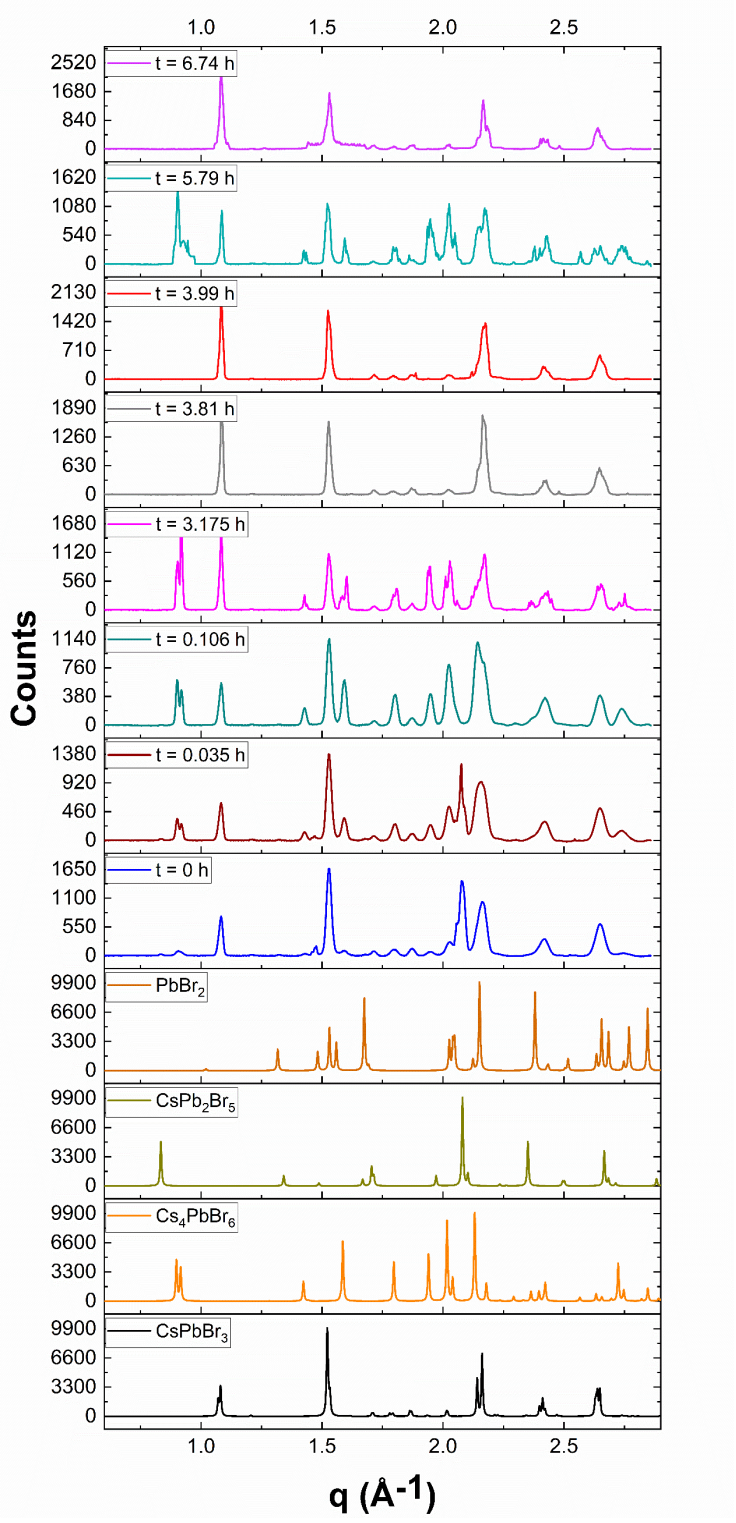

Figure 4.30 Azimuthally-integrated GIWAXS pattern for $CsPbBr_3$ exposed to high humidity (RH 90 ± 5%) at different time.

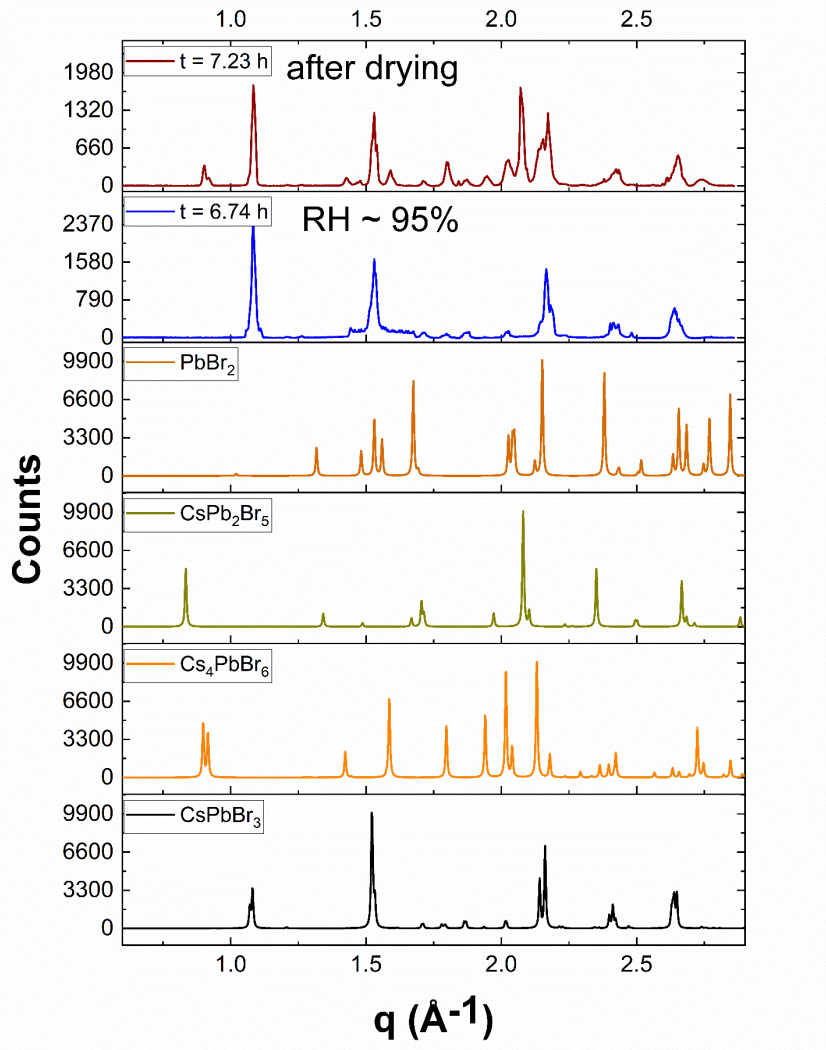

Figure 4.31 Effect of drying for $CsPbBr_3$, azimuthally-integrated GIWAXS pattern for $CsPbBr_3$ at t = 6.74 h, and t = 7.23 h.

Figure 4.32 represents a summarized form of the observed decomposition processes for the compositions studied here. By intercalating water molecules, α-$APbX_3$ can form hydrates which can either revert back to the original perovskite upon drying or slowly convert into PbX_2 and/or other decomposition products. In this process the hydrate is a metastable intermediate. $MAPbI_3$, $Cs_{0.1}FA_{0.9}PbI_3$, and $Cs_{0.1}MA_{0.15}FA_{0.75}Pb(Br_{0.15}I_{0.85})_3$ appear to follow this pathway. To relieve lattice stress a phase transformation from α-$APbX_3$ to δ-$APbX_3$ can occur. This transition is

catalyzed by humidity. In general, by getting into the crystal lattice, humidity increases the mobility of the ions. This in turn catalyzes the phase transformation process. This is usually irreversible as drying does not help in the recovery of the α-$APbX_3$ phase. $CsPbI_3$ appears to follow this decomposition process. Finally, for the third pathway, humidity decomposes the α-$APbX_3$ by converting into δ-$APbX_3$ and PbX_2. Decomposition of $FAPbI_3$ appears to occur following this pathway.

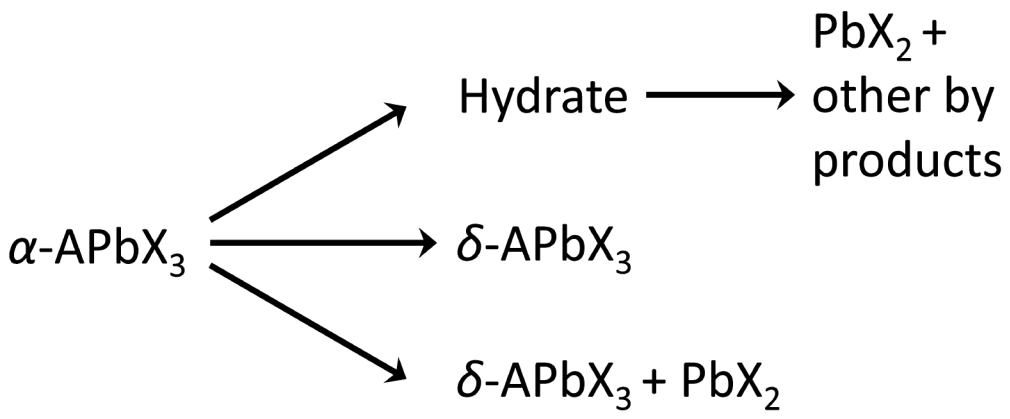

Figure 4.32 Summary of the moisture-induced decomposition mechanism observed in different perovskite compositions.

4.4. Conclusion

Taking advantage of in situ experiments in a controlled environment, 8 different perovskite compositions were successfully screened for moisture stability. Results from in situ absorbance spectroscopic experiments were able to quantitatively evaluate and compare the rates of the degradation kinetics. In situ GIWAXS experiments were used to elucidate the mechanistic pathways of the decomposition process. The results suggest that pure $MAPbBr_3$ and $FAPbBr_3$ are among the most stable compositions whereas $CsPbI_3$, $FAPbI_3$ and $MAPbI_3$ go through rapid

degradation in moist environments. However, mixed perovskite compositions like $Cs_{0.1}FA_{0.9}PbI_3$, and $Cs_{0.1}MA_{0.15}FA_{0.75}Pb(Br_{0.15}I_{0.85})_3$ are more stable than the pure cationic lead iodides. Therefore, these type of mixed composition perovskites will likely increase the moisture resistance of PSCs. This will pave the way towards longer device lifetimes.

5. Discussion, Conclusion and Future Work

5.1. Discussion and General Conclusion

The primary goal of this thesis is to address one of the most relevant problems in the PSC field, which is the instability of PSCs. The success of a photovoltaic technology depends on three major factors: performance, longevity and cost. In order to compete in the commercial market a PV technology needs to have high PCE, long lifetime and low cost. Now, state-of-the-art PSCs have efficiencies over 25%, which is similar to other commercially successful PV technologies such as silicon PV technology. They are projected to have low manufacturing costs[273] and short energy payback times.[62] However, their longevity lags far behind that of other conventional PV technologies. This problem with instability was addressed in this thesis in two ways: the first approach is a physical approach, which focused on applying hydrophobic barrier layers between the perovskite layer and the environment. This approach helps to minimize the impact of environmental stressors like moisture, thus improving the lifetime of PSCs. The second approach was a chemical approach where $MAPbI_3$ was replaced with more stable perovskite compositions.

In the first project (**Chapter 2** of this thesis), poly(3-alkoxythiophene) based HTMs with different hydrophobicities were synthesized and applied as both HTLs and vapor barriers. The moisture-blocking ability of these poly(3-alkoxythiophenes) was comprehensively studied. Owing to both the hydrophobicity and solid state packing efficiency, the highly fluorinated polymers provided an impressive level of protection to the underlying perovskite. However, the efficiency of the fluorinated polymer-based devices was low due to its low hole mobility. The low conductivity may be the result of a low molecular weight and a lack of regioregularity. The findings in this project suggested that incorporating perfluorinated side chains in HTMs may be

an effective strategy to improve the moisture resistance of perovskite devices. Therefore, the synthesis of such HTMs with high hole mobility and effective barrier properties would be our next step toward the production of long-lived, environmentally stable PSCs.

The second project (**Chapter 3**) demonstrated a simple, scalable strategy to improve the moisture resistance and device lifetime of PSCs by using a mixture of two commercially available polymers (P3HT and PMMA). The mixing of these two polymers in a specific ratio produces a highly connected pathways of P3HT nanowires in PMMA matrix. The P3HT nanowires help in hole-transport from the $MAPbI_3$ absorber to the top electrode. PMMA provides a better quality of protection by effectively reducing the moisture ingress even in very damp environments (99% RH). The resulting PMMA/P3HT devices have nearly equivalent performance to that of a compact P3HT layer. However, they have shown more than an order of magnitude improvement in the stability of the PSCs. In addition to being a better vapor barrier, the studies on devices with Ag electrodes show that PMMA/P3HT based HTMs can reduce the diffusion of iodide ions to the top Ag electrode. This hinders the formation of AgI, thus slowing down the degradation of the Ag electrodes. In short, PMMA/P3HT based HTMs result in an improvement in the moisture stability of $MAPbI_3$ based PSCs without sacrificing efficiency.

The third project (**Chapter 4**) of this thesis provided an approach to screening a large number of compositions based on in situ characterization techniques. This approach allows us to find suitable perovskite compositions with better moisture stability. The kinetics study based on in situ absorbance spectroscopy allows us to quantitatively evaluate and compare the degradation rates of the different compositions. The results suggest that pure bromides are among the most stable compositions whereas the iodides go through rapid degradation in moist environment. However, mixed composition perovskites such as $Cs_{0.1}FA_{0.9}PbI_3$, and $Cs_{0.1}MA_{0.15}FA_{0.75}Pb(Br_{0.15}I_{0.85})_3$ are

more stable than the pure cationic lead iodides. Therefore, these mixed composition perovskites will likely increase the moisture resistance of PSCs thus improving the long-term stability of PSCs. This chapter also improves our understanding of the decomposition process by providing a detailed analysis of the decomposition mechanism and identifying the byproducts. This can further assist in our search for robust perovskite candidates.

As a whole, this thesis provides a better understanding of how to address the stability issues in PSCs. The HTMs developed and described in this thesis have improved the stability of PSCs even in very damp conditions. This thesis also shed a light on the different decomposition pathways that occur in different perovskite compositions, thus substantially improving our knowledge of perovskite degradation mechanisms.

5.2. Future Work

The goal of this thesis is to improve the long-term stability of PSCs by providing a better understanding of the decomposition process and designing better barrier materials or more stable compositions. Based on the findings of this thesis, here I propose a set of future projects to further advance this field.

5.2.1.Proposed Project 1: Designing New Moisture-resistive Layers

As a continuation of the approaches described in **Chapter 2** and **3** (physical approaches), new moisture-resistive barrier layers can be developed to improve the longevity of PSCs. This could be done either by incorporating additional moisture-resistive layers in a perovskite device stack or by modifying or replacing the layers (ETLs, HTLs or top electrode) which are already part of a perovskite device. Here I propose designing a new moisture resistive barrier layer which uses silver nanowires (AgNWs) embedded in a water-resistive polymer such as PMMA or polyethylene

terephthalate (PET). This AgNW/PMMA or PET layer will be deposited between two or more gold electrodes (as shown in the **Figure 5.1**). The AgNW network will serve as a conductive network connecting the two Au electrodes. The polymeric matrix (PMMA or PET) will act as a protective barrier layer reducing moisture ingress into the perovskite layer. **Figure 5.1** shows the proposed device architecture.

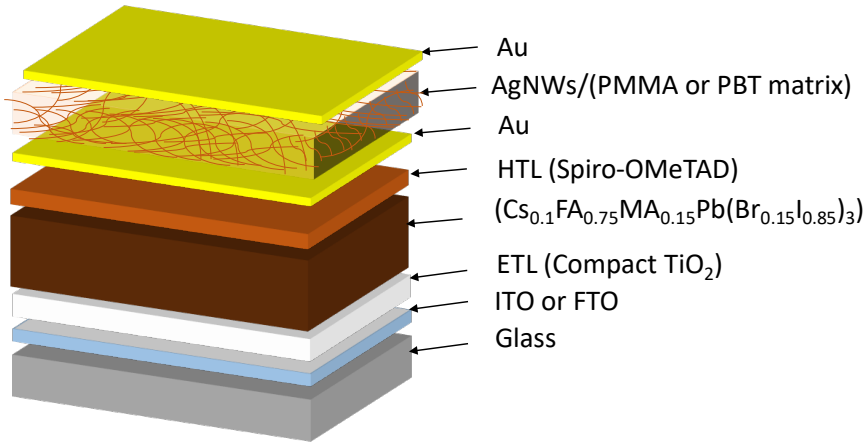

Figure 5.1 Schematic representation of the proposed architecture: FTO/TiO_2/ $Cs_{0.1}FA_{0.75}MA_{0.15}Pb(Br_{0.15}I_{0.85})_3$/spiro-OMeTAD/Au/(AgNW/PMMA or PET layer)/Au

5.2.1.1. Deposition of AgNW/PMMA or PET

AgNWs have been used in the literature to produce semi-transparent and flexible electrodes for electronic devices including solar cells.[274-277] They are inexpensive with good mechanical properties. The AgNW/PMMA or PET layer could be deposited several ways. AgNWs (dispersed in dry isopropanol) and PMMA or PET (in dry chlorobenzene) will be mixed in an appropriate ratio to get AgNW/PMMA or PET. Then the mixture will be spin-coated. Alternatively, AgNWs and PMMA or PET could be spin coated separately.

5.2.2. Proposed Project 2: Study the Decomposition Kinetics of Ag Electrodes in Iodide and Bromide Perovskites in the Presence of Humidity

Silver is one of the low-cost electrode materials commonly used in PSCs. However, owing to ion migration Ag electrodes suffer from corrosion.[122, 278] This results in decomposition of the Ag electrode within several days.[122] According to Kato et al., moisture ingress into $MAPbI_3$ first leads to local decomposition of $MAPbI_3$ into PbI_2.[122] Iodide ions then diffuse through the HTL to the top Ag electrode and react to form AgI. This results in the corrosion of the Ag electrode and a reduction in device PCE. This can even happen to the devices stored in an inert atmosphere; however the process is relatively slow. Other factors like heat and light can also facilitate the corrosion process.[278] Therefore, it is of utter importance to find a solution to this problem.

Two major factors contribute to the corrosion of Ag electrode; iodide ion migration and the reactivity of Ag towards iodine. In order to mitigate these factors, here I propose to replace iodide with bromide in $APbX_3$. Usually, bromide perovskites are more stable than their iodide counterparts.[126 132] Therefore, the moisture/heat induced decomposition of $APbBr_3$ to $PbBr_2$ will be limited. As bromides are less polarizable than iodides, Ag has lesser affinity towards bromides. Therefore, in theory the Ag electrodes will be more stable toward the bromide perovskites.

5.2.2.1. Experiment Design

To prove our theory, first $MAPbI_3$/P3HT/Ag and $MAPbBr_3$/P3HT/Ag films will be exposed to ambient humidity and the corrosion of the Ag electrode will be tracked by pXRD, SEM and optical microscopy. In situ GIWAXS at high RH (as described in **Chapter 4**) will be used to track any changes occurring in the films. To track any changes in the oxidation states, XPS will be used. Finally, changes in PCE will be tracked based on FTO/TiO_2/$MAPbX_3$/P3HT/Ag devices at high RH.

5.2.3. Proposed Project 3: In situ Investigation of Decomposition of Layered Perovskites by UV-vis Spectroscopy and GIWAXS

This proposed work is a continuation of the work described in **Chapter 4**. With rigorous work going on in search of stable perovskite compositions, 2D and 2D/3D layered perovskites are popular due to their improved moisture stability.[148, 279-281] However, very little is known about their degradation process. Here I propose a comprehensive study of the decomposition kinetics of the layered perovskites by using in situ UV-visible spectroscopy and in situ GIWAXS techniques.

6. References

(1) RENEWABLES 2019 GLOBAL STATUS REPORT. https://www.ren21.net/reports/global-status-report/ (acessed 02 January 2020).

(2) J. Y. Tsao, N. S. L. a. G. W. C., In Energy, U. S. D. o., Ed. 2006; pp 1-24.

(3) Becquerel, M. E., Memoire sur les Effets Electriques Produits sous l'Influence des Rayons Solaires. *Comptes Rendus Hebdomadaires des Seances de L'Academie des Sciences* **1839,** 9, 561-567.

(4) Williams, R., Becquerel Photovoltaic Effect in Binary Compounds. *J.Chem. Phys.* **1960,** 32, 1505-1514.

(5) Fritts, C. E., On a new form of selenium cell, and some electrical discoveries made by its use. *Am. J. Sci.* **1883,** Series 3 Vol. 26, 465-472.

(6) Blakers, A. W.; Green, M. A., 20% efficiency silicon solar cells. *Appl. Phys. Lett.* **1986,** 48, 215-217.

(7) Best Research-Cell Efficiency Chart. https://www.nrel.gov/pv/cell-efficiency.html (acessed 24 August 2019).

(8) Green, M. A.; Dunlop, E. D.; Hohl-Ebinger, J.; Yoshita, M.; Kopidakis, N.; Ho-Baillie, A. W. Y., Solar cell efficiency tables (Version 55). *Prog. Photovolt. Res. Appl.* **2020,** 28, 3-15.

(9) Lee, Y.-J.; Kim, B.-S.; Ifitiquar, S. M.; Park, C.; Yi, J., Silicon solar cells: Past, present and the future. *J. Korean Phys, Soc.* **2014,** 65, 355-361.

(10) Green, M. A., Radiative efficiency of state-of-the-art photovoltaic cells. *Prog. Photovolt. Res. Appl.* **2012,** 20, 472-476.

(11) Anspaugh, B., GaAs solar cell radiation handbook. In Jet Propulsion Lab, California Inst. of Tech., Pasadena, CA United States: 1996.

(12) Yin, W.-J.; Yang, J.-H.; Kang, J.; Yan, Y.; Wei, S.-H., Halide perovskite materials for solar cells: a theoretical review. *J. Mater. Chem. A* **2015,** 3, 8926-8942.

(13) Leguy, A. M. A.; Azarhoosh, P.; Alonso, M. I.; Campoy-Quiles, M.; Weber, O. J.; Yao, J.; Bryant, D.; Weller, M. T.; Nelson, J.; Walsh, A.; van Schilfgaarde, M.; Barnes, P. R. F., Experimental and theoretical optical properties of methylammonium lead halide perovskites. *Nanoscale* **2016,** 8, 6317-6327.

(14) Song, Z.; Chen, C.; Li, C.; Awni, R. A.; Zhao, D.; Yan, Y., Wide-bandgap, low-bandgap, and tandem perovskite solar cells. *Semicond. Sci. Technol.* **2019,** 34, 093001.

(15) Borriello, I.; Cantele, G.; Ninno, D., Ab initio investigation of hybrid organic-inorganic perovskites based on tin halides. *Phys. Rev. B* **2008,** 77, 235214.

(16) Saliba, M.; Matsui, T.; Domanski, K.; Seo, J.-Y.; Ummadisingu, A.; Zakeeruddin, S. M.; Correa-Baena, J.-P.; Tress, W. R.; Abate, A.; Hagfeldt, A.; Grätzel, M., Incorporation of rubidium cations into perovskite solar cells improves photovoltaic performance. *Science* **2016**, aah5557.

(17) Stoumpos, C. C.; Malliakas, C. D.; Kanatzidis, M. G., Semiconducting Tin and Lead Iodide Perovskites with Organic Cations: Phase Transitions, High Mobilities, and Near-Infrared Photoluminescent Properties. *Inorg. Chem.* **2013,** 52, 9019-9038.

(18) Eperon, G. E.; Stranks, S. D.; Menelaou, C.; Johnston, M. B.; Herz, L. M.; Snaith, H. J., Formamidinium lead trihalide: a broadly tunable perovskite for efficient planar heterojunction solar cells. *Energy Environ. Sci.* **2014,** 7, 982-988.

(19) Xu, Q.; Yang, D.; Lv, J.; Sun, Y.-Y.; Zhang, L., Perovskite Solar Absorbers: Materials by Design. *Small Methods* **2018,** 2, 1700316.

(20) Uma, S.; Raju, A. R.; Gopalakrishnan, J., Bridging the Ruddlesden–Popper and the Dion–Jacobson series of layered perovskites: synthesis of layered oxides, A2–La2Ti3–NbO10(A = K, Rb), exhibiting ion exchange. *J. Mater. Chem.* **1993,** 3, 709-713.

(21) Korshunova, K.; Winterfeld, L.; Beenken, W. J. D.; Runge, E., Thermodynamic stability of mixed Pb:Sn methyl-ammonium halide perovskites. *Phys. Status Solidi (B)* **2016,** 253, 1907-1915.

(22) Song, D. H.; Jang, M. H.; Lee, M. H.; Heo, J. H.; Park, J. K.; Sung, S.-J.; Kim, D.-H.; Hong, K.-H.; Im, S. H., A discussion on the origin and solutions of hysteresis in perovskite hybrid solar cells. *J. Phys. D: Appl. Phys.* **2016,** 49, 473001.

(23) Wang, K.-H.; Li, L.-C.; Shellaiah, M.; Wen Sun, K., Structural and Photophysical Properties of Methylammonium Lead Tribromide (MAPbBr3) Single Crystals. *Sci. Rep.* **2017,** 7, 13643.

(24) Green, M. A.; Ho-Baillie, A.; Snaith, H. J., The emergence of perovskite solar cells. *Nat. Photonics* **2014,** 8, 506-514.

(25) Chen, T.; Foley, B. J.; Park, C.; Brown, C. M.; Harriger, L. W.; Lee, J.; Ruff, J.; Yoon, M.; Choi, J. J.; Lee, S.-H., Entropy-driven structural transition and kinetic trapping in formamidinium lead iodide perovskite. *Sci. Adv.* **2016,** 2, e1601650.

(26) Amat, A.; Mosconi, E.; Ronca, E.; Quarti, C.; Umari, P.; Nazeeruddin, M. K.; Grätzel, M.; De Angelis, F., Cation-Induced Band-Gap Tuning in Organohalide Perovskites: Interplay of Spin–Orbit Coupling and Octahedra Tilting. *Nano Lett.* **2014,** 14, 3608-3616.

(27) Marronnier, A.; Roma, G.; Boyer-Richard, S.; Pedesseau, L.; Jancu, J.-M.; Bonnassieux, Y.; Katan, C.; Stoumpos, C. C.; Kanatzidis, M. G.; Even, J., Anharmonicity and Disorder in the Black Phases of Cesium Lead Iodide Used for Stable Inorganic Perovskite Solar Cells. *ACS Nano* **2018,** 12, 3477-3486.

(28) Straus, D. B.; Guo, S.; Cava, R. J., Kinetically Stable Single Crystals of Perovskite-Phase CsPbI3. *J. Am. Chem. Soc.* **2019,** 141, 11435-11439.

(29) MØLler, C. K., Crystal Structure and Photoconductivity of Cæsium Plumbohalides. *Nature* **1958,** 182, 1436-1436.

(30) Stoumpos, C. C.; Kanatzidis, M. G., The Renaissance of Halide Perovskites and Their Evolution as Emerging Semiconductors. *Acc. Chem. Res.* **2015,** 48, 2791-2802.

(31) Swarnkar, A.; Mir, W. J.; Nag, A., Can B-Site Doping or Alloying Improve Thermal- and Phase-Stability of All-Inorganic CsPbX3 (X = Cl, Br, I) Perovskites? *ACS Energy Lett.* **2018,** 3, 286-289.

(32) Hirotsu, S.; Harada, J.; Iizumi, M.; Gesi, K., Structural Phase Transitions in CsPbBr3. *J. Phys. Soc. Jpn.* **1974,** 37, 1393-1398.

(33) Chen, X.; Lu, H.; Yang, Y.; Beard, M. C., Excitonic Effects in Methylammonium Lead Halide Perovskites. *J. Phys. Chem. Lett.* **2018,** 9, 2595-2603.

(34) Yang, Z.; Surrente, A.; Galkowski, K.; Bruyant, N.; Maude, D. K.; Haghighirad, A. A.; Snaith, H. J.; Plochocka, P.; Nicholas, R. J., Unraveling the Exciton Binding Energy and the Dielectric Constant in Single-Crystal Methylammonium Lead Triiodide Perovskite. *J. Phys. Chem. Lett.* **2017,** 8, 1851-1855.

(35) Dong, Q.; Fang, Y.; Shao, Y.; Mulligan, P.; Qiu, J.; Cao, L.; Huang, J., Electron-hole diffusion lengths > 175 μm in solution-grown CH₃NH₃PbI₃ single crystals. *Science* **2015,** 347, 967-970.

(36) Yang, Z.; Yu, Z.; Wei, H.; Xiao, X.; Ni, Z.; Chen, B.; Deng, Y.; Habisreutinger, S. N.; Chen, X.; Wang, K.; Zhao, J.; Rudd, P. N.; Berry, J. J.; Beard, M. C.; Huang, J., Enhancing electron diffusion length in narrow-bandgap perovskites for efficient monolithic perovskite tandem solar cells. *Nat. Commun.* **2019,** 10, 4498.

(37) Herz, L. M., Charge-Carrier Mobilities in Metal Halide Perovskites: Fundamental Mechanisms and Limits. *ACS Energy Lett.* **2017,** 2, 1539-1548.

(38) Kepenekian, M.; Even, J., Rashba and Dresselhaus Couplings in Halide Perovskites: Accomplishments and Opportunities for Spintronics and Spin–Orbitronics. *J. Phys. Chem. Lett.* **2017,** 8, 3362-3370.

(39) Todd, S. B.; Riley, D. B.; Binai-Motlagh, A.; Clegg, C.; Ramachandran, A.; March, S. A.; Hoffman, J. M.; Hill, I. G.; Stoumpos, C. C.; Kanatzidis, M. G.; Yu, Z.-G.; Hall, K. C., Detection of Rashba spin splitting in 2D organic-inorganic perovskite via precessional carrier spin relaxation. *APL Mater.* **2019,** 7, 081116.

(40) Kojima, A.; Teshima, K.; Shirai, Y.; Miyasaka, T., Organometal Halide Perovskites as Visible-Light Sensitizers for Photovoltaic Cells. *J. Am. Chem. Soc.* **2009,** 131, 6050-6051.

(41) Lee, M. M.; Teuscher, J.; Miyasaka, T.; Murakami, T. N.; Snaith, H. J., Efficient Hybrid Solar Cells Based on Meso-Superstructured Organometal Halide Perovskites. *Science* **2012,** 338, 643-647.

(42) Malinkiewicz, O.; Yella, A.; Lee, Y. H.; Espallargas, G. M.; Graetzel, M.; Nazeeruddin, M. K.; Bolink, H. J., Perovskite solar cells employing organic charge-transport layers. *Nat. Photonics* **2014,** 8, 128-132.

(43) Liu, M.; Johnston, M. B.; Snaith, H. J., Efficient planar heterojunction perovskite solar cells by vapour deposition. *Nature* **2013,** 501, 395-398.

(44) Docampo, P.; Ball, J. M.; Darwich, M.; Eperon, G. E.; Snaith, H. J., Efficient organometal trihalide perovskite planar-heterojunction solar cells on flexible polymer substrates. *Nat. Commun.* **2013,** 4, 2761.

(45) Salim, T.; Sun, S.; Abe, Y.; Krishna, A.; Grimsdale, A. C.; Lam, Y. M., Perovskite-based solar cells: impact of morphology and device architecture on device performance. *J. Mater. Chem. A* **2015,** 3, 8943-8969.

(46) Hussain, I.; Tran, H. P.; Jaksik, J.; Moore, J.; Islam, N.; Uddin, M. J., Functional materials, device architecture, and flexibility of perovskite solar cell. *Emergent Materials* **2018,** 1, 133-154.

(47) Jiang, Q.; Zhao, Y.; Zhang, X.; Yang, X.; Chen, Y.; Chu, Z.; Ye, Q.; Li, X.; Yin, Z.; You, J., Surface passivation of perovskite film for efficient solar cells. *Nat. Photonics* **2019,** 13, 460-466.

(48) Zheng, X.; Chen, B.; Dai, J.; Fang, Y.; Bai, Y.; Lin, Y.; Wei, H.; Zeng, Xiao C.; Huang, J., Defect passivation in hybrid perovskite solar cells using quaternary ammonium halide anions and cations. *Nat. Energy* **2017,** 2, 17102.

(49) Im, J.-H.; Lee, C.-R.; Lee, J.-W.; Park, S.-W.; Park, N.-G., 6.5% efficient perovskite quantum-dot-sensitized solar cell. *Nanoscale* **2011,** 3, 4088-4093.

(50) Shi, Z.; Jayatissa, A. H., Perovskites-Based Solar Cells: A Review of Recent Progress, Materials and Processing Methods. *Materials* **2018,** 11, 729.

(51) Snaith, H. J.; Abate, A.; Ball, J. M.; Eperon, G. E.; Leijtens, T.; Noel, N. K.; Stranks, S. D.; Wang, J. T.-W.; Wojciechowski, K.; Zhang, W., Anomalous Hysteresis in Perovskite Solar Cells. *J. Phys. Chem. Lett.* **2014,** 5, 1511-1515.

(52) Unger, E. L.; Hoke, E. T.; Bailie, C. D.; Nguyen, W. H.; Bowring, A. R.; Heumüller, T.; Christoforo, M. G.; McGehee, M. D., Hysteresis and transient behavior in current–voltage measurements of hybrid-perovskite absorber solar cells. *Energy Environ. Sci.* **2014,** 7, 3690-3698.

(53) Kang, D.-H.; Park, N.-G., On the Current–Voltage Hysteresis in Perovskite Solar Cells: Dependence on Perovskite Composition and Methods to Remove Hysteresis. *Adv. Mater.* **2019,** 31, 1805214.

(54) Liu, P.; Wang, W.; Liu, S.; Yang, H.; Shao, Z., Fundamental Understanding of Photocurrent Hysteresis in Perovskite Solar Cells. *Adv. Energy Mater.* **2019,** 9, 1803017.

(55) Tress, W.; Marinova, N.; Moehl, T.; Zakeeruddin, S. M.; Nazeeruddin, M. K.; Grätzel, M., Understanding the rate-dependent J–V hysteresis, slow time component, and aging in CH3NH3PbI3 perovskite solar cells: the role of a compensated electric field. *Energy Environ. Sci.* **2015,** 8, 995-1004.

(56) Chen, B.; Yang, M.; Priya, S.; Zhu, K., Origin of J–V Hysteresis in Perovskite Solar Cells. *J. Phys. Chem. Lett.* **2016,** 7, 905-917.

(57) Zhang, T.; Chen, H.; Bai, Y.; Xiao, S.; Zhu, L.; Hu, C.; Xue, Q.; Yang, S., Understanding the relationship between ion migration and the anomalous hysteresis in high-efficiency perovskite solar cells: A fresh perspective from halide substitution. *Nano Energy* **2016,** 26, 620-630.

(58) Lan, D., The physics of ion migration in perovskite solar cells: Insights into hysteresis, device performance, and characterization. *Prog. Photovolt. Res. Appl.* doi.org/10.1002/pip.3203.

(59) Kim, H.-S.; Jang, I.-H.; Ahn, N.; Choi, M.; Guerrero, A.; Bisquert, J.; Park, N.-G., Control of I–V Hysteresis in CH3NH3PbI3 Perovskite Solar Cell. *J. Phys. Chem. Lett.* **2015,** 6, 4633-4639.

(60) Guo, Q.; Wu, J.; Yang, Y.; Liu, X.; Lan, Z.; Lin, J.; Huang, M.; Wei, Y.; Dong, J.; Jia, J.; Huang, Y., High-Performance and Hysteresis-Free Perovskite Solar Cells Based on Rare-Earth-Doped SnO2 Mesoporous Scaffold. *Research* **2019,** 2019, 13.

(61) Son, D.-Y.; Kim, S.-G.; Seo, J.-Y.; Lee, S.-H.; Shin, H.; Lee, D.; Park, N.-G., Universal Approach toward Hysteresis-Free Perovskite Solar Cell via Defect Engineering. *J. Am. Chem. Soc.* **2018,** 140, 1358-1364.

(62) Gong, J.; Darling, S. B.; You, F., Perovskite photovoltaics: life-cycle assessment of energy and environmental impacts. *Energy Environ. Sci.* **2015,** 8, 1953-1968.

(63) Kamat, P. V., Evolution of Perovskite Photovoltaics and Decrease in Energy Payback Time. *J. Phys. Chem. Lett.* **2013,** 4, 3733-3734.

(64) Yang, J.; Kelly, T. L., Decomposition and Cell Failure Mechanisms in Lead Halide Perovskite Solar Cells. *Inorg. Chem.* **2017,** 56, 92-101.

(65) Juarez-Perez, E. J.; Ono, L. K.; Maeda, M.; Jiang, Y.; Hawash, Z.; Qi, Y., Photodecomposition and thermal decomposition in methylammonium halide lead perovskites and inferred design principles to increase photovoltaic device stability. *J. Mater. Chem. A* **2018,** 6, 9604-9612.

(66) Boyd, C. C.; Cheacharoen, R.; Leijtens, T.; McGehee, M. D., Understanding Degradation Mechanisms and Improving Stability of Perovskite Photovoltaics. *Chem. Rev.* **2019,** 119, 3418-3451.

(67) Gangishetty, M. K.; Scott, R. W. J.; Kelly, T. L., Effect of relative humidity on crystal growth, device performance and hysteresis in planar heterojunction perovskite solar cells. *Nanoscale* **2016,** 8, 6300-6307.

(68) Yang, J.; Siempelkamp, B. D.; Liu, D.; Kelly, T. L., Investigation of CH3NH3PbI3 Degradation Rates and Mechanisms in Controlled Humidity Environments Using in Situ Techniques. *ACS Nano* **2015,** 9, 1955-1963.

(69) Christians, J. A.; Miranda Herrera, P. A.; Kamat, P. V., Transformation of the Excited State and Photovoltaic Efficiency of CH3NH3PbI3 Perovskite upon Controlled Exposure to Humidified Air. *J. Am. Chem. Soc.* **2015,** 137, 1530-1538.

(70) Leguy, A. M. A.; Hu, Y.; Campoy-Quiles, M.; Alonso, M. I.; Weber, O. J.; Azarhoosh, P.; van Schilfgaarde, M.; Weller, M. T.; Bein, T.; Nelson, J.; Docampo, P.; Barnes, P. R. F., Reversible Hydration of CH3NH3PbI3 in Films, Single Crystals, and Solar Cells. *Chem. Mater.* **2015,** 27, 3397-3407.

(71) Berhe, T. A.; Su, W.-N.; Chen, C.-H.; Pan, C.-J.; Cheng, J.-H.; Chen, H.-M.; Tsai, M.-C.; Chen, L.-Y.; Dubale, A. A.; Hwang, B.-J., Organometal halide perovskite solar cells: degradation and stability. *Energy Environ. Sci.* **2016,** 9, 323-356.

(72) Deretzis, I.; Smecca, E.; Mannino, G.; La Magna, A.; Miyasaka, T.; Alberti, A., Stability and Degradation in Hybrid Perovskites: Is the Glass Half-Empty or Half-Full? *J. Phys. Chem. Lett.* **2018,** 9, 3000-3007.

(73) Niu, G.; Li, W.; Meng, F.; Wang, L.; Dong, H.; Qiu, Y., Study on the stability of CH3NH3PbI3 films and the effect of post-modification by aluminum oxide in all-solid-state hybrid solar cells. *J. Mater. Chem. A* **2014,** 2, 705-710.

(74) Shirayama, M.; Kato, M.; Miyadera, T.; Sugita, T.; Fujiseki, T.; Hara, S.; Kadowaki, H.; Murata, D.; Chikamatsu, M.; Fujiwara, H., Degradation mechanism of CH3NH3PbI3 perovskite materials upon exposure to humid air. *J. Appl. Phys.* **2016,** 119, 115501.

(75) Li, D.; Bretschneider, S. A.; Bergmann, V. W.; Hermes, I. M.; Mars, J.; Klasen, A.; Lu, H.; Tremel, W.; Mezger, M.; Butt, H.-J.; Weber, S. A. L.; Berger, R., Humidity-Induced Grain Boundaries in MAPbI3 Perovskite Films. *J. Phys. Chem. C* **2016,** 120, 6363-6368.

(76) Koehl, M.; Heck, M.; Wiesmeier, S.; Wirth, J., Modeling of the nominal operating cell temperature based on outdoor weathering. *Sol. Energy Mater. Sol. Cells* **2011,** 95, 1638-1646.

(77) Dualeh, A.; Gao, P.; Seok, S. I.; Nazeeruddin, M. K.; Grätzel, M., Thermal Behavior of Methylammonium Lead-Trihalide Perovskite Photovoltaic Light Harvesters. *Chem. Mater.* **2014,** 26, 6160-6164.

(78) Nenon, D. P.; Christians, J. A.; Wheeler, L. M.; Blackburn, J. L.; Sanehira, E. M.; Dou, B.; Olsen, M. L.; Zhu, K.; Berry, J. J.; Luther, J. M., Structural and chemical evolution of methylammonium lead halide perovskites during thermal processing from solution. *Energy Environ. Sci.* **2016,** 9, 2072-2082.

(79) Yang, J.; Siempelkamp, B. D.; Mosconi, E.; De Angelis, F.; Kelly, T. L., Origin of the Thermal Instability in CH3NH3PbI3 Thin Films Deposited on ZnO. *Chem. Mater.* **2015,** 27, 4229-4236.

(80) Tan, K. W.; Moore, D. T.; Saliba, M.; Sai, H.; Estroff, L. A.; Hanrath, T.; Snaith, H. J.; Wiesner, U., Thermally Induced Structural Evolution and Performance of Mesoporous Block Copolymer-Directed Alumina Perovskite Solar Cells. *ACS Nano* **2014,** 8, 4730-4739.

(81) Dualeh, A.; Tétreault, N.; Moehl, T.; Gao, P.; Nazeeruddin, M. K.; Grätzel, M., Effect of Annealing Temperature on Film Morphology of Organic–Inorganic Hybrid Pervoskite Solid-State Solar Cells. *Adv. Funct. Mater.* **2014,** 24, 3250-3258.

(82) Chang, C.-Y.; Huang, Y.-C.; Tsao, C.-S.; Su, W.-F., Formation Mechanism and Control of Perovskite Films from Solution to Crystalline Phase Studied by in Situ Synchrotron Scattering. *ACS Appl. Mater. Int.* **2016,** 8, 26712-26721.

(83) Zhao, Y.; Nardes, A. M.; Zhu, K., Mesoporous perovskite solar cells: material composition, charge-carrier dynamics, and device characteristics. *Faraday Discuss.* **2014,** 176, 301-312.

(84) Williams, A. E.; Holliman, P. J.; Carnie, M. J.; Davies, M. L.; Worsley, D. A.; Watson, T. M., Perovskite processing for photovoltaics: a spectro-thermal evaluation. *J. Mater. Chem. A* **2014,** 2, 19338-19346.

(85) Bækbo, M. J.; Hansen, O.; Chorkendorff, I.; Vesborg, P. C. K., Deposition of methylammonium iodide via evaporation – combined kinetic and mass spectrometric study. *RSC Adv.* **2018,** 8, 29899-29908.

(86) Juarez-Perez, E. J.; Hawash, Z.; Raga, S. R.; Ono, L. K.; Qi, Y., Thermal degradation of CH3NH3PbI3 perovskite into NH3 and CH3I gases observed by coupled thermogravimetry–mass spectrometry analysis. *Energy Environ. Sci.* **2016,** 9, 3406-3410.

(87) Ciccioli, A.; Latini, A., Thermodynamics and the Intrinsic Stability of Lead Halide Perovskites CH3NH3PbX3. *J. Phys. Chem. Lett.* **2018,** 9, 3756-3765.

(88) Wu, Y.; Xie, F.; Chen, H.; Yang, X.; Su, H.; Cai, M.; Zhou, Z.; Noda, T.; Han, L., Thermally Stable MAPbI3 Perovskite Solar Cells with Efficiency of 19.19% and Area over 1 cm2 achieved by Additive Engineering. *Adv. Mater.* **2017,** 29, 1701073.

(89) Chen, W.; Wu, Y.; Yue, Y.; Liu, J.; Zhang, W.; Yang, X.; Chen, H.; Bi, E.; Ashraful, I.; Grätzel, M.; Han, L., Efficient and stable large-area perovskite solar cells with inorganic charge extraction layers. *Science* **2015,** 350, 944-948.

(90) Tsai, H.; Nie, W.; Blancon, J.-C.; Stoumpos, C. C.; Asadpour, R.; Harutyunyan, B.; Neukirch, A. J.; Verduzco, R.; Crochet, J. J.; Tretiak, S.; Pedesseau, L.; Even, J.; Alam, M. A.; Gupta, G.; Lou, J.; Ajayan, P. M.; Bedzyk, M. J.; Kanatzidis, M. G.; Mohite, A. D., High-efficiency two-dimensional Ruddlesden–Popper perovskite solar cells. *Nature* **2016,** 536, 312.

(91) Wojciechowski, K.; Leijtens, T.; Siprova, S.; Schlueter, C.; Hörantner, M. T.; Wang, J. T.-W.; Li, C.-Z.; Jen, A. K. Y.; Lee, T.-L.; Snaith, H. J., C60 as an Efficient n-Type Compact Layer in Perovskite Solar Cells. *J. Phys. Chem. Lett.* **2015,** 6, 2399-2405.

(92) Seo, S.; Jeong, S.; Bae, C.; Park, N.-G.; Shin, H., Perovskite Solar Cells with Inorganic Electron- and Hole-Transport Layers Exhibiting Long-Term (≈500 h) Stability at 85 °C under Continuous 1 Sun Illumination in Ambient Air. *Adv. Mater.* **2018,** 30, 1801010.

(93) Wang, Z.; Lin, Q.; Wenger, B.; Christoforo, M. G.; Lin, Y.-H.; Klug, M. T.; Johnston, M. B.; Herz, L. M.; Snaith, H. J., High irradiance performance of metal halide perovskites for concentrator photovoltaics. *Nat. Energy* **2018,** 3, 855-861.

(94) Bush, K. A.; Palmstrom, A. F.; Yu, Z. J.; Boccard, M.; Cheacharoen, R.; Mailoa, J. P.; McMeekin, D. P.; Hoye, R. L. Z.; Bailie, C. D.; Leijtens, T.; Peters, I. M.; Minichetti, M. C.; Rolston, N.; Prasanna, R.; Sofia, S.; Harwood, D.; Ma, W.; Moghadam, F.; Snaith, H. J.; Buonassisi, T.; Holman, Z. C.; Bent, S. F.; McGehee, M. D., 23.6%-efficient monolithic perovskite/silicon tandem solar cells with improved stability. *Nat. Energy* **2017,** 2, 17009.

(95) Yang, J.; Hong, Q.; Yuan, Z.; Xu, R.; Guo, X.; Xiong, S.; Liu, X.; Braun, S.; Li, Y.; Tang, J.; Duan, C.; Fahlman, M.; Bao, Q., Unraveling Photostability of Mixed Cation Perovskite Films in Extreme Environment. *Adv. Opt. Mater.* **2018,** 6, 1800262.

(96) Chen, B.; Song, J.; Dai, X.; Liu, Y.; Rudd, P. N.; Hong, X.; Huang, J., Synergistic Effect of Elevated Device Temperature and Excess Charge Carriers on the Rapid Light-Induced Degradation of Perovskite Solar Cells. *Adv. Mater.* **2019,** 31, 1902413.

(97) Sekimoto, T.; Matsui, T.; Nishihara, T.; Uchida, R.; Sekiguchi, T.; Negami, T., Influence of a Hole-Transport Layer on Light-Induced Degradation of Mixed Organic–Inorganic Halide Perovskite Solar Cells. *ACS Appl. Energy Mater.* **2019,** 2, 5039-5049.

(98) Akbulatov, A. F.; Frolova, L. A.; Griffin, M. P.; Gearba, I. R.; Dolocan, A.; Vanden Bout, D. A.; Tsarev, S.; Katz, E. A.; Shestakov, A. F.; Stevenson, K. J.; Troshin, P. A., Effect of Electron-Transport Material on Light-Induced Degradation of Inverted Planar Junction Perovskite Solar Cells. *Adv. Energy Mater.* **2017,** 7, 1700476.

(99) Deng, Y.; Xiao, Z.; Huang, J., Light-Induced Self-Poling Effect on Organometal Trihalide Perovskite Solar Cells for Increased Device Efficiency and Stability. *Adv. Energy Mater.* **2015,** 5, 1500721.

(100) Zhao, C.; Chen, B.; Qiao, X.; Luan, L.; Lu, K.; Hu, B., Revealing Underlying Processes Involved in Light Soaking Effects and Hysteresis Phenomena in Perovskite Solar Cells. *Adv. Energy Mater.* **2015,** 5, 1500279.

(101) Hong, J.; Kim, H.; Hwang, I., Aging-induced light-soaking effects and open-circuit voltage hysteretic behavior of inverted perovskite solar cells incorporating a hole transport metal halide layer via morphology-dependent inflow of iodide ions. *J. Mater. Chem. C* **2019,** 7, 1173-1181.

(102) Tsai, H.; Asadpour, R.; Blancon, J.-C.; Stoumpos, C. C.; Durand, O.; Strzalka, J. W.; Chen, B.; Verduzco, R.; Ajayan, P. M.; Tretiak, S.; Even, J.; Alam, M. A.; Kanatzidis, M. G.; Nie, W.; Mohite, A. D., Light-induced lattice expansion leads to high-efficiency perovskite solar cells. *Science* **2018,** 360, 67-70.

(103) Nie, W.; Blancon, J.-C.; Neukirch, A. J.; Appavoo, K.; Tsai, H.; Chhowalla, M.; Alam, M. A.; Sfeir, M. Y.; Katan, C.; Even, J.; Tretiak, S.; Crochet, J. J.; Gupta, G.; Mohite, A. D., Light-activated photocurrent degradation and self-healing in perovskite solar cells. *Nat. Commun.* **2016,** 7, 11574.

(104) Yoon, S. J.; Draguta, S.; Manser, J. S.; Sharia, O.; Schneider, W. F.; Kuno, M.; Kamat, P. V., Tracking Iodide and Bromide Ion Segregation in Mixed Halide Lead Perovskites during Photoirradiation. *ACS Energy Lett.* **2016,** 1, 290-296.

(105) Das, C.; Wussler, M.; Hellmann, T.; Mayer, T.; Jaegermann, W., In situ XPS study of the surface chemistry of MAPI solar cells under operating conditions in vacuum. *Phys. Chem. Chem. Phys.* **2018,** 20, 17180-17187.

(106) Hong, Q.-M.; Xu, R.-P.; Jin, T.-Y.; Tang, J.-X.; Li, Y.-Q., Unraveling the light-induced degradation mechanism of CH3NH3PbI3 perovskite films. *Org. Electron.* **2019,** 67, 19-25.

(107) Xu, R.-P.; Li, Y.-Q.; Jin, T.-Y.; Liu, Y.-Q.; Bao, Q.-Y.; O'Carroll, C.; Tang, J.-X., In Situ Observation of Light Illumination-Induced Degradation in Organometal Mixed-Halide Perovskite Films. *ACS Appl. Mater. Int.* **2018,** 10, 6737-6746.

(108) Huang, W.; Yoon, S. J.; Sapkota, P., Effect of Light Illumination on Mixed Halide Lead Perovskites: Reversible or Irreversible Transformation. *ACS Appl. Energy Mater.* **2018,** 1, 2859-2865.

(109) Hoke, E. T.; Slotcavage, D. J.; Dohner, E. R.; Bowring, A. R.; Karunadasa, H. I.; McGehee, M. D., Reversible photo-induced trap formation in mixed-halide hybrid perovskites for photovoltaics. *Chem. Sci.* **2015,** 6, 613-617.

(110) deQuilettes, D. W.; Zhang, W.; Burlakov, V. M.; Graham, D. J.; Leijtens, T.; Osherov, A.; Bulović, V.; Snaith, H. J.; Ginger, D. S.; Stranks, S. D., Photo-induced halide redistribution in organic–inorganic perovskite films. *Nat. Commun.* **2016,** 7, 11683.

(111) Tang, X.; Brandl, M.; May, B.; Levchuk, I.; Hou, Y.; Richter, M.; Chen, H.; Chen, S.; Kahmann, S.; Osvet, A.; Maier, F.; Steinrück, H.-P.; Hock, R.; Matt, G. J.; Brabec, C. J., Photoinduced degradation of methylammonium lead triiodide perovskite semiconductors. *J. Mater. Chem. A* **2016,** 4, 15896-15903.

(112) Li, Y.; Xu, X.; Wang, C.; Ecker, B.; Yang, J.; Huang, J.; Gao, Y., Light-Induced Degradation of CH3NH3PbI3 Hybrid Perovskite Thin Film. *J. Phys. Chem. C* **2017,** 121, 3904-3910.

(113) Long, M.; Zhang, T.; Liu, M.; Chen, Z.; Wang, C.; Xie, W.; Xie, F.; Chen, J.; Li, G.; Xu, J., Abnormal Synergetic Effect of Organic and Halide Ions on the Stability and Optoelectronic Properties of a Mixed Perovskite via In Situ Characterizations. *Adv. Mater.* **2018,** 30, 1801562.

(114) Bryant, D.; Aristidou, N.; Pont, S.; Sanchez-Molina, I.; Chotchunangatchaval, T.; Wheeler, S.; Durrant, J. R.; Haque, S. A., Light and oxygen induced degradation limits the operational stability of methylammonium lead triiodide perovskite solar cells. *Energy Environ. Sci.* **2016,** 9, 1655-1660.

(115) Senocrate, A.; Acartürk, T.; Kim, G. Y.; Merkle, R.; Starke, U.; Grätzel, M.; Maier, J., Interaction of oxygen with halide perovskites. *J. Mater. Chem. A* **2018,** 6, 10847-10855.

(116) Abdelmageed, G.; Jewell, L.; Hellier, K.; Seymour, L.; Luo, B.; Bridges, F.; Zhang, J. Z.; Carter, S., Mechanisms for light induced degradation in MAPbI3 perovskite thin films and solar cells. *Appl. Phys. Lett.* **2016,** 109, 233905.

(117) Leijtens, T.; Eperon, G. E.; Pathak, S.; Abate, A.; Lee, M. M.; Snaith, H. J., Overcoming ultraviolet light instability of sensitized TiO2 with meso-superstructured organometal tri-halide perovskite solar cells. *Nat. Commun.* **2013,** 4, 2885.

(118) Habisreutinger, S. N.; Leijtens, T.; Eperon, G. E.; Stranks, S. D.; Nicholas, R. J.; Snaith, H. J., Carbon Nanotube/Polymer Composites as a Highly Stable Hole Collection Layer in Perovskite Solar Cells. *Nano Lett.* **2014,** 14, 5561-5568.

(119) Li, Z.; Xiao, C.; Yang, Y.; Harvey, S. P.; Kim, D. H.; Christians, J. A.; Yang, M.; Schulz, P.; Nanayakkara, S. U.; Jiang, C.-S.; Luther, J. M.; Berry, J. J.; Beard, M. C.; Al-Jassim, M. M.; Zhu, K., Extrinsic ion migration in perovskite solar cells. *Energy Environ. Sci.* **2017,** 10, 1234-1242.

(120) Bailie, C. D.; Unger, E. L.; Zakeeruddin, S. M.; Grätzel, M.; McGehee, M. D., Melt-infiltration of spiro-OMeTAD and thermal instability of solid-state dye-sensitized solar cells. *Phys. Chem. Chem. Phys.* **2014,** 16, 4864-4870.

(121) Jena, A. K.; Ikegami, M.; Miyasaka, T., Severe Morphological Deformation of Spiro-OMeTAD in (CH3NH3)PbI3 Solar Cells at High Temperature. *ACS Energy Lett.* **2017,** 2, 1760-1761.

(122) Kato, Y.; Ono, L. K.; Lee, M. V.; Wang, S.; Raga, S. R.; Qi, Y., Silver Iodide Formation in Methyl Ammonium Lead Iodide Perovskite Solar Cells with Silver Top Electrodes. *Adv. Mater. Interfaces* **2015,** 2, 1500195.

(123) Han, Y.; Meyer, S.; Dkhissi, Y.; Weber, K.; Pringle, J. M.; Bach, U.; Spiccia, L.; Cheng, Y.-B., Degradation observations of encapsulated planar CH3NH3PbI3 perovskite solar cells at high temperatures and humidity. *J. Mater. Chem. A* **2015,** 3, 8139-8147.

(124) Divitini, G.; Cacovich, S.; Matteocci, F.; Cinà, L.; Di Carlo, A.; Ducati, C., In situ observation of heat-induced degradation of perovskite solar cells. *Nat. Energy* **2016,** 1, 15012.

(125) Domanski, K.; Correa-Baena, J.-P.; Mine, N.; Nazeeruddin, M. K.; Abate, A.; Saliba, M.; Tress, W.; Hagfeldt, A.; Grätzel, M., Not All That Glitters Is Gold: Metal-Migration-Induced Degradation in Perovskite Solar Cells. *ACS Nano* **2016,** 10, 6306-6314.

(126) Noh, J. H.; Im, S. H.; Heo, J. H.; Mandal, T. N.; Seok, S. I., Chemical Management for Colorful, Efficient, and Stable Inorganic–Organic Hybrid Nanostructured Solar Cells. *Nano Lett.* **2013,** 13, 1764-1769.

(127) Suarez, B.; Gonzalez-Pedro, V.; Ripolles, T. S.; Sanchez, R. S.; Otero, L.; Mora-Sero, I., Recombination Study of Combined Halides (Cl, Br, I) Perovskite Solar Cells. *J. Phys. Chem. Lett.* **2014,** 5, 1628-1635.

(128) Kulkarni, S. A.; Baikie, T.; Boix, P. P.; Yantara, N.; Mathews, N.; Mhaisalkar, S., Band-gap tuning of lead halide perovskites using a sequential deposition process. *J. Mater. Chem. A* **2014,** 2, 9221-9225.

(129) Samu, G. F.; Janáky, C.; Kamat, P. V., A Victim of Halide Ion Segregation. How Light Soaking Affects Solar Cell Performance of Mixed Halide Lead Perovskites. *ACS Energy Lett.* **2017,** 2, 1860-1861.

(130) Yoon, S. J.; Kuno, M.; Kamat, P. V., Shift Happens. How Halide Ion Defects Influence Photoinduced Segregation in Mixed Halide Perovskites. *ACS Energy Lett.* **2017,** 2, 1507-1514.

(131) Mahesh, S.; Ball, J. M.; Oliver, R. D. J.; McMeekin, D. P.; Nayak, P. K.; Johnston, M. B.; Snaith, H. J., Revealing the origin of voltage loss in mixed-halide perovskite solar cells. *Energy Environ. Sci.* **2020,** 13, 258-267.

(132) Buin, A.; Comin, R.; Xu, J.; Ip, A. H.; Sargent, E. H., Halide-Dependent Electronic Structure of Organolead Perovskite Materials. *Chem. Mater.* **2015,** 27, 4405-4412.

(133) Tai, Q.; You, P.; Sang, H.; Liu, Z.; Hu, C.; Chan, H. L. W.; Yan, F., Efficient and stable perovskite solar cells prepared in ambient air irrespective of the humidity. *Nat. Commun.* **2016,** 7, 11105.

(134) Jiang, Q.; Rebollar, D.; Gong, J.; Piacentino, E. L.; Zheng, C.; Xu, T., Pseudohalide-Induced Moisture Tolerance in Perovskite CH3NH3Pb(SCN)2I Thin Films. *Angew. Chem., Int. Ed.* **2015,** 54, 7617-7620.

(135) Lee, J.-W.; Kim, D.-H.; Kim, H.-S.; Seo, S.-W.; Cho, S. M.; Park, N.-G., Formamidinium and Cesium Hybridization for Photo- and Moisture-Stable Perovskite Solar Cell. *Adv. Energy Mater.* **2015,** 5, 1501310.

(136) Li, Z.; Yang, M.; Park, J.-S.; Wei, S.-H.; Berry, J. J.; Zhu, K., Stabilizing Perovskite Structures by Tuning Tolerance Factor: Formation of Formamidinium and Cesium Lead Iodide Solid-State Alloys. *Chem. Mater.* **2016,** 28, 284-292.

(137) Yi, C.; Luo, J.; Meloni, S.; Boziki, A.; Ashari-Astani, N.; Grätzel, C.; Zakeeruddin, S. M.; Röthlisberger, U.; Grätzel, M., Entropic stabilization of mixed A-cation ABX3 metal halide perovskites for high performance perovskite solar cells. *Energy Environ. Sci.* **2016,** 9, 656-662.

(138) Leyden, M. R.; Lee, M. V.; Raga, S. R.; Qi, Y., Large formamidinium lead trihalide perovskite solar cells using chemical vapor deposition with high reproducibility and tunable chlorine concentrations. *J. Mater. Chem. A* **2015,** 3, 16097-16103.

(139) Frost, J. M.; Butler, K. T.; Brivio, F.; Hendon, C. H.; van Schilfgaarde, M.; Walsh, A., Atomistic Origins of High-Performance in Hybrid Halide Perovskite Solar Cells. *Nano Lett.* **2014,** 14, 2584-2590.

(140) Poorkazem, K.; Kelly, T. L., Compositional Engineering To Improve the Stability of Lead Halide Perovskites: A Comparative Study of Cationic and Anionic Dopants. *ACS Appl. Energy Mater.* **2018,** 1, 181-190.

(141) Saliba, M.; Matsui, T.; Seo, J.-Y.; Domanski, K.; Correa-Baena, J.-P.; Nazeeruddin, M. K.; Zakeeruddin, S. M.; Tress, W.; Abate, A.; Hagfeldt, A.; Grätzel, M., Cesium-containing triple cation perovskite solar cells: improved stability, reproducibility and high efficiency. *Energy Environ. Sci.* **2016,** 9, 1989-1997.

(142) Smith, I. C.; Hoke, E. T.; Solis-Ibarra, D.; McGehee, M. D.; Karunadasa, H. I., A Layered Hybrid Perovskite Solar-Cell Absorber with Enhanced Moisture Stability. *Angew. Chem., Int. Ed.* **2014,** 53, 11232-11235.

(143) Yang, S.; Wang, Y.; Liu, P.; Cheng, Y.-B.; Zhao, H. J.; Yang, H. G., Functionalization of perovskite thin films with moisture-tolerant molecules. *Nat. Energy* **2016,** 1, 15016.

(144) Koh, T. M.; Thirumal, K.; Soo, H. S.; Mathews, N., Multidimensional Perovskites: A Mixed Cation Approach Towards Ambient Stable and Tunable Perovskite Photovoltaics. *ChemSusChem* **2016,** 9, 2541-2558.

(145) Tsai, H.; Nie, W.; Blancon, J.-C.; Stoumpos, C. C.; Asadpour, R.; Harutyunyan, B.; Neukirch, A. J.; Verduzco, R.; Crochet, J. J.; Tretiak, S.; Pedesseau, L.; Even, J.; Alam, M. A.; Gupta, G.; Lou, J.; Ajayan, P. M.; Bedzyk, M. J.; Kanatzidis, M. G.; Mohite, A. D., High-efficiency two-dimensional Ruddlesden–Popper perovskite solar cells. *Nature* **2016,** 536, 312-316.

(146) Dou, L.; Wong, A. B.; Yu, Y.; Lai, M.; Kornienko, N.; Eaton, S. W.; Fu, A.; Bischak, C. G.; Ma, J.; Ding, T.; Ginsberg, N. S.; Wang, L.-W.; Alivisatos, A. P.; Yang, P., Atomically thin two-dimensional organic-inorganic hybrid perovskites. *Science* **2015,** 349, 1518-1521.

(147) Huo, C.; Cai, B.; Yuan, Z.; Ma, B.; Zeng, H., Two-Dimensional Metal Halide Perovskites: Theory, Synthesis, and Optoelectronics. *Small Methods* **2017,** 1, 1600018.

(148) Thrithamarassery Gangadharan, D.; Ma, D., Searching for stability at lower dimensions: current trends and future prospects of layered perovskite solar cells. *Energy Environ. Sci.* **2019,** 12, 2860-2889.

(149) Quan, L. N.; Yuan, M.; Comin, R.; Voznyy, O.; Beauregard, E. M.; Hoogland, S.; Buin, A.; Kirmani, A. R.; Zhao, K.; Amassian, A.; Kim, D. H.; Sargent, E. H., Ligand-Stabilized Reduced-Dimensionality Perovskites. *J. Am. Chem. Soc.* **2016,** 138, 2649-2655.

(150) Grancini, G.; Roldán-Carmona, C.; Zimmermann, I.; Mosconi, E.; Lee, X.; Martineau, D.; Narbey, S.; Oswald, F.; De Angelis, F.; Graetzel, M.; Nazeeruddin, M. K., One-Year stable perovskite solar cells by 2D/3D interface engineering. *Nat. Commun.* **2017,** 8, 15684.

(151) Wang, Z.; Lin, Q.; Chmiel, F. P.; Sakai, N.; Herz, L. M.; Snaith, H. J., Efficient ambient-air-stable solar cells with 2D–3D heterostructured butylammonium-caesium-formamidinium lead halide perovskites. *Nat. Energy* **2017,** 2, 17135.

(152) Lee, D. S.; Yun, J. S.; Kim, J.; Soufiani, A. M.; Chen, S.; Cho, Y.; Deng, X.; Seidel, J.; Lim, S.; Huang, S.; Ho-Baillie, A. W. Y., Passivation of Grain Boundaries by Phenethylammonium in Formamidinium-Methylammonium Lead Halide Perovskite Solar Cells. *ACS Energy Lett.* **2018,** 3, 647-654.

(153) Hu, Y.; Qiu, T.; Bai, F.; Ruan, W.; Zhang, S., Highly Efficient and Stable Solar Cells with 2D MA3Bi2I9/3D MAPbI3 Heterostructured Perovskites. *Adv. Energy Mater.* **2018,** 8, 1703620.

(154) Yun, J. S.; Kim, J.; Young, T.; Patterson, R. J.; Kim, D.; Seidel, J.; Lim, S.; Green, M. A.; Huang, S.; Ho-Baillie, A., Humidity-Induced Degradation via Grain Boundaries of HC(NH2)2PbI3 Planar Perovskite Solar Cells. *Adv. Funct. Mater.* **2018,** 28, 1705363.

(155) Wang, Q.; Chen, B.; Liu, Y.; Deng, Y.; Bai, Y.; Dong, Q.; Huang, J., Scaling behavior of moisture-induced grain degradation in polycrystalline hybrid perovskite thin films. *Energy Environ. Sci.* **2017,** 10, 516-522.

(156) Liao, H.-C.; Guo, P.; Hsu, C.-P.; Lin, M.; Wang, B.; Zeng, L.; Huang, W.; Soe, C. M. M.; Su, W.-F.; Bedzyk, M. J.; Wasielewski, M. R.; Facchetti, A.; Chang, R. P. H.; Kanatzidis, M. G.; Marks, T. J.,

Enhanced Efficiency of Hot-Cast Large-Area Planar Perovskite Solar Cells/Modules Having Controlled Chloride Incorporation. *Adv. Energy Mater.* **2017,** 7, 1601660.

(157) Xiao, Z.; Dong, Q.; Bi, C.; Shao, Y.; Yuan, Y.; Huang, J., Solvent Annealing of Perovskite-Induced Crystal Growth for Photovoltaic-Device Efficiency Enhancement. *Adv. Mater.* **2014,** 26, 6503-6509.

(158) Zhao, Y.; Wei, J.; Li, H.; Yan, Y.; Zhou, W.; Yu, D.; Zhao, Q., A polymer scaffold for self-healing perovskite solar cells. *Nat. Commun.* **2016,** 7, 10228.

(159) Zhao, H.; Wang, S.; Sun, M.; Zhang, F.; Li, X.; Xiao, Y., Enhanced stability and optoelectronic properties of MAPbI3 films by a cationic surface-active agent for perovskite solar cells. *J. Mater. Chem. A* **2018,** 6, 10825-10834.

(160) Zhang, F.; Shi, W.; Luo, J.; Pellet, N.; Yi, C.; Li, X.; Zhao, X.; Dennis, T. J. S.; Li, X.; Wang, S.; Xiao, Y.; Zakeeruddin, S. M.; Bi, D.; Grätzel, M., Isomer-Pure Bis-PCBM-Assisted Crystal Engineering of Perovskite Solar Cells Showing Excellent Efficiency and Stability. *Adv. Mater.* **2017,** 29, 1606806.

(161) Qian, F.; Yuan, S.; Cai, Y.; Han, Y.; Zhao, H.; Sun, J.; Liu, Z.; Liu, S., Novel Surface Passivation for Stable FA0.85MA0.15PbI3 Perovskite Solar Cells with 21.6% Efficiency. *Solar RRL* **2019,** 3, 1900072.

(162) Carvalho, B. A. d.; Kavadiya, S.; Huang, S.; Niedzwiedzki, D. M.; Biswas, P., Highly Stable Perovskite Solar Cells Fabricated Under Humid Ambient Conditions. *IEEE J. Photovolt.* **2017,** 7, 532-538.

(163) Kim, W.; Park, J. B.; Kim, H.; Kim, K.; Park, J.; Cho, S.; Lee, H.; Pak, Y.; Jung, G. Y., Enhanced long-term stability of perovskite solar cells by passivating grain boundary with polydimethylsiloxane (PDMS). *J. Mater. Chem. A* **2019,** 7, 20832-20839.

(164) Bi, D.; Yi, C.; Luo, J.; Décoppet, J.-D.; Zhang, F.; Zakeeruddin, Shaik M.; Li, X.; Hagfeldt, A.; Grätzel, M., Polymer-templated nucleation and crystal growth of perovskite films for solar cells with efficiency greater than 21%. *Nat. Energy* **2016,** 1, 16142.

(165) Hu, Y.; Schlipf, J.; Wussler, M.; Petrus, M. L.; Jaegermann, W.; Bein, T.; Müller-Buschbaum, P.; Docampo, P., Hybrid Perovskite/Perovskite Heterojunction Solar Cells. *ACS Nano* **2016,** 10, 5999-6007.

(166) Bai, Y.; Xiao, S.; Hu, C.; Zhang, T.; Meng, X.; Lin, H.; Yang, Y.; Yang, S., Dimensional Engineering of a Graded 3D–2D Halide Perovskite Interface Enables Ultrahigh Voc Enhanced Stability in the p-i-n Photovoltaics. *Adv. Energy Mater.* **2017,** 7, 1701038.

(167) Bi, D.; Gao, P.; Scopelliti, R.; Oveisi, E.; Luo, J.; Grätzel, M.; Hagfeldt, A.; Nazeeruddin, M. K., High-Performance Perovskite Solar Cells with Enhanced Environmental Stability Based on Amphiphile-Modified CH3NH3PbI3. *Adv. Mater.* **2016,** 28, 2910-2915.

(168) Abdelmageed, G.; Sully, H. R.; Bonabi Naghadeh, S.; El-Hag Ali, A.; Carter, S. A.; Zhang, J. Z., Improved Stability of Organometal Halide Perovskite Films and Solar Cells toward Humidity via Surface Passivation with Oleic Acid. *ACS Appl. Energy Mater.* **2018,** 1, 387-392.

(169) Li, X.; Ibrahim Dar, M.; Yi, C.; Luo, J.; Tschumi, M.; Zakeeruddin, S. M.; Nazeeruddin, M. K.; Han, H.; Grätzel, M., Improved performance and stability of perovskite solar cells by crystal crosslinking with alkylphosphonic acid ω-ammonium chlorides. *Nat. Chem.* **2015,** 7, 703-711.

(170) Zhou, P.; Bu, T.; Shi, S.; Li, L.; Zhang, Y.; Ku, Z.; Peng, Y.; Zhong, J.; Cheng, Y.-B.; Huang, F., Efficient and stable mixed perovskite solar cells using P3HT as a hole transporting layer. *J. Mater. Chem. C* **2018,** 6, 5733-5737.

(171) Valero, S.; Collavini, S.; Völker, S. F.; Saliba, M.; Tress, W. R.; Zakeeruddin, S. M.; Grätzel, M.; Delgado, J. L., Dopant-Free Hole-Transporting Polymers for Efficient and Stable Perovskite Solar Cells. *Macromolecules* **2019,** 52, 2243-2254.

(172) Kwon, Y. S.; Lim, J.; Yun, H.-J.; Kim, Y.-H.; Park, T., A diketopyrrolopyrrole-containing hole transporting conjugated polymer for use in efficient stable organic–inorganic hybrid solar cells based on a perovskite. *Energy Environ. Sci.* **2014,** 7, 1454-1460.

(173) Leijtens, T.; Giovenzana, T.; Habisreutinger, S. N.; Tinkham, J. S.; Noel, N. K.; Kamino, B. A.; Sadoughi, G.; Sellinger, A.; Snaith, H. J., Hydrophobic Organic Hole Transporters for Improved Moisture Resistance in Metal Halide Perovskite Solar Cells. *ACS Appl. Mater. Int.* **2016,** 8, 5981-5989.

(174) Wang, Y.-K.; Yuan, Z.-C.; Shi, G.-Z.; Li, Y.-X.; Li, Q.; Hui, F.; Sun, B.-Q.; Jiang, Z.-Q.; Liao, L.-S., Dopant-Free Spiro-Triphenylamine/Fluorene as Hole-Transporting Material for Perovskite Solar Cells with Enhanced Efficiency and Stability. *Adv. Funct. Mater.* **2016,** 26, 1375-1381.

(175) Liu, J.; Wu, Y.; Qin, C.; Yang, X.; Yasuda, T.; Islam, A.; Zhang, K.; Peng, W.; Chen, W.; Han, L., A dopant-free hole-transporting material for efficient and stable perovskite solar cells. *Energy Environ. Sci.* **2014,** 7, 2963-2967.

(176) Liu, Y.; Chen, Q.; Duan, H.-S.; Zhou, H.; Yang, Y.; Chen, H.; Luo, S.; Song, T.-B.; Dou, L.; Hong, Z.; Yang, Y., A dopant-free organic hole transport material for efficient planar heterojunction perovskite solar cells. *J. Mater. Chem. A* **2015,** 3, 11940-11947.

(177) Liu, Y.; Hong, Z.; Chen, Q.; Chen, H.; Chang, W.-H.; Yang, Y.; Song, T.-B.; Yang, Y., Perovskite Solar Cells Employing Dopant-Free Organic Hole Transport Materials with Tunable Energy Levels. *Adv. Mater.* **2016,** 28, 440-446.

(178) Ma, Y.; Chung, Y.-H.; Zheng, L.; Zhang, D.; Yu, X.; Xiao, L.; Chen, Z.; Wang, S.; Qu, B.; Gong, Q.; Zou, D., Improved Hole-Transporting Property via HAT-CN for Perovskite Solar Cells without Lithium Salts. *ACS Appl. Mater. Int.* **2015,** 7, 6406-6411.

(179) Zhang, F.; Yi, C.; Wei, P.; Bi, X.; Luo, J.; Jacopin, G.; Wang, S.; Li, X.; Xiao, Y.; Zakeeruddin, S. M.; Grätzel, M., A Novel Dopant-Free Triphenylamine Based Molecular "Butterfly" Hole-Transport Material for Highly Efficient and Stable Perovskite Solar Cells. *Adv. Energy Mater.* **2016,** 6, 1600401.

(180) Kim, G.-W.; Kang, G.; Kim, J.; Lee, G.-Y.; Kim, H. I.; Pyeon, L.; Lee, J.; Park, T., Dopant-free polymeric hole transport materials for highly efficient and stable perovskite solar cells. *Energy Environ. Sci.* **2016,** 9, 2326-2333.

(181) Jiang, X.; Wang, D.; Yu, Z.; Ma, W.; Li, H.-B.; Yang, X.; Liu, F.; Hagfeldt, A.; Sun, L., Molecular Engineering of Copper Phthalocyanines: A Strategy in Developing Dopant-Free Hole-Transporting Materials for Efficient and Ambient-Stable Perovskite Solar Cells. *Adv. Energy Mater.* **2019,** 9, 1803287.

(182) Xu, J.; Voznyy, O.; Comin, R.; Gong, X.; Walters, G.; Liu, M.; Kanjanaboos, P.; Lan, X.; Sargent, E. H., Crosslinked Remote-Doped Hole-Extracting Contacts Enhance Stability under Accelerated Lifetime Testing in Perovskite Solar Cells. *Adv. Mater.* **2016,** 28, 2807-2815.

(183) Mali, S. S.; Patil, J. V.; Kim, H.; Luque, R.; Hong, C. K., Highly efficient thermally stable perovskite solar cells via Cs:NiOx/CuSCN double-inorganic hole extraction layer interface engineering. *Materials Today* **2019,** 26, 8-18.

(184) Kim, J. H.; Liang, P.-W.; Williams, S. T.; Cho, N.; Chueh, C.-C.; Glaz, M. S.; Ginger, D. S.; Jen, A. K.-Y., High-Performance and Environmentally Stable Planar Heterojunction Perovskite Solar Cells Based on a Solution-Processed Copper-Doped Nickel Oxide Hole-Transporting Layer. *Adv. Mater.* **2015,** 27, 695-701.

(185) Cao, J.; Yu, H.; Zhou, S.; Qin, M.; Lau, T.-K.; Lu, X.; Zhao, N.; Wong, C.-P., Low-temperature solution-processed NiOx films for air-stable perovskite solar cells. *J. Mater. Chem. A* **2017,** 5, 11071-11077.

(186) Zhang, H.; Wang, H.; Chen, W.; Jen, A. K.-Y., CuGaO2: A Promising Inorganic Hole-Transporting Material for Highly Efficient and Stable Perovskite Solar Cells. *Adv. Mater.* **2017,** 29, 1604984.

(187) Akin, S.; Liu, Y.; Dar, M. I.; Zakeeruddin, S. M.; Grätzel, M.; Turan, S.; Sonmezoglu, S., Hydrothermally processed CuCrO2 nanoparticles as an inorganic hole transporting material for low-cost perovskite solar cells with superior stability. *J. Mater. Chem. A* **2018,** 6, 20327-20337.

(188) Jung, E. H.; Jeon, N. J.; Park, E. Y.; Moon, C. S.; Shin, T. J.; Yang, T.-Y.; Noh, J. H.; Seo, J., Efficient, stable and scalable perovskite solar cells using poly(3-hexylthiophene). *Nature* **2019,** 567, 511-515.

(189) Yang, J.; Fransishyn, K. M.; Kelly, T. L., Comparing the Effect of Mesoporous and Planar Metal Oxides on the Stability of Methylammonium Lead Iodide Thin Films. *Chem. Mater.* **2016,** 28, 7344-7352.

(190) Yin, J.; Cao, J.; He, X.; Yuan, S.; Sun, S.; Li, J.; Zheng, N.; Lin, L., Improved stability of perovskite solar cells in ambient air by controlling the mesoporous layer. *J. Mater. Chem. A* **2015,** 3, 16860-16866.

(191) You, J.; Meng, L.; Song, T.-B.; Guo, T.-F.; Yang, Y.; Chang, W.-H.; Hong, Z.; Chen, H.; Zhou, H.; Chen, Q.; Liu, Y.; De Marco, N.; Yang, Y., Improved air stability of perovskite solar cells via solution-processed metal oxide transport layers. *Nat. Nanotechnol.* **2016,** 11, 75-81.

(192) Zhu, Z.; Bai, Y.; Liu, X.; Chueh, C.-C.; Yang, S.; Jen, A. K.-Y., Enhanced Efficiency and Stability of Inverted Perovskite Solar Cells Using Highly Crystalline SnO2 Nanocrystals as the Robust Electron-Transporting Layer. *Adv. Mater.* **2016,** 28, 6478-6484.

(193) Hu, T.; Xiao, S.; Yang, H.; Chen, L.; Chen, Y., Cerium oxide as an efficient electron extraction layer for p–i–n structured perovskite solar cells. *Chem. Commun.* **2018,** 54, 471-474.

(194) Liu, X.; Chueh, C.-C.; Zhu, Z.; Jo, S. B.; Sun, Y.; Jen, A. K. Y., Highly crystalline Zn2SnO4 nanoparticles as efficient electron-transporting layers toward stable inverted and flexible conventional perovskite solar cells. *J. Mater. Chem. A* **2016,** 4, 15294-15301.

(195) Mei, A.; Li, X.; Liu, L.; Ku, Z.; Liu, T.; Rong, Y.; Xu, M.; Hu, M.; Chen, J.; Yang, Y.; Grätzel, M.; Han, H., A hole-conductor–free, fully printable mesoscopic perovskite solar cell with high stability. *Science* **2014,** 345, 295-298.

(196) Wei, Z.; Chen, H.; Yan, K.; Yang, S., Inkjet Printing and Instant Chemical Transformation of a CH3NH3PbI3/Nanocarbon Electrode and Interface for Planar Perovskite Solar Cells. *Angew. Chem., Int. Ed.* **2014,** 53, 13239-13243.

(197) Xu, X.; Liu, Z.; Zuo, Z.; Zhang, M.; Zhao, Z.; Shen, Y.; Zhou, H.; Chen, Q.; Yang, Y.; Wang, M., Hole Selective NiO Contact for Efficient Perovskite Solar Cells with Carbon Electrode. *Nano Lett.* **2015,** 15, 2402-2408.

(198) Wei, H.; Xiao, J.; Yang, Y.; Lv, S.; Shi, J.; Xu, X.; Dong, J.; Luo, Y.; Li, D.; Meng, Q., Free-standing flexible carbon electrode for highly efficient hole-conductor-free perovskite solar cells. *Carbon* **2015,** 93, 861-868.

(199) Hu, Y.; Si, S.; Mei, A.; Rong, Y.; Liu, H.; Li, X.; Han, H., Stable Large-Area (10 × 10 cm2) Printable Mesoscopic Perovskite Module Exceeding 10% Efficiency. *Solar RRL* **2017,** 1, 1600019.

(200) Li, X.; Tschumi, M.; Han, H.; Babkair, S. S.; Alzubaydi, R. A.; Ansari, A. A.; Habib, S. S.; Nazeeruddin, M. K.; Zakeeruddin, S. M.; Grätzel, M., Outdoor Performance and Stability under Elevated Temperatures and Long-Term Light Soaking of Triple-Layer Mesoporous Perovskite Photovoltaics. *Energy Technol.* **2015,** 3, 551-555.

(201) Zhao, J.; Brinkmann, K. O.; Hu, T.; Pourdavoud, N.; Becker, T.; Gahlmann, T.; Heiderhoff, R.; Polywka, A.; Görrn, P.; Chen, Y.; Cheng, B.; Riedl, T., Self-Encapsulating Thermostable and Air-Resilient Semitransparent Perovskite Solar Cells. *Adv. Energy Mater.* **2017,** 7, 1602599.

(202) Bush, K. A.; Bailie, C. D.; Chen, Y.; Bowring, A. R.; Wang, W.; Ma, W.; Leijtens, T.; Moghadam, F.; McGehee, M. D., Thermal and Environmental Stability of Semi-Transparent Perovskite Solar Cells for Tandems Enabled by a Solution-Processed Nanoparticle Buffer Layer and Sputtered ITO Electrode. *Adv. Mater.* **2016,** 28, 3937-3943.

(203) Kaltenbrunner, M.; Adam, G.; Głowacki, E. D.; Drack, M.; Schwödiauer, R.; Leonat, L.; Apaydin, D. H.; Groiss, H.; Scharber, M. C.; White, M. S.; Sariciftci, N. S.; Bauer, S., Flexible high power-per-weight perovskite solar cells with chromium oxide–metal contacts for improved stability in air. *Nat. Mater.* **2015,** 14, 1032-1039.

(204) Dong, X.; Fang, X.; Lv, M.; Lin, B.; Zhang, S.; Ding, J.; Yuan, N., Improvement of the humidity stability of organic–inorganic perovskite solar cells using ultrathin Al2O3 layers prepared by atomic layer deposition. *J. Mater. Chem. A* **2015,** 3, 5360-5367.

(205) Koushik, D.; Verhees, W. J. H.; Kuang, Y.; Veenstra, S.; Zhang, D.; Verheijen, M. A.; Creatore, M.; Schropp, R. E. I., High-efficiency humidity-stable planar perovskite solar cells based on atomic layer architecture. *Energy Environ. Sci.* **2017,** 10, 91-100.

(206) Sanehira, E. M.; Tremolet de Villers, B. J.; Schulz, P.; Reese, M. O.; Ferrere, S.; Zhu, K.; Lin, L. Y.; Berry, J. J.; Luther, J. M., Influence of Electrode Interfaces on the Stability of Perovskite Solar Cells: Reduced Degradation Using MoOx/Al for Hole Collection. *ACS Energy Lett.* **2016,** 1, 38-45.

(207) Arora, N.; Dar, M. I.; Hinderhofer, A.; Pellet, N.; Schreiber, F.; Zakeeruddin, S. M.; Grätzel, M., Perovskite solar cells with CuSCN hole extraction layers yield stabilized efficiencies greater than 20%. *Science* **2017,** 358, 768-771.

(208) Zhang, J.; Hu, Z.; Huang, L.; Yue, G.; Liu, J.; Lu, X.; Hu, Z.; Shang, M.; Han, L.; Zhu, Y., Bifunctional alkyl chain barriers for efficient perovskite solar cells. *Chem. Commun.* **2015,** 51, 7047-7050.

(209) Cao, J.; Yin, J.; Yuan, S.; Zhao, Y.; Li, J.; Zheng, N., Thiols as interfacial modifiers to enhance the performance and stability of perovskite solar cells. *Nanoscale* **2015,** 7, 9443-9447.

(210) Fang, R.; Wu, S.; Chen, W.; Liu, Z.; Zhang, S.; Chen, R.; Yue, Y.; Deng, L.; Cheng, Y.-B.; Han, L.; Chen, W., [6,6]-Phenyl-C61-Butyric Acid Methyl Ester/Cerium Oxide Bilayer Structure as Efficient and Stable Electron Transport Layer for Inverted Perovskite Solar Cells. *ACS Nano* **2018,** 12, 2403-2414.

(211) Brinkmann, K. O.; Zhao, J.; Pourdavoud, N.; Becker, T.; Hu, T.; Olthof, S.; Meerholz, K.; Hoffmann, L.; Gahlmann, T.; Heiderhoff, R.; Oszajca, M. F.; Luechinger, N. A.; Rogalla, D.; Chen, Y.; Cheng, B.; Riedl, T., Suppressed decomposition of organometal halide perovskites by impermeable electron-extraction layers in inverted solar cells. *Nat. Commun.* **2017,** 8, 13938.

(212) Wu, S.; Chen, R.; Zhang, S.; Babu, B. H.; Yue, Y.; Zhu, H.; Yang, Z.; Chen, C.; Chen, W.; Huang, Y.; Fang, S.; Liu, T.; Han, L.; Chen, W., A chemically inert bismuth interlayer enhances long-term stability of inverted perovskite solar cells. *Nat. Commun.* **2019,** 10, 1161.

(213) Bi, E.; Chen, H.; Xie, F.; Wu, Y.; Chen, W.; Su, Y.; Islam, A.; Grätzel, M.; Yang, X.; Han, L., Diffusion engineering of ions and charge carriers for stable efficient perovskite solar cells. *Nat. Commun.* **2017,** 8, 15330.

(214) Jiang, Z., GIXSGUI: a MATLAB toolbox for grazing-incidence X-ray scattering data visualization and reduction, and indexing of buried three-dimensional periodic nanostructured films. *J. Appl. Crystallogr.* **2015,** 48, 917-926.

(215) Schlipf, J.; Müller-Buschbaum, P., Structure of Organometal Halide Perovskite Films as Determined with Grazing-Incidence X-Ray Scattering Methods. *Adv. Energy Mater.* **2017,** 7, 1700131.

(216) Hildner, R.; Köhler, A.; Müller-Buschbaum, P.; Panzer, F.; Thelakkat, M., π-Conjugated Donor Polymers: Structure Formation and Morphology in Solution, Bulk and Photovoltaic Blends. *Adv. Energy Mater.* **2017,** 7, 1700314.

(217) Richter, L. J.; DeLongchamp, D. M.; Amassian, A., Morphology Development in Solution-Processed Functional Organic Blend Films: An In Situ Viewpoint. *Chem. Rev.* **2017,** 117, 6332-6366.

(218) Müller-Buschbaum, P., The Active Layer Morphology of Organic Solar Cells Probed with Grazing Incidence Scattering Techniques. *Adv. Mater.* **2014,** 26, 7692-7709.

(219) Altamura, D.; Sibillano, T.; Siliqi, D.; Caro, L. D.; Giannini, C., Assembled Nanostructured Architectures Studied by Grazing Incidence X-Ray Scattering. *Nanomater. Nanotechnol.* **2012,** 2, 16.

(220) Reinspach, J. A.; Diao, Y.; Giri, G.; Sachse, T.; England, K.; Zhou, Y.; Tassone, C.; Worfolk, B. J.; Presselt, M.; Toney, M. F.; Mannsfeld, S.; Bao, Z., Tuning the Morphology of Solution-Sheared P3HT:PCBM Films. *ACS Appl. Mater. Int.* **2016,** 8, 1742-1751.

(221) Verploegen, E.; Miller, C. E.; Schmidt, K.; Bao, Z.; Toney, M. F., Manipulating the Morphology of P3HT–PCBM Bulk Heterojunction Blends with Solvent Vapor Annealing. *Chem. Mater.* **2012,** 24, 3923-3931.

(222) Schmidt-Hansberg, B.; Sanyal, M.; Klein, M. F. G.; Pfaff, M.; Schnabel, N.; Jaiser, S.; Vorobiev, A.; Müller, E.; Colsmann, A.; Scharfer, P.; Gerthsen, D.; Lemmer, U.; Barrena, E.; Schabel, W., Moving through the Phase Diagram: Morphology Formation in Solution Cast Polymer–Fullerene Blend Films for Organic Solar Cells. *ACS Nano* **2011,** 5, 8579-8590.

(223) DeLongchamp, D. M.; Kline, R. J.; Fischer, D. A.; Richter, L. J.; Toney, M. F., Molecular Characterization of Organic Electronic Films. *Adv. Mater.* **2011,** 23, 319-337.

(224) Fransishyn, K. M.; Kundu, S.; Kelly, T. L., Elucidating the Failure Mechanisms of Perovskite Solar Cells in Humid Environments Using In Situ Grazing-Incidence Wide-Angle X-ray Scattering. *ACS Energy Lett.* **2018,** 3, 2127-2133.

(225) Saliba, M.; Tan, K. W.; Sai, H.; Moore, D. T.; Scott, T.; Zhang, W.; Estroff, L. A.; Wiesner, U.; Snaith, H. J., Influence of Thermal Processing Protocol upon the Crystallization and Photovoltaic Performance of Organic–Inorganic Lead Trihalide Perovskites. *J. Phys. Chem. C* **2014,** 118, 17171-17177.

(226) Alsari, M.; Bikondoa, O.; Bishop, J.; Abdi-Jalebi, M.; Y. Ozer, L.; Hampton, M.; Thompson, P.; T. Hörantner, M.; Mahesh, S.; Greenland, C.; Macdonald, J. E.; Palmisano, G.; Snaith, H. J.; Lidzey, D. G.; Stranks, S. D.; Friend, R. H.; Lilliu, S., In situ simultaneous photovoltaic and structural evolution of perovskite solar cells during film formation. *Energy Environ. Sci.* **2018,** 11, 383-393.

(227) Barrit, D.; Cheng, P.; Tang, M.-C.; Wang, K.; Dang, H.; Smilgies, D.-M.; Liu, S.; Anthopoulos, T. D.; Zhao, K.; Amassian, A., Impact of the Solvation State of Lead Iodide on Its Two-Step Conversion to MAPbI3: An In Situ Investigation. *Adv. Funct. Mater.* **2019,** 29, 1807544.

(228) Szostak, R.; Marchezi, P. E.; Marques, A. d. S.; da Silva, J. C.; de Holanda, M. S.; Soares, M. M.; Tolentino, H. C. N.; Nogueira, A. F., Exploring the formation of formamidinium-based hybrid perovskites by antisolvent methods: in situ GIWAXS measurements during spin coating. *Sustainable Energy Fuels* **2019,** 3, 2287-2297.

(229) Kavadiya, S.; Strzalka, J.; Niedzwiedzki, Dariusz M.; Biswas, P., Crystal reorientation in methylammonium lead iodide perovskite thin film with thermal annealing. *J. Mater. Chem. A* **2019,** 7, 12790-12799.

(230) Hsieh, C.-M.; Yu, Y.-L.; Chen, C.-P.; Chuang, S.-C., Effects of the additives n-propylammonium or n-butylammonium iodide on the performance of perovskite solar cells. *RSC Adv.* **2017,** 7, 55986-55992.

(231) Chang, C.-Y.; Wang, C.-P.; Raja, R.; Wang, L.; Tsao, C.-S.; Su, W.-F., High-efficiency bulk heterojunction perovskite solar cell fabricated by one-step solution process using single solvent: synthesis and characterization of material and film formation mechanism. *J. Mater. Chem. A* **2018,** 6, 4179-4188.

(232) Schelhas, L. T.; Christians, J. A.; Berry, J. J.; Toney, M. F.; Tassone, C. J.; Luther, J. M.; Stone, K. H., Monitoring a Silent Phase Transition in CH3NH3PbI3 Solar Cells via Operando X-ray Diffraction. *ACS Energy Lett.* **2016,** 1, 1007-1012.

(233) Shimomura, T.; Takahashi, T.; Ichimura, Y.; Nakagawa, S.; Noguchi, K.; Heike, S.; Hashizume, T., Relationship between structural coherence and intrinsic carrier transport in an isolated poly(3-hexylthiophene) nanofiber. *Phys. Rev. B* **2011,** 83, 115314.

(234) Liu, D.; Gangishetty, M. K.; Kelly, T. L., Effect of CH3NH3PbI3 thickness on device efficiency in planar heterojunction perovskite solar cells. *J. Mater. Chem. A* **2014,** 2, 19873-19881.

(235) Dalvi, V. H.; Rossky, P. J., Molecular origins of fluorocarbon hydrophobicity. *Proc. Natl. Acad. Sci. U. S. A.* **2010,** 107, 13603-13607.

(236) Biffinger, J. C.; Kim, H. W.; DiMagno, S. G., The Polar Hydrophobicity of Fluorinated Compounds. *ChemBioChem* **2004,** 5, 622-627.

(237) Kundu, S.; Kelly, T. L., Hydrophobic polythiophene hole-transport layers to address the moisture-induced decomposition problem of perovskite solar cells. *Can. J. Chem.* **2018,** 97, 435-441.

(238) Guo, X.; Watson, M. D., Conjugated Polymers from Naphthalene Bisimide. *Org. Lett.* **2008,** 10, 5333-5336.

(239) Shi, C.; Yao, Y.; Yang; Pei, Q., Regioregular Copolymers of 3-Alkoxythiophene and Their Photovoltaic Application. *J. Am. Chem. Soc.* **2006,** 128, 8980-8986.

(240) Sheina, E. E.; Khersonsky, S. M.; Jones, E. G.; McCullough, R. D., Highly Conductive, Regioregular Alkoxy-Functionalized Polythiophenes: A New Class of Stable, Low Band Gap Materials. *Chem. Mater.* **2005,** 17, 3317-3319.

(241) Beek, W. J. E.; Wienk, M. M.; Kemerink, M.; Yang, X.; Janssen, R. A. J., Hybrid Zinc Oxide Conjugated Polymer Bulk Heterojunction Solar Cells. *J. Phys. Chem. B* **2005,** 109, 9505-9516.

(242) Liu, D.; Kelly, T. L., Perovskite solar cells with a planar heterojunction structure prepared using room-temperature solution processing techniques. *Nat. Photonics* **2014,** 8, 133-138.

(243) Kim, H.-S.; Lee, C.-R.; Im, J.-H.; Lee, K.-B.; Moehl, T.; Marchioro, A.; Moon, S.-J.; Humphry-Baker, R.; Yum, J.-H.; Moser, J. E.; Grätzel, M.; Park, N.-G., Lead Iodide Perovskite Sensitized All-Solid-State Submicron Thin Film Mesoscopic Solar Cell with Efficiency Exceeding 9%. *Sci. Rep.* **2012,** 2, 591.

(244) Liu, D.; Kelly, T. L., Perovskite solar cells with a planar heterojunction structure prepared using room-temperature solution processing techniques. *Nat. Photonics* **2013,** 8, 133.

(245) Huo, L.; Zhou, Y.; Li, Y., Alkylthio-Substituted Polythiophene: Absorption and Photovoltaic Properties. *Macromol. Rapid Commun.* **2009,** 30, 925-931.

(246) Yang, Y.-L.; Lee, Y.-H.; Lee, Y.-P.; Chiang, C.-J.; Shen, C.; Wu, C.-C.; Ohta, Y.; Yokozawa, T.; Dai, C.-A., Synthesis and characterization of poly(3-hexylthiophene)–poly(3-hexyloxythiophene) random copolymers with tunable band gap via Grignard metathesis polymerization. *Polym. Int.* **2014,** 63, 2068-2075.

(247) Hu, X.; Xu, L., Structure and properties of 3-alkoxy substituted polythiophene synthesized at low temperature. *Polymer* **2000,** 41, 9147-9154.

(248) Koeckelberghs, G.; Vangheluwe, M.; Samyn, C.; Persoons, A.; Verbiest, T., Regioregular Poly(3-alkoxythiophene)s: Toward Soluble, Chiral Conjugated Polymers with a Stable Oxidized State. *Macromolecules* **2005,** 38, 5554-5559.

(249) Loewe, R. S.; Ewbank, P. C.; Liu, J.; Zhai, L.; McCullough, R. D., Regioregular, Head-to-Tail Coupled Poly(3-alkylthiophenes) Made Easy by the GRIM Method: Investigation of the Reaction and the Origin of Regioselectivity. *Macromolecules* **2001,** 34, 4324-4333.

(250) Loewe, R. S.; Khersonsky, S. M.; McCullough, R. D., A Simple Method to Prepare Head-to-Tail Coupled, Regioregular Poly(3-alkylthiophenes) Using Grignard Metathesis. *Adv. Mater.* **1999,** 11, 250-253.

(251) Barbarella, G.; Bongini, A.; Zambianchi, M., Regiochemistry and Conformation of Poly(3-hexylthiophene) via the Synthesis and the Spectroscopic Characterization of the Model Configurational Triads. *Macromolecules* **1994,** 27, 3039-3045.

(252) Chen, T.-A.; Wu, X.; Rieke, R. D., Regiocontrolled Synthesis of Poly(3-alkylthiophenes) Mediated by Rieke Zinc: Their Characterization and Solid-State Properties. *J. Am. Chem. Soc.* **1995,** 117, 233-244.

(253) Leclerc, M.; Daoust, G., Structural effects in alkyl and alkoxy-substituted polythiophenes. *Synth. Met.* **1991,** 41, 529-532.

(254) Ballantyne, A. M.; Chen, L.; Dane, J.; Hammant, T.; Braun, F. M.; Heeney, M.; Duffy, W.; McCulloch, I.; Bradley, D. D. C.; Nelson, J., The Effect of Poly(3-hexylthiophene) Molecular Weight on Charge Transport and the Performance of Polymer:Fullerene Solar Cells. *Adv. Funct. Mater.* **2008,** 18, 2373-2380.

(255) Causin, V.; Marega, C.; Marigo, A.; Valentini, L.; Kenny, J. M., Crystallization and Melting Behavior of Poly(3-butylthiophene), Poly(3-octylthiophene), and Poly(3-dodecylthiophene). *Macromolecules* **2005,** 38, 409-415.

(256) Kim, J. S.; Lee, J. H.; Park, J. H.; Shim, C.; Sim, M.; Cho, K., High-Efficiency Organic Solar Cells Based on Preformed Poly(3-hexylthiophene) Nanowires. *Adv. Funct. Mater.* **2011,** 21, 480-486.

(257) Aronggaowa, B.; Toda, Y.; Ito, N.; Shikinaka, K.; Shimomura, T., Transparent Conductive Films Fabricated from Polythiophene Nanofibers Composited with Conventional Polymers. *Polymers* **2013,** 5, 1325.

(258) Wang, S.; Chen, Z.; Wang, Y., The effect of the electric-field on the phase separation of semiconductor-insulator composite film. *Chem. Commun.* **2015,** 51, 765-767.

(259) Wang, X.; Lee, W. H.; Zhang, G.; Wang, X.; Kang, B.; Lu, H.; Qiu, L.; Cho, K., Self-stratified semiconductor/dielectric polymer blends: vertical phase separation for facile fabrication of organic transistors. *J. Mater. Chem. C* **2013,** 1, 3989-3998.

(260) Kundu, S.; Kelly, T. L., Improving the moisture stability of perovskite solar cells by using PMMA/P3HT based hole-transport layers. *Mater. Chem. Front.* **2018,** 2, 81-89.

(261) Qiu, L.; Lim, J. A.; Wang, X.; Lee, W. H.; Hwang, M.; Cho, K., Versatile Use of Vertical-Phase-Separation-Induced Bilayer Structures in Organic Thin-Film Transistors. *Adv. Mater.* **2008,** 20, 1141-1145.

(262) Di Giacomo, F.; Razza, S.; Matteocci, F.; D'Epifanio, A.; Licoccia, S.; Brown, T. M.; Di Carlo, A., High efficiency CH3NH3PbI(3−x)Clx perovskite solar cells with poly(3-hexylthiophene) hole transport layer. *J. Power Sources* **2014,** 251, 152-156.

(263) Cai, B.; Xing, Y.; Yang, Z.; Zhang, W.-H.; Qiu, J., High performance hybrid solar cells sensitized by organolead halide perovskites. *Energy Environ. Sci.* **2013,** 6, 1480-1485.

(264) Nagarjuna, P.; Narayanaswamy, K.; Swetha, T.; Rao, G. H.; Singh, S. P.; Sharma, G. D., CH3NH3PbI3 Perovskite Sensitized Solar Cells Using a D-A Copolymer as Hole Transport Material. *Electrochim. Acta* **2015,** 151, 21-26.

(265) Kato, Y.; Ono, L. K.; Lee, M. V.; Wang, S.; Raga, S. R.; Qi, Y., Silver Iodide Formation in Methyl Ammonium Lead Iodide Perovskite Solar Cells with Silver Top Electrodes. *Adv. Mater. Interfaces* **2015,** 2, 1500195-n/a.

(266) Kulbak, M.; Gupta, S.; Kedem, N.; Levine, I.; Bendikov, T.; Hodes, G.; Cahen, D., Cesium Enhances Long-Term Stability of Lead Bromide Perovskite-Based Solar Cells. *J. Phys. Chem. Lett.* **2016,** 7, 167-172.

(267) Han, Q.; Bae, S.-H.; Sun, P.; Hsieh, Y.-T.; Yang, Y.; Rim, Y. S.; Zhao, H.; Chen, Q.; Shi, W.; Li, G.; Yang, Y., Single Crystal Formamidinium Lead Iodide (FAPbI3): Insight into the Structural, Optical, and Electrical Properties. *Adv. Mater.* **2016,** 28, 2253-2258.

(268) Yang, W. S.; Noh, J. H.; Jeon, N. J.; Kim, Y. C.; Ryu, S.; Seo, J.; Seok, S. I., High-performance photovoltaic perovskite layers fabricated through intramolecular exchange. *Science* **2015,** 348, 1234-1237.

(269) Fan, Y.; Meng, H.; Wang, L.; Pang, S., Review of Stability Enhancement for Formamidinium-Based Perovskites. *Solar RRL* **2019,** 3, 1900215.

(270) Dastidar, S.; Egger, D. A.; Tan, L. Z.; Cromer, S. B.; Dillon, A. D.; Liu, S.; Kronik, L.; Rappe, A. M.; Fafarman, A. T., High Chloride Doping Levels Stabilize the Perovskite Phase of Cesium Lead Iodide. *Nano Lett.* **2016,** 16, 3563-3570.

(271) Singh, T.; Miyasaka, T., Stabilizing the Efficiency Beyond 20% with a Mixed Cation Perovskite Solar Cell Fabricated in Ambient Air under Controlled Humidity. *Adv. Energy Mater.* **2018,** 8, 1700677.

(272) Wang, C.; Zhang, C.; Wang, S.; Liu, G.; Xia, H.; Tong, S.; He, J.; Niu, D.; Zhou, C.; Ding, K.; Gao, Y.; Yang, J., Low-Temperature Processed, Efficient, and Highly Reproducible Cesium-Doped Triple Cation Perovskite Planar Heterojunction Solar Cells. *Solar RRL* **2018,** 2, 1700209.

(273) Song, Z.; McElvany, C. L.; Phillips, A. B.; Celik, I.; Krantz, P. W.; Watthage, S. C.; Liyanage, G. K.; Apul, D.; Heben, M. J., A technoeconomic analysis of perovskite solar module manufacturing with low-cost materials and techniques. *Energy Environ. Sci.* **2017,** 10, 1297-1305.

(274) Kumar, D.; Stoichkov, V.; Brousseau, E.; Smith, G. C.; Kettle, J., High performing AgNW transparent conducting electrodes with a sheet resistance of 2.5 Ω Sq−1 based upon a roll-to-roll compatible post-processing technique. *Nanoscale* **2019,** 11, 5760-5769.

(275) Kwon, J.; Suh, Y. D.; Lee, J.; Lee, P.; Han, S.; Hong, S.; Yeo, J.; Lee, H.; Ko, S. H., Recent progress in silver nanowire based flexible/wearable optoelectronics. *J. Mater. Chem. C* **2018,** 6, 7445-7461.

(276) Guo, F.; Azimi, H.; Hou, Y.; Przybilla, T.; Hu, M.; Bronnbauer, C.; Langner, S.; Spiecker, E.; Forberich, K.; Brabec, C. J., High-performance semitransparent perovskite solar cells with solution-processed silver nanowires as top electrodes. *Nanoscale* **2015,** 7, 1642-1649.

(277) Kim, A.; Lee, H.; Kwon, H.-C.; Jung, H. S.; Park, N.-G.; Jeong, S.; Moon, J., Fully solution-processed transparent electrodes based on silver nanowire composites for perovskite solar cells. *Nanoscale* **2016,** 8, 6308-6316.

(278) Li, J.; Dong, Q.; Li, N.; Wang, L., Direct Evidence of Ion Diffusion for the Silver-Electrode-Induced Thermal Degradation of Inverted Perovskite Solar Cells. *Adv. Energy Mater.* **2017,** 7, 1602922.

(279) Huang, P.; Kazim, S.; Wang, M.; Ahmad, S., Toward Phase Stability: Dion–Jacobson Layered Perovskite for Solar Cells. *ACS Energy Lett.* **2019,** 4, 2960-2974.

(280) Lin, Y.; Fang, Y.; Zhao, J.; Shao, Y.; Stuard, S. J.; Nahid, M. M.; Ade, H.; Wang, Q.; Shield, J. E.; Zhou, N.; Moran, A. M.; Huang, J., Unveiling the operation mechanism of layered perovskite solar cells. *Nat. Commun.* **2019,** 10, 1008.

(281) Ahmad, S.; Guo, X., Rapid development in two-dimensional layered perovskite materials and their application in solar cells. *Chin. Chem. Lett.* **2018,** 29, 657-663.